



The author of the doctoral dissertation: Aleksandra Laska  
Scientific discipline: Mechanical Engineering

## **DOCTORAL DISSERTATION**

Title of doctoral dissertation: Influence of friction stir welding technological parameters on the properties of the joints of selected aluminum alloys

Title of doctoral dissertation (in Polish): Wpływ parametrów technologicznych zgrzewania tarcowego z przemieszaniem na własności złączy z wybranych stopów aluminium

Supervisor	Second supervisor
<i>Signature</i>	Not applicable <i>signature</i>
Dr hab. inż. Marek Szkodo, prof. GUT	-
Auxiliary supervisor	Cosupervisor
<i>Signature</i>	Not applicable <i>signature</i>
Dr inż. Grzegorz Gajowiec	-





## STATEMENT

The author of the doctoral dissertation: Aleksandra Laska

I, the undersigned, declare that I am aware that in accordance with the provisions of Art. 27 (1) and (2) of the Act of 4<sup>th</sup> February 1994 on Copyright and Related Rights (Journal of Laws of 2021, item 1062), the university may use my doctoral dissertation entitled: Influence of friction stir welding technological parameters on the properties of the joints of selected aluminum alloys

for scientific or didactic purposes.<sup>1</sup>

Gdańsk,.....

.....  
*signature of the PhD student*

Aware of criminal liability for violations of the Act of 4<sup>th</sup> February 1994 on Copyright and Related Rights and disciplinary actions set out in the Law on Higher Education and Science (Journal of Laws 2021, item 478), as well as civil liability, I declare, that the submitted doctoral dissertation is my own work.

I declare, that the submitted doctoral dissertation is my own work performed under and in cooperation with the supervision of Marek Szkodo, the auxiliary supervision of Grzegorz Gajowiec.

This submitted doctoral dissertation has never before been the basis of an official procedure associated with the awarding of a PhD degree.

All the information contained in the above thesis which is derived from written and electronic sources is documented in a list of relevant literature in accordance with Art. 34 of the Copyright and Related Rights Act.

I confirm that this doctoral dissertation is identical to the attached electronic version.

Gdańsk,.....

.....  
*signature of the PhD student*

I, the undersigned, agree to include an electronic version of the above doctoral dissertation in the open, institutional, digital repository of Gdańsk University of Technology.

Gdańsk,.....

.....  
*signature of the PhD student*

---

<sup>1</sup> Art 27. 1. Educational institutions and entities referred to in art. 7 sec. 1 points 1, 2 and 4–8 of the Act of 20 July 2018 – Law on Higher Education and Science, may use the disseminated works in the original and in translation for the purposes of illustrating the content provided for didactic purposes or in order to conduct research activities, and to reproduce for this purpose disseminated minor works or fragments of larger works.  
2. If the works are made available to the public in such a way that everyone can have access to them at the place and time selected by them, as referred to in para. 1, is allowed only for a limited group of people learning, teaching or conducting research, identified by the entities listed in paragraph 1.





## **DESCRIPTION OF DOCTORAL DISSERTATION**

**The Author of the doctoral dissertation:** Aleksandra Laska

**Title of doctoral dissertation:** Influence of friction stir welding technological parameters on the properties of the joints of selected aluminum alloys

**Title of doctoral dissertation in Polish:** Wpływ parametrów technologicznych zgrzewania tarcowego z przemieszaniem na własności złączy z wybranych stopów aluminium

**Language of doctoral dissertation:** English

**Supervisor:** dr hab. inż. Marek Szkodo, prof. GUT

**Auxiliary supervisor:** dr inż. Grzegorz Gajowiec

**Date of doctoral defense:** -

**Keywords of doctoral dissertation in Polish:** zgrzewanie tarcowe z przemieszaniem, FSW, stopy aluminium, mikrostruktura, korozja, twardość, własności mechaniczne, naprężenia własne, gęstość dyslokacji

**Keywords of doctoral dissertation in English:** friction stir welding, FSW, aluminum alloys, microstructure, corrosion, hardness, mechanical properties, residual stresses, dislocation density

**Summary of doctoral dissertation in Polish:** Celem niniejszej pracy było określenie wpływu parametrów technologicznych zgrzewania tarcowego z przemieszaniem na własności spoin z wybranych stopów aluminium, z uwzględnieniem naprężeń własnych oraz gęstości dyslokacji w złączach. Ponadto, celem niniejszej pracy było wytworzenie spoin wolnych od defektów, charakteryzujących się wysokimi własnościami mechanicznymi i elektrochemicznymi. W ramach dysertacji wytworzono jednoimienne spoiny ze stopu AA6082 oraz różnoimienne spoiny ze stopów AA6082/AA6060 oraz AA5083/AA6060. Analizowane parametry obejmowały geometrię narzędzia, prędkość liniową narzędzia, prędkość obrotową narzędzia oraz kąt jego pochylenia. Po inspekcji wizualnej, wytworzone spoiny badano pod kątem mikrostruktury, wytrzymałości na rozciąganie, twardości i odporności elektrochemicznej. Ponadto, przedmiotem badań była analiza wpływu naprężeń własnych oraz gęstości i mobilności dyslokacji na własności spoin. W pracy stwierdzono istotny wpływ parametrów technologicznych procesu na naprężenia w spoinach oraz charakter dyslokacji, co z kolei wpływało na wynikające własności mechaniczne i elektrochemiczne złączy.

**Summary of doctoral dissertation in English:** The purpose of this dissertation was to determine the effect of friction stir welding technological parameters on the properties of selected aluminum alloy joints, with consideration of the residual stresses and dislocation density in the joints. The goal of the present work was also to produce defect-free joints with high mechanical and electrochemical properties. In the dissertation, similar welds of AA6082 alloy and dissimilar welds of AA6082/AA6060 and AA5083/AA6060 alloys were produced. The parameters analyzed included tool geometry, tool traverse speed, tool rotational speed, and tool tilt angle. After visual inspection, the produced welds were studied for microstructure, tensile strength, hardness, and electrochemical resistance. In addition, the object of the study was to analyze the influence of residual stresses and the density and mobility of dislocations



on the properties of the welds. The thesis concluded that the technological parameters of the process had a considerable effect on the residual stresses in the welds and the nature of the dislocations, which consequently affected the resulting mechanical and electrochemical properties of the joints.

**Summary of doctoral dissertation in language, in which it was written\*\*:**  
not applicable

**Keywords of doctoral dissertation in language, in which it was written\*\*:**  
not applicable

*\*\*applies to doctoral dissertations written in other languages, than Polish or English*

## ACKNOWLEDGEMENTS

*I would like to express my sincere thanks to my supervisor, **Prof. Marek Szkodo**, for his substantive help, valuable comments, kindness, patience, and support during the entire process of preparing this dissertation.*

*I would also like to thank my auxiliary supervisor, **Dr. Grzegorz Gajowiec**. - for his scientific support, valuable advice, and friendliness.*

*Words cannot express my gratitude to **Prof. Pasquale Cavaliere** from the University of Salento. For his constant support and motivation, invaluable conversations, but most of all for the great inspiration – grazie mille.*

*I would also like to thank **all my Colleagues** from the Institute of Manufacturing and Materials Technology of the Faculty of Mechanical Engineering and Ship Technology of the Gdańsk University of Technology for all the discussions, joint research, and valuable advice.*

*I could not have undertaken this journey without my **Family and Friends**.*

*Thank you for your patience, and motivation. I am deeply indebted to **Michał** for his unwavering support and belief in me.*





**The following dissertation provides  
a guide to scientific publications  
in the form of a coherent thematic  
collection.**



# TABLE OF CONTENTS

LIST OF KEY DESIGNATIONS AND ABBREVIATIONS .....	15
LIST OF SCIENTIFIC PUBLICATIONS PROVIDING THE BASIS FOR THE DISSERTATION.....	17
1. INTRODUCTION .....	19
1.1. Aluminum and its alloys – properties, applications, and weldability .....	19
1.2. Friction stir welding .....	23
1.3. Parameters of friction stir welding of aluminum alloys and resulting properties of the joints .....	27
2. MOTIVATION AND OBJECTIVES OF THE THESIS.....	31
3. METHODOLOGY OF THE CONDUCTED RESEARCH .....	33
3.1. Selection of a tool geometry [P3].....	33
3.2. Manufacturing and process parameter analysis for similar AA6082 aluminum alloy joints [P4, P5].....	35
3.3. Manufacturing and process parameter analysis for dissimilar AA6082/AA6060 aluminum alloy joints [P6].....	36
3.4. Manufacturing and process parameter analysis for dissimilar AA5083/AA6060 aluminum alloy joints [P7].....	38
4. RESULTS AND DISCUSSION.....	41
4.1. Macro- and microstructure observations.....	41
4.1.1. <i>Visual inspection</i> .....	41
4.1.2. <i>Macrostructure</i> .....	41
4.1.3. <i>Microstructure</i> .....	42
4.2. Analysis of precipitates in aluminum joints .....	43
4.3. Hardness studies .....	44
4.4. Tensile strength of joints.....	46
4.5. Electrochemical properties of the joints .....	46
4.6. Residual stresses analysis.....	48
4.7 Dislocation density and mobility calculations .....	49
4.8. Description of major research observations.....	50
5. SUMMARY .....	52
6. REFERENCES .....	54
7. THE CONTENT OF THE PUBLICATIONS WITH A DESCRIPTION OF THE CONTRIBUTION OF THE DOCTORAL CANDIDATE .....	61
7.1. [P1] Friction Stir Welding – an overview of tool geometry and process parameters.....	61
7.1.1. Declaration of the contribution of the doctoral candidate.....	61
7.1.2. Content of the publication .....	62

<b>7.2. [P2] Manufacturing Parameters, Materials, and Welds Properties of Butt Friction Stir Welded Joints – Overview.....</b>	<b>84</b>
7.2.1. Declaration of the contribution of the doctoral candidate.....	84
7.2.2. Content of the publication .....	85
<b>7.3. [P3] Temperature evolution, material flow and resulting mechanical properties as a function of tool geometry during Friction Stir Welding of AA6082.....</b>	<b>131</b>
7.3.1. Declaration of the contribution of the doctoral candidate.....	131
7.3.2. Content of the publication .....	132
<b>7.4. [P4] Effect of Processing Parameters on Strength and Corrosion Resistance of Friction Stir-Welded AA6082.....</b>	<b>152</b>
7.4.1. Declaration of the contribution of the doctoral candidate.....	152
7.4.2. Content of the publication .....	153
<b>7.5. [P5] Analysis of Residual Stresses and Dislocation Density of AA6082 Butt Welds Produced by Friction Stir Welding.....</b>	<b>169</b>
7.5.1. Declaration of the contribution of the doctoral candidate.....	169
7.5.2. Content of the publication .....	170
<b>7.6. [P6] Corrosion Properties of Dissimilar AA6082/AA6060 Friction Stir Welded Butt Joints in Different NaCl concentrations. ....</b>	<b>185</b>
7.6.1. Declaration of the contribution of the doctoral candidate.....	185
7.6.2. Content of the publication .....	186
<b>7.7. [P7] Influence of the Tool Rotational Speed on Physical and Chemical Properties of Dissimilar Friction-Stir-Welded AA5083/AA6060 Joints.....</b>	<b>207</b>
7.7.1. Declaration of the contribution of the doctoral candidate.....	207
7.7.2. Content of the publication .....	208
<b>8. DECLARATIONS OF THE CONTRIBUTION OF CO-AUTHORS.....</b>	<b>229</b>
8.1. [P1] Friction Stir Welding – an overview of tool geometry and process parameters. ....	229
8.2. [P2] Manufacturing Parameters, Materials, and Welds Properties of Butt Friction Stir Welded Joints – Overview.....	230
8.3. [P3] Temperature evolution, material flow and resulting mechanical properties as a function of tool geometry during Friction Stir Welding of AA6082.....	231
8.4. [P4] Effect of Processing Parameters on Strength and Corrosion Resistance of Friction Stir-Welded AA6082.....	236
8.5. [P5] Analysis of Residual Stresses and Dislocation Density of AA6082 Butt Welds Produced by Friction Stir Welding.....	239
8.6. [P6] Corrosion Properties of Dissimilar AA6082/AA6060 Friction Stir Welded Butt Joints in Different NaCl concentrations. ....	243
8.7. [P7] Influence of the Tool Rotational Speed on Physical and Chemical Properties of Dissimilar Friction-Stir-Welded AA5083/AA6060 Joints.....	246
<b>9. SCIENTIFIC AND ORGANIZATIONAL ACHIEVEMENTS OF THE DOCTORAL CANDIDATE.....</b>	<b>249</b>



<b>9.1. Bibliometric indicators.....</b>	<b>249</b>
<b>9.2. List of publications .....</b>	<b>249</b>
<b>9.3. Conference presentations.....</b>	<b>251</b>
<b>9.4. Projects .....</b>	<b>252</b>
<b>9.5. Professional training .....</b>	<b>252</b>
<b>9.6. Research internships .....</b>	<b>253</b>
<b>9.7. Awards.....</b>	<b>253</b>
<b>9.8. Organizational activities .....</b>	<b>254</b>



## LIST OF KEY DESIGNATIONS AND ABBREVIATIONS

- AS – advancing side
- BM – base metal
- CFD – computational fluid dynamics
- CR – corrosion rate, [mm/year]
- E – Young’s modulus, [GPa]
- $E_{\text{corr}}$  – corrosive potential, [V]
- EDS – X-ray energy dispersive spectrometer
- EIS – electrochemical impedance spectroscopy
- FSW – friction stir welding
- H – hardness, [GPa]
- HAZ – heat-affected zone
- $i_{\text{corr}}$  – corrosion current density, [A/cm<sup>2</sup>]
- OCP – open circuit potential, [V]
- RS – retreating side
- SEM – scanning electron microscopy
- SZ – stir zone
- $T_m$  – melting temperature, [° C]
- TMAZ – thermo-mechanically affected zone
- UTS – ultimate tensile strength, [MPa]
- $v$  – tool traverse speed, [mm/min]
- WN – weld nugget
- XRD – X-ray diffraction
- $\alpha$  – tool tilt angle, [°]
- $\varepsilon$  – strain, [-]
- $\rho$  – dislocation density, [m<sup>-2</sup>]
- $\sigma_R$  – residual stress, [MPa]
- $\omega$  – tool rotational speed, [RPM]







# LIST OF SCIENTIFIC PUBLICATIONS PROVIDING THE BASIS FOR THE DISSERTATION

## Review publications:

[P1] **Laska A.\***, Szkodo M., Friction Stir Welding – an overview of tool geometry and process parameters. Under Review in International Journal of Materials Research (IF = 0.678, 40 points of the Polish Ministry of Science and Higher Education)

[P2] **Laska A.\***, Szkodo M., Manufacturing Parameters, Materials, and Welds Properties of Butt Friction Stir Welded Joints – Overview. *Materials*. 13(21), 4940; 2020. doi:10.3390/ma13214940. (IF = 3.748, 140 points of the Polish Ministry of Science and Higher Education)

## Original research publications:

[P3] **Laska A.\***, Sadeghi B., Sadeghian B., Taherizadeh A., Szkodo M., Cavaliere P., Temperature evolution, material flow and resulting mechanical properties as a function of tool geometry during Friction Stir Welding of AA6082. Major Revision (II round of Under Review after Major Revision status) in *Journal of Materials Engineering and Performance* (IF = 2.036, 70 points of the Polish Ministry of Science and Higher Education)

[P4] **Laska A.**, Szkodo M., Koszlow D., Cavaliere P.\*, Effect of Processing Parameters on Strength and Corrosion Resistance of Friction Stir-Welded AA6082. *Metals*. 12(2), 192; 2022. doi:10.3390/met12020192. (IF = 2.695, 70 points of the Polish Ministry of Science and Higher Education)

[P5] **Laska A.\***, Szkodo M., Cavaliere P., Moszczyńska D., Mizera J., Analysis of Residual Stresses and Dislocation Density of AA6082 Butt Welds Produced by Friction Stir Welding. *Metallurgical and Materials Transactions A – Physical Metallurgy and Materials Science*. 54, 211-225; 2023. doi:10.1007/s11661-022-06862-4. (IF = 2.726, 200 points of the Polish Ministry of Science and Higher Education)

[P6] **Laska A.\***, Szkodo M., Pawłowski Ł., Gajowiec G., Corrosion Properties of Dissimilar AA6082/AA6060 Friction Stir Welded Butt Joints in Different NaCl concentrations. *International Journal of Precision Engineering and Manufacturing – Green Technology*. 10, 457-477; 2023. doi: 10.1007/s40684-022-00441-z. (IF = 4.66, 200 points of the Polish Ministry of Science and Higher Education)

[P7] **Laska A.**, Szkodo M., Cavaliere P.\*, Perrone A., Influence of the Tool Rotational Speed on Physical and Chemical Properties of Dissimilar Friction-Stir-Welded AA5083/AA6060 Joints. *Metals*. 12(10), 1658; 2022. doi: 10.3390/met12101658. (IF = 2.695, 70 points of the Polish Ministry of Science and Higher Education)

\* corresponding author

Total *Impact Factor* and points of the Polish Ministry of Science and Higher Education for the published publications ([P2], [P4], [P5], [P6], [P7]) amounted to respectively

- IF: 19.238 (11.533<sup>#</sup>)
- Points of the Polish Ministry of Science and Higher Education: 680 (461<sup>#</sup>)

<sup>#</sup> considering the percentage contribution of the doctoral candidate in the preparation of the above publications.



# 1. INTRODUCTION

This chapter is devoted to describing the theoretical issues related to the topic of the dissertation. The first part briefly characterizes the properties of aluminum alloys with particular emphasis on their weldability, the second part characterizes the friction stir welding method. The third part of the chapter refers to a brief review of applications of the friction stir welding method to aluminum alloys with a special emphasis on the process parameters. An extensive literature review and analysis of the current state of the art is included in two review articles provided as part of this dissertation.

## 1.1. Aluminum and its alloys – properties, applications, and weldability

Aluminum is a silver-white-colored element with the chemical symbol Al and an atomic number 13. Its amount in the Earth's crust is estimated at 8 %. With this respect, it ranks as the third most abundant element after oxygen (45,5 %) and silicon (25,7 %) [1]. It can be found in many minerals, always in combination with other elements. It is a metal with relatively good corrosion resistance and good conductivity of electricity and heat. Aluminum is one of the lightest metals on Earth [2]. Its specific weight of approximately  $2.70 \text{ kg/dm}^3$  is the equivalent of about one-third that of steel ( $7.9 \text{ kg/dm}^3$ ) or copper ( $8.93 \text{ kg/dm}^3$ ) [3]. The use of aluminum in its pure form is limited, mainly because of its low strength. Yield strength is almost always lower than that of steel [4]. However, this disadvantage is balanced by its lower density, allowing the cross-sectional area of the component to be increased until the desired strength is reached while retaining a lower weight. Pure aluminum is used for electrical conductors, in the manufacturing of foils, in powders for plating utensils, paints, and as a component of alloys [5].

Much greater use is found in aluminum alloys, which are also called light alloys due to their low density. The most commonly used alloying elements are copper, silicon, magnesium, manganese, nickel, and zinc. Alloying additives primarily increase strength, corrosion resistance and improve machinability [6]. Aluminum alloys are divided into cast and wrought alloys. Wrought and cast aluminum alloys employ distinct identification systems. Cast aluminum alloys have a four- or five-digit number followed by a decimal point. The numeral in the hundredth place indicates the component of the alloy, while the digit after the decimal point identifies the form (cast shape or ingot). The most commonly accepted naming system for wrought alloys is consistent with the International Alloy Designation System [7]. Each alloy is characterized by four numbers. The first identifies the principal alloying elements, the second - if it is different than 0 - specifies the alloy variety, while the third and fourth digits define the specific alloy in the series. The series identification is presented in Table 1.

Table 1 – Identification designation of wrought aluminum alloys

Series	Description
1000	Essentially pure aluminum, with a minimum 99 % aluminum content by weight. Can be work hardened.
2000	Alloys with copper as a main alloying element. Can be precipitation hardened to strengths comparable to steel. Formerly defined as duralumin.
3000	Alloys with manganese as a main alloying element. Can be work hardened.
4000	Alloys with silicon as a main alloying element.
5000	Alloys with magnesium as a main alloying element. Most 5000 series alloys include also manganese. Characterized by very good corrosion resistance.
6000	Alloys with magnesium and silicon as the main alloying elements. Can be precipitation hardened, but not to a high strength.
7000	Alloys with zinc as a main alloying element. Most 7000 series alloys include also magnesium and copper. Can be precipitation hardened to the highest strengths of any aluminum.
8000	Alloys with alloying elements not covered by the above series (for example with lithium as a main alloying element).

Both cast and wrought aluminum alloys can be further divided into heat-treatable and non-heat-treatable alloys. The temper indication follows the alloy designation number with a dash, a letter, and a one- or three-digit number. The designations of tempers are presented in Table 2.

Table 2 – Designation of tempers for aluminum alloys

Temper designation	Description
F	As fabricated
H	Cold worked, with or without thermal treatment, among them: H1 - Strain hardened, with no thermal treatment H2 - Strain hardened, partially annealed H3 - Strain hardened, stabilized by low-temperature heating
O	Annealed
T	Heat treated to produce stable tempers, among them: T1 - Cooled from hot working, naturally aged T2 - Cooled from hot working, cold worked, naturally aged T3 - Solution heat treated, cold worked T4 - Solution heat treated, naturally aged T5 - Cooled from hot working, artificially aged T6 - Solution heat treated, artificially aged T7 - Solution heat treated, stabilized T8 - Solution heat treated, cold worked, artificially aged T9 - Solution heat treated, artificially aged, cold worked T10 - Cooled from hot working, cold worked, artificially aged
W	Solution heat treated

Aluminum, and especially its alloys, due to its unique properties - high strength relative to low density, ability to self-passivation, good electrical and thermal conductivity, and good machinability result in an increasing construction application of this material. Aluminum alloys are second behind only steel in use as structural metals [3]. In Western Europe, the production of primary aluminum (from ore) is over 3 million tons per year and the production of secondary or recycled aluminum is almost 2 million tons per year [8]. The economic issues of using aluminum alloys are making them increasingly popular in many industries. Due primarily to its low specific weight, aluminum alloys are widely used in the aerospace industry [9]. Aluminum alloy panels are used in Airbus 380 construction [10]. In Comac ARJ21 aircraft there is about 50 kg aluminum alloy skin plate [11]. Aluminum alloys, especially from series 6000 are

commonly used in the high-speed train industry to produce profiles and carriage components [12,13]. By reducing the weight of components of aluminum, the energy needed to accelerate and decelerate a car is lower. Owing to that, the payload of a vehicle can be increased. It might significantly affect the machine running costs [14]. Aluminum alloys are also widely used in civil engineering. The history of aluminum alloys in the bridge industry dates back to 1933, when a bridge on an existing structure, the Smithfield Street Bridge in Pittsburgh, USA, was constructed from this material [15]. The Arvida Bridge is currently the longest aluminum bridge structure with a center span of 88.4 meters [16]. Aluminum alloys are also extremely popular in the automotive industry. Back in 1913, NSU produced a car with a body made entirely of aluminum. Another examples, among many others, are Ford 2000 aluminum body both and a higher class Audi A8 made of stamped aluminum parts [17]. The 5000 and 6000 series alloys are applied in shipbuilding due to their good corrosion resistance [18–20].

Welding is a common manufacturing process employed in the production of aluminum alloy components. It is an effective and economical way of joining two or more pieces of metal together. Aluminum welding is a very extensive issue, and only the correct proposal of the method and parameters of the process will make it possible to obtain reliable welds. Determination of the weldability of aluminum alloys strictly depends on their chemical composition. In general, some aluminum alloys can be considered relatively weldable, while some alloying additives cause the use of conventional welding methods to be difficult. Aluminum itself also exhibits properties that are challenging from a weldability perspective. Aluminum has a high thermal conductivity (about  $200 \frac{W}{m \cdot K}$ ) [21]. This value is almost four times higher than for steel [22]. This makes it difficult to concentrate energy during welding, which is why high-energy sources such as laser or electron beam welding are particularly recommended [23–25]. Due to the high thermal conductivity, the cooling of the metal in the weld pool is also a concern. Rapid solidification of the liquid metal affects the increased risk of porosity in the weld. Aluminum alloys are one of the metals most susceptible to porosity [26]. Particularly dangerous in terms of a potential porosity of a weld is hydrogen. Hydrogen appears to be present due to water vapor or hydrocarbon contamination from oils, greases, lubricants, and solvents. It is crucial to clean the components to be joined and the filler wire immediately before the process, as well as to use shielding gases. The chemical composition of the alloy also affects the porosity of the weld [27]. Magnesium reduces hydrogen absorption into the liquid metal, up to twice with an alloying addition of magnesium in aluminum of 6 %. Copper and silicon, in contrast, have the opposite effect [8]. As mentioned earlier, aluminum has the ability to be passivated. This means that a tight layer of  $Al_2O_3$  is formed on the surface of the metal, which protects the metal from corrosion [28]. However, it should be noted that the  $Al_2O_3$  melting temperature is about 2050 °C, while aluminum alloys melt at about 660 °C. This negatively



affects the weldability of aluminum alloys. Therefore, achieving the melting point of the aluminum alloy during welding is insufficient to melt the aluminum oxide. A continuous or fractured ceramic layer will remain in the weld. It might result in severe incomplete fusion defects. It is extremely important to remove the oxide layer immediately before welding. Aluminum oxide can be removed by mechanical processes (brushing with a stainless steel brush, cutting with a saw, or grinding with semi-flexible grinding discs), chemical etching, or pickling [8]. Degreasing should be also performed before mechanical cleaning. Another important aspect is the high coefficient of thermal expansion of aluminum ( $23.6 \cdot 10^{-6} \frac{1}{^{\circ}\text{C}}$ ). Its value is twice as high as for steel. This causes large welding deformations [29]. High stresses affect the occurrence of weld cracks. Solidification cracking occurs in the center line of the weld, typically extending along the line during solidification. Solidification cracking can also occur in the weld crater at the completion of the welding procedure. Liquation cracking can also be observed in the case of welding of aluminum alloys. It occurs in the heat-affected zone, when layers with a low melting point are formed at the grain boundaries. They are not able to withstand the contraction stresses created during the solidification and cooling of the weld metal [30].

It should be noted that most of the issues affecting the weldability problems of aluminum are caused by a change in the state of the metal. Therefore, it is preferable to use joining methods in which the melting point of the metal is not reached. Thus, fusion welding techniques are being replaced by solid-state welding techniques. An example of such a method is friction stir welding (FSW).

## **1.2. Friction stir welding**

Friction stir welding is an innovative solid-state welding method, invented in 1991 in The Welding Institute of the United Kingdom [31]. This method, initially dedicated to aluminum alloys, today is also successfully used to join copper and its alloys [32–34], magnesium and its alloys [35–37], steels and ferroalloys [38–40], and even titanium and its alloys [41–43]. It is also widely used in joining polymers [44–46], metallic and polymer matrix composites [47–49]. It also allows the manufacture of dissimilar joints, with materials that differ significantly in mechanical and physicochemical properties [50–52]. According to its definition, friction stir welding is a solid-state welding process. This implies that the materials can be joined without reaching their melting point. Thus, several problems occurring during the fusion welding process due to a change of a state, described before, can be eliminated [53].

The principle of forming a joint by friction stir welding is relatively simple. The essence of creating a joint is to use a tool with a specially designed geometry, which, by its very principle, should be non-consumable. In this regard, a very important issue is the proper selection of the

material for the tool. The tool consists of two integral parts - a pin and a shoulder. The tool put into rotational motion plunges into the material on the joint line. Due to the forces involved, it is necessary to rigidly fix the components to be welded, the surfaces of which on the joint line must be pressed together. During the process, the contact between the surfaces of the shoulder and the workpieces to be welded must be strictly controlled. One of the process parameters is the axial force and plunge depth of the shoulder. The tool pin is plunged into the material and is primarily responsible for mixing the material. Then the tool, all the time performing rotational motion at a certain speed, begins to move in a linear motion along the joint line, forming the weld. In the course of the process, the kinetic energy of a non-consumable welding tool fitted with a uniquely devised shoulder and pin transforms into thermal energy generated by the friction of a tool traveling along the edge of a contact line. Heat and softening of the material are provided by the friction generated on the interface between the tool and components. The rotating tool leads to the plastic deformation of the material of the workpiece. Plasticized material is mixed and extruded around the tool in a backward direction and a final joint is formed.

A butt joint is shown in Figure 1 as an illustration of the process, however, FSW allows the fabrication of joints of other types. Typically, this method is used to produce butt welds, lap welds, and corner welds [54,55].



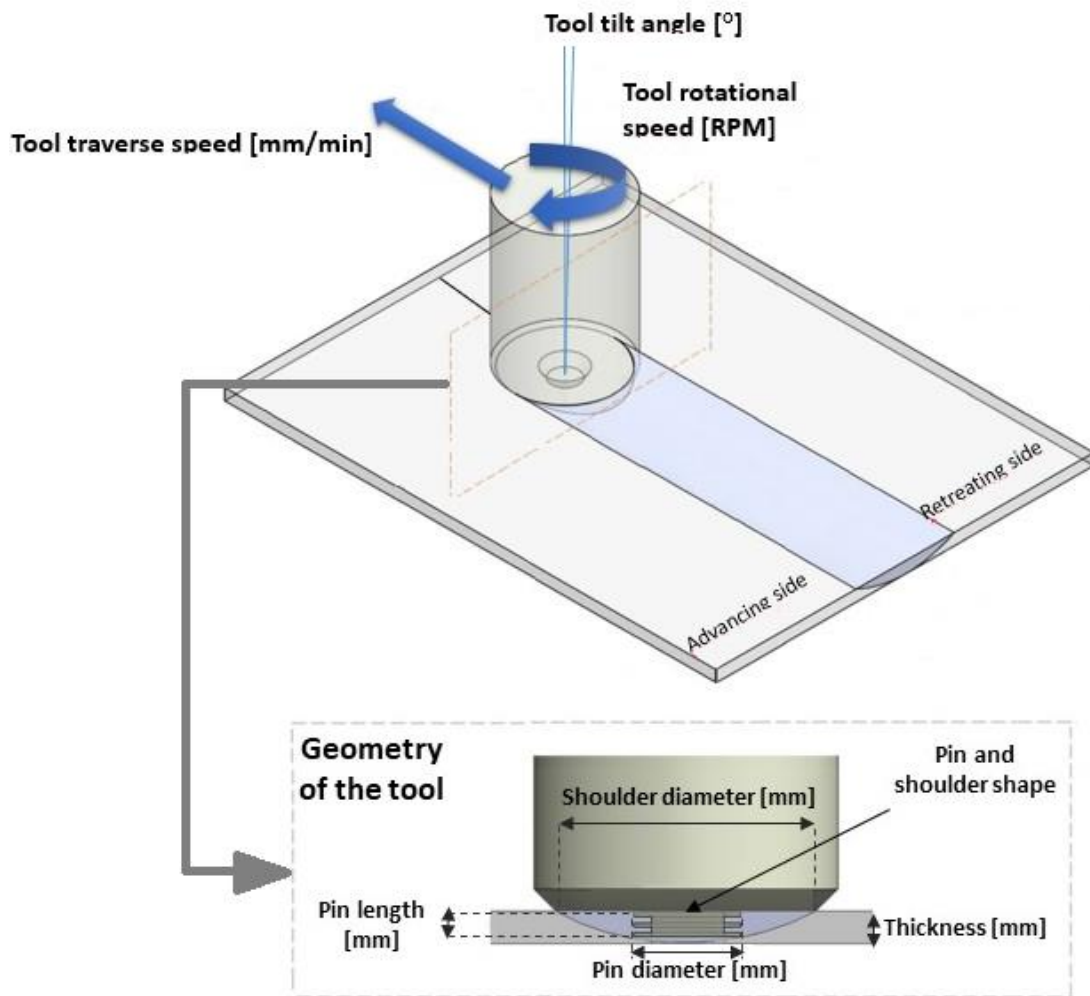


Figure 1. Schematic illustration of friction stir welding process.

This method is considered a green technology. Since the melting point of materials is not reached during the process, energy consumption is lower. In addition, the process uses a non-consumable tool. There is no need for fluxes, electrodes, or shielding gases. Furthermore, the amount of CO<sub>2</sub> released into the atmosphere can be reduced [56]. The control of the process in the FSW method is easier to be realized. After establishing the optimal set of parameters there is no need to apply non-destructive testing. This allows for reducing the pollution generated by sprays used in magnetic and visual inspections or, in the case of applying X-ray tests, radiation exposure.

One of the main process parameters is the geometry of the tool. The geometry directly affects the process of generating frictional forces, the amount of heat introduced, and the nature of the mixing of the plasticized material. The special design of the tool has been a matter of concern since the FSW method was considered a big step in metal joining techniques. A ratio of diameters of the shoulder and the pin is critical from the heating aspects, while a tool design

governs process loads, properties, and uniformity of microstructure. There are plenty of shapes of the shoulder and the pin. They can also be modified with features like threads, scrolls, or grooves. The process temperature is always lower than the melting point of the welded material, due to the forces acting during the process, special attention should be focused on the uncontrolled degradation of the tool. Therefore, it is necessary to select the tool material so that it is characterized by high wear resistance, high hardness and is suitable for operation at corresponding temperatures. These materials include but are not limited to tool steels [50,57], high-speed steel (HSS) [58,59], metal carbides [60–62], nitrides [63–65], and ceramics [66,67].

In addition to tool geometry, the most important process parameters are tool rotational speed ( $\omega$ ), tool traverse speed (called also welding speed) ( $v$ ), and tool tilt angle ( $\alpha$ ). Stirring and mixing of the material around the pin is a result of the rotation of the tool. The linear movement of the tool moves the mixed material from the front to the back of the probe and it accomplishes the welding process. It is also possible to observe an increase in the temperature in all the zones characteristic for FSW joints caused by a tilt angle increase [68]. The reason for that is an increase in the friction heat caused by a wider contact area between the workpiece and the pin as well as increased plastic work of deformation energy. A large tilt angle additionally favors high hydrostatic pressure and high temperature which, in turn, translate into enhanced integrity of the nugget. However, severe tool wear may occur due to high hydrostatic pressure and high temperature in the welding zone. In the majority of cases tilt angle ranges from 0 to 3° [52,69–71].

Due to the solid-state nature of the FSW process, a very specific microstructure occurs. In the most general terms, there are four zones to be distinguished: stir zone (SZ), thermo-mechanically affected zone (TMAZ), heat-affected zone (HAZ), and base metal (BM). Formation of the stir zone also known as a nugget results from the recrystallization occurring in the thermo-mechanically affected zone. For aluminum alloys, it is characteristic that fine grain size material composes the nugget. Additionally, it is considered that it experiences plastic deformations resulting from the interaction with the pin of the welding tool. Occasionally, a nugget may mimic the pin intersection shape. A unique transition zone occurring between the base material and the nugget zone is one of the characteristic features of the FSW process. Thermo-mechanically affected zone (TMAZ) is exposed to deformation and temperature during the process. In this zone, elongated grains of parent material are to a large extent deformed in an upward direction following the pattern surrounding the nugget zone. The material in TMAZ is subjected to plastic deformation but because of insufficient deformation strain, there is no recrystallization. Exposure to high temperatures during the FSW process causes the dissolution of some precipitates in the TMAZ. Moreover, it has been demonstrated that grains contained within TMAZ can possibly feature a high-density of sub-boundaries [72]. The heat-affected

zone is located beyond TMAZ and is subjected to a thermal cycle. There are no plastic deformation of any kind in the HAZ. The grain structure of the HAZ is unchanged concerning the parent material, however, the exposure to temperatures significantly affects the structure of the precipitate. The HAZ is sufficiently heated during the process so it alters the properties of that material without any plastic deformation. The modification of properties in the HAZ includes changes in toughness, ductility, corrosion susceptibility, and strength.

The solid-state welding characteristics of this method make the joints have high mechanical strength and electrochemical properties. Also, the risk of defects in the joints is lower. The next subsection of this dissertation will focus on the analysis of the properties of FSW joints, with particular emphasis on aluminum alloy welds.

Due to the above advantages over fusion welding techniques, there is growing interest in this method. To date, hundreds of patents have been approved for this method, and the number of scientific publications is growing exponentially [73,74].

### **1.3. Parameters of friction stir welding of aluminum alloys and resulting properties of the joints**

The FSW method was originally intended to be used to join aluminum and its alloys. Although in recent years it has been successfully applied to join other materials as well, it is aluminum and its alloys that are most often joined using this method. Because of the difficulty of welding aluminum with conventional methods, FSW provides an effective solution for welding these materials, providing reliability, easy process parameter control, and reduced risk of defects contributing to reduced mechanical properties of the welds. The temperature is typically maintained below 500 °C during the FSW process of aluminum and its alloys [75]. Large deformations caused by mechanical mixing of the material during welding cause measurement of temperature to be difficult. It is suggested that it is near the solidus temperature [76].

The parameters of the FSW process significantly affect the properties of the resulting joints. However, the current state of knowledge does not allow to clearly define these relationships. Tool geometry is one of the most important parameters in the FSW process, as it directly affects the generation of heat generation and material flow. The material movement around the pin depends on the geometrical features of the tool. The special design of the tool has been a matter of concern since the FSW method was considered as a big step in metal joining techniques. The possible thickness of workpieces, the type of material to be welded, and possible welding positions are conditioned by the tool geometry [54]. Zhao et al. [77] proposed four different tool geometries to join AA2014 - cylindrical pin, tapered pin, cylindrical screw thread pin, and tapered screw thread pin. It was observed that the use of a taper screw thread pin

resulted in the formation of a joint of high quality. Elangovan et al. [78] applied five different tool pin geometries (triangular, square, straight cylindrical, threaded cylindrical, and tapered cylindrical) to weld AA2219. Only the application of a square pin profile tool resulted in the production of defect-free welds with high mechanical properties. Krasnowski et al. [79] proposed a triflute pin profile to joint AA6082 alloy by the FSW method. Ji et al. [80] found that a thread design of a pin is critical in terms of the plasticized material flow in AA2024 alloy. In the studies of Aldanondo et al. [81] it was observed that the application of the tool characterized by 3 flats and mixed thread resulted in enhanced properties of the AA2060 and AA2099 joints compared to the joints produced with a conventional threaded tool. Ramanjaneyulu et al. [82] found that the heating generation rate and the peak temperatures achieved are comparatively higher for non-circular pin sections, increasing with the number of flat profiles. Vairis et al. [83] observed the highest weld efficiency achieved with a cylindrical pin tool for AA7075 friction stir welded joints. The current state of knowledge does not allow the selection of a one reliable tool geometry to produce defect-free welds with advanced properties. Analyzed scientific reports are often contradictory, and it is impossible to draw clear conclusions.

Apart from the geometry of the tool, the dimensions of the tool also have a significant impact on the FSW process. The analysis of tool dimensions mainly considers the length of the pin, its diameter, the diameter of the shoulder, and the ratio of the diameter of the shoulder to the diameter of the pin. The length of the pin affects the penetration level of the plasticized material in the nugget zone. The length of the pin must be sufficient to penetrate the weld. However, it should not be too long so that it does not rub against the backing plate. The heat input in the FSW process highly depends on the dimensions of the tool. In investigations of friction stir welding of aluminum alloys by Dehghani et al. [52], Khodir and Shibayanagi [84], Cavaliere et al. [85], Leitao et al. [86], and Peel et al. [87] it was concluded that the thermal input has a bigger impact on weld properties than the mechanical deformation by the tool. The ratio of shoulder diameter to the pin diameter, for aluminum and its alloys, should be in the range of 2.5:1 to 4.5:1 [84–90].

Another crucial variable during the FSW of aluminum and its alloys is a tool tilt angle. A tilt angle of 0 to 3 is recommended for aluminum alloys [88–92]. Ensuring the proper angle of the tool helps the mixed material re-coalesce at the rear end of the tool. It is possible to observe an increase in the temperature in the nugget, heat-affected zone, and thermo-mechanically affected zone caused by a tilt angle increase [68]. The reason for that is an increase of the friction heat caused by a larger contact area between the workpiece and the pin as well as increased plastic work of deformation energy. A large tilt angle additionally favors high hydrostatic pressure and high temperature which, in turn, translate into enhanced integrity of the nugget [93]. However,



severe tool wear may occur due to high hydrostatic pressure and high temperature in the welding zone. The relation between the tilt angle and microstructure and mechanical properties of dissimilar aluminum alloy joints AA6061/AA5083 was investigated by Hamid et al. [90]. In their experiments, tilt angles within the range of 0 to 4 ° with 1 ° increments were used. Micrographic examination of the welded joints showed that a tilt angle equal to 3 ° produced a defect-free joint. Lower tilt angles produced joints with tunnel defects in the bottom section of the weld nugget which, in turn, caused the strength reduction. Vijayaraghavan et al. [94] produced welds of dissimilar aluminum alloys applying various tilt angles ranging from 1 to 3 °, with a plate of AA7075 alloy on the advancing side and AA6082 on the retreating side. The relation between the tilt angle and tensile strength was investigated. The experiments proved that a higher tilt angle applied during the process produces a weld with a lower tensile strength. Additionally, the increase in the tilt angle translated into a decrease in the impact strength of the welded joint.

The Friction Stir Welding method is mostly characterized by two parameters: tool rotational rate ( $\omega$ ) and tool traverse speed ( $v$ ) along the line of edges to be welded [95]. The rotation movement of a tool can be in a clockwise or counterclockwise direction. Choosing the proper tool traverse speed and tool rotational rate is a fundamental problem in the design of the FSW process. The traverse and rotational speed values of the tool depend primarily on the thickness of the components to be welded. In the study of Raweni et al. [55] Taguchi method was applied to propose the optimized set of the FSW parameters to weld AA5083 plates. The mathematical formulas enabled to predict the characteristics of the welds prepared under different conditions. The results show that the traverse speed has the highest effect on the fracture toughness and the crack propagation energy is the highest when the tool traverse speed is the highest. The optimum parameters for the total input energy and the energy for crack initiation were equal to 600 RPM for the rotational speed and 125 mm/min for the tool traverse speed. Balasubramanian [96] investigated the macrostructure of FSW joints using five different aluminum alloys – AA1050, AA6061, AA2024, AA7039, and AA7075. All the fabricated welds were analysed at low magnification by an optical microscope. Different values of the tool traverse speed at the constant tool rotational speed of 1200 RPM were used. Of the five tool traverse speed values used, the welds fabricated with the traverse speed of 135 mm/min for AA1050 alloy resulted in defect-free joints. The welding speed of 75 mm/min for AA2024, 100 mm/min for AA6061, 45 mm/min for AA7039, and 22 mm/min for AA7075 alloys resulted in the formation of defect-free joints. The same investigations were conducted for the varying tool rotational speed. The constant tool traverse speed of 75 mm/min was kept. Joints fabricated with a rotational speed equal to 900 RPM for AA1050, 1100 RPM for AA6061, 1200 RPM for AA2024, 1300 RPM for AA7039, and 1500 RPM for AA7075 alloys resulted in the formation of defect-free joints.

For other combinations of parameters defects like pin holes, tunnel defects, piping defects, kissing bonds, and cracks occurred. Feng et al. [97] investigated the microhardness of the FSW AA7075 alloy welds made using different tool traverse speed values. At a constant tool rotational speed of 800 RPM, as the tool traverse speed increased from 100 to 400 mm/min, the hardness values increased and the width of the lowest hardness zone decreased. The same investigations were made for the constant tool traverse speed and the increasing tool rotational speed from 800 to 1200 RPM. The width of the low hardness zone had almost no change and the hardness values did not change significantly either. However, the location of the low hardness zone changed and moved outward. The same relationship for FSW AA6061 alloy was proved by Feng et al. [98]. In the research conducted by Zhang et al. [99] AA2024 plates were successfully welded by the FSW method at the varying tool rotational rate from 400 to 1200 RPM in steps of 400 RPM and at the tool traverse speed equal to 100, 200, and 400 mm/min. The ultimate tensile strength increased from 408 to 451 MPa, respectively with an increase of the tool traverse speed, for the joints made with a tool rotational speed of 800 RPM. The elongation at those parameters increased with an increase in the tool traverse speed.

Considering the extensive literature review in [P1] and [P2] included in this dissertation, it can be concluded that the selection of appropriate traverse and rotational speed of the tool, tool geometry and tool tilt angle is still a current issue. The present state of knowledge does not allow to unambiguously determine the optimal parameters of the FSW process, and the analysed scientific publications are often in contradiction with each other.

## 2. MOTIVATION AND OBJECTIVES OF THE THESIS

The research thesis of the doctoral dissertation claims that it is possible to shape the physicochemical and mechanical properties of similar and dissimilar joints of selected aluminum alloys by appropriate selection of the parameters of the FSW process, which includes both the geometry and inclination of the tool and its rotational and traverse speed. The correlation between the FSW process parameters and the properties of the joints of selected aluminum alloys is possible due to the change in the dislocation structure of the joint material depending on the selected process parameters.

The scientific objective of the dissertation was to determine the influence of friction stir welding process parameters on the residual stresses, dislocation densities and mobility, and the resulting mechanical and electrochemical properties of joints from selected aluminum alloys.

The functional objective of the dissertation was to produce joints of selected aluminum alloys without defects, which are characterized by high mechanical and electrochemical properties.

The current state of knowledge does not allow a clear determination of the influence of the parameters of the friction stir welding process on the stress state of the resulting joints and the densities, types, and mobility of dislocations. These properties significantly affect the mechanical and electrochemical properties of the joints. The process is influenced by parameters such as tool geometry, tool traverse and rotational speed, and tool tilt angle. These parameters not only determine the mixing process of the plasticized material but also affect the amount of heat introduced and the distribution of forces. This translates directly into the resulting residual stresses in the material and also completely changes the material properties. The material subjected to the welding process is characterized not only by a different microstructure but also by changed dislocation densities. The types of dislocations and their mobility also change. This directly affects the resulting mechanical and electrochemical properties.

The expected result of the work was to design a tool and propose parameters for the friction stir welding process in such a way that defect-free joints of selected aluminum alloys with high strength and corrosion resistance could be achieved.

The scope of work conducted as part of this dissertation included:

1. An extensive literature review on the determination of the state of the art from the field of friction stir welding method with particular emphasis on the application to joining aluminum alloys.
2. Design of tools to produce sound similar and dissimilar joints from aluminum alloys.

3. Selecting the appropriate methodology for producing FSW welds - selection of traverse and rotational speed of the tool, tool tilt angle, and tool geometry in order to obtain similar and dissimilar joints from selected aluminum alloys that do not exhibit serious material discontinuities and defects.
4. Studies of produced similar joints of AA6082 alloy, and dissimilar AA6060/AA6082 and AA5083/AA6060 alloys joints- macro- and microstructural studies, analysis of precipitation, measurements of hardness and tensile strength, electrochemical tests, studies on residual stresses and dislocation density and mobility.
5. Analysis of the effects of process parameters such as tool geometry, tool traverse speed, tool rotational speed, and tool tilt angle on the mechanical, electrochemical, and physicochemical properties of AA6082, AA6060, and AA5083 alloy joints.
6. Analysis of the obtained research results and preparation of scientific publications.

The result of the work conducted as part of the dissertation is a series of coherent collection of publications. It includes 2 review articles and 5 research articles. 5 articles have been published and 2 are in review. All of these articles have been published or are in review in JCR-listed journals.



### 3. METHODOLOGY OF THE CONDUCTED RESEARCH

#### 3.1. Selection of a tool geometry [P3].

Choosing the proper tool geometry is a key aspect of the successful manufacturing of sound joints. On the basis of an extensive review of the literature, with a particular focus on the effect of tool geometry on the properties of fabricated joints (section “2. *Geometry of the tool*” in [P1]), two different tool geometries were selected. The exact geometries of the proposed tools, with their full dimensioning, are presented in Figure 1.

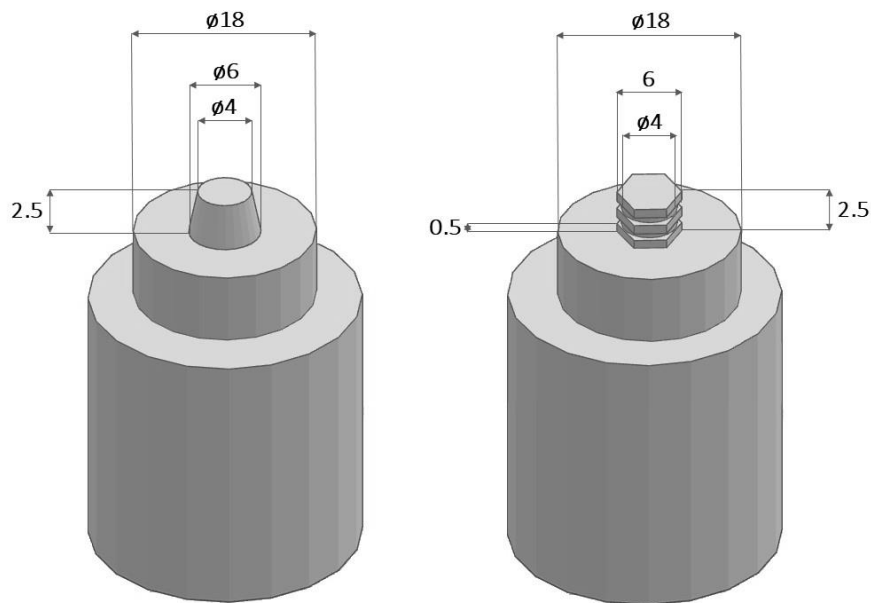


Figure 1. Schematic illustration of the geometries of the tools used for Friction Stir Welding.

Both tools were designed in such a form that they possessed interchangeable pins. According to the FSW process, the tool should be made non-consumable by its nature. However, due to the high temperatures of the process and the forces applied, there is a risk of gradual degradation of the tool. In order to keep the pin's geometry constant, due to its interchangeability, the cost of using such a tool is much lower. The tools also have extendable pins, so the length can be defined in a controlled manner. The suggested length of the pins has been proposed for welding 3 mm thick metal sheets. The material of the pins was 73MoV52 tool steel, with a hardness of 58 HRC (Wilson Mechanical Instrument Co. Inc., USA). Both the body of the tool and its shoulders are made of X210Cr12 tool steel, with a hardness of 61 HRC (Wilson Mechanical Instrument Co. Inc., USA). Based on the literature review in [P2], the traverse speed of the tool was proposed to be equal to 250 mm/min, the tool rotational speed of 1000 RPM, and the tool tilt angle of 2 °.

The material used was AA6082 aluminum alloy, solution heat-treated and artificially aged to T651 condition. The rolled sheets of 3 mm in thickness were used to perform computer simulations and the friction stir welding process.

Analysis of the influence of tool geometry involved computer simulations in COMSOL Multiphysics® 5.3 software with an applied computational fluid dynamics (CFD) approach. In order to simulate the heat generated in the tool/ workpiece interface, the steady-state solution was used. In this model, the tool was placed in the center of the part and the temperature distribution model was considered based on the steady-state heat transfer equation. Also, the heat generation process was divided into two general parts: heat produced by friction and heat produced by plastic deformation, and this issue was considered in the models.

The welding process was conducted on a conventional milling machine (FU251, Friedrich Engels Kazanluk, Bulgaria). The employed process parameters were identical as in the case of conducted simulations – the tool traverse speed was 250 mm/min, the tool rotational speed was 1000 RPM and the tool tilt angle was 2 °.

The welded samples were investigated with respect to their macro- and microstructure. The specimens were cut in cross-sections. The samples were wet-ground to the final gradation of #4000 and polished with a 1µm diamond suspension. Firstly, the metallographic samples were etched in a 2(wt) % NaOH solution for 60 s. Then, the samples were immersed for 10 s in a solution of 4 g KMnO<sub>4</sub>, 1 g NaOH, and 100 mL of distilled water (Weck's etchant). The microstructural observations were performed using an optical microscope (BX51, OLYMPUS, Japan), in accordance with the ASTM E3 standard - Standard Guide for Preparation of Metallographic Specimens. The average grain size was calculated with the use of the linear intercept method, according to ASTM E112-13 standard - Standard Test Methods for Determining Average Grain Size.

The microhardness distribution measurements were performed on the cross-sections of the produced joints at a distance of 1.5 mm from the weld face (central line of cross-sections). The length of the measurement line was 32 mm and measurements were made every 0.25 mm. This allowed observation of all zones of the joint – a weld nugget, a thermo-mechanically affected zone, the heat-affected zone, and a base metal. A Vickers microhardness tester (Future-Tech FM-800, Japan) with a load of 1 N was used.

The tensile properties of the produced welds were performed with a universal testing machine (Zwick/Roell 100, Germany). Three samples were tested in order to calculate their standard deviation. The fracture surfaces of the samples after the tensile tests were investigated by a high-resolution scanning electron microscope (SEM) (Phenom XL, Thermo Fisher Scientific, Netherlands) with a backscattered electron detector (BSE).



### 3.2. Manufacturing and process parameter analysis for similar AA6082 aluminum alloy joints [P4, P5].

After selecting a proper tool geometry, which was a tool with a hexagonal pin with grooves, the next research focused on the selection of other process parameters – tool traverse speed, tool rotational speed, and the tool tilt angle. Based on the literature review in [P2] two different tool traverse speeds (200 and 250 mm/min), two different tool rotational speeds (1000 and 1250 RPM), and two different tool tilt angles (0 and 2 °) were selected. The welding process was conducted on a conventional milling machine (FU251, Friedrich Engels Kazanluk, Bulgaria). The process was performed on AA6082-T6 aluminum alloy sheets with a thickness of 3 mm.

The produced samples were cut and wet ground to the final gradation #4000 and polished with a diamond suspension. To observe macrostructure the Keller's etchant was used, consisting of 95 mL H<sub>2</sub>O, 2.5 mL HNO<sub>3</sub>, 1.5 mL HCl and 1 mL HF. For the microscopic observations, the procedure introduced in the previous section was also employed with the use of an optical microscope (BX51, OLYMPUS, Japan). Moreover, the electron backscattered diffraction method (EBSD) was applied using scanning electron microscopy (Hitachi SU-70, Japan). The samples were prepared with the use of argon ion polishing at 5 kV (Hitachi IM4000, Japan). EBSD maps were collected in the nugget zone, thermo-mechanically affected zone, heat-affected zone, and the base metal with an acceleration voltage equal to 20 kV with a step size of 0.2 μm. The analysis of the data was performed with HKL Channel 5 software (Oxford Instruments, United Kingdom).

The nugget zones of the welds produced were also analyzed for phase composition by X-ray diffraction method (XRD) (Philips X'Pert Pro, Netherlands). The diffractometer with Cu K $\alpha$  radiation was applied with a wavelength of 0.15418 nm. It operated with 30 kV and 50 mA. The patterns were observed with a Bragg-Brentano geometry over 2 $\theta$  range 20-90 ° with a step of 0.02 °. The Rietveld refinement method was used for the quantitative analysis of phases using MAUD software.

To calculate crystallite sizes and microstrains in the nugget zones and the base metal the Williamson-Hall analysis was proposed. The procedure is described in detail in [P5]. To calculate residual stresses based on the value of microstrains, the indentation method was applied (Nanotest Vantage, Micro Materials, United Kingdom). The maximum force during indentation tests was equal to 5 N, the loading and unloading time during each experiment was 20 s, and the dwell period of 5 s was defined. The specimens were subjected to 10 measurements to calculate standard deviations. The values of reduced Young's modulus were obtained. The calculated values of the Young's modulus were analyzed in terms of residual stresses. To calculate the

dislocation densities the modified Williamson-Hall procedure was applied. The method is described in detail in [P5]. Also, to calculate the dislocation mobility, the dwell period during the indentation tests was studied.

The microhardness tests were performed with the force of 2 N with a Vickers indenter (Future-Tech FM-800, Japan) in three lines on the cross-section of the joints – top (0.5 mm from the weld face), middle (1.5 mm from the weld face) and bottom (2.5 mm from the weld face). This approach allowed to observe the shape of the exact zones on the cross-sections.

The welds produced were also studied for their electrochemical resistance. The tests were performed according to the standard ASTM G5-94. The tests were conducted in an environment simulating seawater. The proposed concentration of sodium chloride was equal to 3.5 %, which is the average salinity of seawater in the world. The temperature of the process was kept constant (20 °C), using potentiostat/galvanostat (Atlas 0531, Atlas Solich, Poland). A three-electrode system was used (a counted electrode – platinum, a reference – a calomel electrode, a working electrode – a weld nugget). The open circuit potential (OCP) was measured in 60 min and the corrosion curves were obtained within the range of potential from – 2 to + 1 V. The Tafel extrapolation method was applied to determine the corrosive potential ( $E_{\text{corr}}$ ) and corrosion current density ( $i_{\text{corr}}$ ) (Atlas 0532 Electrochemical unit). Scanning electron microscopy (SEM) with a backscattered electron detector was applied to observe the surfaces of the samples after electrochemical tests (Phenom XL, Thermo Fisher Scientific, Netherlands).

The whole analysis was performed also with respect to the revolutionary pitch values, defined as the tool rotational speed divided by the tool traverse speed. The revolutionary pitch indicated the heat input during the process.

### **3.3. Manufacturing and process parameter analysis for dissimilar AA6082/AA6060 aluminum alloy joints [P6].**

The results obtained on the similar AA6082 joints were decided to be confronted with the results of the studies on dissimilar aluminum alloy joints. The dissimilar aluminum alloy joints were produced with AA6082 alloy on the advancing side of the joint and AA6060 alloy on the retreating side. Both alloys were solution heat-treated to T6 condition. The thickness of the sheets was equal to 3 mm. The process was performed on the same milling machine (FU251, Friedrich Engels Kazanluk, Bulgaria). The tool with a hexagonal pin with grooves was used. Based on the previous results, it was decided to keep the tool inclined, with the tool tilt angle equal to 2 °. The tool rotational speed was kept constant at 1250 RPM. Two different tool traverse speeds were chosen: 160 mm/min and 200 mm/min.

The microstructure observations methodology was identical to the procedure presented for AA6082 aluminum alloy joints.

Also, the XRD testing was performed with the same procedure as described before. Based on the Williamson-Hall analysis, the crystallite size and microstrains were calculated for the welds nuggets and base metal. Nanoindentation tests were performed with a pyramidal Berkovich indenter, and 25 measurements were performed for each specimen to calculate deviations. The maximum force was equal to 10 N, the loading time was equal to 20 s, and the unloading time was 15 s. The dwell time with the maximum force was equal to 5 s. The distance between indents was equal to 200  $\mu\text{m}$ . From the obtained reduced Young's modulus value, the Young's modulus was calculated, based on the Olivier -Pharr procedure. Considering microstrains and Young's modulus values, the residual stresses were calculated.

Based on the data obtained during indentation tests, the geometrically necessary dislocation density, statistically stored dislocation density, and the mobility of dislocation were calculated for all the tested specimens.

To discuss the electrochemical performance of the produced welds, the potentiodynamic and electrochemical impedance spectroscopy (EIS) tests were performed. The research was aimed at determining corrosion resistance in seawater. Due to the varying salinity concentrations of seawater around the world, especially in the Baltic Sea, tests were performed at three different NaCl concentrations: 0.2, 0.7, and 1.2 %. Electrochemical measurements were completed with the use of a potentiostat/galvanostat (Atlas 0531, Atlas Solich, Poland). The same three-electrode system was proposed. The OCP data were collected within 60 min. The EIS studies were performed at the frequency from 1 Hz to 100 kHz. The signal amplitude was equal to 10 mV, and 10 points per decade were collected. The EIS spectra were collected at the OCP potential value. To fit the obtained EIS data, the ZView software (Scribner Associates Inc., USA) was applied. The  $\chi^2$  representing goodness of fit was kept on a level lower than  $10^{-3}$ . Potentiodynamic studies were performed within the range of potential from -2 to +1 V. The scan rate was 1 mV/s. AtlasLab software (Atlas Solich, Poland) was used to perform Tafel extrapolation. Before and after the electrochemical tests the weight of the samples was measured (Pioneer PA114CM/1, OHAUS, Switzerland) with an accuracy of 0.1 mg.

Before and after the corrosion studies the surface of all the samples was observed by a high-resolution SEM (Jeol, JSM-7800 F, Jeol, Japan) with a BED detector at 5 kV voltage.

The degradation tests were also performed on the welded samples and both base metals. All the samples were immersed in individual containers containing 200 mL of a solution of H<sub>2</sub>O with NaCl with a concentration of 3.5 %. After 168 h of keeping the samples immersed at room temperature, the weight loss of the samples was checked (Pioneer PA114CM/1, OHAUS,



Switzerland). The accuracy of the collected data was equal to 0.1 mg. The corrosion rate (CR) was collected using the formula:

$$CR \left[ \frac{mm}{year} \right] = \frac{\Delta m [g]}{d \left[ \frac{g}{cm^3} \right] \cdot S [cm^2] \cdot t [h]} \cdot 87600$$

where  $\Delta m$  is a weight loss (in g),  $d$  is the density of the alloy (for both alloys it's equal to 2.710 g/cm<sup>3</sup>),  $S$  is the surface area of the sample (in cm<sup>2</sup>) and  $t$  is the time of immersion (in h). The tests were performed 3 times for each type of specimen to calculate the deviation.

### **3.4. Manufacturing and process parameter analysis for dissimilar AA5083/AA6060 aluminum alloy joints [P7].**

The study included the characterization of dissimilar FSWed butt joints, with AA5083-O alloy on the advancing side and AA6060-T on the retreating side. The thickness of both sheets was equal to 3 mm. The process was performed on the same milling machine (FU251, Friedrich Engels Kazanluk, Bulgaria). The tool with a hexagonal pin with grooves was used. In this study, the tool tilt angle was kept constant at the value of 2 °. The tool traverse speed was also constant and equal to 100 mm/min. The welding process was carried out at different tool rotational speed values – 800, 1000, and 1200 RPM.

The microstructure observations methodology was identical to the procedure presented for similar AA6082 aluminum alloy joints and dissimilar AA6082/AA6060 aluminum alloy joints.

Indentation tests were employed to perform hardness measurements on the cross-sections of the produced welds. The tests were performed in the middle line of the cross-section (1.5 mm from the weld face). The indents were spaced at 0.5 mm. 60 independent measurements were performed for each sample in the line of the length of 30 mm. This methodology allowed to examine all the zones of the joints – weld nugget, thermo-mechanically affected zone, heat-affected zone, and the base metal. A diamond Berkovich indenter was used, and the applied force was equal to 1 N. The loading and unloading time was 20 s, the dwell time was 5 s. Based on the obtained data not only hardness values were discussed. Also, the density of geometrically necessary dislocations and statistically stored dislocations, and the dislocation mobility were calculated based on the procedure described in detail in [P7].

The potentiodynamic studies were performed with the use of potentiostat/galvanostat (Atlas 0531, Atlas Solich, Poland). The selected NaCl concentration was equal to 3.5 %, the average concentration of seawater worldwide. Disc samples cut from the nugget zone of the produced joints and the base metals with an area of 1 cm<sup>2</sup> were tested. The temperature of the solution during the entire process was kept constant at 20 °C. A three-electrode system defined before was used. The OCP measurement was performed with a procedure explained before. The

corrosion curves were also obtained with the procedure the same as for the previous samples, as well as the Tafel extrapolation. The samples after the corrosion investigations were observed with the use of a high-resolution SEM with BSE (Phenom XL, Thermo Fisher Scientific, Netherlands).

The whole analysis was performed also with respect to the revolutionary pitch values, defined as the tool rotational speed divided by the tool traverse speed. The revolutionary pitch indicated the heat input during the process.

Figure 2 presents the diagram of the methodology of the conducted research within the framework of the doctoral dissertation, with respect to the order of the executed activities. Detailed procedures of the conducted tests are presented in the original research papers (P3-P8) that are the subject of this dissertation.

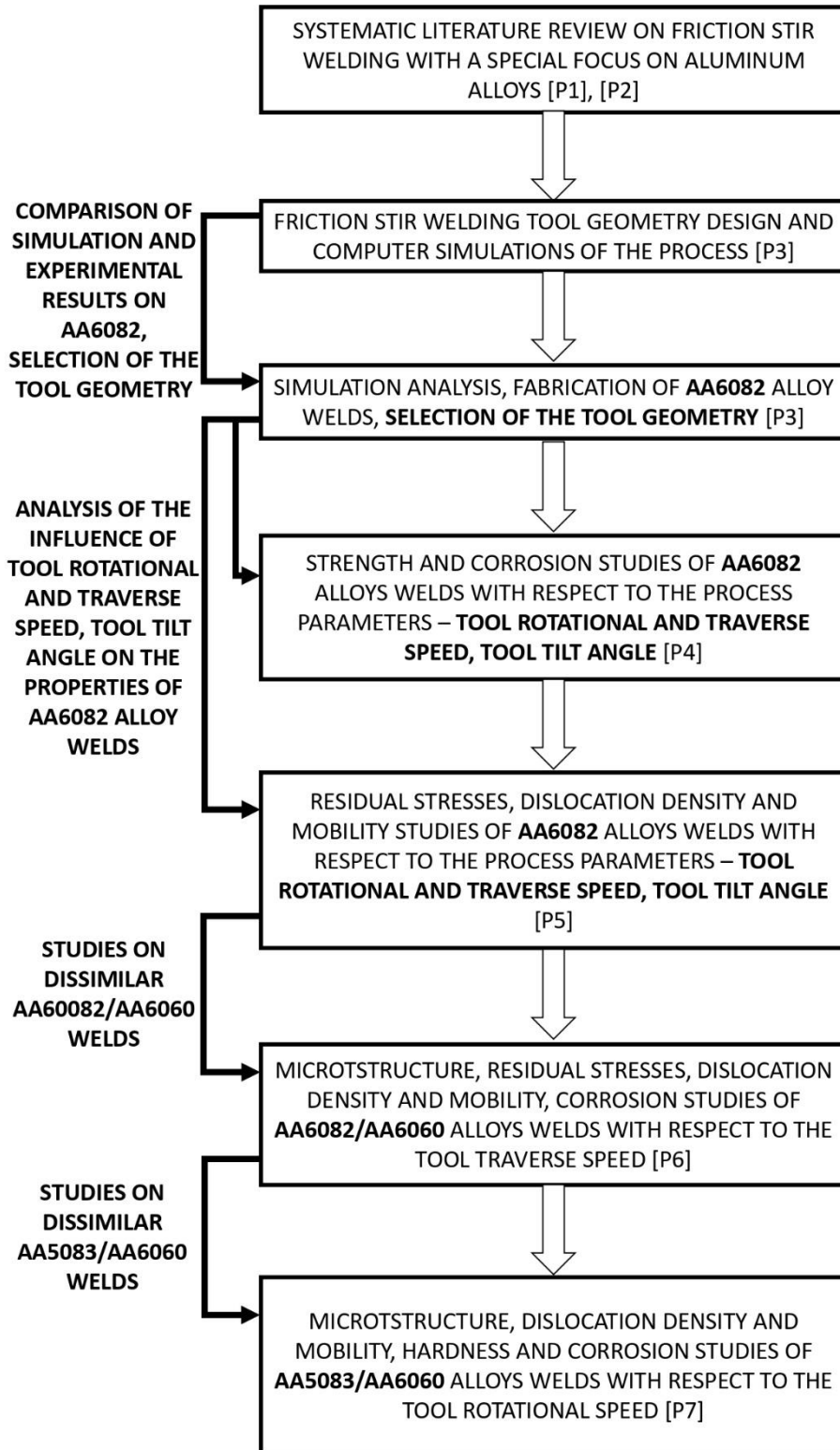


Figure 2. Diagram of the conducted research within the framework of the doctoral dissertation



## 4. RESULTS AND DISCUSSION

### 4.1. Macro- and microstructure observations

#### 4.1.1. Visual inspection

For all the fabricated welds, the analysis began with visual inspections of the joints. In every case, there were no significant defects found. The studies conducted in this dissertation allowed the production of welds without serious weld discontinuities for both similar AA6082 and dissimilar AA6060/AA6082 and AA5083/AA6060 joints.

In the case of AA6082 joints, no material outflow was found [P3, P4, P5]. The weld faces exhibited no serious imperfections like lack of bonding or grooves. Only in the case of the AA6082 weld produced with a tapered cylindrical pin, some cavitation losses could be observed [P3]. For all the AA6082 joints produced with a tool with a hexagonal pin with grooves non-defected weld seam was found. The performed computer simulations revealed that by applying the hexagonal pin with grooves, the amount of heat generated during the process is around 20 % higher when compared to the process with the use of a tapered cylindrical pin. It is claimed that the key factors determining the quality of the weld are adequate heat input and proper stirring of the plasticized material. Therefore, for the weld produced with the hexagonal pin, higher heat input and better plasticization and mixing of the material resulted in the formation of a non-defective weld seam.

In the case of AA5083/AA6060 welds produced with a hexagonal pin with grooves, little material outflow was found in the case of the samples produced with tool rotational speeds of 800 and 1000 RPM, but by applying the tool rotational speed of 1200 RPM no irregularities on the weld seam were noted on the surface [P7]. With an increase in the tool rotational speed, there is a higher heat input to the material. Thus, sufficient plasticizing and mixing resulted in the formation of a non-defective weld.

#### 4.1.2. Macrostructure

Based on the studies on similar AA6082 joints in [P3], it can be concluded that the geometry of the tool strongly influences the macrostructure of the weld. In the case of the weld produced with a tapered cylindrical pin, the width of the stir zone was larger. The width of the stir zone measured in the center line of the cross-section was equal to 8.25 mm for the tapered cylindrical pin, and 6.80 mm for the case of the hexagonal pin with grooves. Despite the temperature being about 5 % higher when using a complex pin compared to a straight pin and the greater total heat input, the mixing process differed between the two cases. The simulation results showed that mixing the plasticized material through the complex pin lead to the trapping of the material in some areas and the flow around the pin was reduced. With a simple pin, due to the slope, the

material found a simpler flow around the pin, so it had a higher velocity. It resulted in a wider stir zone area. Also, in [P5], the width size of the stir zones was measured in the mid-thickness of the cross-sections of AA6082 joints. The results were discussed in terms of other process parameters – tool traverse and rotational speed, as well as tool tilt angle. When the tool tilt angle was  $0^\circ$ , the width of the stir zone was lower, compared to the welds where the tool tilt angle of  $2^\circ$  was applied. Also, by decreasing the tool traverse speed from 250 mm/min to 200 mm/min, a larger stir zone was found. This is due to the greater heat input when the tool traverse speed is reduced and when the tool is tilted. For the AA6082 weld produced with a non-tilted tool, the lowest rotational speed (1000 RPM) and the highest tool traverse speed (250 mm/min), the width of the stir zone was the lowest and was equal to 6.43 mm.

Macrostructure studies on dissimilar AA6060/AA6082 aluminum alloy joints revealed that the curvature of the top surface of the welds could be observed due to the tool shoulder plunge into the aluminum components for both applied tool traverse speed values – 160 mm/min and 200 mm/min. Also, a little material outflow was noted on both the advancing and the retreating side [P6].

In the macroscopic observations of AA5083/AA6060 joints a characteristic basin shape of the weld nugget was also distinguished [P7].

#### 4.1.3. Microstructure

Based on the microstructural observations, in all the cases the asymmetries of the weld cross-sections were observed, indicating the advancing (AS) and retreating (RS) sides of the welds. In all the cases, the characteristic shape of the nugget zone could be observed, as a result of the move of the pin between sheets. It is a typical basin shape of this zone. Four characteristic zones for the friction stir welding process were recognized in all the cases [P3, P4, P5, P6, P7]. Typically for a FSW joint, the weld nugget zone consists of a fine-grained structure formed by the recrystallization process in the stir zone (SZ). Also, the thermo-mechanically affected zone (TMAZ) and the heat-affected zone (HAZ) could be distinguished.

For AA6082, in [P3] the average grain size in the SZ of the weld produced with the simple pin was equal to about  $14 \pm 1 \mu\text{m}$ , and for the weld produced with the hexagonal pin  $10 \pm 1 \mu\text{m}$ . When using a hexagonal pin with grooves, due to the higher heat input, the recrystallization process occurred more efficiently, resulting in a finer-grained microstructure. In [P4] the average grain size in the stir zone of AA6082 welds was also discussed in terms of other process parameters – tool traverse speed, tool rotational speed, and the tool tilt angle. It was revealed that when the tilted tool was used during the process, the average grain size was lower compared to the welds produced with the same tool traverse and rotational speed, but  $0^\circ$  tool tilt angle. This is due to higher heat input when an inclined tool is used. For the same reason, when



increasing the tool rotational speed, and decreasing the tool traverse speed, a small grain size was observed. The lowest grain size in the stir zone equal to  $9.8 \pm 1.5 \mu\text{m}$  was observed for the sample produced with 1250 RPM for rotational speed, 200 mm/min for traverse speed, and  $2^\circ$  for the tool tilt angle. On the contrary, the largest grains with an average size of  $17.3 \pm 1.5 \mu\text{m}$  were observed when the highest traverse speed (250 mm/min), the lowest rotational speed (1000 RPM), and the non-inclined tool were applied. Also, in [P4] the relationship between the average grain size in the nugget zone of all the tested samples and the revolutionary pitch, defined as the tool rotational speed divided by the tool traverse speed was presented. Also, EBSD studies confirmed the existence of four characteristic for the FSW process zones, based on the example of AA6082 aluminum alloy joints in [P5].

Microstructure observations on AA6060/AA6082 joints revealed the existence of the SZ, TMAZ, and HAZ. Two welds produced with different tool traverse speeds - 160 mm/min and 200 mm/min displayed no significant differences in the grain size of the nugget zone.

In experiments on AA5083/AA6060 joints, it was noted that the stir zone experienced the highest heat input and high plastic deformation during stirring through the mandrel. This caused recrystallization in the zone and led to the finest microstructure. The TMAZ on both sides of the welds also experienced high temperature peaks and plastic deformation due to stirring by the tool. The recrystallization process was not observed in TMAZ due to insufficient heat input. HAZ on both sides was formed only due to thermal evolution. No recrystallization process occurred in the heat-affected zones. Approaching both parent metals, the material was already characterized by the original microstructures of both alloys.

#### **4.2. Analysis of precipitates in aluminum joints**

On the basis of the XRD tests performed, the analysis of precipitates in welds and parent metals was conducted. The quantitative phase analysis was performed using Rietveld refinement of the obtained XRD patterns. For AA6082 similar aluminum alloy joints it was concluded that after the FSW process, the precipitate content in the weld nugget is reduced for all the produced joints regardless of process parameters. In [P5] the dependence of the total percentage of precipitates on the value of the rotational/linear speed ratio was determined. Such analysis was performed for joints produced with a non-inclined tool and with an inclination of  $2^\circ$ . It was observed that the use of a tilted tool resulted in more significant dissolution of the precipitate, while the use of a non-tilted tool resulted in a reduction in dissolution precipitation. It was connected to a higher heat input while the tilted tool was applied during the process of FSW. The minimum reduction of precipitation fraction was observed for the tool tilt angle of  $0^\circ$ , the tool rotational speed of 1000 RPM, and the tool traverse speed of 250 mm/min. The reduction was equal to 48 % compared to the base material. The maximum reduction of the precipitation fraction

(almost 64 % of reduction compared to the base AA6082 metal), was noted for the tool traverse speed of 1250 RPM, the tool rotational speed of 200 mm/min, and the tool tilt angle of 2 °. When increasing the tool rotational speed the heat input is also increased and the precipitation dissolution is higher, leading to the reduction of their fraction. The same when decreasing the tool traverse speed. Also, by applying the inclined tool, the heat input during the process is increased, compared to the use of the non-inclined tool. Stress on the leading edge of the tool is increased when the tool is inclined, and this is the reason for improved frictional heating.

In the case of dissimilar welds AA6060/AA6082, the main diffraction peaks in the XRD pattern were indexed as originating from pure aluminum. Also, peaks corresponding to the phases of the main alloying elements – magnesium, silicon, and manganese were found.

In the FSW process, heat is generated due to friction, leading to an increase in material temperature. Aluminum alloys in the 6000 series containing magnesium and silicon as the main alloying additives belong to the group of precipitation-hardened alloys. Due to the precipitates, the material is strengthened and the movement of dislocations is inhibited in the crystal structure. Dissolution of precipitates in the metal leads to a decrease in hardness and strength. Advanced mixing of the material during the process and recrystallization of the grains are the basis for ensuring high joint strength. At the same time, the dissolution of precipitates by increasing the temperature in the process reduces the strength of precipitation-hardened alloys.

#### **4.3. Hardness studies**

For similar AA6082 aluminum alloy joints, the hardness profiles on the cross-sections were presented for the welds produced with two proposed tools [P3]. As described in the section 4.1.3, a smaller grain size was noted in the SZ in the weld produced with a hexagonal pin with grooves and it strongly influenced the hardness of this sample. Higher heat input when applying more complex tool geometry during the FSW process resulted in greater grain refinement due to more efficient recrystallization, which enhanced the strength of the SZ. In the stir zone, the value of  $89.9 \pm 3.1$  HV was found for the weld produced with a hexagonal pin. The measured microhardness of the base metal AA6082 was established as  $96 \pm 3.9$  HV. In the case of a cylindrical pin, the value of  $86.2 \pm 2.7$  was observed in the SZ. Microscopic observations allowed to observe lower grain size in the nugget zone of the weld produced with the hexagonal pin. The reduction of the grain size led to an increase in the hardness, according to the Hall-Petch relationship. The lowest values of approximately 62 and 67 HV were observed in the HAZ on the advancing side of the welds produced with the cylindrical and hexagonal pins, respectively. A more significant decrease in hardness in the HAZ on the advancing side is consistent with the results of the simulations performed. There, a greater heat input was observed on the advancing side for the process involving both tools. As the temperature in the HAZ

increased, the process of dissolution of precipitates was intensified, leading to the decrease in strength in this zone. This is the reason for the significant decrease in hardness in this area. In the case of the weld produced with a cylindrical tool, the microhardness on the cross-sections revealed that the nugget zone was larger, which was also proved by macroscopic imaging explained in the section 4.1. In [P4], the influence of other process parameters like tool traverse and rotational speed, and tool tilt angle were discussed for the joints produced with a hexagonal pin with grooves on AA6082 alloy. In the case of the samples produced with the tool tilt angle of  $0^\circ$ , lower hardness values were found compared to the welds produced with an inclined tool. Also when the rotational speed increased and the traverse speed decreased, the measured hardness values in the nugget zone were higher. The main reason for this is the lower grain size in the stir zones, influenced directly by the total heat input during the process. The hardness measurements were performed in three lines on the cross-sections – top, middle, and bottom. For all the tested welds the lowest hardness was noted at the bottom of the cross-sections, while the highest was observed at the top of the samples. The top of the weld experienced the most serious heating due to the contact with the shoulder of the tool and the frictional heating. It resulted in the finest microstructure and the highest microhardness. Comparing all the welds, the maximum hardness, reaching approximately 92 % of the base material, was observed for the sample produced with the tool tilt angle of  $2^\circ$ , the tool rotational speed of 1250 RPM, and the tool traverse speed of 200 mm/min. In [P5] the indentation measurements on similar AA6082 revealed that the lowest hardness exhibited the weld produced with the tool tilt angle of  $0^\circ$ , the lowest tool rotational speed of 1000 RPM and the highest tool traverse speed of 250 mm/min. Based on the performed hardness measurements in [P4], the width of the stir zone was also measured. The highest width size was observed at the top of all the samples and the lowest at the bottom, which reflected the characteristic basin shape of the stir zone.

In the case of AA5083/AA6060 [P7], the indentation studies were performed in the middle line of the cross-sections of the joints. The hardness of base metal AA5083 was equal to 0.754 GPa and of AA6060 1.103 GPa. The hardness analysis for AA5083/AA6060 joints revealed that the profiles were clearly asymmetrical. The reason for that is the application of aluminum alloys from two different series. The alloys in the 5000 series are non-heat-treatable alloys and their increase in strength can be achieved through cold working or hardening process. The AA5083 alloy sheets were delivered in the condition “O”, which means they were annealed. The alloys in the 6000 series are heat-treatable alloys. By adding alloying elements the strength is initially formed. These elements exhibit increasing solid solubility in increased temperatures. When subjected to solid solution treatment, additional strengthening is provided. The AA6060 sheets were delivered in T6 condition, which means they were solution heat treated and artificially aged. Because of the different series of used alloys, and they different conditions, unsymmetrical

hardness profiles were found. From the side of AA6060 alloy, the typical shape profile for FSW joints was found, with a minimum hardness in the heat-affected zone. In the stir zone, a great recovery was observed. On the advancing side of the joints, where AA5083 alloy was placed, a typical decrease in hardness in HAZ was not found. FSW joints produced from annealed alloys, do not exhibit the drop in hardness in HAZ. In the direction of the weld nugget, higher hardness was observed due to the modest hot-working hardening and eventually grain refinement in the nugget zone. The measured hardness values were discussed in terms of the influence of the tool rotational speed. It was revealed that in the stir zone, the increase in hardness was observed with the increase in the tool rotational speed. These observations are consistent with research on AA6082 and AA6060/AA6082, where the grain size and final hardness of the stir zone depended on the heat input during the FSW process. When the tool rotational speed increased, a higher heat input could be observed.

#### **4.4. Tensile strength of joints**

The tensile strength of the joints of AA6082 was measured, with respect to the geometry of the tool applied [P3]. The highest value of UTS was found for AA6082 base material equal to  $371 \pm 21$  MPa. In the case of the welds, the values of  $269 \pm 18$  MPa and  $207 \pm 32$  MPa were noted for the joints produced with the tool with the hexagonal pin with grooves and the tapered cylindrical pin, respectively. It corresponds to the joint efficiency of  $72.5 \pm 4.9$  % and  $55.8 \pm 8.6$  %, respectively. In both cases, the location of the failure was detected in the HAZ on the advancing side of the welds. Also, the lowest hardness was found in the HAZ on AS of the welds for both cases, as was described in section 4.3. In the HAZ, due to sufficient heat input, the precipitations dissolve and overaging occurs, where enlargement and roughening of pre-existing particles can be observed, and no recrystallization process occurs, which is especially crucial for the precipitation hardened alloys like AA6082. It was for this reason that the lowest hardness was observed in this zone, and it was the area of fracture in the static tensile test. The SEM observations on the fracture surfaces of the welded samples produced with both tools revealed that the material cracked simultaneously in multiple parallel planes, and the individual cracks were connected by perpendicular interplanar cracks. Also, the cracking proceeded in a ductile nature. In the case of the base material, the dominant mechanism was ductile cracking with several brittle precipitations present, around which local voids were formed. The fracture surface of the base material consisted of long and flat areas corresponded to the elongated grains revealed by microstructural observations, due to the rolling process of the base metal.

#### **4.5. Electrochemical properties of the joints**

Potentiodynamic studies were performed on AA6082 to determine the influence of the tool rotational speed, tool traverse speed, and tool tilt angle on the electrochemical properties of



similar joints of AA6082 [P4]. The highest density corrosion current (the lowest corrosion resistance) was observed for AA6082 base metal ( $42.564 \mu\text{A}\cdot\text{cm}^{-2}$ ). It was revealed that all the welded samples exhibited higher corrosion resistance. In the study, it was found that samples produced with a non-tilted tool showed less corrosion resistance compared to samples produced with a tilt angle of  $2^\circ$ . It was also observed that with an increase in the tool rotational speed and a decrease in the tool traverse speed, the corrosion current density decreased (the corrosion resistance increased). Changes in the electrochemical properties of FSW welds are due not only to a change in the microstructure but also to a different state of precipitation and residual stresses values. The lowest corrosion current density ( $16.029 \mu\text{A}\cdot\text{cm}^{-2}$ ) was found for the weld produced with the inclined tool when the tool rotational speed was equal to 1250 RPM and the tool traverse speed was equal to 200 mm/min. Among the produced welds, the highest corrosion current density ( $23.907 \mu\text{A}\cdot\text{cm}^{-2}$ ) and the lowest corrosion resistance were observed for the sample produced with the non-inclined tool, when the tool traverse speed was equal to 250 mm/min and the tool rotational speed was equal to 1000 RPM. Scanning electron microscopy studies also confirmed these observations.

In the case of dissimilar AA6060/AA6082 joints, potentiodynamic and electrochemical impedance spectroscopy testing was performed to discuss the corrosion resistance [P6]. Three different NaCl concentrations were used. The corrosion current density of the welded samples was similar and lower in comparison to both parent materials. The corrosion current density of the sample produced with the tool traverse speed of 160 mm/min was equal to  $8.162 \mu\text{A}\cdot\text{cm}^{-2}$  and for 200 mm/min  $8.006 \mu\text{A}\cdot\text{cm}^{-2}$  for the NaCl concentration of 0.2 %. For the concentrations of 0.7 % and 1.2 % slightly lower values of corrosion current density were also observed for the weld made at a higher linear speed. In all cases, both parent metals showed higher values of corrosion current density, with lower resistance demonstrated by alloy AA6082. The electrochemical impedance spectroscopy tests allowed to characterize to electrochemical properties of the oxide layer on an aluminum alloy sample, as well as on a metallic sample itself. It was noted that the resistances of the native aluminum oxide layer were markedly higher in the case of welded samples, compared to both base alloys AA6082 and AA6060. This may have been due to the passive layer at the interfaces being more homogeneous, thus providing a greater barrier to Al ions passing into the NaCl solution. This is connected to the fine-grain microstructure of the stir zone of the welds. Finer grain microstructure has a more reactive surface. The formation of the oxide layer progresses faster. SEM observations of the samples revealed that the area covered by the corrosion process was larger for AA6082 and AA6060 alloys than for friction stir welded samples. It was noted that corrosion in friction stir welds mostly appeared on the edges of the curves resulting from a mix of rotational and traverse movements of the tool. This was caused by the triaxial state of stress at these locations in the

passive layer. This reduced the resistance of the passive layer to delamination during stress corrosion processes.

In [P7] electrochemical properties of dissimilar AA5083/AA6060 joints were discussed with respect to the tool traverse speed influence. It was revealed the AA5083 parent material exhibited the highest corrosion resistance ( $i_{\text{corr}} = 4.506 \pm 0.278 \mu\text{A}\cdot\text{cm}^{-2}$ ). The parent metal AA6060, on the contrary, exhibited the lowest corrosion resistance ( $i_{\text{corr}} = 9.047 \pm 0.768 \mu\text{A}\cdot\text{cm}^{-2}$ ). It should be particularly emphasized that in general, the aluminum alloys of series 5000 are characterized by better corrosion resistance than the alloys in series 6000, due to the alloying elements. The corrosion current densities were equal to  $8.075 \pm 0.182$ ,  $7.592 \pm 0.442$ , and  $6.935 \pm 0.199 \mu\text{A}\cdot\text{cm}^{-2}$  for the welds produced with the tool rotational speed of 800 RMP, 1000 RPM, and 1200 RPM, respectively. These observations were proven by scanning electron microscopy observations. By providing higher rotational speed, higher heat input was also provided, and better corrosion properties of the weld were noted. These observations are consistent with the observations on AA6082 similar welds, discussed in [P4].

#### 4.6. Residual stresses analysis

For AA6082 similar friction stir welded joints, the simulations of thermal residual stresses were performed to determine the influence of the tool geometry on the process performance [P3]. Since the residual thermal stresses were the result of thermal expansion and contraction of the material, by comparing the thermal distribution simulations and the residual stress simulation results, it could be seen that due to the presence of a region with a maximum temperature in the middle line of welding, the stress in this region was higher and it was of tensile nature. In the far areas and around the edge of the workpiece, the stress was compressive. The residual stress in the case of the cylindrical pin was at least 13 % lower than in the hexagonal pin case. The reason for this was higher average temperature due to higher shear stress around the hexagonal pin, than for the use of the simple pin. This caused a higher maximum temperature in the center line of the and therefore the thermal residual stress increased.

In [P5], the residual stresses in AA6082 were analyzed with respect to the process parameters such as tool traverse speed, tool rotational speed, and tool tilt angle. A hexagonal pin with grooves was used in the tool. The procedure to calculate residual strains was Williamson-Hall analysis, which is described in detail in [P5]. To calculate the residual stresses based on the microstrain values Young's modulus values are needed. Indentation tests were performed to calculate Young's modulus values for the welds and the base metal. The results of performed calculations are consistent with the simulation results. In the stir zone, the character of residual stresses is tensile.



The same procedure to calculate residual stresses was applied for the dissimilar AA6060/AA6982 welds in [P6]. It was noted that the residual stresses of the tensile nature were observed for both parent materials. For both of the welds, the residual compressive stresses were noted. The compressive character of residual stresses could be the result of a strong compression reaction by the tool shoulder. Also, based on macrostructure observations, the curvature of the top surface of the welds was observed due to the tool shoulder plunge into the aluminum components. It should be noted that in the case of studies on dissimilar welding, different process parameters were applied compared to the AA6082 similar welding. The tilt angle was equal to 0°, the tool rotational speed was equal to 1250 RPM and the traverse speed values were equal to 160 mm/min and 200 mm/min. During the FSW process, large strains of the metal matrix could be observed. The material in the stir zone was both tensiled and compressed by friction and, at the same time, is exposed to the thermal stresses because of the heat input. By applying different process parameters, the stirring processes are different and also, the heat input is not constant. In the above studies, it was noted that the process parameters significantly affect the generation of stresses in the material.

#### **4.7 Dislocation density and mobility calculations**

In [P5] the analysis of process parameters (such as tool rotational and traverse speed, and tool tilt angle) was discussed with respect to dislocation density and mobility in AA6082 friction stir welded joints. The modified Williamson-Hall analysis was applied with this approach. The most significant finding with regard to the dislocation analysis is that a change in dislocation type was observed in the FSW joints. The AA6082 native material was characterized by a predominance of screw-type dislocations, while all welds were of the edge type. In addition, it was found that if more heat is applied during the process - in the form of tilting the tool, increasing the rotational speed, or decreasing the traverse speed - the density of dislocations decreases and their mobility increases. During the welding, the precipitations dissolve. By applying more heat, the dissolution of precipitates is enhanced. The inhibition of the dislocation movement is weakened. This means that such material may have lower strength.

Another approach was applied to calculate the dislocation density of dissimilar AA6060/AA6082 joints. In [P6] the calculations were based on indentation tests. It allowed to calculate the geometrically necessary dislocation density and statistically stored dislocation density. Higher dislocation densities were observed in FSW welds, in the nugget zone, compared to native materials. The influence of the tool rotational speed was not significant in this case.

The same procedure as described in [P6] was applied to calculate dislocation density and mobility in AA5083/AA6060 dissimilar welds. In [P7] the effect of the tool rotational speed

was discussed. Moreover, the analysis covered all the zones of welded joints – stir zones, thermo-mechanically affected zones, heat-affected zones, as well as both base metals. The dislocation densities in the stir zones of welds produced with different rotational speeds were lower than the dislocation density of the base metal AA6060 while higher than that of the base AA5083 alloy. One of the most important observations was that the zone with the lowest dislocation density and highest mobility was the heat-affected zone on the AA6060 alloy side. The lowest hardness was also observed in this zone. This is in accordance with the theory that an increase in dislocation density and a decrease in dislocation mobility affects the increase in metal strength.

#### **4.8. Description of major research observations**

Studies performed on the AA6082, AA6060/AA6082, and AA5083/AA6060 friction stir welded joints allowed to specify the most relevant conclusions:

- The use of a self-designed tool with a hexagonal pin with grooves allows to produce sound similar AA6082 and dissimilar AA6060/AA6082 and AA5083/AA6060 joints without serious defects.
- In all the produced welds the characteristic for friction stir welding zones are found – stir zone, thermo-mechanically affected zone, heat-affected zone, and base metal.
- The asymmetry of the hardness profiles of AA6082 and AA5083/AA6060 joints indicates the existence of AS and RS.
- Welding with the tool with a hexagonal pin with grooves provides a maximum temperature at least 5 % higher than when welding with the use of the tapered cylindrical pin with no grooves based on the performed computer simulations.
- In the produced similar welds of AA6082, greater grain refinement is observed in the SZ as a result of applying the hexagonal pin with grooves, compared to the cylindrical pin with no grooves. This is a result of total heat input.
- Using the non-inclined tool results in a larger average grain size in the weld nugget zone of AA6082 than when using an inclined tool. The average grain size decreases with an increase in the tool rotational speed and a decrease in the tool traverse speed to the increased heat input. Also, with the higher heat input the radius of the nugget zone also increases. These observations are consistent with the studies on dissimilar AA5083/AA6060 joints.
- Reduction of precipitation fraction can be observed in a nugget zone of AA6082 similar friction stir welded joint.

- Hardness measurements on AA6082 joints revealed that the weld produced with a hexagonal pin with grooves has a higher hardness in the SZ compared to the weld produced with the cylindrical pin. This is consistent with the Hall-Petch relationship.
- Performed tensile tests on AA6082 joints revealed that the location of the lowest strength is the HAZ on the advancing side. This location is also characterized by the lowest hardness.
- The friction stir welding process improves the corrosion properties of the similar and dissimilar welds of aluminum alloys of the 6000 series. When welding dissimilar alloys of 5000 and 6000 series, the corrosion properties of the welds are improved with respect to 6000 series alloy.
- A linear correlation is found for the relationship between residual stress and corrosion resistance of AA6060/AA6082 joints.
- The friction stir welding process results in an increase in the fraction of edge-type dislocations. They are also characterized by higher mobility.
- The lowest dislocation density with the highest mobility is found in the HAZ of AA5083/AA6060. Also, the HAZ is characterized by the lowest strength.
- A linear decreasing relationship is observed in AA6082 welds between the ratio of dislocation density and mobility, and the introduced heat input – by applying higher tool rotational speed, lower tool traverse speed of using an inclined tool.

## 5. SUMMARY

The conducted research demonstrated that process parameters such as tool geometry, tool traverse and rotational speed, and tool tilt angle significantly affect the properties of the produced similar and dissimilar joints of selected aluminum alloys.

The two author's tool geometries proposed in the dissertation produced defect-free welds. The welds produced with the tool with a hexagonal pin with grooves exhibited better properties. It was observed that the process parameters directly affect the stress state of the joints. During the FSW process, the type of dislocations, their density, and mobility change, which directly affects the strength of the material. The FSW process parameters were also found to have a significant effect on the microstructure of the joints, the size of the different zones characteristic of a friction stir welded joint, hardness, electrochemical, and strength properties. Also, experiments were performed that allowed to determine not only the corrosion resistance of the metallic joint material, but also of the oxide layer.

In accordance with the above conclusions and the description of the main achievements of this dissertation, it can be concluded that the research thesis has been proven. The parameters of the friction stir welding process - the geometry of the tool, tool rotational and traverse speed and tool tilt angle affect the generation of residual stresses, change the dislocation characteristics of the joint, and have a direct influence on the mechanical and electrochemical properties of similar and dissimilar joints of selected aluminum alloys. It is possible to shape the physicochemical and mechanical properties of similar and dissimilar joints of selected aluminum alloys by appropriate selection of the parameters of the FSW process. The correlation between the FSW process parameters and the properties of the joints of selected aluminum alloys was found.

Both the scientific and functional objectives of this dissertation have been fulfilled. The effects of friction stir welding process parameters on the residual stresses, dislocation densities, and mobility, and the resulting mechanical and electrochemical properties of joints from selected aluminum alloys were determined. The joints of selected aluminum alloys without defects, which are characterized by high mechanical and electrochemical properties were produced.

The research performed allowed confirmation of the thesis posed but at the same time left new and intriguing questions. Further research work is planned on aluminum alloys of other series. In addition, the issues of dissimilar joints of different materials, whose mechanical and physicochemical properties are completely different, seem to be of interest. Also of interest are all kinds of modifications of the friction stir welding method, such as pulse friction stir welding, bobbin tool friction stir welding, or friction stir spot welding.

The experimental studies were conducted at the Gdansk University of Technology (Poland) in collaboration with scientists from the Warsaw University of Technology (Poland), the University of Salento (Italy), and the Isfahan University of Technology (Iran).

## 6. REFERENCES

- [1] R.L. Rudnick, Earth's Continental Crust. In: White, W.M. (eds) Encyclopedia of Geochemistry. Encyclopedia of Earth Sciences Series., Springer, 2018. [https://doi.org/https://doi.org/10.1007/978-3-319-39312-4\\_277](https://doi.org/https://doi.org/10.1007/978-3-319-39312-4_277).
- [2] A. Luo, A.K. Sachdev, D. Apelian, Alloy development and process innovations for light metals casting, *J. Mater. Process. Technol.* 306 (2022). <https://doi.org/10.1016/j.jmatprotec.2022.117606>.
- [3] J.R. Davis, *Alloying: Understanding the Basics*, 2001. <https://doi.org/10.1361/autb2001p351>.
- [4] C. Koulochieris, D. and Vossou, Exploration of Equivalent Design Approaches for Tanks Transporting Flammable Liquids, *Computation*. 8 (2020) 1–22. <https://doi.org/doi:10.3390/computation8020033>.
- [5] G. De Matteis, G. Brando, F.M. Mazzolani, Pure aluminium: An innovative material for structural applications in seismic engineering, *Constr. Build. Mater.* 26 (2012) 677–686. <https://doi.org/10.1016/j.conbuildmat.2011.06.071>.
- [6] B. Stojanovic, M. Bukvic, I. Epler, Application of aluminum and aluminum alloys in engineering, *Appl. Eng. Lett.* 3 (2018) 52–62. <https://doi.org/10.18485/aeletters.2018.3.2.2>.
- [7] J.G. Kaufman, *Introduction to Aluminum Alloys and Tempers*, ASM International, 2000. <https://doi.org/10.1361/iaat2000p023>.
- [8] G. Mathers, *Welding of aluminium and its alloys*, Woodhead Publishing Limited, 2002. <https://doi.org/10.1038/177568b0>.
- [9] K. Zheng, D.J. Politis, L. Wang, J. Lin, A review on forming techniques for manufacturing lightweight complex—shaped aluminium panel components, *Int. J. Light. Mater. Manuf.* 1 (2018) 55–80. <https://doi.org/10.1016/j.ijlmm.2018.03.006>.
- [10] P. Rambabu, N. Prasad, V. Kutumbarao, R. Wanhill, Aluminium Alloys for Aerospace Applications, in: *Aerosp. Mater. Mater. Technol.*, Springer, 2017: pp. 29–52. [https://doi.org/10.1007/978-981-10-2134-3\\_2](https://doi.org/10.1007/978-981-10-2134-3_2).
- [11] Y. Wu, Application of aluminum alloy in aircraft, *J. Phys. Conf. Ser.* 2228 (2022). <https://doi.org/10.1088/1742-6596/2228/1/012024>.
- [12] Q. Liu, R. Han, Y. Gao, L. Ke, Numerical investigation on thermo-mechanical and material flow characteristics in friction stir welding for aluminum profile joint, *Int. J. Adv. Manuf. Technol.* 114 (2021) 2457–2469. <https://doi.org/10.1007/s00170-021-06978-8>.
- [13] X. Chen, Y. Peng, S. Peng, S. Yao, C. Chen, P. Xu, Flow and fracture behavior of aluminum alloy 6082-T6 at different tensile strain rates and triaxialities, *PLoS One*. 12 (2017) 1–28. <https://doi.org/10.1371/journal.pone.0181983>.
- [14] T. Kawasaki, T. Makino, K. Masai, H. Ohba, Y. Ina, M. Ezumi, Application of friction stir welding to construction of railway vehicles, *JSME Int. Journal, Ser. A Solid Mech. Mater. Eng.* 47 (2004) 502–511. <https://doi.org/10.1299/jsmea.47.502>.
- [15] P. Kossakowski, Stopy aluminium jako materiał konstrukcyjny ustrojów nośnych mostów, *Zesz. Nauk. Politech. Częstochowskiej. Bud.* 172 (2017) 159–170. <https://doi.org/10.17512/znb.2016.1.15>.
- [16] T. Siwowski, Aluminium bridges - Past, present and future, *Struct. Eng. Int. J. Int.*

Assoc. Bridg. Struct. Eng. 16 (2006) 286–293.  
<https://doi.org/10.2749/101686606778995137>.

- [17] M. Tisza, Z. Lukács, High strength aluminum alloys in car manufacturing, *IOP Conf. Ser. Mater. Sci. Eng.* 418 (2018). <https://doi.org/10.1088/1757-899X/418/1/012033>.
- [18] A.M.N. Arifuddin, T. Hidayat, M. Usawah Pawara, M. Zulkifli, Experimental Study of Aluminium Joint Plate Between AA5052 with AA5083: Application on Hull Vessel Material, *Int. J. Mar. Eng. Innov. Res.* 7 (2022).  
<https://doi.org/10.12962/j25481479.v7i2.12896>.
- [19] P. Pankaj, A. Tiwari, L.N. Dhara, P. Biswas, Multiphase CFD simulation and experimental investigation of friction stir welded high strength shipbuilding steel and aluminum alloy, *CIRP J. Manuf. Sci. Technol.* 39 (2022) 37–69.  
<https://doi.org/10.1016/j.cirpj.2022.07.001>.
- [20] D. Istrate, B.G. Sbârcea, A.M. Demian, A.D. Buzatu, L. Salcianu, I. Bordeasu, L.M. Micu, C. Ghera, B. Florea, B. Ghiban, Correlation between Mechanical Properties—Structural Characteristics and Cavitation Resistance of Cast Aluminum Alloy Type 5083, *Crystals.* 12 (2022). <https://doi.org/10.3390/cryst12111538>.
- [21] A. Zhang, Y. Li, Thermal Conductivity of Aluminum Alloys—A Review, *Materials (Basel).* 16 (2023). <https://doi.org/10.3390/ma16082972>.
- [22] M.J. Peet, H.S. Hasan, H.K.D.H. Bhadeshia, Prediction of thermal conductivity of steel, *Int. J. Heat Mass Transf.* 54 (2011) 2602–2608.  
<https://doi.org/10.1016/j.ijheatmasstransfer.2011.01.025>.
- [23] F. Hayat, Electron beam welding of 7075 aluminum alloy: Microstructure and fracture properties, *Eng. Sci. Technol. an Int. J.* 34 (2022) 101093.  
<https://doi.org/10.1016/j.jestch.2022.101093>.
- [24] D. Wallerstein, A. Riveiro, J. delVala, R. Comesaña, F. Lusquiñosa, J. Poua, Developments in laser welding of aluminum alloys, *Adv. Weld. Deform.* (2021) 127–150. <https://doi.org/10.1016/B978-0-12-822049-8.00005-0>.
- [25] X. Cao, W. Wallace, C. Poon, J.-P. Immarrigeon, Research and Progress in Laser Welding of Wrought Aluminum Alloys. I. Laser Welding Processes, *Mater. Manuf. Process.* 18 (2003) 1–22. <https://doi.org/10.1081/AMP-120017586>.
- [26] A.M. Samuel, E. Samuel, V. Songmene, F.H. Samuel, A Review on Porosity Formation in Aluminum-Based Alloys, *Materials (Basel).* 16 (2023).  
<https://doi.org/10.3390/ma16052047>.
- [27] P.N. Anyalebechi, Analysis of the effects of alloying elements on hydrogen solubility in liquid aluminum alloys, *Scr. Metall. Mater.* 33 (1995) 1209–1216.  
[https://doi.org/10.1016/0956-716X\(95\)00373-4](https://doi.org/10.1016/0956-716X(95)00373-4).
- [28] H. Parangusan, J. Bhadra, N. Al-Thani, A review of passivity breakdown on metal surfaces: influence of chloride- and sulfide-ion concentrations, temperature, and pH, *Emergent Mater.* 4 (2021) 1187–1203. <https://doi.org/10.1007/s42247-021-00194-6>.
- [29] Y. Xing, F. Wang, J. Lu, S. Xu, Welding deformation analysis of aluminum alloy and steel sheet metal parts based on resistance spot welding, *Proc. Inst. Mech. Eng. Part B J. Eng. Manuf.* 233(3):797 (2019). <https://doi.org/10.1177/0954405418755819>.
- [30] M. Taheri, M. Razavi, S.F. Kashani-Bozorg, M.J. Torkamany, Relationship between solidification and liquation cracks in the joining of GTD-111 nickel-based superalloy by Nd:YAG pulsed-laser welding, *J. Mater. Res. Technol.* 15 (2021) 5635–5649.  
<https://doi.org/10.1016/j.jmrt.2021.11.007>.

- [31] W.M. Thomas, E.D. Nicholas, J.C. Needham, M.G. Murch, P. Templesmith, C.J. Dawes, G. B. Patent Application No. 9125978.8, 1991.
- [32] N. Ethiraj, T. Sivabalan, S. Meikeerthy, K.L.V.R. Kumar, G. Chaithanya, G.P.K. Reddy, Comparative study on conventional and underwater friction stir welding of copper plates, *Int. Conf. Mater. Manuf. Mach.* 2019. 2128 (2019) 030003. <https://doi.org/10.1063/1.5117946>.
- [33] J.W. Lin, H.C. Chang, M.H. Wu, Comparison of mechanical properties of pure copper welded using friction stir welding and tungsten inert gas welding, *J. Manuf. Process.* 16 (2014) 296–304. <https://doi.org/10.1016/j.jmapro.2013.09.006>.
- [34] L.S. Raju, A. Kumar, S.R. Prasad, Microstructure and mechanical properties of friction stir welded pure copper, *Appl. Mech. Mater.* 592–594 (2014) 499–503. <https://doi.org/10.4028/www.scientific.net/AMM.592-594.499>.
- [35] P.K. Sahu, S. Pal, Effect of FSW parameters on microstructure and mechanical properties of AM20 welds, *Mater. Manuf. Process.* 33 (2018) 288–298. <https://doi.org/10.1080/10426914.2017.1279295>.
- [36] I. Singh, G.S. Cheema, A.S. Kang, An experimental approach to study the effect of welding parameters on similar friction stir welded joints of AZ31B-O Mg alloy, *Procedia Eng.* 97 (2014) 837–846. <https://doi.org/10.1016/j.proeng.2014.12.358>.
- [37] N. Afrin, D.L. Chen, X. Cao, M. Jahazi, Strain hardening behavior of a friction stir welded magnesium alloy, *Scr. Mater.* 57 (2007) 1004–1007. <https://doi.org/10.1016/j.scriptamat.2007.08.001>.
- [38] M. Mahoney, T. Nelson, C. Sorenson, S. Packer, Friction stir welding of ferrous alloys: Current status, *Mater. Sci. Forum.* 638–642 (2010) 41–46. <https://doi.org/10.4028/www.scientific.net/MSF.638-642.41>.
- [39] S. Ragu Nathan, V. Balasubramanian, S. Malarvizhi, A.G. Rao, Effect of welding processes on mechanical and microstructural characteristics of high strength low alloy naval grade steel joints, *Def. Technol.* 11 (2015) 308–317. <https://doi.org/10.1016/j.dt.2015.06.001>.
- [40] S. Sabooni, F. Karimzadeh, M.H. Enayati, A.H.W. Ngan, H. Jabbari, Gas tungsten arc welding and friction stir welding of ultrafine grained AISI 304L stainless steel: Microstructural and mechanical behavior characterization, Elsevier B.V., 2015. <https://doi.org/10.1016/j.matchar.2015.08.009>.
- [41] H. Fujii, Y. Sun, H. Kato, K. Nakata, Investigation of welding parameter dependent microstructure and mechanical properties in friction stir welded pure Ti joints, *Mater. Sci. Eng. A.* 527 (2019) 3386–3391. <https://doi.org/10.1016/j.msea.2010.02.023>.
- [42] N. Kulkarni, M. Ramulu, Experimental and Numerical Analysis of Mechanical Behavior in Friction Stir Welded Different Titanium Alloys, in: *ASME 2014 Int. Mech. Eng. Congr. Expo. IMECE2014*, 2014: pp. 1–8.
- [43] A. Steuwer, D.G. Hattingh, M.N. James, U. Singh, T. Buslaps, Residual stresses, microstructure and tensile properties in Ti-6Al-4V friction stir welds, *Sci. Technol. Weld. Join.* 17 (2012) 525–533. <https://doi.org/10.1179/136217112X13439160184196>.
- [44] A. Arici, T. Sinmaz, Effects of double passes of the tool on friction stir welding of polyethylene, *J. Mater. Sci.* 40 (2005) 3313–3316. <https://doi.org/10.1007/s10853-005-2709-x>.
- [45] S.K. Sahu, D. Mishra, R.P. Mahto, V.M. Sharma, S.K. Pal, K. Pal, S. Banerjee, P. Dash, Friction stir welding of polypropylene sheet, *Eng. Sci. Technol. an Int. J.* 21



- (2018) 245–254. <https://doi.org/10.1016/j.jestch.2018.03.002>.
- [46] A. Zafar, M. Awang, S.R. Khan, S. Emamian, Investigating friction stir welding on thick nylon 6 plates, *Weld. J.* 95 (2016) 210s-218s.
- [47] S. Mozammil, J. Karloopia, R. Verma, P.K. Jha, Mechanical response of friction stir butt weld Al-4.5%Cu/TiB<sub>2</sub>/2.5p in situ composite: Statistical modelling and optimization, *J. Alloys Compd.* 826 (2020) 154184. <https://doi.org/10.1016/j.jallcom.2020.154184>.
- [48] D.D. Jafrey, K. Panneerselvam, Study on Tensile Strength, Impact Strength and Analytical Model for Heat Generation in Friction Vibration Joining of Polymeric Nanocomposite Joints Daniel, *Polym. Eng. Sci.* (2016). <https://doi.org/10.1002/pen.24443>.
- [49] S. Kumar, T. Medhi, B.S. Roy, *Friction Stir Welding of Thermoplastic Composites*, Springer Singapore, 2019. <https://doi.org/10.1007/978-981-13-6412-9>.
- [50] M.J. Peel, A. Steuwer, P.J. Withers, T. Dickerson, Q. Shi, H. Shercliff, Dissimilar friction stir welds in AA5083-AA6082. Part I: Process parameter effects on thermal history and weld properties, *Metall. Mater. Trans. A Phys. Metall. Mater. Sci.* 37 (2006) 2183–2193. <https://doi.org/10.1007/BF02586138>.
- [51] H. Kasai, Y. Morisada, H. Fujii, Dissimilar FSW of immiscible materials: Steel/magnesium, *Mater. Sci. Eng. A.* 624 (2015) 250–255. <https://doi.org/10.1016/j.msea.2014.11.060>.
- [52] M. Dehghani, A. Amadeh, S.A.A. Akbari Mousavi, Investigations on the effects of friction stir welding parameters on intermetallic and defect formation in joining aluminum alloy to mild steel, *Mater. Des.* 49 (2013) 433–441. <https://doi.org/10.1016/j.matdes.2013.01.013>.
- [53] R.S. Mishra, Z.Y. Ma, *Friction stir welding and processing*, 2005. <https://doi.org/10.1016/j.mser.2005.07.001>.
- [54] K.J. Colligan, *The friction stir welding process: An overview*, Woodhead Publishing Limited, 2009. <https://doi.org/10.1533/9781845697716.1.15>.
- [55] A. Raweni, V. Majstorović, A. Sedmak, S. Tadić, S. Kirin, Optimization of AA5083 friction stir welding parameters using taguchi method, *Teh. Vjesn.* 25 (2018) 861–866. <https://doi.org/10.17559/TV-20180123115758>.
- [56] P. Tasi, I. Hajro, D. Hodži, D. Dobraš, Energy Efficient Welding Technology : Fsw, in: 11th Int. Conf. Accompl. Electr. Mech. Engineering Inf. Technol., 2013: pp. 429–442.
- [57] R. Palanivel, P. Koshy Mathews, N. Murugan, I. Dinaharan, Effect of tool rotational speed and pin profile on microstructure and tensile strength of dissimilar friction stir welded AA5083-H111 and AA6351-T6 aluminum alloys, *Mater. Des.* 40 (2012) 7–16. <https://doi.org/10.1016/j.matdes.2012.03.027>.
- [58] S. Ugender, A. Kumar, A.S. Reddy, Microstructure and Mechanical Properties of AZ31B Magnesium Alloy by Friction Stir Welding, *Procedia Mater. Sci.* 6 (2014) 1600–1609. <https://doi.org/10.1016/j.mspro.2014.07.143>.
- [59] P. Sevel, V. Jaiganesh, Characterization of mechanical properties and microstructural analysis of friction stir welded AZ31B Mg alloy thorough optimized process parameters, *Procedia Eng.* 97 (2014) 741–751. <https://doi.org/10.1016/j.proeng.2014.12.304>.
- [60] A.N. Siddiquee, S. Pandey, Experimental investigation on deformation and wear of

WC tool during Friction Stir Welding (FSW) of stainless steel, *Int. J. Adv. Manuf. Technol.* 73(1):479- (2014). <https://doi.org/10.1007/s00170-014-5846-z>.

- [61] R. Fernández, J. Ibáñez, F. Cioffi, D. Verdera, G. González-Doncel, Friction stir welding of 25%SiC/2124Al composite with optimal mechanical properties and minimal tool wear, *Sci. Technol. Weld. Join.* 22 (2017) 526–535. <https://doi.org/10.1080/13621718.2016.1268368>.
- [62] M.M.Z. Ahmed, K.A. Abdelazem, M.M. El-Sayed Seleman, B. Alzahrani, K. Touileb, N. Jouini, I.G. El-Batanony, H.M. Abd El-Aziz, Friction stir welding of 2205 duplex stainless steel: Feasibility of butt joint groove filling in comparison to gas tungsten arc welding, *Materials (Basel)*. 14 (2021) 1–21. <https://doi.org/10.3390/ma14164597>.
- [63] Y.S. Sato, T.W. Nelson, C.J. Sterling, R. Steel, C.O. Pettersson, Microstructure and mechanical properties of friction stir welded SAF 2507 super duplex stainless steel, *Mater. Sci. Eng. A.* 397(1–2):3 (2005). <https://doi.org/10.1016/j.msea.2005.02.054>.
- [64] T. Hartman, M.P. Miles, S.T. Hong, R. Steel, S. Kelly, Effect of PCBN tool grade on joint strength and tool life in friction stir spot welded DP 980 steel, *Wear*. 328–329 (2015) 531–536. <https://doi.org/10.1016/j.wear.2015.03.001>.
- [65] R. Sarkar, T.K. Pal, M. Shome, Material flow and intermixing during friction stir spot welding of steel, *J. Mater. Process. Technol.* 227 (2016) 96–109. <https://doi.org/10.1016/j.jmatprotec.2015.08.006>.
- [66] M. Santella, Y. Hovanski, T.Y. Pan, Friction Stir Spot Welding (FSSW) of Advanced High Strength Steel (AHSS), *SAE Int. J. Mater. Manuf.* 5 (2012) 382–387. <https://doi.org/10.4271/2012-01-0480>.
- [67] P. Mysliwiec, R.E. Sliwa, R. Ostrowski, Friction stir welding of ultrathin AA2024-T3 aluminum sheets using ceramic tool, *Arch. Metall. Mater.* 64 (2019) 1385–1394. <https://doi.org/10.24425/amm.2019.130105>.
- [68] G. Buffa, J. Hua, R. Shivpuri, L. Fratini, A continuum based fem model for friction stir welding - Model development, *Mater. Sci. Eng. A.* 419 (2006) 389–396. <https://doi.org/10.1016/j.msea.2005.09.040>.
- [69] N. Xu, Q. Song, Y. Jiang, Y. Bao, H. Fujii, Large load friction stir welding of Mg–6Al–0.4Mn–2Ca magnesium alloy, *Mater. Sci. Technol. (United Kingdom)*. 34 (2018) 1118–1130. <https://doi.org/10.1080/02670836.2018.1424794>.
- [70] W. Wang, D. Deng, Z. Mao, Y. Tong, Y. Ran, Influence of tool rotation rates on temperature profiles and mechanical properties of friction stir welded AZ31 magnesium alloy, *Int. J. Adv. Manuf. Technol.* 88 (2017) 2191–2200. <https://doi.org/10.1007/s00170-016-8918-4>.
- [71] J. Chen, R. Ueji, H. Fujii, Double-sided friction-stir welding of magnesium alloy with concave-convex tools for texture control, *Mater. Des.* 76 (2015) 181–189. <https://doi.org/10.1016/j.matdes.2015.03.040>.
- [72] Y. Sato, H. Kokawa, M. Enomoto, S. Jogan, Microstructural evolution of 6063 aluminum during friction-stir welding, *Metall. Mater. Trans. A Phys. Metall. Mater. Sci.* 30 (1999) 2429–2437. <https://doi.org/10.1007/s11661-999-0251-1>.
- [73] K. Singh, G. Singh, H. Singh, Review on friction stir welding of magnesium alloys, *J. Magnes. Alloy.* 6 (2018) 399–416. <https://doi.org/10.1016/j.jma.2018.06.001>.
- [74] V.M. Magalhães, C. Leitão, D.M. Rodrigues, Friction stir welding industrialisation and research status, *Sci. Technol. Weld. Join.* 23 (2018) 400–409. <https://doi.org/10.1080/13621718.2017.1403110>.

- [75] A.P. Reynolds, W.D. Lockwood, T.U. Seidel, Processing-property correlation in friction stir welds, *Mater. Sci. Forum.* 331 (2000) 1719–1724. <https://doi.org/10.4028/www.scientific.net/msf.331-337.1719>.
- [76] P.A. Colegrove, H.R. Shercliff, Experimental and numerical analysis of aluminium alloy 7075-T7351 friction stir welds, *Sci. Technol. Weld. Join.* 8 (2003) 360–368. <https://doi.org/10.1179/136217103225005534>.
- [77] Y. Zhao, S. Lin, L. Wu, F. Qu, The influence of pin geometry on bonding and mechanical properties in friction stir weld 2014 Al alloy, *Mater. Lett.* 59 (2005) 2948–2952. <https://doi.org/10.1016/j.matlet.2005.04.048>.
- [78] K. Elangovan, V. Balasubramanian, Influences of tool pin profile and welding speed on the formation of friction stir processing zone in AA2219 aluminium alloy, *J. Mater. Process. Technol.* 200 (2008) 163–175. <https://doi.org/https://doi.org/10.1016/j.jmatprotec.2007.09.019>.
- [79] K. Krasnowski, C. Hamilton, S. Dymek, Influence of the tool shape and weld configuration on microstructure and mechanical properties of the Al 6082 alloy FSW joints, *Arch. Civ. Mech. Eng.* 15 (2015) 133–141. <https://doi.org/https://doi.org/10.1016/j.acme.2014.02.001>.
- [80] S. Ji, Z. Li, Z. Zhou, B. Wu, Effect of Thread and Rotating Speed on Material Flow Behavior and Mechanical Properties of Friction Stir Lap Welding Joints, *J. Mater. Eng. Perform.* 26 (2017) 1–12. <https://doi.org/10.1007/s11665-017-2928-8>.
- [81] E. Aldanondo, J. Vivas, P. Alvarez, I. Hurtado, Effect of Tool Geometry and Welding Parameters on Friction Stir Welded Lap Joint Formation with AA2099-T83 and AA2060-T8E30 Aluminium Alloys, *Metals (Basel)*. 10 (2020) 1–11.
- [82] K. Ramanjaneyulu, G. Reddy, A. Rao, R. Markandeya, Structure-Property Correlation of AA2014 Friction Stir Welds: Role of Tool Pin Profile, *J. Mater. Eng. Perform.* 22 (2013). <https://doi.org/10.1007/s11665-013-0512-4>.
- [83] A. Vairis, M. Petousis, N. Mountakis, C. Tsarouchidou, N. Vidakis, The Effect of Tool Geometry on the Strength of FSW Aluminum Thin Sheets, *Materials (Basel)*. 15 (2022). <https://doi.org/10.3390/ma15228187>.
- [84] S.A. Khodir, T. Shibayanagi, Friction stir welding of dissimilar AA2024 and AA7075 aluminum alloys, *Mater. Sci. Eng. B Solid-State Mater. Adv. Technol.* 148 (2008) 82–87. <https://doi.org/10.1016/j.mseb.2007.09.024>.
- [85] P. Cavaliere, Friction stir welding of Al alloys: Analysis of processing parameters affecting mechanical behavior, *Procedia CIRP*. 11 (2013) 139–144. <https://doi.org/10.1016/j.procir.2013.07.039>.
- [86] C. Leitão, R. Louro, D.M. Rodrigues, Analysis of high temperature plastic behaviour and its relation with weldability in friction stir welding for aluminium alloys AA5083-H111 and AA6082-T6, *Mater. Des.* 37 (2012) 402–409. <https://doi.org/10.1016/j.matdes.2012.01.031>.
- [87] M. Peel, A. Steuwer, M. Preuss, P.J. Withers, Microstructure, mechanical properties and residual stresses as a function of welding speed in aluminium AA5083 friction stir welds, *Acta Mater.* 51 (2003) 4791–4801. [https://doi.org/10.1016/S1359-6454\(03\)00319-7](https://doi.org/10.1016/S1359-6454(03)00319-7).
- [88] S.D. Meshram, G. Madhusudhan Reddy, Influence of tool tilt angle on material flow and defect generation in friction stir welding of AA2219, *Def. Sci. J.* 68 (2018) 512–518. <https://doi.org/10.14429/dsj.68.12027>.

- [89] N. Dialami, M. Cervera, M. Chiumenti, Effect of the tool tilt angle on the heat generation and the material flow in friction stir welding, *Metals (Basel)*. 9 (2019). <https://doi.org/10.3390/met9010028>.
- [90] H.A.D. Hamid, A.A. Roslee, Study the Role of Friction Stir Welding Tilt Angle on Microstructure and Hardness, *Appl. Mech. Mater.* 799–800 (2015) 434–438. <https://doi.org/10.4028/www.scientific.net/amm.799-800.434>.
- [91] G.G. Krishna, P.R. Reddy, M.M. Hussain, Effect of Tool Tilt Angle on Aluminum 2014 Friction Stir Welds, *Glob. J. Res. Eng.* 14 (2014) 61–70.
- [92] U. Acharya, B.S. Roy, S.C. Saha, Effect of tool rotational speed on the particle distribution in friction stir welding of AA6092/17.5 SiCp-T6 composite plates and its consequences on the mechanical property of the joint, *Def. Technol.* 16 (2020) 381–391. <https://doi.org/10.1016/j.dt.2019.08.017>.
- [93] L. Dubourg, P. Dacheux, Design and properties of FSW tools : a literature review, *Technology*. (2006).
- [94] L. Vijayaraghavan, K. Hemachandra Reddy, S.M. Jameel Basha, Emerging Trends in Mechanical Engineering, 2018. <https://doi.org/https://doi.org/10.1007/978-981-32-9931-3> ©.
- [95] A.K. Hussain, S. Azam, P. Quadri, Evaluation of Parameters of Friction Stir Welding for Aluminium Aa6351 Alloy, *Int. J. Eng. Sci. Technol.* 2 (2010) 5977–5984.
- [96] V. Balasubramanian, Relationship between base metal properties and friction stir welding process parameters, *Mater. Sci. Eng. A.* 480 (2008) 397–403. <https://doi.org/10.1016/j.msea.2007.07.048>.
- [97] A.H. Feng, D.L. Chen, Z.Y. Ma, Microstructure and cyclic deformation behavior of a friction-stir-welded 7075 al alloy, *Metall. Mater. Trans. A Phys. Metall. Mater. Sci.* 41 (2010) 957–971. <https://doi.org/10.1007/s11661-009-0152-3>.
- [98] A.H. Feng, D.L. Chen, Z.Y. Ma, Microstructure and low-cycle fatigue of a friction-stir-welded 6061 aluminum alloy, *Metall. Mater. Trans. A Phys. Metall. Mater. Sci.* 41 (2010) 2626–2641. <https://doi.org/10.1007/s11661-010-0279-2>.
- [99] Z. Zhang, B.L. Xiao, Z.Y. Ma, Hardness recovery mechanism in the heat-affected zone during long-term natural aging and its influence on the mechanical properties and fracture behavior of friction stir welded 2024Al-T351 joints, *Acta Mater.* 73 (2014) 227–239. <https://doi.org/10.1016/j.actamat.2014.04.021>.

## **7. THE CONTENT OF THE PUBLICATIONS WITH A DESCRIPTION OF THE CONTRIBUTION OF THE DOCTORAL CANDIDATE**

### **7.1. [P1] Friction Stir Welding – an overview of tool geometry and process parameters.**

**Laska A.\***, Szkodo M., Friction Stir Welding – an overview of tool geometry and process parameters. Under Review in International Journal of Materials Research (IF = 0.678, 40 points of the Polish Ministry of Science and Higher Education)

#### 7.1.1. Declaration of the contribution of the doctoral candidate

My contribution to the preparation of this publication included a systematic review of the literature selected from Scopus and ScienceDirect databases. The keywords such as "Friction Stir Welding", "FSW", "solid type welding" or "solid-state welding" were selected for the research. Several hundred documents from prominent journals publishing on FSW were reviewed. The area of analysis included articles published from the date of the invention of the FSW process (1991) up to the date. More than half of the references are publications from the last 10 years. Based on the reviewed publications, I prepared the text of the manuscript. I also acted as a correspondence author.

.....  
Aleksandra Laska

## 7.1.2. Content of the publication

### **Friction Stir Welding – an overview of tool geometry and process parameters**

Aleksandra Laska\*, Marek Szkodo

Faculty of Mechanical Engineering and Ship Technology, Gdansk University of Technology,  
Narutowicza 11/12, 80-233 Gdańsk, Poland

Corresponding author: [aleksandra.laska@pg.edu.pl](mailto:aleksandra.laska@pg.edu.pl)

**Abstract:** Friction Stir Welding (FSW) is a modern method that allows joining metals and their alloys, composites and polymers. The growing interest in this method and the increasing number of published articles affect the dynamic development of this method. The tool geometry is modified to ensure proper plasticizing and mixing of the material to be welded. The process parameters are selected in a way that minimizes the formation of defects typical for this method, such as kissing bonds, piping defects, tunnel defects.

This paper introduces the basic concepts relevant to the study and use of the Friction Stir Welding method. The overview discusses the welding tool design, the influence of process parameters on the joint mechanical properties and the characteristics of the possible weld defects. The characteristic microstructure of welds fabricated by the FSW method was also presented.

**Key words:** FSW; friction stir welding; tool geometry; welding parameters; joint microstructure; joint defects

#### 1. Introduction

Friction Stir Welding (FSW) is a novel method of joining materials invented by Wayne Thomas at The Welding Institute of the United Kingdom and patented in 1991 [1]. Initially, it was applied only to aluminium and its alloys but now it is a widely used method to join other materials, such as steel and ferrous alloys [2–4], titanium and its alloys [5–13], magnesium and its alloys [14–19], copper [20–25], polymers [26–31] and composites [32–37]. Friction Stir Welding is defined as a solid-state welding process, which means that the objects can be joined without reaching a melting point. It allows avoiding many of the difficulties that arise from a changing state, such as changes in gas solubility and changes in volumetric, that are often problems in fusion welding processes [38].

The basic concept of Friction Stir Welding is simple. During the process, the kinetic energy of a non-consumable rotating tool with a specially designed pin and shoulder is transformed into thermal energy generated by the friction of the tool moving along the edge of a contact line. The friction between the tool and the components provides the heat and softening of the material. The plastic deformation of the workpiece is accomplished by the rotating movement of the tool. After the tool is put into frictional heating and softening the material of the components, the tool is traversed into the joint line. The plasticized material is welded and extruded around the probe backward. Before cooling down the parts of the components are stirred and upset by the shoulder. Fig. 1 shows a butt joint for an illustration, but other types of joints can also be fabricated.

Friction Stir Welding method is considered to be the most significant metal joining development in the last three decades. Due to its versatility, environment friendliness and energy efficiency it is considered to be in a category of green technologies [39]. Comparing to other conventional welding methods, the FSW method consumes less energy, uses no gas or

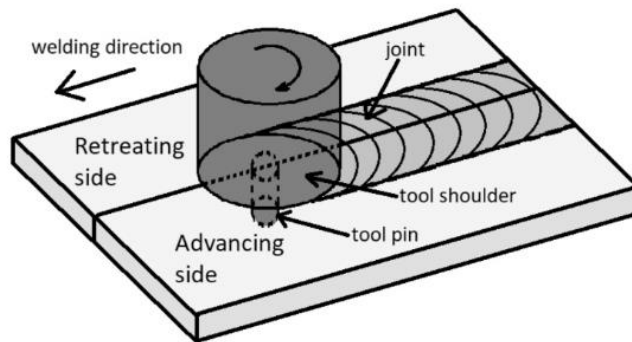


Fig. 1. Nomenclature of a tool for FSW process

flux and does not involve any filler material [40,41]. Furthermore, FSW can be applied to various types of joints [42]. Typically, this method is used to produce butt welds, lap welds and corner welds [43,44]. Applicability in all welding positions, excellent mechanical properties of the joints and ability for welding materials whose weldability by conventional techniques is low, make this method noteworthy for many industry branches. The FSW method is successfully applied in the aerospace industry (fuel tanks, fuselages, wings, cryogenic tanks) [45–47] as well as in the railway industry (wagons, underground carriages, container bodies) [48]. FSW has also found its applications in the land transportation (wheel rims, tail lifts and mobile cranes) [49], marine and shipbuilding industries (deck panels, hulls, offshore accommodation, masts, booms) [50] and construction industry (frames, pipelines, bridges, reactors) [51,52].

The above advantages of FSW over the conventional welding techniques have an impact on rapid development in the FSW field. There are hundreds of patent applications filed relating to this method and a number of publications grows exponentially [14,53]. In this paper, the current state of understanding and development of the FSW method is reviewed.

## 2. Geometry of a tool

A shape of a mixing tool is one of the most basic welding parameters, but it is also considered as one of the most important factors during the process. The material movement around the pin depends on the geometrical features of the tool [54]. The special design of the tool has been a matter of concern since the FSW method was considered as a big step in metal joining techniques. It resulted in improvement in throughput, weld quality and joint strength. A possible thickness of workpieces, type of materials to be welded and possible welding positions are conditioned by the tool geometry [43]. The main parts of the tool are a pin and a shoulder. Schematic geometry of the tool and its nomenclature is shown in Fig. 2.

The pin is a part that is directly plunged between parts of the workpiece to be welded. The friction between the pin and the welded components primarily produces the heat and the softening of the material [43,55]. The tool should be plunged into the workpiece till the shoulder touches the surface of the components and all the pin length is plunged between the pieces of the material to be welded [56]. A shoulder diameter to pin diameter ratio is critical from the

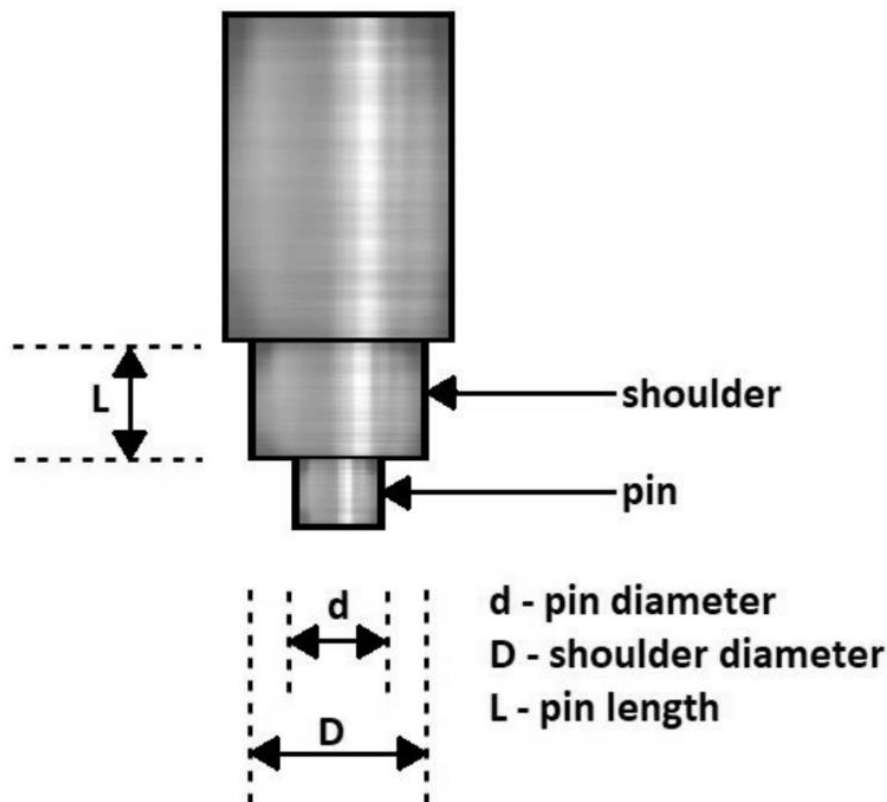


Fig. 2. Nomenclature of a tool for FSW process

heating aspects, while a tool design governs process loads, properties and uniformity of microstructure [39]. A shoulder diameter ( $D$ ) to pin diameter ( $d$ ) ratio has a significant role in providing heat at the time of material stirring. In their investigations of friction stir welding of aluminum alloys Dehghani et al. [57], Khodir and Shibayanagi [58], Cavaliere et al. [59], Leitao et al. [60] and Peel et al. [61] found that the thermal input has bigger impact on weld properties than the mechanical deformation by the tool.  $D/d$  ratio has an impact on the size of the stir zone and it plays an important role in the quality of welds. Consequently, the  $D/d$  ratio has to be chosen carefully to guarantee desired results. The effect of shoulder diameter to pin diameter ratio on tensile strength of friction stir welded 6063 aluminum alloy was studied by Khan et al [62]. The results of the studies demonstrated that a  $D/d$  ratio of 2.8 gives the minimum tensile strength and the  $D/d$  ratio of 2.6 results in the maximum tensile strength. In another paper, Saravan et al. investigated the effect of  $D/d$  ratio on mechanical properties of dissimilar friction stir welded AA2024-T6 and AA7075-T6 aluminum alloy joints [63]. The ratio was varied from 2 to 4, to create five different welds. It was observed that the weld fabricated by a tool with a  $D/d$  ratio of 3 results in the best mechanical properties when compared to other welds. Vijayvel et al. [64] used stir cast LM25 aluminum-based Metal Matrix Composite (MMCs) with 5% SiCp to fabricate friction stir welded joints using five different tools with  $D/d$  ratio in a range from 2 to 4. The analysis demonstrated that the  $D/d$  ratio of 3 yielded higher hardness and tensile properties.



Due to increased experience and understanding of material flow improvement, the geometry of tools has been developed significantly. The aim of creating new complex features to the geometry of tools is to reduce process loads and modify the mechanism of material flow. A shoulder of the tool is designed to heat the workpiece surface by friction. The shoulder also produces downward forging actions. It is necessary for welding consolidation and constraining heated material beneath the bottom surface of the shoulder. Two types of a shoulder outer surface shape can be distinguished – cylindrical and conical outer surface. A conical surface is used occasionally. The shape of the shoulder outer surface does not have a significant influence on the joint quality since the shoulder plunge depth is relatively small (from 1 to 5% of the gauge thickness) [39]. There are also three types of shoulder end surface shape – flat, concave and convex. The simplest design of the shoulder end surface is the flat shape, but this solution is not effective for trapping the material under the bottom shoulder, which results in the production of excessive material flash. The most popular for restricting extrusion of material from the sides of the shoulder is a concave shoulder [65,66]. The end surface of the shoulder can be featured with scrolls, ridges, knurling, grooves and concentric circles. It can also stay featureless. All of these features can be applied to any shoulder ends. The most popular feature used in FSW tools is the end surface with scrolls [67]. The aim of designing features is to increase material friction, shear and deformation. It results in better mixing of workpiece material and increases weld quality. Fig. 3. summarizes shoulder shapes and shoulder surface features.

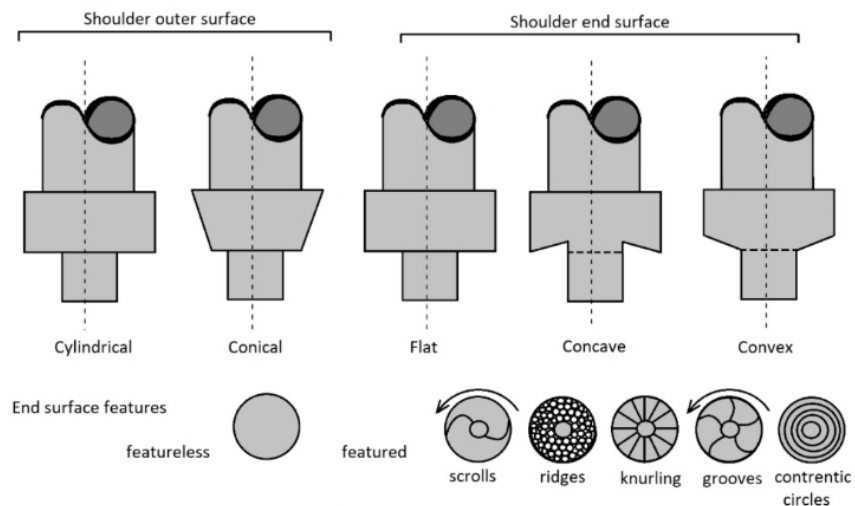


Fig. 3. Shoulder shapes and its surface features

A pin is an element of the FSW tool that is designed to provide frictional and deformational heating and mix soften the material of the workpiece in order to receive the joint. The depth of deformation is mainly governed by the pin. Fig. 4 shows the pin shapes and their features. The end surface of the pin can be flat or domed [68]. The flat pin might cause high forge force during plunging, while with the domed pin this problem can be minimalized. The researches prove that the best results are achieved when a ratio of a dome radius to the probe diameter is equal to 0,75 [69]. The outer surface shape can be cylindrical or tapered. Generally, cylindrical pins are widely used for plates with thickness up to 12 mm [70]. The outer surface of a pin might have features as threads, flats or flutes. Threaded pins are used for alloys with low abrasion, while threadless pins can be successfully used for highly abrasive materials [68]. In

his researches, Patel et al. [49] used three types of FSW tools to weld plates of magnesium alloys AZ91 with a thickness of 6 mm: threaded straight cylinder pin, taper cylindrical pin and straight cylindrical pin. The ratio of shoulder diameter to pin diameter was equal to 3. After performing all experiments it was observed that all the joints that were created by taper cylindrical pin had defects like voids, cracks and unwelded zones.

The best results were performed by welds created with the threaded straight cylindrical pin. In those welds, no defects were observed and the welds performed high tensile strength. Kadian et al. [71] investigated the effect of tool pin profile on the material flow characteristics. The aluminum AA6061 plates were prepared to be welded. Seven different types of pins were used: tapered, tapered with threads, tapered with grooves, cylindrical, square, trigonal curved and trigonal. The investigation of the material flow characteristics shows that cylindrical and

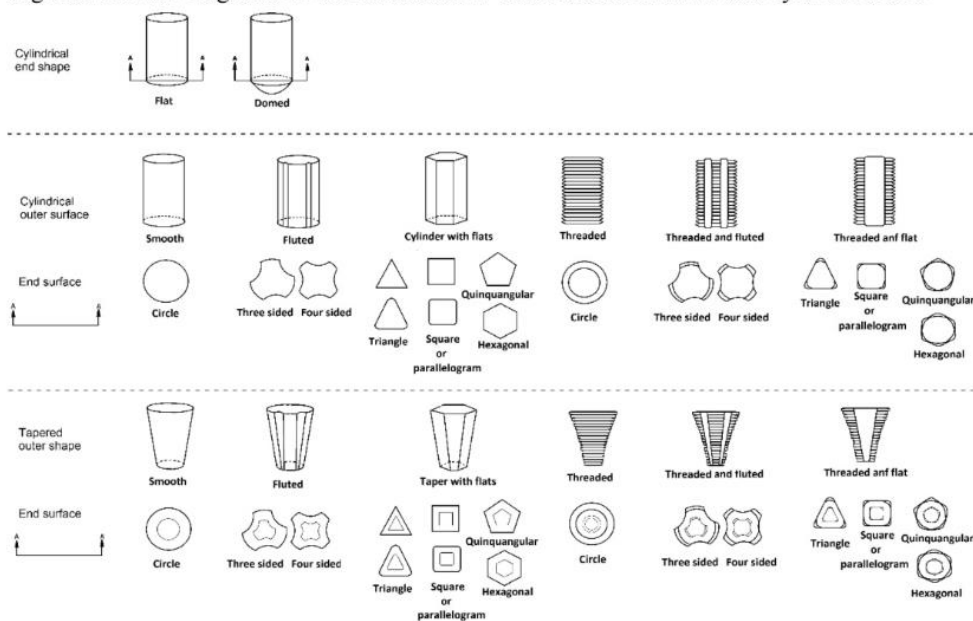


Fig. 4. Pin shapes and their main features

tapered pin profiles provide higher homogeneity in deforming regions. Featureless tools defected the material in the welding zones. Moreover, the grooved tool geometry provided higher material movement but unable the material to move near the pin due to the increase of material viscosity.

The tool geometry is one of the most basic process parameters, but it is also considered as the most important one. The tool provides frictional heating of the material, softening and mixing in the welding zone. There are plenty of shapes of the shoulder and the pin. They can also be modified with features like threads, scrolls, grooves. A proper selection of the geometry of the tool effects in mechanical properties of the joint and enable to minimize the risk of defects in the joint.

### 3. Welding parameters

The Friction Stir Welding method is mostly characterized by two parameters: tool rotational rate ( $\omega$ ) and tool traverse speed ( $v$ ) along the line of edges to be welded [72]. The rotation movement of a tool can be in a clockwise or counterclockwise direction. Stirring and mixing of

the material around the pin is a result of the rotation of the tool. The linear movement of the tool moves the stirred material from the front to the back of the pin and it finishes the welding process [73]. Choosing the proper tool traverse speed and tool rotational rate is a fundamental problem in the design in the FSW process. Fujii et al. [6] welded commercially pure titanium plates with 2 mm in thickness by the FSW method at a tool traverse speed from 50 to 300 mm/min. The grain size and hardness of the samples welded at a different welding speed were measured. The highest welding speed equal to 300 mm/min resulted in the highest hardness of 190 HV and the smallest grain size equal to 3.5  $\mu\text{m}$ . In general, all the welds had a grain size smaller than the base metal. The welding process resulted in a significant decrease in the grain size due to the occurrence of dynamic recrystallization. The grain refinement increased the hardness in the stir zone. The tensile strength of the stir zone at different welding speed was measured. The tensile strength of the base material was equal to 420 MPa. For the samples processed at the welding speed lower than 200 mm/min, the tensile strength was lower than for the base metal. However, the tensile strength increased with increasing the welding speed due to the microstructure refinement. When the welding speed increased to 200 mm/min, the tensile strength of the weld exceeded that of the base material and was equal to 450 MPa. When the welding speed increased to 300 mm/min, the tensile strength of the joint decreased despite the significant refinement of the microstructure, due to the formation of the weld defects in the stir zone, which was caused by the insufficient plastic flow during the welding process. Kumar et al. [32] investigated the influence of tool rotational speed and tool traverse speed during friction stir welding of polymer matrix composite (PMC). Sheets of glass-filled Nylon 6 with a thickness of 5 mm were welded at a tool traverse speed from 0,2 to 0,4 mm/s in steps of 0,1 mm/s and at a tool rotational speed from 400 to 600 rpm in steps of 100 rpm. The ultimate tensile strength and elongation were measured as a function of the tool rotational speed. The ultimate tensile strength of glass-filled Nylon 6 increased to a maximum value at 600 rpm. It was observed that lower tool rotational speed led to defects like wormholes, cracks and tunnel defects in the retreating side due to less heat generation. In comparison to the base material, all of the welded plates showed lower elongation, which is attributed to the concentration of high plastic strain within the thermo-mechanically affected zone. The deformations were concentrated at the zone between the base material and the weld nugget. The elongation of the samples increased with the increase of the tool rotational speed. The effect of tool traverse speed on the ultimate tensile strength and elongation was investigated. The ultimate tensile strength and elongation decreased with the decreasing tool traverse speed from 0,2 to 0,4 mm/s. Moreover, at the tool traverse speed value lower than 0,2 mm/s the tensile strength was lower and the weld zone was not uniform. This may be caused by overheating of the weld zone. Yoo et al. [74] used the FSW method to join Al-Li alloy. The mechanical properties and macrostructure of the joint were investigated. To compare the results, the rotational speed and the traverse speed of the tool were selected as process parameters. After welding, the material was inspected by non-destructive tests using the x-ray to find defects. The range of the rotational speed was 300-800 rpm and 120-420 mm/min for the traverse speed. The results show that with an increasing tool traverse speed, the possibility of a defect formation was higher. For the tool rotational speed of 300 rpm the tool traverse speed of 240 mm/min resulted in the formation of defects. At the same tool rotational speed and lower tool traverse speed, no defects were observed. For the tool rotational speed in the range from 400 to 800 rpm. The tool traverse speed of 360 mm/min made the defects occurred. Higher tool traverse speed also resulted in the formation of defects. Tensile tests were conducted to verify the strength and elongation of the joints using defect-free specimens. The highest strength values were observed when the tool rotational speed is in a range of 400 to 600 rpm while the tool traverse speed is in a range of 230-300 mm/min. The maximum ultimate strength of the joint was equal to 73,9% of base metal, while the lowest value was equal to 63,3% when the tool rotational speed was high and



the tool traverse speed was low. Elongation results performed more wide distribution – from 44,2% to 100,1% of the base metal. The lowest elongation was observed at the highest tool rotational speed equal to 800 rpm. The highest values of relative elongation were observed at the tool rotational speed in a range of 400 rpm. Fujii et al. [75] successfully applied the FSW method to weld three types of carbon steels with different carbon contents (IF steel, S12C and S35C). The ultimate strength was measured as a function of the welding traverse speed, which was in a range from 50 to 450 mm/min. For both kinds of carbon steel, the strength of the friction stir welded joints increased in comparison to the base material. The welding conditions significantly affected the mechanical properties of the carbon steel samples. The ultimate strength of S12C steel joints increased with the increase of traverse speed. The ultimate strength of S35C steel firstly increased to around 800 MPa at the welding speed of 200 mm/min. When the welding speed increased above that value, the ultimate strength decreased significantly. The mechanical properties of IF steel joints are not significantly changed by the welding conditions and the initial grain size. Peel et al. [61] used the FSW method to weld AA5083 plates of 3 mm thickness. All the butt welds were welded under identical conditions and at the same tool rotational speed. The tool traverse speed was varied and was equal to 100, 150 and 200 mm/min. The ultimate tensile strength decreased and was equal to 304, 216 and 186 MPa, respectively, while the ultimate tensile strength of the parent material was equal to 457 MPa. With higher tool traverse speed, the defects on the weld line occurred. Moreover, the microstructure analysis proved that the reducing traverse speed increases heat input and this causes the nugget zone to become wider, more homogeneous and flatter. In the study of Sayer et al. [76] AA6063 plates were welded by friction stir welding. Three values of tool rotational speed (900, 1600 and 2800 rpm) and three values of tool traverse speed (100, 200 and 400 mm/min) were selected. The tensile properties of the welds were lower than those of the parental material. In terms of tensile properties, an optimum welding speed of 100 mm/min and rotational speed of 2800 rpm were stated. The ultimate tensile strength under these parameters was equal to 70% of the base material strength. The yield strength of the specimens was measured and for all combinations of the tool traverse speed and the tool rotational speed was equal to about 40% of the base material value. The variation of the welding parameters did not significantly affect the yield strength. Moreover, the lower tool rotational speed was applied, the higher possibility of the weld defects occurred. Peel et al. [77] investigated the effect of changing the rotational and traverse tool speed on the mechanical properties of the dissimilar material welds. AA5083 and AA6082 were used for both advancing and retreating sides. The tool rotational speed varied from 280 to 840 rpm in steps of 280 rpm and the traverse speed varied from 100 to 300 mm/min in steps of 100 mm/min. The ultimate tensile strength and elongations to failure were measured. For the joints welded at the traverse speed of 100 mm/min and with AA5083 in the advancing side, the ultimate tensile strength decreased from 204 MPa to 199 MPa when the rotational speed increased from 280 to 840 rpm. When the traverse speed increased to 200 and 300 mm/min, the opposite dependence can be observed. In all cases, the tool rotational speed did not have a significant influence on the ultimate tensile strength. For the welds with AA6082 in the advancing side, similar conclusions can be drawn. However, for those specimens, more defects were observed. For both cases, when different material was in the advancing side, the ultimate tensile strength increased with the increase of the tool rotational speed. Elongation to failure for both cases was also investigated. The best results were observed with the highest traverse speed of the tool equal to 300 mm/min for both materials in the advancing side. In the study of Raweni et al. [44] Taguchi method was applied to propose the optimized set of the FSW parameters to weld AA5083 plates. The mathematical formulas enabled to predict the characteristics of the welds prepared under different conditions. The results show that the traverse speed has the highest effect on the fracture toughness and the crack propagation energy is the highest when the tool traverse speed is the highest. The optimum parameters for the total



input energy and the energy for crack initiation were equal to 600 rpm for the rotational speed and 125 mm/min for the tool traverse speed. Feng et al. [78] investigated the microhardness of the FSW 7075Al-T651 alloy welds made using different tool traverse speed values. At a constant tool rotational speed of 800 rpm, as the tool traverse speed increased from 100 to 400 mm/min, the hardness values increased and the width of the lowest hardness zone decreased. The same investigations were made for the constant tool traverse speed and the increasing tool rotational speed from 800 to 1200 rpm. The width of the low hardness zone had almost no change and the hardness values did not change significantly either. However, the location of the low hardness zone changed and moved outward. The same relationship for FSW 6061Al-T651 alloy was proved by Feng et al. [79]. In the research conducted by Zhang et al. [80] 2024Al-T351 plates were successfully welded by the FSW method at the varying tool rotational rate from 400 to 1200 rpm in steps of 400 rpm and at the tool traverse speed equal to 100, 200 and 400 mm/min. The ultimate tensile strength increased from 408 to 451 MPa, respectively with an increase of the tool traverse speed, for the joints made with a tool rotational speed of 800 rpm. The elongation at those parameters increased with an increase of the tool traverse speed. No significant influence on ultimate tensile strength and elongation was observed with a change of the tool rotational speed from 400 to 1200 rpm. The same results were observed by Feng et al. [81] on 7075Al-T651 FSW joints and Liu et al. [82] at 6061Al-T651 FSW joints. Balasubramanian [83] investigated macrostructure of FSW joints using five different aluminum alloys – AA1050, AA6061, AA2024, AA7039, AA7075. All the fabricated welds were analyzed at low magnification by an optical microscope. Different values of the tool traverse speed at the constant tool rotational speed of 1200 rpm were used. Of the five tool traverse speed values used, the welds fabricated with the traverse speed of 135 mm/min for AA1050 alloy resulted in defect-free joints. The welding speed of 75 mm/min for AA2024, 100 mm/min for AA6061, 45 mm/min for AA7039 and 22 mm/min for AA7075 alloys resulted in a formation of defect-free joints. The same investigations were conducted for the varying tool rotational speed. The constant tool traverse speed of 75 mm/min was kept. Joints fabricated with a rotational speed equal to 900 rpm for AA1050, 1100 rpm for AA6061, 1200 rpm for AA2024, 1300 rpm for AA7039 and 1500 rpm for AA7075 alloys resulted in the formation of defect-free joints. For other combinations of parameters defects like pin holes, tunnel defects, piping defects, kissing bonds and cracks occurred. Sevel et al. [51] investigated the impact of the tool traverse speed and the tool rotational speed to a formation of defects on friction stir welded AZ31B magnesium alloy lap joints. The lowest tool rotational speed of 500 rpm resulted in a formation of tunnel defects for all the selected tool traverse speed values. Of the selected process parameters, the joint fabricated under the combination of the highest tool rotational speed equal to 1000 rpm and the tool traverse speed of 0,5 mm/min was found to be defect-free.

Another parameter, widely considered in the context of the influence on the weld properties is the tilt angle of the tool during the FSW process. It can be observed that the temperature in the nugget, the heat-affected zone and the thermo-mechanically affected zone increases with the increase of the tilt angle [84]. This phenomenon is caused by both the increase in friction heat due to a bigger contact area between the workpiece and the pin and the increase of plastic work deformation energy. A large tilt angle also promoted high hydrostatic pressure in the weld zone, which significantly enhances nugget integrity [85]. However, high hydrostatic pressure and high temperature in the welding zone may favor severe tool wear. Generally, the welding force increased as decreasing the tool inclination angle [59]. Usually, a tilt angle in the range from 1 to 3° is used [15,47,57,72,76,86–92]. Hamid et al. [93] investigated the effect of the tilt angle on microstructure and mechanical properties of dissimilar aluminum alloy sheets between AA6061 and AA5083 sheets. For the experiments, the tilt angles from 0 to 4°, in steps of 1° were used. The welding speed of 86 mm/min and the tool rotational speed of 910 rpm were set.



The micrographic overviews of the welds revealed that the tilt angle of  $3^\circ$  resulted in the joint with no defects, while lower tilt angles resulted in the formation of tunnel defects on the bottom part on the weld nugget which resulted in the decrement of strength. The hardness of all the prepared welds was investigated. The observations showed that the hardness of the weld nugget zone was slightly higher than the hardness of the base material. Moreover, the hardness of the heat-affected zone and the thermo-mechanically affected zone was lower than the hardness of the weld nugget. The hardness of the weld prepared with the tilt angle of  $3^\circ$  was higher than the joints produced with different tilt angles. Vijayaraghavan et al. [94] prepared welds between plates of dissimilar aluminum alloys using different tilt angles in the range from  $1$  to  $3^\circ$ . A plate of AA7075 alloy on the advancing side and AA6082 on the retreating side were prepared. The influence of the tilt angle on tensile strength was investigated. The experiments proved that the higher tilt angle is used, the lower tensile strength of the weld is performed. The impact strength of the joints also decreased with the increase of the tilt angle. Kumar et al. [32] investigated the influence of the tilt angle on the mechanical properties of glass-filled Nylon 6 composite. The effect of different tilt angles in the range from  $0$  to  $2^\circ$ , on the ultimate tensile strength and the elongation, were investigated. The ultimate tensile strength and the elongation increased to a maximum value as the tool tilt angle increases from  $0$  to  $2^\circ$ . This phenomenon may be mostly attributed to creating extra pressure and heat generation for the proper mixing of weld material by the edge of the shoulder. The obtained results of ultimate tensile strength were also correlated to the results of Sadeghian et al. [95].

The above examples lead to the conclusion that the ultimate tensile strength of the welded materials increases to the highest value and then has a tendency to decrease with the increase of the tool traverse speed. Moreover, the elongation increases with an increase in the tool traverse speed. The ultimate tensile strength increase with an increase of the tool rotational speed for polymer matrix composites, but the opposite tendency can be observed for joining dissimilar aluminum alloys. The elongation of polymer matrix composite welds increases with the increase of the tool rotational speed but decreases with the increase of the tool rotational speed for Al-Li alloys.

#### 4. Weld microstructure

The solid-state nature of the friction stir welding process results in a very characteristic microstructure. Some of the distinguished regions are common to all welding techniques, including the ones, in which the material melts. Some zones are characteristics only to the FSW technique, in which the material does not reach the melting point. A typical cross-section of the FSW weld is shown in Fig.5.



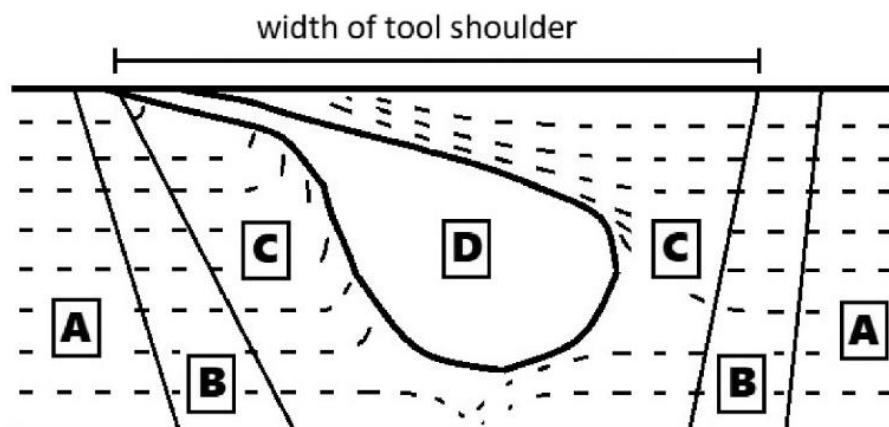


Fig.5. Schematic cross-section of a typical FSW weld including four distinct zones: A – base material, B – heat-affected zone, C – thermo-mechanically affected zone, D – stirred zone (nugget)

The formation of the stir zone called nugget is the result of recrystallization in the thermo-mechanically affected zone. In aluminum alloys, the nugget is generally composed of fine grain size material. Further, it is considered to be experienced plastic deformations from the interaction with the welding tool pin. In some cases, the nugget may mimic the shape of the pin profile. According to Rhodes et al. [96] and Liu et al. [97] in the interior of the recrystallized grains, there is usually a low density of dislocation. However, some investigators proved that the recrystallized grains of the weld nugget zone contain high density of sub-boundaries [98], dislocations [99] and subgrains [100]. The interface between the tool and the nugget zone and the parent material is relatively sharp on the advancing side of the tool and diffuse on the retreating side [101]. Depending on the process parameters, various types of nugget zone shapes are observed. In general, the nugget shape may be classified into two types. The first one is the basin-shaped nugget that widens near the upper surface. Elliptical nuggets may be also observed. Sato et al. [98] notified the existence of the basin-shaped nugget created by the FSW process of 6063Al-T5 plates. It was suggested that the upper surface of a weld is experienced by extreme deformation and heating due to contact with a cylindrical-tool shoulder, which results in the generation of the basin-shaped nugget zone. Mahoney et al. [102] noticed the existence of the elliptical nugget zone of 7075Al-T651 welded plates. Martin et al. [103] investigated an effect of the process parameters on the properties and microstructure of A356 cast aluminum alloy friction stir welded joints. It was observed that the lower tool rotational speed of 300-500 rpm resulted in forming basin-shaped nuggets. Elliptical nuggets were observed when the tool rotational speed was higher than 700 rpm. This indicates that not only tool geometry, but also changing process parameters affect the nugget shape. Reynolds et al. [104] investigated the influence of the pin size on the nugget size. For all experiments, the nugget zone size was slightly bigger than the pin diameter, except at the bottom of the weld, where the pin was tapered to a hemispherical termination. Further, as the pin diameter increases, the nugget acquires a more rounded shape.

The existence of a unique transition zone between the base material and the nugget zone is characteristic for the FSW process. The thermo-mechanically affected zone (TMAZ)



experiences both deformation and temperature during the process. In the TMAZ the parent metal elongated grains are highly deformed in an upward flowing pattern around the nugget zone. The material in the TMAZ undergoes plastic deformation however, the recrystallization does not occur due to insufficient deformation strain. Due to high-temperature exposure during the FSW process, the dissolution of some precipitates is observed in the TMAZ. Furthermore, it is revealed that the grains in TMAZ might contain a high density of sub-boundaries [98]. In aluminum alloys, the TMAZ represents a significant area [43]. The TMAZ usually has lower microhardness and the corrosion susceptibility is increased.

The heat-affected zone is located beyond the TMAZ and experiences a thermal cycle. In the HAZ does not occur any plastic deformation. The HAZ experiences a temperature rise above 250°C for a heat-treatable aluminum alloy [105]. Although the HAZ retains the same grain structure as the parent material, the thermal exposure above 250°C causes a significant effect on the precipitate structure. The HAZ is sufficiently heated during the process so it alters the properties of that material without any plastic deformation. The alteration of properties in the HAZ includes changes in ductility, toughness, corrosion susceptibility and strength, but does not change the grain size or chemical makeup.

Li et al. [106], Ma et al. [107], Kwon et al. [108–110] and Sato et al. [42] investigated the influence of the process parameters on the microstructure of friction stir welded aluminum alloys. It was reported that the size of the recrystallized grains can be reduced by decreasing tool rotational rate with a constant tool traverse speed or by decreasing the ratio of the tool rotational speed to the tool traverse speed. A higher tool rotational speed at a constant tool traverse speed or a higher ratio of the tool rotational speed to the tool traverse speed results in an increase of a degree of deformation and an increase of a peak temperature of the thermal cycle. The increase in the peak temperature during the FSW process results in a generation of coarse recrystallized grains, which leads to a remarkable grains growth. Kwon et al. [80-82] noted that with the increase of the tool rotational speed from 560 to 1840 rpm, the average grain size increases from ~0,5  $\mu\text{m}$  to 4  $\mu\text{m}$  for 1050Al alloy with a constant tool traverse speed of 155 mm/min. Sato et al. [42] noted that increasing the tool rotational rate from 800 to 2450 rpm, the size of recrystallized grain increases from 5,9 to 17,8  $\mu\text{m}$  for 6063Al alloy welded at the tool traverse speed of 360 mm/min. Ma et al. [107] reported that with a decrease of the ratio of the tool rotational speed to the tool traverse speed from 400 rpm/102 mm/min to 350 rpm/152 mm/min, the size of the recrystallized grain size decrease from 7,5 to 3,8  $\mu\text{m}$  for friction stir welded 7075Al-T7651 alloy.

A tendency to increase of the grain size in the weld zone can be observed with the decreasing of the distance to the top of the weld zone. The grain size decreases with the increasing distance of both sides of the weld-zone centreline. This phenomenon correspond roughly to a temperature variation in the weld zone [102,106,111]. Mishra et al. [112] investigated a variation in the grain size as a function of the distance from the top of the 7050Al weld. The average size of the grain ranges from 3,2  $\mu\text{m}$  at the bottom of the weld to 5,3  $\mu\text{m}$  at the top. Pao et al. [113] reported that for friction stir welded 2519Al plates the average grain size ranges from 12  $\mu\text{m}$  to 2  $\mu\text{m}$  in the top and bottom region of the weld nugget, respectively.

## 5. Weld defects

The friction stir welding method allows producing welds free from solidification-related defects since the material does not reach a melting point [20]. Therefore, all the defects related to the presence of brittle interdendritic and eutectic phase are eliminated [114]. Compared with conventional welding techniques, the possibility of the occurrence of defects during the FSW process decreases by 10% [115]. Although the material is only plasticized during the process, it is susceptible to create defects such as tunnel defects, pin holes, piping defects, kissing bonds,





zigzag lines and cracks. In general, the reason for creating the defects is improper material flow and insufficient consolidation of the material in the weld nugget zone [116].

One of the most important process parameters is the tool geometry. The heat is mostly generated at the interface between the workpiece and the tool shoulder. Heterogeneity in heat generation leads to the formation of defects in the form of excess flash due to the overheating of the surface [117,118]. Palanivel et al. [119] examined the influence of the tool geometry on the formation of defects in the welds of dissimilar aluminum alloys AA5083-H111 and AA6351-T6. Five different tool pin profiles were used: straight square, straight hexagon, straight octagon, tapered square and tapered octagon. All the welds fabricated using straight hexagon, straight square and straight octagon pins were defect-free. The welds fabricated using tapered pins demonstrated the presence of the tunnel defects in the welds. Elangovan et al. [120] investigated the effect of the tool pin design on the tendency to defect formation of friction stir welded AA2219 aluminum alloys. Straight cylindrical, tapered cylindrical, threaded cylindrical, triangular and square pin profiles were used. The square shape pin fabricated the least defect content in the welds. Furthermore, a square tool performed high eccentricity, which means the ratio of the dynamic volume swept by the tool to the static volume of the tool was the highest.

In general, the tendency to crack propagation increases with the increase of the welding speed, but also the alloy-dependence can be observed [121]. Moreover, at high tool traverse speed and at low tool rotational speed, inadequate heat input may cause insufficient plastic flow, which results in a formation of defects like tunnel holes or groove-like defects. High tool rotational speed may be a reason to emerge plastic flow defects, causing internal defects [118]. At high tool traverse speed and high tool rotational speed, the abnormal stirring may occur defects caused by the different temperatures between the upper part at the surface of the weld and the bottom of the weld. The shape of the weld formed with abnormal stirring is different from the shape of the proper weld – the top part on the advancing side suggests the discontinuous flow of the material [118]. Rouhi et al. [122] suggested that due to the excessive frictional heat at a high tool rotational speed, material adhere to the pin, which results in creation of wormhole defects. Yoo et al. [74] investigated the influence of the tool traverse speed and the tool rotational speed on the tendency to create defects during the FSW process of Al-Li alloys. The tool traverse speed higher than 300 mm/min resulted in the formation of defects for all investigated tool rotational speed (from 300 to 800 rpm). Furthermore, at the tool rotational speed of 300 rpm, the defects appear at 240 mm/min.

One of the most specific to the FSW method defects is the hooking defect, observed in the TMAZ, mostly considered to a friction stir lap welded magnesium alloys. The limited informations on the friction stir lap welded aluminum alloys indicate that the hooking defects and unwelded lap oxide layers reduce the effective thickness of the top workpiece and can orientate the unwelded lap as a pre-crack to a more preferred crack propagation direction, which significantly reduces the fatigue properties [118,123–126]. Naik et al. [127] characterized friction stir lap welded AZ32B-H24 magnesium alloy welds in terms of the presence of the hooking defects. It was observed that the tool rotational rate has the most significant influence on the formation of hooking defects – with the decrease of the tool rotational speed from 1500 rpm to 1000 rpm, the height of the hook was reduced from 1,4 to 0,14 mm. The increase of the tool traverse speed from 10 to 20 mm/s resulted in the nonsignificant reduction of the height of the hook from 1,4 to 1,3 mm. A relatively “cold” weld leads to the almost complete elimination of hooking defects. Yet other investigations suggest that the low tool rotational speed induces the formation of other types of defects. Mironov et al. [128] fabricated friction stir welded joints of AZ31 magnesium alloy. At a tool rotational speed lower than 1000 rpm tunnel-type defects were observed at the weld root, due to the relatively unstable character of the material flow at low process temperatures. It is noteworthy, that at the low tool rotational speed, consequently, at the low temperature fabricated welds, the stir zone closely resemble the shape of the pin,



while at higher temperatures, the stir zone has an elliptical shape, which is an effect of a change in the material flow in higher temperature.

Investigations on applying the FSW method to polymers prove that the poor thermal conductivity of this group of materials creates a nonuniform distribution of temperature that restricts heat from advancing side to retreating side. Hence the defects are mainly located the retreating side [129,130]. At extreme low tool rotational speed wormholes, tunnel defects and cracks are observed in the retreating side. Too high tool rotational speed may cause the burn of the material [95,131]. Mendes et al. [130] examined the main factors affecting acrylonitrile butadiene styrene (ABD) during the friction stir welding method performed by a robotic system. The increase in the rotational speed resulted in a decrease in the size and quantity of defects. Furthermore, the welds fabricated with lower axial force present external and internal defects like gaps on the surface on the retreating side of the weld, cavities and pores on the border of stiffing zone and thermo-mechanical affected zone of the retreating side of the welds. Moreover, the deformations on the surface occur mostly on the advancing side due to higher heating and softening of the material on the advancing side than the retreating side [132]. Although the tool shape and welding parameters like the tool traverse speed and the tool rotational speed affect materials flow patterns no specific character has been related to the formations of pores and other defects [46].

## 6. Summary

This article briefly summarized the basic concept of the friction stir welding and the influence of the process parameters on the joints properties. Despite the short history of the process, it is applied in many diverse industries such as aerospace industry, railway industry, marine and shipbuilding industry, land transportation, construction industry and more. The most important principle that distinguishes the FSW process from traditional welding techniques is only plasticizing the material without reaching a melting point. This feature allows materials that are difficult to weld by conventional methods to be joined by the FSW technique. Due to the relatively high thermal conductivity of aluminium and its alloys, FSW welding has brought enormous progress in the field of joining this material. This method allows also to join hard materials such as steel and other engineering alloys, as well as composites and polymers. Significant progress has been made in the understanding of the influence of the tool geometry on the mechanical properties of the joints and the possibility to create weld defects. Due to increased experience, tool geometry has been developed significantly. New features of the geometry allow to reduce process loads and control the material flow during the process.

During the FSW process, a variety of microstructural changes are identified in various zones. In the nugget zone, full recrystallization can be observed and it leads to the refinement of the grain size. In the thermo-mechanically affected zone, typical for the FSW method, the material undergoes plastic deformations, but the recrystallization cannot be observed. The changes in mechanical properties can also be observed in the heat-affected zone, although it retains the same grain size as the parent material.

Next to the tool geometry, the most important process parameters are the tool traverse speed and the tool rotational speed. The proper choice of these parameters has been a fundamental problem in the process design. Numerous experimental and computer models led to the conclusion that with the increase of the tool traverse speed, the ultimate tensile strength of the welds initially increases to the highest value and then decreases. In all presented examples, the elongation increases with an increase in the tool traverse speed. The ambiguous conclusions are observed in the influence of the tool rotational speed on the ultimate tensile strength and elongation. The material dependence exacts the proper selection of the appropriate parameters for the material. Based on the literature review, a tilt angle in the range from 1 to 3° is usually



used. With the increase of a tilt angle, the temperature in the nugget, the heat-affected zone and the thermo-mechanically affected zone increases.

Although all the defects related to the solidification of the welded material are eliminated, there are several possible defects that occur only at the FSW method. Tunnel defects, pin holes, piping defects, kissing bonds, zigzag lines and cracks are ones of the most popular occurring defects. The tool geometry has an important influence on the possibility of creating defects. During the FSW process, the heat needed to plasticize the material is generated at the interface between the workpiece and the tool shoulder.

Despite many studies conducted on the mechanical properties of FSW welded joints, there are no universal conclusions regarding the impact of process parameters on the properties of joints. Researches show that, depending on the material characteristics, process parameters can affect the mechanical properties of joints differently.

Future research should focus on improving the welding tool geometry, examining the impact of process parameters on joint properties and standardizing the trends of these relationships for different materials.

This research did not receive any specific grant from funding agencies in the public, commercial, or not-for-profit sectors.

#### References

- [1] R. V. Arunprasad, G. Surendhiran, M. Ragul, T. Soundarrajan, S. Moutheepan, S. Boopathi, Review on Friction Stir Welding Process, *Int. J. Appl. Eng. Res.* ISSN. 13 (2018) 5750–5758.
- [2] H. Fujii, Friction Stir Welding, *Weld. Int.* 25 (2011) 260–273. <https://doi.org/10.1080/09507111003655358>.
- [3] M. Mahoney, T. Nelson, C. Sorenson, S. Packer, Friction stir welding of ferrous alloys: Current status, *Mater. Sci. Forum.* 638–642 (2010) 41–46. <https://doi.org/10.4028/www.scientific.net/MSF.638-642.41>.
- [4] K.M. Venkatesh, M. Arivarsu, M. Manikandan, N. Arivazhagan, Review on friction stir welding of steels, *Mater. Today Proc.* 5 (2018) 13227–13235. <https://doi.org/10.1016/j.matpr.2018.02.313>.
- [5] A. Lauro, Friction stir welding of titanium alloys, *Weld. Int.* 26 (2011) 8–21. <https://doi.org/10.1080/09507116.2011.581351>.
- [6] H. Fujii, Y. Sun, H. Kato, K. Nakata, Investigation of welding parameter dependent microstructure and mechanical properties in friction stir welded pure Ti joints, *Mater. Sci. Eng. A.* 527 (2019) 3386–3391. <https://doi.org/10.1016/j.msea.2010.02.023>.
- [7] G. Buffa, D. Campanella, M. Cammalleri, A. Ducato, A. Astarita, A. Squillace, S. Esposito, L. Fratini, Experimental and Numerical Analysis of Microstructure Evolution during Linear Friction Welding of Ti6Al4V, *Procedia Manuf.* 1 (2015) 429–441. <https://doi.org/10.1016/j.promfg.2015.09.053>.
- [8] K. Gangwar, M. Ramulu, Friction stir welding of titanium alloys: A review, *Mater. Des.* 141 (2018) 230–255. <https://doi.org/10.1016/j.matdes.2017.12.033>.
- [9] C. Rajendran, K. Srinivasan, V. Balasubramanian, H. Balaji, P. Selvaraj, Effect of tool tilt angle on strength and microstructural characteristics of friction stir welded lap joints of AA2014-T6 aluminum alloy, *Trans. Nonferrous Met. Soc. China (English Ed.)* 29 (2019) 1824–1835. [https://doi.org/10.1016/S1003-6326\(19\)65090-9](https://doi.org/10.1016/S1003-6326(19)65090-9).
- [10] H.J. Liu, L. Zhou, Microstructural zones and tensile characteristics of friction stir

- welded joint of TC4 titanium alloy, *Trans. Nonferrous Met. Soc. China (English Ed.* 20 (2010) 1873–1878. [https://doi.org/10.1016/S1003-6326\(09\)60388-5](https://doi.org/10.1016/S1003-6326(09)60388-5).
- [11] L. Zhou, H.J. Liu, L.Z. Wu, Texture of friction stir welded Ti-6Al-4V alloy, *Trans. Nonferrous Met. Soc. China (English Ed.* 24 (2014) 368–372. [https://doi.org/10.1016/S1003-6326\(14\)63070-3](https://doi.org/10.1016/S1003-6326(14)63070-3).
- [12] D. Ghahremani Moghadam, K. Farhangdoost, Influence of welding parameters on fracture toughness and fatigue crack growth rate in friction stir welded nugget of 2024-T351 aluminum alloy joints, *Trans. Nonferrous Met. Soc. China (English Ed.* 26 (2016) 2567–2585. [https://doi.org/10.1016/S1003-6326\(16\)64383-2](https://doi.org/10.1016/S1003-6326(16)64383-2).
- [13] S. Mironov, Y.S. Sato, H. Kokawa, Development of grain structure during friction stir welding of pure titanium, *Acta Mater.* 57 (2009) 4519–4528. <https://doi.org/10.1016/j.actamat.2009.06.020>.
- [14] K. Singh, G. Singh, H. Singh, Review on friction stir welding of magnesium alloys, *J. Magnes. Alloy.* 6 (2018) 399–416. <https://doi.org/10.1016/j.jma.2018.06.001>.
- [15] N. Xu, Q. Song, Y. Jiang, Y. Bao, H. Fujii, Large load friction stir welding of Mg–6Al–0.4Mn–2Ca magnesium alloy, *Mater. Sci. Technol. (United Kingdom).* 34 (2018) 1118–1130. <https://doi.org/10.1080/02670836.2018.1424794>.
- [16] R.C. Zeng, W. Dietzel, R. Zettler, W.M. Gan, X.X. Sun, Microstructural evolution and delayed hydride cracking of FSW-AZ31 magnesium alloy during SSRT, *Trans. Nonferrous Met. Soc. China (English Ed.* 24 (2014) 3060–3069. [https://doi.org/10.1016/S1003-6326\(14\)63443-9](https://doi.org/10.1016/S1003-6326(14)63443-9).
- [17] K. Wang, Y. Shen, X. rong Yang, X. hong Wang, K. wei Xu, Evaluation of Microstructure and Mechanical Property of FSW Welded MB3 Magnesium Alloy, *J. Iron Steel Res. Int.* 13 (2006) 75–78. [https://doi.org/10.1016/S1006-706X\(06\)60082-4](https://doi.org/10.1016/S1006-706X(06)60082-4).
- [18] W. Wang, P. Han, K. Qiao, T. Li, K. Wang, J. Cai, L. Wang, Effect of the rotation rate on the low-cycle fatigue behavior of friction-stir welded AZ31 magnesium alloy, *Eng. Fract. Mech.* 228 (2020) 106925. <https://doi.org/10.1016/j.engfracmech.2020.106925>.
- [19] P. Gulati, D.K. Shukla, A. Gupta, Defect formation analysis of Friction Stir welded Magnesium AZ31B alloy, *Mater. Today Proc.* 4 (2017) 1005–1012. <https://doi.org/10.1016/j.matpr.2017.01.113>.
- [20] T.S. Rao, G.M. Reddy, G.S. Rao, S.R.K. Rao, Studies on salt fog corrosion behavior of friction stir welded AA7075-T651 aluminum alloy, *Int. J. Mater. Res.* 105 (2014) 375–385. <https://doi.org/10.3139/146.111033>.
- [21] A. Forsström, S. Bossuyt, Y. Yagodzinsky, K. Tsuzaki, H. Hänninen, Strain localization in copper canister FSW welds for spent nuclear fuel disposal, *J. Nucl. Mater.* 523 (2019) 347–359. <https://doi.org/10.1016/j.jnucmat.2019.06.024>.
- [22] S. Shankar, S. Chattopadhyaya, Friction stir welding of commercially pure copper and 1050 aluminum alloys, *Mater. Today Proc.* (2019). <https://doi.org/10.1016/j.matpr.2019.07.719>.
- [23] P. Nagabharam, D. Srikanth Rao, J. Manoj Kumar, N. Gopikrishna, Investigation of Mechanical Properties of Friction Stir Welded pure Copper Plates, *Mater. Today Proc.* 5 (2018) 1264–1270. <https://doi.org/10.1016/j.matpr.2017.11.210>.
- [24] M. Ebrahimi, M.A. Par, Twenty-year uninterrupted endeavor of friction stir processing by focusing on copper and its alloys, *J. Alloys Compd.* 781 (2019) 1074–1090. <https://doi.org/10.1016/j.jallcom.2018.12.083>.
- [25] A.N. Rao, L.S. Naik, C. Srinivas, Evaluation and Impacts of Tool Profile and Rotational Speed on Mechanical Properties of Friction Stir Welded Copper 2200 Alloy, *Mater. Today Proc.* 4 (2017) 1225–1229. <https://doi.org/10.1016/j.matpr.2017.01.141>.
- [26] D. Mishra, S.K. Sahu, R.P. Mahto, S.K. Pal, *Strengthening and Joining by Plastic Deformation*, Springer Singapore, 2019. <https://doi.org/10.1007/978-981-13-0378-4>.

- [27] S. Eslami, T. Ramos, P.J. Tavares, P.M.G.P. Moreira, Shoulder design developments for FSW lap joints of dissimilar polymers, *J. Manuf. Process.* 20 (2015) 15–23. <https://doi.org/10.1016/j.jmapro.2015.09.013>.
- [28] S. Eslami, P.J. Tavares, P.M.G.P. Moreira, Fatigue Life Assessment of Friction Stir welded Dissimilar Polymers, *Procedia Struct. Integr.* 5 (2017) 1433–1438. <https://doi.org/10.1016/j.prostr.2017.07.208>.
- [29] F. Simoes, D.M. Rodrigues, Material flow and thermo-mechanical conditions during Friction Stir Welding of polymers: Literature review, experimental results and empirical analysis, *Mater. Des.* 59 (2014) 344–351. <https://doi.org/10.1016/j.matdes.2013.12.038>.
- [30] K. Panneerselvam, K. Lenin, Joining of Nylon 6 plate by friction stir welding process using threaded pin profile, *Mater. Des.* 53 (2014) 302–307. <https://doi.org/10.1016/j.matdes.2013.07.017>.
- [31] S.K. Sahu, D. Mishra, R.P. Mahto, V.M. Sharma, S.K. Pal, K. Pal, S. Banerjee, P. Dash, Friction stir welding of polypropylene sheet, *Eng. Sci. Technol. an Int. J.* 21 (2018) 245–254. <https://doi.org/10.1016/j.jestch.2018.03.002>.
- [32] S. Kumar, T. Medhi, B.S. Roy, Friction Stir Welding of Thermoplastic Composites, Springer Singapore, 2019. <https://doi.org/10.1007/978-981-13-6412-9>.
- [33] L. ZUO, X. ZHAO, Z. LI, D. ZUO, H. WANG, A review of friction stir joining of SiCp/Al composites, *Chinese J. Aeronaut.* (2019). <https://doi.org/10.1016/j.cja.2019.07.019>.
- [34] P. Cavaliere, G.L. Rossi, R. Di Sante, M. Moretti, Thermoelasticity for the evaluation of fatigue behavior of 7005/Al<sub>2</sub>O<sub>3</sub>/10p metal matrix composite sheets joined by FSW, *Int. J. Fatigue.* 30 (2008) 198–206. <https://doi.org/10.1016/j.ijfatigue.2007.01.021>.
- [35] S. Mozammil, J. Karloopia, R. Verma, P.K. Jha, Mechanical response of friction stir butt weld Al-4.5%Cu/TiB<sub>2</sub>/2.5p in situ composite: Statistical modelling and optimization, *J. Alloys Compd.* 826 (2020) 154184. <https://doi.org/10.1016/j.jallcom.2020.154184>.
- [36] Sachinkumar, S. Narendranath, D. Chakradhar, Effect of FSW on microstructure and hardness of AA6061/SiC/fly ash MMCs, *Mater. Today Proc.* 5 (2018) 17866–17872. <https://doi.org/10.1016/j.matpr.2018.06.113>.
- [37] S.J. Lee, S.E. Shin, Y. Sun, H. Fujii, Y. Park, Friction stir welding of multi-walled carbon nanotubes reinforced Al matrix composites, *Mater. Charact.* 145 (2018) 653–663. <https://doi.org/10.1016/j.matchar.2018.09.033>.
- [38] P. Kossakowski, W. Weislik, M. Bakalarz, Macrostructural Analysis of Friction Stir Welding (FSW) Joints, *J. Chem. Inf. Model.* 1 (2018) 1689–1699. <https://doi.org/10.1017/CBO9781107415324.004>.
- [39] R. Mishra, Z.Y. Ma, Friction Stir Welding and Processing II Article in Materials Science and Engineering R Reports · September 2005, *Mater. Sci. Eng. R.* 50 (2014) 1–78. <https://doi.org/10.1016/j.mser.2005.07.001>.
- [40] A. Shrivastava, M. Kronen, F.E. Pfefferkorn, Comparison of energy consumption and environmental impact of friction stir welding and gas metal arc welding for aluminum, *CIRP J. Manuf. Sci. Technol.* 9 (2015) 159–168. <https://doi.org/10.1016/j.cirpj.2014.10.001>.
- [41] A. El-Domiaty, H. Abd El-hafez, An energy model for friction stir welding, *Mater. Sci. Technol. Conf. Exhib. MS T'07 - "Exploring Struct. Process. Appl. Across Mult. Mater. Syst.* 3 (2007) 1709–1721.
- [42] Y.S. Sato, M. Urata, H. Kokawa, Parameters controlling microstructure and hardness during friction-stir welding of precipitation-hardenable aluminum alloy 6063, *Metall. Mater. Trans. A.* 33 (2002) 625–635. <https://doi.org/10.1007/s11661-002-0124-3>.

- [43] K.J. Colligan, *The friction stir welding process: An overview*, Woodhead Publishing Limited, 2009. <https://doi.org/10.1533/9781845697716.1.15>.
- [44] A. Raweni, V. Majstorović, A. Sedmak, S. Tadić, S. Kirin, Optimization of AA5083 friction stir welding parameters using taguchi method, *Teh. Vjesn.* 25 (2018) 861–866. <https://doi.org/10.17559/TV-20180123115758>.
- [45] F. Micari, G. Buffa, S. Pellegrino, L. Fratini, Friction Stir Welding as an effective alternative technique for light structural alloys mixed joints, *Procedia Eng.* 81 (2014) 74–83. <https://doi.org/10.1016/j.proeng.2014.09.130>.
- [46] R. Nandan, T. DebRoy, H.K.D.H. Bhadeshia, Recent advances in friction-stir welding - Process, weldment structure and properties, *Prog. Mater. Sci.* 53 (2008) 980–1023. <https://doi.org/10.1016/j.pmatsci.2008.05.001>.
- [47] W. Wang, D. Deng, Z. Mao, Y. Tong, Y. Ran, Influence of tool rotation rates on temperature profiles and mechanical properties of friction stir welded AZ31 magnesium alloy, *Int. J. Adv. Manuf. Technol.* 88 (2017) 2191–2200. <https://doi.org/10.1007/s00170-016-8918-4>.
- [48] I. Singh, G.S. Cheema, A.S. Kang, An experimental approach to study the effect of welding parameters on similar friction stir welded joints of AZ31B-O Mg alloy, *Procedia Eng.* 97 (2014) 837–846. <https://doi.org/10.1016/j.proeng.2014.12.358>.
- [49] N. Patel, K.D. Bhatt, V. Mehta, Influence of Tool Pin Profile and Welding Parameter on Tensile Strength of Magnesium Alloy AZ91 During FSW, *Procedia Technol.* 23 (2016) 558–565. <https://doi.org/10.1016/j.protcy.2016.03.063>.
- [50] K. Singh, G. Singh, H. Singh, Investigation of microstructure and mechanical properties of friction stir welded AZ61 magnesium alloy joint, *J. Magnes. Alloy.* 6 (2018) 292–298. <https://doi.org/10.1016/j.jma.2018.05.004>.
- [51] P. Sevvel, V. Jaiganesh, Characterization of mechanical properties and microstructural analysis of friction stir welded AZ31B Mg alloy through optimized process parameters, *Procedia Eng.* 97 (2014) 741–751. <https://doi.org/10.1016/j.proeng.2014.12.304>.
- [52] U. Singarapu, K. Adepu, S.R. Arumalle, Influence of tool material and rotational speed on mechanical properties of friction stir welded AZ31B magnesium alloy, *J. Magnes. Alloy.* 3 (2015) 335–344. <https://doi.org/10.1016/j.jma.2015.10.001>.
- [53] V.M. Magalhães, C. Leitão, D.M. Rodrigues, Friction stir welding industrialisation and research status, *Sci. Technol. Weld. Join.* 23 (2018) 400–409. <https://doi.org/10.1080/13621718.2017.1403110>.
- [54] P. Surendrababu, A. Gopala Krishna, C. Srinivasa Rao, Material Flow Behaviour in Friction Stir Welding Process-A Critical Review on Process Parameters and Modeling Methodologies, *Int. J. Emerg. Technol. Adv. Eng. Website Wwww.ijetae.com ISO Certif. J.* 3 (2013) 219–225.
- [55] R.P. Dobriyal, B.K. Dhindaw, S. Muthukumar, S.K. Mukherjee, Microstructure and properties of friction stir butt-welded AE42 magnesium alloy, *Mater. Sci. Eng. A.* 477 (2008) 243–249. <https://doi.org/10.1016/j.msea.2007.06.028>.
- [56] H. Jamshidi Aval, S. Serajzadeh, A.H. Kokabi, Evolution of microstructures and mechanical properties in similar and dissimilar friction stir welding of AA5086 and AA6061, *Mater. Sci. Eng. A.* 528 (2011) 8071–8083. <https://doi.org/10.1016/j.msea.2011.07.056>.
- [57] M. Dehghani, A. Amadeh, S.A.A. Akbari Mousavi, Investigations on the effects of friction stir welding parameters on intermetallic and defect formation in joining aluminum alloy to mild steel, *Mater. Des.* 49 (2013) 433–441. <https://doi.org/10.1016/j.matdes.2013.01.013>.
- [58] S.A. Khodir, T. Shibayanagi, Friction stir welding of dissimilar AA2024 and AA7075

- aluminum alloys, *Mater. Sci. Eng. B Solid-State Mater. Adv. Technol.* 148 (2008) 82–87. <https://doi.org/10.1016/j.mseb.2007.09.024>.
- [59] P. Cavaliere, Friction stir welding of Al alloys: Analysis of processing parameters affecting mechanical behavior, *Procedia CIRP*. 11 (2013) 139–144. <https://doi.org/10.1016/j.procir.2013.07.039>.
- [60] C. Leitão, R. Louro, D.M. Rodrigues, Analysis of high temperature plastic behaviour and its relation with weldability in friction stir welding for aluminium alloys AA5083-H111 and AA6082-T6, *Mater. Des.* 37 (2012) 402–409. <https://doi.org/10.1016/j.matdes.2012.01.031>.
- [61] M. Peel, A. Steuwer, M. Preuss, P.J. Withers, Microstructure, mechanical properties and residual stresses as a function of welding speed in aluminium AA5083 friction stir welds, *Acta Mater.* 51 (2003) 4791–4801. [https://doi.org/10.1016/S1359-6454\(03\)00319-7](https://doi.org/10.1016/S1359-6454(03)00319-7).
- [62] N.Z. Khan, Z.A. Khan, A.N. Siddiquee, Effect of Shoulder Diameter to Pin Diameter (D/d) Ratio on Tensile Strength of Friction Stir Welded 6063 Aluminium Alloy, *Mater. Today Proc.* 2 (2015) 1450–1457. <https://doi.org/10.1016/j.matpr.2015.07.068>.
- [63] V. Saravanan, S. Rajakumar, N. Banerjee, R. Amuthakkannan, Effect of shoulder diameter to pin diameter ratio on microstructure and mechanical properties of dissimilar friction stir welded AA2024-T6 and AA7075-T6 aluminum alloy joints, *Int. J. Adv. Manuf. Technol.* 87 (2016) 3637–3645. <https://doi.org/10.1007/s00170-016-8695-0>.
- [64] P. Vijayavel, V. Balasubramanian, S. Sundaram, Effect of shoulder diameter to pin diameter (D/d) ratio on tensile strength and ductility of friction stir processed LM25AA-5% SiCp metal matrix composites, *Mater. Des.* 57 (2014) 1–9. <https://doi.org/10.1016/j.matdes.2013.12.008>.
- [65] A.P. Reynolds, F. Duvall, Digital image correlation for determination of weld and base metal constitutive behavior, *Weld. J. (Miami, Fla.)* 78 (1999) 355–s.
- [66] R.W. Fonda, J.F. Bingert, Texture variations in an aluminum friction stir weld, *Scr. Mater.* 57 (2007) 1052–1055. <https://doi.org/10.1016/j.scriptamat.2007.06.068>.
- [67] K.J. Colligan, J. Xu, J.R. Pickens, Welding tool and process parameter effects in friction stir welding of aluminum alloys, *TMS Annu. Meet.* (2003) 181–190.
- [68] Y.N. Zhang, X. Cao, S. Larose, P. Wanjara, Review of tools for friction stir welding and processing, *Can. Metall. Q.* 51 (2012) 250–261. <https://doi.org/10.1179/1879139512Y.0000000015>.
- [69] C.J. Dawes, P.L. Threadgill, E.J.R. Spurgin, D.G. Staines, Development of the New Friction Stir Technique for Welding Aluminum-Phase II, *TWI Memb. Rep.* (1995).
- [70] S. Vaze, J. Xu, R. Ritter, K. Colligan, J. Jr, J. Pickens, Friction Stir Processing of Aluminum Alloy 5083 Plate for Cold Bending, *Mater. Sci. Forum - MATER SCI FORUM*. 426–432 (2003) 2979–2986. <https://doi.org/10.4028/www.scientific.net/MSF.426-432.2979>.
- [71] A.K. Kadian, P. Biswas, Effect of tool pin profile on the material flow characteristics of AA6061, *J. Manuf. Process.* 26 (2017) 382–392. <https://doi.org/10.1016/j.jmapro.2017.03.005>.
- [72] A.K. Hussain, S. Azam, P. Quadri, Evaluation of Parameters of Friction Stir Welding for Aluminium Aa6351 Alloy, *Int. J. Eng. Sci. Technol.* 2 (2010) 5977–5984.
- [73] C. Elanchezhian, B. Vijaya Ramnath, P. Venkatesan, S. Sathish, T. Vignesh, R. V. Siddharth, B. Vinay, K. Gopinath, Parameter optimization of friction stir welding of AA8011-6062 using mathematical method, *Procedia Eng.* 97 (2014) 775–782. <https://doi.org/10.1016/j.proeng.2014.12.308>.
- [74] J.T. Yoo, J.H. Yoon, K.J. Min, H.S. Lee, Effect of Friction Stir Welding Process

- Parameters on Mechanical Properties and Macro Structure of Al-Li Alloy, *Procedia Manuf.* 2 (2015) 325–330. <https://doi.org/10.1016/j.promfg.2015.07.057>.
- [75] H. Fujii, L. Cui, K. Nakata, K. Nogi, Mechanical properties of friction stir welded carbon steel joints - Friction stir welding with and without transformation, *Weld. World.* 52 (2008) 75–81. <https://doi.org/10.1007/BF03266672>.
- [76] S. Sayer, V. Ceyhun, Ö. Tezcan, The influence of friction stir welding parameters on the mechanical properties and low cycle fatigue in AA 6063 (AlMgSi0.5) alloy, *Kov. Mater.* 46 (2008) 157–164.
- [77] M.J. Peel, A. Steuwer, P.J. Withers, T. Dickerson, Q. Shi, H. Shercliff, Dissimilar friction stir welds in AA5083-AA6082. Part I: Process parameter effects on thermal history and weld properties, *Metall. Mater. Trans. A Phys. Metall. Mater. Sci.* 37 (2006) 2183–2193. <https://doi.org/10.1007/BF02586138>.
- [78] A.H. Feng, D.L. Chen, Z.Y. Ma, Microstructure and cyclic deformation behavior of a friction-stir-welded 7075 al alloy, *Metall. Mater. Trans. A Phys. Metall. Mater. Sci.* 41 (2010) 957–971. <https://doi.org/10.1007/s11661-009-0152-3>.
- [79] A.H. Feng, D.L. Chen, Z.Y. Ma, Microstructure and low-cycle fatigue of a friction-stir-welded 6061 aluminum alloy, *Metall. Mater. Trans. A Phys. Metall. Mater. Sci.* 41 (2010) 2626–2641. <https://doi.org/10.1007/s11661-010-0279-2>.
- [80] Z. Zhang, B.L. Xiao, Z.Y. Ma, Hardness recovery mechanism in the heat-affected zone during long-term natural aging and its influence on the mechanical properties and fracture behavior of friction stir welded 2024Al-T351 joints, *Acta Mater.* 73 (2014) 227–239. <https://doi.org/10.1016/j.actamat.2014.04.021>.
- [81] A.H. Feng, D.L. Chen, Z.Y. Ma, W.Y. Ma, R.J. Song, Microstructure and strain hardening of a friction stir welded high-strength Al-Zn-Mg alloy, *Acta Metall. Sin. (English Lett.)* 27 (2014) 723–729. <https://doi.org/10.1007/s40195-014-0109-4>.
- [82] F.C. Liu, Z.Y. Ma, Influence of tool dimension and welding parameters on microstructure and mechanical properties of friction-stir-welded 6061-T651 aluminum alloy, *Metall. Mater. Trans. A Phys. Metall. Mater. Sci.* 39 (2008) 2378–2388. <https://doi.org/10.1007/s11661-008-9586-2>.
- [83] V. Balasubramanian, Relationship between base metal properties and friction stir welding process parameters, *Mater. Sci. Eng. A.* 480 (2008) 397–403. <https://doi.org/10.1016/j.msea.2007.07.048>.
- [84] G. Buffa, J. Hua, R. Shivpuri, L. Fratini, A continuum based fem model for friction stir welding - Model development, *Mater. Sci. Eng. A.* 419 (2006) 389–396. <https://doi.org/10.1016/j.msea.2005.09.040>.
- [85] L. Dubourg, P. Dacheux, Design and properties of FSW tools : a literature review, *Technology.* (2006).
- [86] R.N. Shubhvardhan, M.M. Rahman, Effect of FSW Parameters on Hook formation , Microstructure and Fracture Strength of Al , Mg alloys, *Int. J. Eng. Dev. Res.* 5 (2017) 1730–1736.
- [87] C.B. Jagadeesha, Analysis and design of friction stir welding tool, *J. Mech. Behav. Mater.* 25 (2017) 7–10. <https://doi.org/10.1515/jmbm-2017-0006>.
- [88] I. Uygur, Influence of shoulder diameter on mechanical response and microstructure of FSW welded 1050 Al-alloy, *Arch. Metall. Mater.* 57 (2012) 53–60. <https://doi.org/10.2478/v10172-011-0152-3>.
- [89] F. Pan, A. Xu, J. Ye, A. Tang, X. Jiang, Y. Ran, W. Du, Effects of rotation rate on microstructure and mechanical properties of friction stir-welded Mg-5Al-1Sn magnesium alloy, *Int. J. Adv. Manuf. Technol.* 91 (2017) 389–397. <https://doi.org/10.1007/s00170-016-9752-4>.
- [90] J. Chen, R. Ueji, H. Fujii, Double-sided friction-stir welding of magnesium alloy with





- concave-convex tools for texture control, *Mater. Des.* 76 (2015) 181–189. <https://doi.org/10.1016/j.matdes.2015.03.040>.
- [91] F. Chai, D. Zhang, Y. Li, Microstructures and tensile properties of submerged friction stir processed AZ91 magnesium alloy, *J. Magnes. Alloy.* 3 (2015) 203–209. <https://doi.org/10.1016/j.jma.2015.08.001>.
- [92] W. Boonchouytan, T. Ratanawilai, P. Muangjunburee, Effect of pre/post heat treatment on the friction stir welded SSM 356 aluminum alloys, *Adv. Mater. Res.* 488–489 (2012) 328–334. <https://doi.org/10.4028/www.scientific.net/AMR.488-489.328>.
- [93] H.A.D. Hamid, A.A. Roslee, Study the Role of Friction Stir Welding Tilt Angle on Microstructure and Hardness, *Appl. Mech. Mater.* 799–800 (2015) 434–438. <https://doi.org/10.4028/www.scientific.net/amm.799-800.434>.
- [94] L. Vijayaraghavan, K. Hemachandra Reddy, S.M. Jameel Basha, *Emerging Trends in Mechanical Engineering*, 2018. <https://doi.org/https://doi.org/10.1007/978-981-32-9931-3> ©.
- [95] N. Sadeghian, M.K. Besharati Givi, Experimental optimization of the mechanical properties of friction stir welded Acrylonitrile Butadiene Styrene sheets, *Mater. Des.* 67 (2015) 145–153. <https://doi.org/10.1016/j.matdes.2014.11.032>.
- [96] C.G. Rhodes, M.W. Mahoney, W.H. Bingel, R.A. Spurling, C.C. Bampton, Effects of friction stir welding on microstructure of 7075 aluminum, *Scr. Mater.* 36 (1997) 69–75. [https://doi.org/10.1016/S1359-6462\(96\)00344-2](https://doi.org/10.1016/S1359-6462(96)00344-2).
- [97] G. Liu, L.E. Murr, C.S. Niou, J.C. McClure, F.R. Vega, Microstructural aspects of the friction-stir welding of 6061-T6 aluminum, *Scr. Mater.* 37 (1997) 355–361. [https://doi.org/10.1016/S1359-6462\(97\)00093-6](https://doi.org/10.1016/S1359-6462(97)00093-6).
- [98] Y. Sato, H. Kokawa, M. Enomoto, S. Jogan, Microstructural evolution of 6063 aluminum during friction-stir welding, *Metall. Mater. Trans. A Phys. Metall. Mater. Sci.* 30 (1999) 2429–2437. <https://doi.org/10.1007/s11661-999-0251-1>.
- [99] K. V. Jata, K.K. Sankaran, J.J. Ruschau, Friction-stir welding effects on microstructure and fatigue of aluminum alloy 7050-T7451, *Metall. Mater. Trans. A Phys. Metall. Mater. Sci.* 31 (2000) 2181–2192. <https://doi.org/10.1007/s11661-000-0136-9>.
- [100] B. Heinz, B. Skrotzki, Characterization of a friction-stir-welded aluminum alloy 6013, *Metall. Mater. Trans. B Process Metall. Mater. Process. Sci.* 33 (2002) 489–498. <https://doi.org/10.1007/s11663-002-0059-5>.
- [101] A. Khorsid, A. Moustafa, I. Sabry, Investigation of the mechanical properties of Friction Stir Welded 6061 Al plates, *Jeaconf.Org.* (n.d.) 1–15. <http://www.jeaconf.org/UploadedFiles/Document/97626981-7e64-4048-8a70-6a0e1f6f9847.pdf>.
- [102] M.W. Mahoney, C.G. Rhodes, J.G. Flintoff, R.A. Spurling, W.H. Bingel, Properties of friction-stir-welded 7075 T651 aluminum, *Metall. Mater. Trans. A Phys. Metall. Mater. Sci.* 29 (1998) 1955–1964. <https://doi.org/10.1007/s11661-998-0021-5>.
- [103] J. Martin, S. Wei, Friction Stit Welding Technology For Marine Applications, *Frict. Stir Weld. Process.* VIII (2015) 2019–226.
- [104] A.P. Reynolds, Visualisation of material flow in autogenous friction stir welds, *Sci. Technol. Weld. Join.* 5 (2000) 120–124. <https://doi.org/10.1179/136217100101538119>.
- [105] M. Hakem, M. Khatir, R.R. Otmani, T. Fahssi, N. Debbache, D. Allou, Heat treatment and welding effects on mechanical properties and microstructure evolution of 2024 and 7075 aluminium alloys, *Weld. World.* 51 (2007) 163–170.
- [106] Y. Li, L.E. Murr, J.C. McClure, Flow visualization and residual microstructures associated with the friction-stir welding of 2024 aluminum to 6061 aluminum, *Mater. Sci. Eng. A.* 271 (1999) 213–223. [https://doi.org/10.1016/S0921-5093\(99\)00204-X](https://doi.org/10.1016/S0921-5093(99)00204-X).
- [107] Z.Y. Ma, R.S. Mishra, M.W. Mahoney, Superplastic deformation behaviour of friction

stir processed 7075 Al alloy, *Acta Mater.* 50 (2002) 4419–4430.  
[https://doi.org/10.1016/S1359-6454\(02\)00278-1](https://doi.org/10.1016/S1359-6454(02)00278-1).

- [108] Y.J. Kwon, N. Saito, I. Shigematsu, Friction stir process as a new manufacturing technique of ultrafine grained aluminum alloy, *J. Mater. Sci. Lett.* 21 (2002) 1473–1476. <https://doi.org/10.1023/A:1020067609451>.
- [109] J. Kwon, I. Shigematsu, N. Saito, Production of Ultra-Fine Grained Aluminum Alloy by Friction Stir Process, *J. Japan Inst. Met.* 66 (2002) 1325–1332.  
[https://doi.org/https://doi.org/10.2320/jinstmet1952.66.12\\_1325](https://doi.org/https://doi.org/10.2320/jinstmet1952.66.12_1325).
- [110] Y.J. Kwon, I. Shigematsu, N. Saito, Mechanical properties of fine-grained aluminum alloy produced by friction stir process, *Scr. Mater.* 49 (2003) 785–789.  
[https://doi.org/10.1016/S1359-6462\(03\)00407-X](https://doi.org/10.1016/S1359-6462(03)00407-X).
- [111] L.E. Murr, Intercalation vortices and related microstructural features in the friction-stir welding of dissimilar metals, *Mater. Res. Innov.* 2 (1998) 150–163.  
<https://doi.org/10.1007/s100190050078>.
- [112] R. Mishra, R.K. Islamgaliev, T. Nelson, Y. Hovanski, M.W. Mahoney, Abnormal grain growth during high temperature exposure in friction stir processed 7050 and 2519 aluminum alloys, *Frict. Stir Weld. Process.* (2001) 205–216.
- [113] P.S. Pao, S.J. Gill, C.R. Feng, K.K. Sankaran, Corrosion-fatigue crack growth in friction stir welded Al 7050, *Scr. Mater.* 45 (2001) 605–612.  
[https://doi.org/10.1016/S1359-6462\(01\)01070-3](https://doi.org/10.1016/S1359-6462(01)01070-3).
- [114] P.L. Threadgill, A.J. Leonard, H. Shercliff, Friction Stir Welding of Aluminium Alloys, *Int. Mater. Rev.* 54 (2009) 49–93.  
<https://doi.org/https://doi.org/10.1179/174328009X411136>.
- [115] T. Fukuda, Friction stir welding (FSW) process, *J. Japan Weld. Soc.* 15 (2009) 37–41.  
<https://doi.org/10.1080/09507110109549412>.
- [116] Satyanarayan, K.N. Prabhu, Wetting behaviour and interfacial microstructure of Sn-Ag-Zn solder alloys on nickel coated aluminium substrates, *Mater. Sci. Technol.* 27 (2011) 1157–1162. <https://doi.org/10.1179/026708310X12815992418337>.
- [117] R. Crawford, G.E. Cook, A.M. Strauss, D.A. Hartman, M.A. Stremmler, Experimental defect analysis and force prediction simulation of high weld pitch friction stir welding, *Sci. Technol. Weld. Join.* 11 (2006) 657–665.  
<https://doi.org/10.1179/174329306X147742>.
- [118] Y.G. Kim, H. Fujii, T. Tsumura, T. Komazaki, K. Nakata, Three defect types in friction stir welding of aluminum die casting alloy, *Mater. Sci. Eng. A.* 415 (2006) 250–254.  
<https://doi.org/10.1016/j.msea.2005.09.072>.
- [119] R. Palanivel, P. Koshy Mathews, N. Murugan, I. Dinaharan, Effect of tool rotational speed and pin profile on microstructure and tensile strength of dissimilar friction stir welded AA5083-H111 and AA6351-T6 aluminum alloys, *Mater. Des.* 40 (2012) 7–16.  
<https://doi.org/10.1016/j.matdes.2012.03.027>.
- [120] K. Elangovan, V. Balasubramanian, Influences of pin profile and rotational speed of the tool on the formation of friction stir processing zone in AA2219 aluminium alloy, *Mater. Sci. Eng. A.* 459 (2007) 7–18. <https://doi.org/10.1016/j.msea.2006.12.124>.
- [121] R. Leal, A. Loureiro, Defects formation in friction stir welding of aluminium alloys, *Mater. Sci. Forum.* 455–456 (2004) 299–302.  
<https://doi.org/10.4028/www.scientific.net/msf.455-456.299>.
- [122] S. Rouhi, A. Mostafapour, M. Ashjari, Effects of welding environment on microstructure and mechanical properties of friction stir welded AZ91C magnesium alloy joints, *Sci. Technol. Weld. Join.* 21 (2016) 25–31.  
<https://doi.org/10.1179/1362171815Y.0000000058>.
- [123] G.M.D. Cantin, S.A. David, W.M. Thomas, E. Lara-Curzio, S.S. Babu, Friction Skew-

- stir welding of lap joints in 5083-0 aluminium, *Sci. Technol. Weld. Join.* 10 (2005) 268–280. <https://doi.org/10.1179/174329305X39301>.
- [124] M. Ericsson, L.Z. Jin, R. Sandström, Fatigue properties of friction stir overlap welds, *Int. J. Fatigue.* 29 (2007) 57–68. <https://doi.org/10.1016/j.ijfatigue.2006.02.052>.
- [125] D. Fersini, A. Pirondi, Fatigue behaviour of Al2024-T3 friction stir welded lap joints, *Eng. Fract. Mech.* 74 (2007) 468–480. <https://doi.org/10.1016/j.engfracmech.2006.07.010>.
- [126] D. Fersini, A. Pirondi, Analysis and modelling of fatigue failure of friction stir welded aluminum alloy single-lap joints, *Eng. Fract. Mech.* 75 (2008) 790–803. <https://doi.org/10.1016/j.engfracmech.2007.04.013>.
- [127] B.S. Naik, D.L. Chen, X. Cao, P. Wanjara, Microstructure and fatigue properties of a friction stir lap welded magnesium alloy, *Metall. Mater. Trans. A Phys. Metall. Mater. Sci.* 44 (2013) 3732–3746. <https://doi.org/10.1007/s11661-013-1728-5>.
- [128] S. Mironov, T. Onuma, Y.S. Sato, H. Kokawa, Microstructure evolution during friction-stir welding of AZ31 magnesium alloy, *Acta Mater.* 100 (2015) 301–312. <https://doi.org/10.1016/j.actamat.2015.08.066>.
- [129] S. Eslami, P.J. Tavares, P.M.G.P. Moreira, Friction stir welding tooling for polymers: review and prospects, *Int. J. Adv. Manuf. Technol.* 89 (2017) 1677–1690. <https://doi.org/10.1007/s00170-016-9205-0>.
- [130] N. Mendes, A. Loureiro, C. Martins, P. Neto, J.N. Pires, Morphology and strength of acrylonitrile butadiene styrene welds performed by robotic friction stir welding, *Mater. Des.* 64 (2014) 81–90. <https://doi.org/10.1016/j.matdes.2014.07.047>.
- [131] M.S. Khaliel Youssif, M.A. El-Sayed, A.E.F.M. Khourshid, Influence of critical process parameters on the quality of friction stir welded nylon 6, *Int. Rev. Mech. Eng.* 10 (2016) 501–507. <https://doi.org/10.15866/ireme.v10i7.9690>.
- [132] R. Nandan, G.G. Roy, T.J. Lienert, T. Debroy, Three-dimensional heat and material flow during friction stir welding of mild steel, *Acta Mater.* 55 (2007) 883–895. <https://doi.org/10.1016/j.actamat.2006.09.009>.



## 7.2. [P2] Manufacturing Parameters, Materials, and Welds Properties of Butt Friction Stir Welded Joints – Overview.

**Laska A.\***, Szkodo M., Manufacturing Parameters, Materials, and Welds Properties of Butt Friction Stir Welded Joints – Overview. *Materials*. 13(21), 4940; 2020. doi:10.3390/ma13214940. (IF = 3.748, 140 points of the Polish Ministry of Science and Higher Education)

### 7.2.1. Declaration of the contribution of the doctoral candidate

My contribution to the preparation of this publication included a systematic review of the literature published since 1991 (the invention of the FSW process). The bibliographic references under analysis were mainly selected from Scopus and ScienceDirect databases, using keywords such as "Friction Stir Welding", "FSW", "solid type welding" or "solid-state welding". Several hundred documents from prominent journals publishing on FSW were reviewed. Nearly 70 % of the publications presented in the review were published within the last ten years. On the basis of the reviewed publications, I prepared the text of the manuscript. I was also responsible for responses to reviewers and acted as correspondence author.

My percentage contribution to the preparation of the manuscript was equal to 95 %.

.....

Aleksandra Laska



Review

## Manufacturing Parameters, Materials, and Welds Properties of Butt Friction Stir Welded Joints—Overview

Aleksandra Laska \* and Marek Szkodo

Department of Materials Engineering and Bonding, Faculty of Mechanical Engineering, Gdansk University of Technology, Narutowicza 11/12, 80-233 Gdansk, Poland; mszkodo@pg.edu.pl

\* Correspondence: aleksandra.laska@pg.edu.pl; Tel.: +48-698-071-526

Received: 2 October 2020; Accepted: 31 October 2020; Published: 3 November 2020



**Abstract:** The modern and eco-friendly friction stir welding (FSW) method allows the combination of even such materials that are considered to be non-weldable. The development of FSW technology in recent years has allowed a rapid increase in the understanding of the mechanism of this process and made it possible to perform the first welding trials of modern polymeric and composite materials, the joining of which was previously a challenge. The following review work focuses on presenting the current state of the art on applying this method to particular groups of materials. The paper has been divided into subchapters focusing on the most frequently used construction materials, with particular emphasis on their properties, applications, and usage of the FSW method for these materials. Mechanisms of joint creation are discussed, and the microstructure of joints and the influence of material characteristics on the welding process are described. The biggest problems observed during FSW of these materials and potential causes of their occurrence are quoted. The influence of particular parameters on the properties of manufactured joints for each group of materials is discussed on the basis of a wide literature review.

**Keywords:** friction stir welding; FSW; solid type welding; mechanical properties; weld strength

### 1. Introduction

Friction stir welding (FSW) is a method invented at the Welding Institute of the United Kingdom and patented by Wayne Thomas in 1991 [1]. It is considered to be one of the most prospective material joining developments in the last 30 years. Primarily, this method was dedicated to joining aluminum and its alloys, but today it is widely used for titanium and its alloys, magnesium and its alloys, steel and ferrous alloys, and copper, but also polymers and composites. The FSW process is defined as a solid-state method. Materials to be joined do not melt during the process. Since the melting point is not reached, typical problems of fusion welding techniques are eliminated. These problems are usually related to a change of state, such as changes of volume and solubility of gases, and these effects are not observed during friction stir welding process [2–4].

During the process, a specially designed tool is put into linear movement along a joint line, rotating at the same time. The kinetic energy of the tool is transformed into thermal energy, generated by the friction on the interface between the tool and the components. The heated material is plasticized by a tool and extruded around the pin in a backward direction of a tool moving along the edge of a contact line. The FSW method is usually used to produce butt welds, but it also allows the fabrication of joints of other types, such as corner welds, T-welds, lap welds, and fillet welds [5–8]. A schematic illustration of a friction stir welded butt joint is shown in Figure 1. Nowadays, the FSW method is widely used in many industrial areas, such as aerospace (wings, fuel and cryogenic tanks,

fuselages [9–12], railways (underground carriages, wagons, container bodies) [13–15], marine and shipbuilding (deck panels, hulls, booms, masts, offshore accommodation) [14,16], construction industry (frames, bridges, pipelines) [17,18] and land transportation (wheel rims, mobile cranes, tail lifts) [19]. The FSW technology is also applied in sectors such as machinery equipment, electronics, metalworking, and the R&D sector [20].

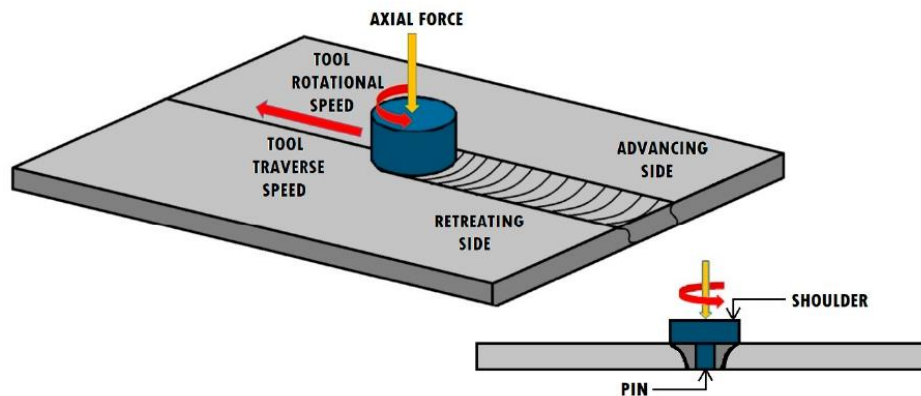
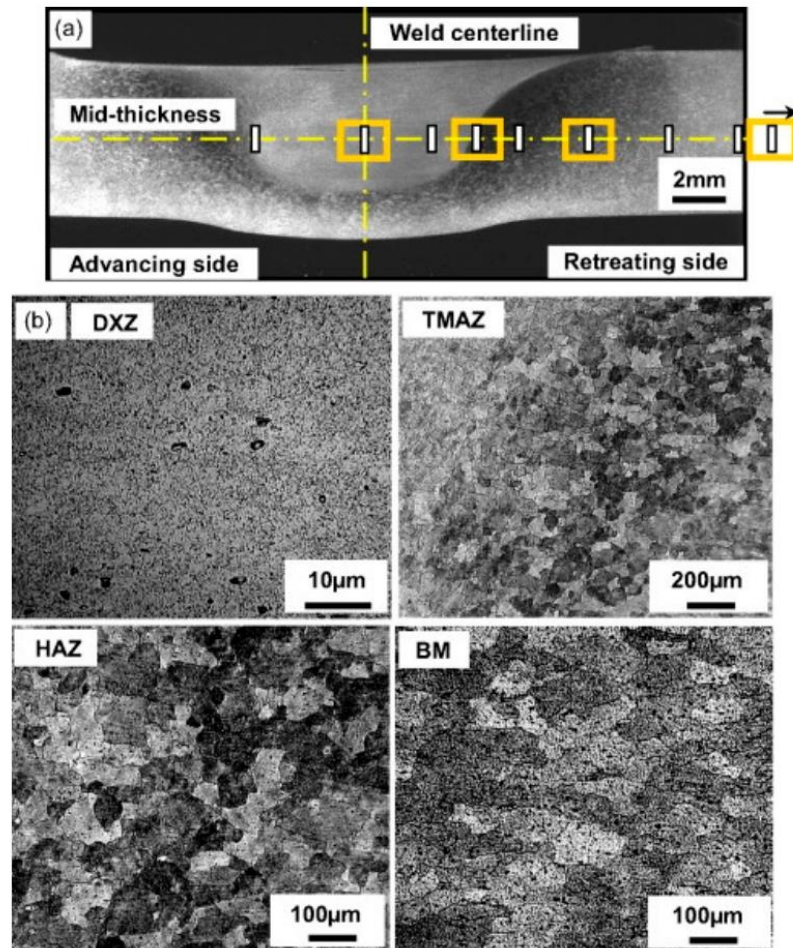


Figure 1. Schematic illustration of a friction stir welding process.

In the cross-section of the friction stir welded joint, a specific microstructure is observed. Due to the solid-state nature of the process, the zones that are not found in welds produced by conventional welding methods can be distinguished. Based on thermomechanical actions of the FSW tool, four distinct zones can be observed: weld nugget (stir zone, SZ), thermo-mechanically affected zone (TMAZ), heat affected zone (HAZ), and base material (unaffected zone, BM). The presence of the stir zone is a result of the recrystallization in the middle part of the thermo-mechanically affected zone. The nugget is formed by fine grain sized metal. The material of the SZ experiences plastic deformation due to the interactions with the tool. Rhodes et al. [21] and Liu et al. [22] claimed that in the recrystallized grains, a low density of dislocations is observed. However, other studies proved that the recrystallized grains of the SZ contain high density of sub-boundaries [23], dislocations [24] and subgrains [25]. Between the SZ and the HAZ, a unique transition zone, called the thermo-mechanically affected zone, can be observed. TMAZ is exposed to both temperature and deformations during the process. Because of insufficient deformations, strain recrystallization is not observed. Exposure to high temperatures during welding might cause the dissolution of precipitates in TMAZ. Beyond TMAZ, the heat-affected zone is observed. In that region, there are no plastic deformations, but it is still subjected to a thermal cycle. The alteration of properties in HAZ, compared to the base material, includes changes in ductility, toughness, corrosion susceptibility, and strength. The changes in grain size or chemical makeup are not observed [26]. The typical cross-section of the FSW joint and the microstructures of different zones are shown in Figure 2.





**Figure 2.** (a) Typical weld macrostructure of 6061-T6 Al alloy in FSW, (b) microstructure of the joint-stir zone (DXZ, dynamic recrystallized zone), TMAZ, HAZ, and BM taken at yellow square marks shown in (a) [27].

The FSW technology is classified as a green technology. As a melting point is not reached during the process, less energy is used in comparison to fusion welding techniques. Moreover, CO<sub>2</sub> emission to the atmosphere can be significantly reduced [28]. It is relatively easy to control the process and setting optimal parameters allows for a subsequent reduction of necessary non-destructive testing. The pollutions generated by sprays for visual and magnetic inspection and exposure to radiation in the case of X-ray tests are reduced. Additionally, if the optimal parameters are set, post-weld heat treatment is not required [28,29]. It results in the reduction of CO<sub>2</sub>, energy consumption, and other pollutions emitted to the atmosphere. The FSW process uses a non-consumable tool; the use of shielding gas is not necessary.

One of the most important process parameters is the geometry of the tool. The tool consists of a specially designed pin and shoulder. The movement of the plasticized material depends on its geometrical features [30]. Its geometry also conditions the workpiece thickness, possible materials to be welded, and type of the joints [7]. The pin is an element of the tool that is directly plunged between

the surfaces of the workpieces. It is plunged into the material until the shoulder reaches the contact with the surface of the components [31]. The tool design governs the process loads and microstructure of the weld, when from the heating aspects, the most important parameter is a ratio of a shoulder diameter to a pin diameter [32]. The FSW method is mostly characterized by two parameters related to its kinematics—rotational speed ( $\omega$ ) and traverse speed ( $v$ ) along the joint line [33]. Selecting the optimum tool traverse and rotational speed is a crucial concern in the design of the FSW process.

The FSW technique allows the joining of many types of materials, even hard materials such as steel and engineering alloys. Recent studies have also been investigating the joining of metals to polymers through the FSW technique [34–36]. According to the analysis of Magalhaes et al. [20], most of the research and patents on FSW welding have concerned aluminum and its alloys, followed by ferrous alloys, magnesium, titanium, and their alloys. There are also studies regarding the welding of composites, copper, and polymers. The published papers analyze not only the FSW industrialization [37–40], but also the process mechanism, welding parameters, weld properties, and material microstructure. This paper presents the latest results of research on various materials welded using the FSW method and the influence of technological parameters of the process on the mechanical properties of welds and their microstructure, with particular reference to butt joints.

## 2. Methodology

The purpose of the overview is to establish the influence of the process parameters on the mechanical properties of the joints of different groups of materials. The method underpinning this paper is a systematic literature review. The number of papers published on FSW technology grows quickly, and the studies have become very diverse, making important the understanding and assessment of its impact on research and development level. In order to achieve this objective, an analysis of the literature published since 1991 to the current date was performed. The bibliographical references analysed were selected mostly from Scopus and ScienceDirect databases, using keywords such as “FSW”, “friction stir welding”, “solid state welding”, and “solid type welding”. Several hundred papers from the top journals publishing on FSW were analysed. Almost 70% of the articles presented in the review have been published in the last ten years; therefore, the paper is an analysis of the latest developments in the field of FSW process. A meticulous literature review on the applied FSW welding parameters allowed the presentation of the properties of the produced welds, if such information was presented in the quoted articles.

## 3. Aluminum and Its Alloys

Aluminum and its alloys are materials widely processed by FSW. Due to the difficulty of welding aluminum using traditional methods, FSW offers an excellent solution for joining these materials, ensuring reliability, ease of control of process parameters, and minimized risk of defects contributing to a reduction in the mechanical properties of the welds. During the FSW process of aluminum and its alloys, the temperature usually stays below 500 °C [41–43]. The experimental validation of the temperature on the tool surface is difficult to identify due to large deformations at the interface between the material and the tool, but Colegrove et al. [44] suggested that it can be near the solidus temperature.

Aluminum alloys can be divided into precipitation-hardened and solid solution-hardened alloys [32]. Although the precipitation-hardened aluminum alloys are easily welded by FSW, the heat-affected zone might be severely softened, essentially characterized by the dissolution or coarsening of the existent primary precipitates of the original thermal cycle [23]. It is reported that the hardness profile depends mostly on the precipitate distribution, and the grain size is of minor importance [23,45]. The most relevant to the hardness profile of the FSW joints of precipitation-hardened alloys is frictional heating during the process. The thermal hysteresis has an influence on distribution, size, and volume fraction of the strengthening precipitates [45].

The analysis of the state of the art has highlighted that there is no general dependence of mechanical properties of welds as a function of particular process parameters. In the studies of



Krasnowski et al. [46], it was reported that the ultimate tensile strength (UTS) of the AA6082-T6 joints initially decreases as a function of the tool traverse speed and then increases, reaching the maximum value of the UTS for the relatively highest tool traverse speed at the constant rotational speed for three different tool geometries. Opposite results have been observed by Rao et al. [47] during the FSW of IS:65032 aluminum alloy at the tool rotational speed of 1300 rpm and triangular pin shape, but the square pin shape for the same tool rotational speed confirmed the relationship observed before by Krasnowski et al. [46]. The above examples clearly indicate that the shape of the tool plays a key role in the FSW process, and changing only this parameter may cause the opposite effect of other process parameters on the properties of welds. Considering the influence of the tool rotational speed on the UTS of FSW joints, it is worth quoting studies on AA6061 alloy by Emamian et al. [48]. In these studies, it was observed that for linear speed  $v = 40$  mm/min, the initial increase in the tool rotational speed causes an increase in UTS, but when it reaches its maximum, the UTS decreases with the increase in the speed. In the same study, for the tool traverse speed of 100 mm/min, UTS initially decreases with the increase in the tool rotational speed, but when it reaches its minimum, UTS increases with the increase in the tool rotational speed. Rajendran et al. [49] investigated the influence of the tilt angle on the hardness of the nugget zone of AA2014-T6 FSW lap joints. The tilt angle of  $2^\circ$  resulted in the maximum value of the hardness. In the studies on Al 5754 alloy, conducted by Barlas et al. [50], it was reported that the tilt angle equal to  $2^\circ$  provides better mechanical properties of the joints compared to the zero tilt angle. The investigations of Peel et al. [51] showed that the ratio of the shoulder diameter to the pin diameter ( $D/d$ ) equal to 3.6 resulted in the highest ultimate tensile strength and yield strength of the AA5083 FSW joints, while the studies of Khan et al. [52] proved that in the range from 2.6 to 3.2 of the  $D/d$  ratio, the lowest value resulted in the best UTS and elongation of the AA6063-T6 joints. The reason for the different results may be the shape of the tool. The above studies used pins with different geometry—Peel et al. [51] used a threaded pin, while a smooth cylindrical pin was used by Khan et al. [52]. What is more, it is worth noting that the alloys with different chemical compositions were used in the studies, especially in the magnesium content, which could also affect the results obtained.

In the literature, there are few reports about FSW welding of metallic foams. However, the FSW technique is not an ideal solution to join the foams due to their compressibility. The pressure necessary to create frictional forces between the tool and the material is not sufficient after inserting the tool between the components to be joined, or the resulting forces destroy the porous structure of the material. A more popular solution is to implement the FSW method to produce sandwich structures, where a porous structure is placed between two sheets of solid material. In the research of Peng et al. [53], FSW was adopted to prepare aluminum foam sandwich. For this purpose, aluminum foam and solid aluminum AA6061-T6 plates. The aluminum foam panel was inserted between two solid plates and welded on both sides. It was concluded that the FSW technology offers better mechanical properties of the foam sandwiches compared to traditional adhesion and brazing. Busic et al. [54] investigated the influence of tool traverse speed and tilt angle on the mechanical properties of FSW of aluminum foam sandwich panels. Butt welds were produced by double side welding applying insertion of extruded aluminum profile. The studies proved that both tool traverse speed and tilt angle have significant influence on the UTS and flexural strength of the welds. In general, the current state of the art is poor in this type of research. The joining of foams still needs more studies, especially when permanent metallurgical bonding has to be obtained.

It is widely reported that the process parameters play a crucial role in the mechanical properties of the welds. However, the above examples prove there are no generally defined relationships. Table 1 summarizes analyzed studies on friction stir welding of different aluminum alloys. Table 1 presents the selected parameters that provided the highest mechanical properties of the welds, and in parentheses, the properties of the parent material are given for each example.

Table 1. FSW of aluminum and its alloys—process parameters and mechanical properties of the joints.

Material	Plate Thickness [mm]	Process Parameters					Weld Properties					Reference
		v [mm/min]	$\omega$ [rpm]	Tool Shape	Pin D/d Ratio	Tilt Angle [°]	UTS [MPa]	Yield Strength [MPa]	Hardness of the Stir Zone [HV]	Elongation [%]	Defects	
AA2195-T8	7.4	300	400	Cone shape threaded pin, threaded surface of the shoulder	-	-	445.0 (607.9)	-	-	12.50 (12.49)	No defects	[55]
AA356.0-T6 (double side welded)	8	200	1200	Threaded conical pin	3.25	-	200 (244)	123 (140)	-	16.3 (13.4)	-	[56]
AA5083	3	100	-	M6 threaded pin	3.6	2	304 (457)	154 (392)	-	-	-	[51]
AA5086-O	5	150	900	Tapered pin with 3 threads and concave shoulder surface	3.3	-	250 (253)	123 (112)	-	-	-	[31]
AA6013-T4	2.5	450	1400	-	-	-	300 (320)	-	-	-	-	[25]
AA6013-T6	2.5	400	1400	-	-	-	295 (394)	-	-	-	-	[25]
AA6061	5	100	1300	Cylindrical smooth	-	-	227 (308.5)	-153 (266.6)	-	-7.3 (16.28)	Defect free	[47]
AA6061	10	100	1600	Threaded cylindrical pin	3	-	214.4 (305)	-	-	-	No defects	[48]
AA6061-T6	5	150	900	Tapered pin with 3 threads and concave shoulder surface	3.3	-	285 (315)	241 (278)	57	-	-	[31]
AA6061-T651 (double side welded)	8	200	1200	Threaded conical pin	3.25	-	218 (299)	142 (264)	-	23.3 (27.2)	-	[56]
AA6063	5	100	2800	Threaded cylindrical pin	3	3	-150 (220)	-70 (170)	-	4.5 (13)	-	[57]
AA6063-T5	4	600	-	-	-	-	-155 (-220)	-105 (-185)	-	10 (-19)	No defects	[58]
AA6063-T6	4.75	40	900	Cylindrical smooth pin	2.6	1.5	145.34 (220)	-	-	20.85 (14.00)	-	[52]
AA6082-T6	8	900	710	Cylindrical pin with threads and three flutes	3.3	1.5	243.4	-	-	-	-	[46]

Table 1. Cont.

Material	Plate Thickness [mm]	Process Parameters					Weld Properties					Reference	
		v [mm/min]	$\omega$ [rpm]	Tool Shape	Pin D/d Ratio	Tilt Angle [°]	UTS [MPa]	Yield Strength [MPa]	Hardness of the Stir Zone [HV]	Elongation [%]	Defects		
AA6352 (double side welded)	6	115	1350	Tapered pin	-	2	172 (250)	-	90.2 (93.5)	-	-	No significant defects	[33]
AA7050-T7451	6.35	103	396	-	-	-	429 (555)	304 (489)	-	6 (16.7)	-	-	[24]
AA7075-T651	6.35	127	-	-	-	-	525 (622)	365 (571)	-	15 (14.5)	-	-	[42]
SSM 356	4	160	1750	Cylindrical pin	4	3	173.5 (168.7)	138.8 (134.9)	40.9 (36.4)	3.1 (5.3)	-	-	[59]
SSM 356-T6	4	160	1750	Cylindrical pin	4	3	172.9 (295.6)	138.3 (236.5)	68.4 (61.2)	4.5 (4.8)	-	-	[59]

#### 4. Magnesium and Its Alloys

Among commonly used structural materials, magnesium has the lowest density. Because of its hexagonal close-packed (hcp) structure at room temperature, the formability of magnesium is very constrained; however, it increases significantly at temperatures of 230–310 °C [60]. Most of the commercially used magnesium alloys are ternary alloys containing aluminum, zinc, silicon, and rare earth metals [61]. In Mg-Al series, the most common alloys are AZ (Mg-Al-Zn) and AS (Ag-Al-Si) [62,63]. The successful method to join magnesium alloys is arc welding, but some difficulties might occur in joining, especially the cast grades alloys [60]. During fusion welding of aluminum alloys, the shielding gases are necessary due to oxidation at welding temperatures. The most significant problems occurring during fusion welding of magnesium alloys are the porosity of the welds [32], distortions due to high thermal conductivity and thermal expansion of magnesium alloys [10], evaporation, and solute atoms segregation, which leads to softening of the joint area. In addition to the application of the FSW technique mentioned above, friction stir welded magnesium alloys find their applications in industrial equipment of nuclear energy, due to their low neutron absorption, excellent thermal conductivity, and good resistance to carbon dioxide [64].

There are plenty of studies on the microstructure of the FSW magnesium joints. Xin et al. [65] reported that the primary texture does not significantly affect the final microstructure and texture of the nugget zone. However, texture distribution in the thermo-mechanically affected zone influences the mechanical properties of the joints [66]. In the studies of Yang et al. [67], it was reported that the shoulder size does not have an impact of texture modification in the nugget zone of friction stir welded Mg-3Al-1Zn alloy, but it weakens the (0002) texture in the thermo-mechanically affected zone. Commin et al. [68] observed that during FSW of AZ31 hot-rolled base material, the structure is not significantly changed when the shoulder diameter is equal to 13 mm, but the shoulder diameter of 10 mm resulted in the strong texture modification. In their studies, it was also reported that the highest tensile residual stress was observed in the thermo-mechanically affected zone. It was observed that a larger diameter of the shoulder reduced the residual stress due to the higher heat delivered to the welded material.

The analysis of the research conducted so far does not allow the drawing of general conclusions concerning the optimization of process parameters. On the basis of studies carried out by Lim et al. [69], it was concluded that the tensile properties of AZ31B-H24 welds are not significantly affected by FSW process parameters, whereas Lee et al. [70] reported that with an increase of the tool rotational speed, the strength of the joints of the same alloy increased. Wang et al. [11] and Kumar et al. [71] reported that for AZ31 butt welds, the UTS, yield strength, elongation, and hardness primarily increase with an increase of the tool traverse speed and after reaching the maximum value, decrease with a further increase of the welding speed. In the studies of Han et al. [72], the ultimate tensile strength of Mg-Gd alloy increases with an increase of the tool traverse speed. The opposite dependence was presented by Sahu et al. [73] for AM20 butt welds. It should be noted that both tests were performed at a different tool rotational speed, so the amount of heat generated was different. Moreover, both tests were different in the geometry of the tools used. In the study of Sahu et al. [73], the influence of D/d ratio on the mechanical properties was also investigated. In the range from 2 to 4, the highest D/d ratio provided the highest UTS. Sevel et al. [74] and Pareek et al. [75] investigated the influence of the tool rotational and traverse speed on the mechanical properties on AZ31 magnesium alloy. The results of the tests do not allow the drawing of a general conclusion. Sevel et al. [74] proposed the lowest tool traverse speed and the highest rotational speed to obtain the highest ultimate tensile strength and the highest yield strength of the welds, while in the studies of Pareek et al. [75], the highest tool traverse speed and the highest rotational speed resulted in the best mechanical properties of the welds. Sevel et al. proposed the tool rotational speed equal to 1000 rpm, while in the studies of Pareek et al., it was set as 2000 rpm. In this case, a higher tool traverse speed could provide enough heat to the weld, which could be insufficient if the speed was lower, as in the studies of Sevel et al. Studies on the hardness of friction stir welded magnesium alloys show contradictory conclusions. Esparza et al. [76] and

Park et al. [77] reported that the welds exhibit almost the same hardness in the various zones. On the contrary, Xie et al. [78] and Zhang et al. [79] noted that the nugget of the welds has significantly higher hardness than the other zones. It can be explained by breaking up large intermetallic compounds  $Al_2Ca$  in Mg-Al-Ca alloy studied by Zhang et al. [79] and Mg-Zn-Y phases in Mg-Zn-Y-Zr studied by Xie et al. [78] and their dispersion in the stir zone, which resulted in the increase of the hardness. As mentioned earlier, aluminum alloys are divided in two types: precipitation-hardened and solid solution-hardened alloys. Thus, in ternary magnesium alloys containing aluminum as the main alloying element, the hardness of magnesium alloy varies according to the percentage of aluminum present in the structure.

Table 2 presents the properties of FSW joints of magnesium and its alloys and the mechanical properties of the parent material if presented by the authors.

Table 2. FSW of magnesium and its alloys—process parameters and mechanical properties of the joints.

Material	Process Parameters					Weld Properties						Reference
	Plate Thickness [mm]	v [mm/min]	$\omega$ [rpm]	Tool Shape	Pin D/d Ratio	Tilt Angle [°]	UTS [MPa]	Yield Strength [MPa]	Hardness of the Stir Zone [HV]	Elongation [%]	Defects	
AM20	4	63	600	Cylindrical pin	4	-	132.17 (202)	115.56 (160)	61 (46)	2.17 (7)	-	[73]
AZ31	4	90	1500	-	3	-	255 (275)	-	-	-	-	[80]
AZ31	8	120	1200	Conical pin	2	2.5	225.1 (249.5)	130.5 (156.3)	-	5.4 (14)	-	[11]
AZ31-O	2	200	1000	-	2.6	-	-170 (-250)	-90 (-150)	-	-	-	[68]
AZ31B	5	0.5	1000	Tapered cylindrical pin	3	-	183 (262)	101 (179)	-	-	No defects	[74]
AZ31B	5	40	1400	Threaded conical pin	3	2.5	186.76 (215)	139.1 (171)	71 (69)	5.00 (14.7)	-	[81]
AZ31B	5	40	1120	Taper threaded pin	3	2	188 (215)	148 (171)	121 (69.3)	7.3 (14.3)	-	[19]
AZ31B	6	40.2	1600	Threaded cylindrical pin	3.0	0	205 (215)	166 (171)	75 (69.3)	7.3 (14.7)	Defect free	[82]
AZ31B	6	50.8	1200	-	-	-	248	-	67.95 HB	-	-	[71]
AZ31B-O	5	60	1200	Left handed threaded pin	3	-	187.8 (206)	-	64.77 (50)	16.73 (20)	-	[13]
AZ31-H24	3.175	204	2000	-	-	-	225.6 (307.7)	115.3 (227.6)	-	-	No defects	[75]
AZ31B-H24	4.95	4	1000	-	-	-	208 (315)	115 (202)	-	-	-	[83]
AZ61	4	25	1400	Left-handed threaded pin with three flutes	3	-	220 (270)	175 (219)	81 (70)	7.2 (-8.2)	-	[16]
AZ91	6	28	710	Threaded straight cylindrical pin	3	-	76.17	-	-	-	No defects	[84]
AZ91	6	60	600	-	2.8	2.5	262 (106)	132 (55)	-	18.9 (15.2)	No defects on the top surface	[85]

Table 2. Cont.

Material	Plate Thickness [mm]	Process Parameters					Weld Properties					Reference	
		v [mm/min]	$\omega$ [rpm]	Tool Shape	Pin D/d Ratio	Tilt Angle [°]	UTS [MPa]	Yield Strength [MPa]	Hardness of the Stir Zone [HV]	Elongation [%]	Defects		
AZ91D	3	75	500	Left-handed tapered cylindrical pin	2.6	2.5	107 (107)	-	-	-	-	Defect free	[86]
AZ91D	3	90	1200	-	2	-	200 (220)	140 (150)	-	2 (3.6)	-	-	[87]
MB3	3	120	1500	-	-	-	240 (245)	-	-	-	-	No macro defects	[88]
Mg-Y-Nd alloy (double side welded)	20	240	700	Threaded conical pin with three flutes	2	3	277.6 (336.1)	204.1 (245.9)	-	7.27 (10.43)	-	Defect free	[89]

## 5. Steel and Ferrous Alloys

The FSW method was initially dedicated to aluminum and its alloys, but with the development of this technology, other materials are successfully joined. Steel and ferrous alloys are still a challenge due to their high hardness. The biggest problem when welding steel and ferrous alloys is choosing the right tool for this process. The tool material must have high resistance to frictional wear, resistance to cracking, high strength, and resistance to chemical degradation at high temperatures achieved during the process [90,91]. Finding the proper material is a major engineering challenge. There are also studies on various ceramic options [92]. Nevertheless, composite tools made of polycrystalline boron nitride/tungsten rhenium (pcBN/W-Re) are also commonly used in the FSW of steel [93].

The friction stir welding method offers a reduction of the metallurgical changes in the heat-affected zone due to lower heat input compared to fusion welding techniques. The FSW method is a good alternative for joining difficult to fusion weld steel grades. Furthermore, during fusion welding, the normal source of hydrogen might lead to hydrogen cracking, while this problem is eliminated during FSW [32]. Early studies on FSW of steels proved that the peak temperature during the process of 1000–1200 °C is much lower than that observed during conventional welding [10,94,95]. Hence, the region of the heat-affected zone with pearlitic steels, which becomes fully austenitic, is supposed to be narrower. Moreover, the size of the grains of austenite is expected to be finer than in the case of arc welding. The unfavorable transformations, such as untampered martensite, can be avoided in the FSW method [10].

The thermo-mechanical nature of the FSW process induces phase transformations controlled by the selection of appropriate process parameters, such as tool rotational speed and tool traverse speed. Changes in the microstructure of carbon steel depending on the process temperature were presented in the paper of Fujii et al. [96]. In the study of Cui et al. [97], different microstructures of high-carbon steel were observed by controlling both the tool rotational speed and the tool traverse speed. Saeid et al. [98] obtained defect-free welds of duplex stainless steel by the FSW method in relatively low temperatures, which led to the avoidance of phase transformation and the ratio between phases was not changed. In the research of Ghosh et al. [99], the dependency of temperature and rate of deformation on microstructure for high-strength M190 steel was examined. Miura et al. [100] reported that the FSW method on Cr-Mo steel results in the increase of the volume fraction of retained austenite, and the joints perform high ultimate tensile strength and elongation. A similar observation for ferritic stainless steel was noted by Fujii et al. [101]. However, there is no general explanation for this mechanism.

The influence of welding parameters of steel on the mechanical properties of welds is not fully determined. In the research of Mahoney et al. [102], the HSLA-65 alloy was welded and the mechanical properties of the welds in dependence on the rotational speed and traverse speed of the tool were examined. The results showed that the tensile strength of the welds increases with both rotational and linear speed, while the elongation of the welds decreases. The studies of Miura et al. [103] show an inverse relationship: for iron alloys with nickel and carbon, the ultimate tensile strength of the welds and their yield strength decreases with an increase in tool speed. It should be noted that these incompatibilities result from differences in the range of selected parameters. Mahoney et al. applied a tool traverse speed up to 152.4 mm/min, while Miura et al. applied one with maximum 400 mm/min. However, similarly to the studies on HSLA-65 steel alloy of Mahoney et al. [102], the elongation of the welds decreases as the rotational speed increases. In the research of Fujii et al. [104], three carbon steels with different carbon contents were subjected to the FSW method. Their tensile strength was tested depending on the established traverse speed. The results showed that for IF (interstitial-free) steels, this parameter does not significantly affect the UTS, while for S12C and S35C steels, this effect was more visible but not uniform. For S12C, UTS increased with the tool traverse speed, while for S35C, the tensile strength first increased and then decreased with an increase of the tool traverse speed. For both steels, higher UTS than the value for the parent material was achieved. The same dependence as for S35C steel was observed by Reynolds et al. [90] for DH36 steel. Tensile strength and yield strength



first increased and then decreased as both traverse and rotational speed of the tool increased. The mechanical properties of the welds were higher than those of the parent material. In the research of Meshram et al. [105] on ASIS 316 steel, the highest tool rotational speed and the lowest traverse speed of the tool influenced the mechanical properties of the joints. The UTS and hardness exceeded the ones of the base metal. The studies of Maltin et al. [106] on DH36 steel showed that the highest both tool traverse and rotational speed resulted in the highest UTS and yield stress, exceeding the values for the parent material.

Some researchers claimed that FSW of steel is an attractive alternative in comparison to the fusion welding, and the feasibility of the method was proved by many studies, although more scientific research in this field is needed, especially with improving tools' geometry and the proper selection of the tool materials [94]. In contrast, Bhadeshia and DebRoy [107] suggested that the FSW technology is not expected to be widely applied, because fusion welding techniques already allow producing reliable, cost-effective joints.

Table 3 presents the results of selected studies on friction stir welded steels. The process parameters that provided the best mechanical properties of the welds were presented, and the properties of the parent material were given in brackets.

Table 3. FSW of steel and ferrous alloys—process parameters and mechanical properties of the joints.

Material	Plate Thickness [mm]	Process Parameters						Weld Properties				Reference
		v [mm/min]	$\omega$ [rpm]	Tool Shape	Pin D/d Ratio	Tilt Angle [°]	UTS [MPa]	Yield Strength [MPa]	Hardness of the Stir Zone [HV]	Elongation [%]	Defects	
HSLA-65	6	154.2	600	Convex steps-spiral scroll shoulder	-	-	852 (538-690)	662 (448)	-	22.3 (min. 18)	-	[102]
HSLA DMR-249A	5	30	600	Tapered pin with no threads	5	0	664 (610)	-	410 (270)	19 (29)	Free from macro-level defects	[108]
IF	1.6	400	400	Cylindrical pin with no threads	3	3	-310 (284)	-	-	-	-	[104]
S12C	1.6	400	400	Cylindrical pin with no threads	3	3	-480 (317)	-	-	-	-	[104]
S35C	1.6	200	400	Cylindrical pin with no threads	3	3	-780 (574)	-	-	-	-	[104]
DH36	6	450	600	-	-	0	832.51 (531.62)	656.68 (376.71)	-	5.57	-	[106]
DH36	6.4	306	526	Slightly tapered pin with no threads	-	2.5	-940 (-390)	-650 (-350)	-	-	No volumetric defects	[90]
Ultrafine grained AISI 304L	2	80	630	Conical pin	-3	3	-760 (920)	-500 (720)	285 (330)	-42 (47)	-	[109]
AISI 316	4	8	1100	-	-	-	610 (608)	-	230 (190)	35 (49)	-	[105]
AISI 316	4	8	1000	-	-	-	630 (608)	-	-	37 (49)	Defect free	[110]
AISI 1018	5	50	1000	Tapered pin with no threads	2.2	-	457 (421)	424 (361)	-	20 (27)	-	[111]
HNAS (High nitrogen nickel-free austenitic stainless steel)	2.4	100	400	Tapered pin	3.3	0	-1100 (-1060)	-760 (-680)	400 (370)	-37 (-43)	No groove-like defects	[112]
Fe-18.4Cr-15.8Mn-2.1Mo-0.66N-0.04C	2	100	800	-	3	-	980 (967)	580 (604)	-	30 (53)	-	[113]
Fe-18Cr-16Mn-2Mo-0.85N	3	50	800	-	-	2	1375 (1234)	908 (782)	-	25.13 (9.8)	-	[114]
Fe-24Ni-0.1C	1.6	400	200	-	3	3	1283 (793)	390 (336)	-	29.0 (5.6)	-	[103]

## 6. Titanium and Its Alloys

Titanium and its alloys are characterized by very good mechanical properties such as high strength, high corrosion resistance, and a very good strength-to-weight ratio, but their processing at temperatures higher than 550 °C is difficult due to their low resistance to oxidation. In addition, in single-phase titanium alloys, a tendency to grain growth is observed, which results in a decrease in the mechanical properties of the material [115]. When using the FSW method for soft alloys such as aluminum or magnesium, the problem of tool wear and its material selection is not a challenge, but in the case of titanium joining, these problems may arise. The most commonly used tools during the FSW process are those with a developed pin geometry, such as threads, flats, or flutes. When friction stir welding titanium and its alloys, conventional tools can be significantly damaged. It is therefore necessary to modify the geometry in such a way that the material is properly mixed while minimising the problem of wear. These solutions consist of uncomplicated tools with a columnar or conical pin, and the mixing of the material is assisted by appropriate shoulder surface modification, such as scrolls, ridges, knurling, grooves, or concentric circles. Usually, the ratio of shoulder diameter ( $D$ ) to pin diameter ( $d$ ) is chosen to be equal to 3 to provide the best mechanical properties of the joint [116,117]. In the case of FSW of titanium and its alloys, a heat generated by the shoulder cannot flow to the joint root, and a relatively small pin is not able to properly stir the plasticized material. Therefore, usually tools with smaller shoulder diameter and larger pin are used, and the  $D/d$  ratio is smaller, which can be observed in the examples summarized in Table 4. Another important aspect of the tool design process is the selection of the right material. The significant strength of titanium and its alloys at hot working temperatures makes it necessary to select a material for the tool that will be resistant to high forces during the process and be inert for reactive titanium at temperatures reaching 0.8 of its melting point. The most popular materials for FSW of titanium and its alloys are W-, Re-, Mo-based alloys, and TiC [118–123]. Titanium and its alloys have a relatively low thermal conductivity and a high melting point, so a temperature gradient between the advancing and retreating side of the components may appear when friction stir welding. Applying the FSW method to titanium alloys might be challenging due to the thickness of the components and the tool geometry limitation, mostly for alpha and near-alpha alloys. In case of such alloys, the lower thermal conductivity of alpha phase, its higher low stress, and higher heat capacity of titanium makes it difficult to select the proper tool material for titanium alloy with high  $\beta$  trans temperature.  $\beta$  or  $\alpha + \beta$  alloys are susceptible to the temperature of  $\beta$  transus during friction welding in dependence on welding parameters and thermal distribution during the process. Examples of tools used during the process of FSW of titanium and its alloys are tungsten carbide (WC) and titanium carbide (TiC) tools produced by sintering. Specially designed water cooling systems are also successfully used to better dissipate heat from the tool [124].

The mechanical properties of welds are directly influenced by the evolved micro- and macrostructure of the joints. The macrostructure observed in titanium alloys is clearly different from the banded elliptical macrostructure observed in aluminum and its alloys [32] and a parabolic shape of the weld nugget was observed in the research of Gangwar et al. [125] on titanium alloys. Fonda et al. [126], in their research on aluminum alloys, observed that the banding may be attributed to the fluctuations in the second phase particles density or the crystallographic texture changes, while in the titanium alloys, the absence of hard second phases or inclusions suggests the formation of banding formation in the nugget due to texture difference [127]. Gangwar et al. [127] in the review suggested that the elongation of the FSW titanium components is lower than the base metal due to microstructural gradients observed in the gauge length of the transverse tensile specimen, and the strains are mostly carried by the narrow areas of the thermo-mechanically affected zone. However, the examples presented in Table 4 show the opposite conclusions. In the studies of Kulkarni et al. [128] on Ti-54M plates, the increase in specimen elongation was observed with the increase in the tool traverse speed in the FSW process. On the contrary, in the studies of the same authors on Ti-6242 plates of the same thickness and the same process parameters, the decrease of the elongation with the increase of the tool traverse speed was observed. This confirms the assumption that the chemical composition of

the material is very important for FSW welding. These studies also confirm the suggestion that  $\alpha$  and near  $\alpha$  alloys, among them Ti-6242, are more challenging. Similarly, the studies of Su et al. [129] on Ti-6Al-4V a decrease in elongation with an increase in the tool traverse speed was observed, while Mashinini et al. [130] studies on the same alloy showed the opposite relation. This effect is caused by differences in other applied parameters, including tool geometry, tool rotational speed, and tilt angle. In the same studies of Su et al. [129] and Mashinini et al. [130], opposite correlations between UTS and the tool traverse speed were also presented. In the studies of Fujii et al. [131] on pure titanium plates, the UTS firstly increases with the increase of the tool traverse speed and then decreases with the further increase of the tool traverse speed. The opposite relation was observed by Kulkarni et al. [128] in the studies on Ti-6Al-4V titanium alloy. Kulkarni et al. [128] presented a tendency of increasing UTS as a function of the tool rotational speed, while Zhang et al. [120] reported an opposite relation. An in-depth review of the literature did not allow the explanation of the reason for contradictory conclusions in the cited examples, but it should be noted that in all cited studies, tools with different geometry and made of different material were used, and this could have been the reason for obtaining different results.

Table 4 presents the results of friction stir welding on titanium and its alloys and the mechanical properties of the parent material, if presented by the authors.

**Table 4.** FSW of titanium and its alloys—process parameters and mechanical properties of the joints.

Material	Plate Thickness [mm]	Process Parameters					Weld Properties					Reference
		v [mm/min]	$\omega$ [rpm]	Tool Shape	Pin D/d Ratio	Tilt Angle [°]	UTS [MPa]	Yield Strength [MPa]	Hardness of the Stir Zone [HV]	Elongation [%]	Defects	
Pure Ti	2	200	200	-	2.5	-	-430 (420)	-	180 (146)	-	-	[131]
Pure Ti	5.6	50	110	-	-	-	430 (440)	-	-	20 (25)	Defect free	[119]
Ti-5Al fine grain	0.1	100	275	-	-	-	-950 (972)	-780 (889)	-	-5.9 (16.5)	Defect free	[128]
Ti-6Al-4V fine grain	0.1	125	325	-	-	-	-950	-760	-	-4.3	Defect free	[128]
Ti-6Al-4V standard grain	0.1	100	275	-	-	-	-930 (950)	-720 (880)	-	-7.7 (14)	Defect free	[128]
Ti-6Al-4V	2	101.6	900	Smooth cylindrical pin	1.6	2.5	1156.2 (1014.7)	1067.4 (941.8)	-	21.7 (23.1)	Processing defects	[129]
Ti-6Al-4V	2	50	250	Tapered pin	2	-	813 (1013)	-	-	3.2 (8.5)	-	[128]
Ti-6Al-4V	3	75	300	Small shoulder and large tapered pin	-	-	1025.0 (higher than BM)	973.6 (higher than BM)	-	9.7	-	[132]
Ti-6Al-4V	3	60	300	Convex shoulder and tapered pin	~3	-	-1050 (-920)	-950 (-830)	-315	-33 (-21)	Cavity defects	[120]
Ti-6Al-4V	3	45	550	Tapered pin	1.75	0.5	1059 (1000)	-	-	4 (18)	Small root flaws	[133]
Ti-6Al-4V	3.17	40	500	Flat shoulder surface and tapered smooth pin	2	1.5	1040 (1017)	-	-	9 (20)	-	[130]
Ti-6Al-4V	6	100	280	-	-	-	1016 (1045)	971 (978)	335.6 (315.4)	9 (16)	-	[134]
Ti-6242 fine grain	0.1	125	325	-	-	-	-950	-730	-	-4.1	Defect free	[128]
Ti-6242 standard grain	0.1	125	325	-	-	-	-880 (1000)	-730 (895)	-	-8.4 (12)	Defect free	[128]
TC4	2	50	400	Smooth tapered pin	-	2.5	953 (1036)	-	-345 (-325)	-	-	[135]

## 7. Copper and Its Alloys

Copper and its alloys are widely used in many engineering applications due to their properties such as good electrical and thermal conductivity, relatively good mechanical strength, high corrosion resistance, and high formability. The most popular copper alloying elements are zinc, aluminum, nickel, and tin [136]. After steel and ferrous alloys and aluminum and its alloys, copper and its alloys are the most commonly used materials in industries, especially in the marine, aerospace, electronics, and military sectors. However, pure copper strength is not high enough for load bearing components, but it increases by alloying. The most popular copper alloys are solid solution hardened (single-phase). Copper is characterised by low galvanic reactivity, so the risk of reaction or corrosion is low. It is also characterized by high plasticity and resistance to oxidation. The most important applications for copper and its alloys include heat sinks, electrodes for resistance welding, and rotating target neutron sources. The FSW method was also successfully used for joining components for nuclear waste canisters [137,138]. It is also used in processes of soldering and brazing [139].

Joining copper and its alloys using traditional welding methods is difficult due to the high thermal conductivity and high melting point, which makes it necessary to generate a large amount of heat, thus increasing the cost of the process, and the resulting welds may exhibit porosity, distortion, and solidification cracks. Conventional fusion welding techniques require very fast heat delivery due to 10–100 times higher heat conductivity than that of steels [10,32]. Copper and its alloys are ranked as hard-to-weld materials [140]. The most significant problems occurring during the conventional welding of Cu and its alloys are high distortion, irregularities of the weld surface, decrease of strength at the weld surface connected with the formation of ZnO (for high Zn-content alloys), insufficient penetration because of the high thermal conductivity of Cu, and colour change because of the oxidation process. The FSW method is an excellent solution, because the melting temperature is not reached during the process.

Due to the high thermal conductivity of copper and its alloys, the required heat input should be higher than for FSW of other materials. This means that the process is usually conducted at lower tool traverse speed and/or higher tool rotational speed. It is required mostly for FSW of pure copper, which has higher thermal conductivity than its alloys. As for all friction stir welded metal joints, four specific zones can be observed in the cross-section—stir zone (SZ), thermo-mechanically affected zone (TMAZ), heat-affected zone (HAZ), and base metal (BM). For the FSW joints of copper alloys, the HAZ is not highly distinguishable [141,142]. The recrystallization process occurs relatively easily in copper and its alloys, especially single-phase, so the SZ extends almost the TMAZ and the boundaries between those two zones are hard to determine.

In the research of Machniewicz et al. [143], 5 mm pure copper plates were friction stir welded in both the longitudinal direction and perpendicular to the rolling direction. For both examples, the ultimate tensile strength decreased with an increase in the tool traverse speed. Moreover, the microhardness of the welds was measured. The microhardness profile presented a “W” shape, which is characteristic for most friction stir welded joints [144–149]. In the profile of such welds of any metal, a sharp decrease in hardness can be observed in the heat-affected zone, and then the hardness slightly increases in the direction of the weld nugget. This phenomenon is related to the difference in grain size in various zones—in the weld zone, the microstructure is more fine-grained than in the heat-affected zone, and therefore higher hardness is observed there. In the studies of Khodavardizadeh et al. [146], Xue et al. [145], and Surekha et al. [150] on pure copper plates, the ultimate tensile strength of the welds as a function of the tool traverse speed was also determined. The results of those studies are not consistent with those of Machniewicz et al. [143], and the UTS of the welds increased with an increase of the tool traverse speed. In the studies of Khodavardizadeh et al. [146] and Surekha et al. [150], it was observed that the elongation of welded samples increases with an increase of the tool traverse speed, while Xue et al. [145] noted the opposite relationship for the same material. The above quoted studies were carried out with different process parameters and the values of applied tool rotational speed were more than twice as high for tests of Xue et al. [145] as for Surekha et al. [150]. In the studies

of Liu et al. [151] on pure copper plates, the ultimate tensile strength as a function of the tool rotational speed was measured. It was observed that the UTS firstly increased and then slowly decreased with the increase of the tool rotational speed. The same relation was observed while measuring the elongation. The maximum UTS was equal to the value for the base material. In the studies of Xue et al. [145] and Khodavardizadeh et al. [147], the UTS of the welds decreases with an increase of the tool rotational speed, while in the studies of Sahlot et al. [152], Xie et al. [153], and Cartiguyen et al. [154] on the pure copper plates, the opposite relationship was observed. Cartiguyen et al. [154], Xie et al. [153], and Xue et al. [145] reported that the elongation of the copper FSW joints increased with the increase of the tool rotational speed, while the opposite relationship was observed by Khodavardizadeh et al. [147]. In this study, it was also noted that the hardness of the copper weld nuggets increases with the increase of the tool traverse speed, while Surekha et al. [150] observed almost no changes of the hardness, and the measured values were similar to the one of the base material. Khodavardizadeh et al. [146] noted that the hardness of the copper weld nuggets decreases with an increase of the tool rotational speed, while Xie et al. [153] and Cartiguyen et al. [154] noted an opposite relationship. In another study of Cartiguyen et al. [155] on 6 mm thick copper plates, the influence of the pin geometry was investigated. The threaded cylindrical pin provided better mechanical properties of the friction stir welded joints than square, triflute, and hexagonal pins. Different tool geometries were used in all the quoted research or these geometries are not presented in the papers. It should be noted that tool geometry is a key process factor, and it is necessary to define it in published studies.

Table 5 shows an overview of the studies on copper and its alloys conducted so far. Each example contains a set of parameters (if given) that provided the best mechanical properties of the welds and the values of these properties including the properties of the parent material (values in brackets).

**Table 5.** FSW of copper and its alloys—process parameters and mechanical properties of the joints.

Material	Plate Thickness [mm]	Process Parameters					Weld Properties					Reference
		v [mm/min]	$\omega$ [rpm]	Tool Shape	Pin D/d Ratio	Tilt Angle [°]	UTS [MPa]	Yield Strength [MPa]	Hardness of the Stir Zone [HV]	Elongation [%]	Defects	
Pure copper	2	50	1200	Conical pin	2	0	217.56 (237.81)	-	-	2.03 (39)	Defect free	[156]
Pure copper	2	30	1000	-	-	-	231 (273)	1.2 (3.1)	136	-	Defect free	[157]
Pure copper	3	30	2000	Tapered pin	2.9	-	-195 (217)	-	-	-	Defect free	[152]
Pure copper	3	100	400	Right hand threaded cylindrical pin and concave shoulder	4	-	282 (282)	-	-	16.4	Defect free	[151]
Pure copper	3	25	1100	-	-	2.5	194 (212)	70 (68)	-	22.8 (28.1)	-	[158]
Pure copper	3	40	900	Flat shoulder and cylindrical pin	3	3	168 (260)	109 (231)	85 (110)	13.5 (31)	Defect free	[159]
Pure copper	3	250	300	Non-threaded cylindrical pin	2.4	-	328 (270)	261 (209)	113.6 (84.6)	23 (22)	Defect free	[150]
Pure copper	4	61	1250	-	-	3	~225 (-260)	-	~90 (105-110)	-	Defect free	[144]
Pure copper	5	30	910	Straight cylindrical pin	3	-	216.9	-	77.37 HB	9.2	No defects	[160]
Pure copper	5	40	580	Taper pin	~3	0	220.7 (261.2)	101.3 (232.0)	-	-	Defect free	[143]
Pure copper	5	75	600	-	-	-	221 (234)	127 (178)	88 (107)	43 (47)	-	[146]
Pure copper	5	50	400	-	-	2.5	235.9 (236.7)	207.7 (222.9)	-	15.1 (27.7)	Defect free	[145]
Pure copper	5	50	800	Cylindrical threaded pin	~3.3	2.5	~240 (-240)	~140 (-225)	63.1 (82.2)	-45 (-28)	Defect free	[153]
Pure copper	5	112	500	Threaded cylindrical pin	2.5	2.5	326 (331)	134 (137)	~105 (~78)	31 (29)	Defect free	[161]
Pure copper	6	50	350	Threaded cylindrical pin	3	0	228 (279)	209 (271)	92 (82)	-	-	[155]
Pure copper	6	50	350	Square pin	-	0	207 (279)	203 (271)	88 (82)	-	-	[155]
Pure copper	6	50	350	Triflute pin	-	0	196 (279)	196 (271)	90 (82)	-	-	[155]
Pure copper	6	50	350	Hexagonal pin	-	0	165 (279)	163 (271)	97 (82)	-	-	[155]



Table 5. Cont.

Material	Plate Thickness [mm]	Process Parameters					Weld Properties						Reference
		v [mm/min]	$\omega$ [rpm]	Tool Shape	Pin D/d Ratio	Tilt Angle [°]	UTS [MPa]	Yield Strength [MPa]	Hardness of the Stir Zone [HV]	Elongation [%]	Defects		
Pure copper	6	50	500	Concave shoulder and threaded cylindrical pin	3	0	229 (279)	229 (271)	88 (82)	49.9 (34.4)	Defect free	[154]	
Pure copper	6	315	630	Square pin	2.4	2	215 (150)	190 (145)	-	33 (14)	-	[162]	
2200 Copper Alloy	5	31.25	900	Taper pin with no threads	3.3	1	-	-	-	26.98	-	[163]	
2200 Copper Alloy	5	31.25	900	Cylindrical with no threads	3.3	1	-	-	-	10.56	-	[163]	
Brass 60%-Cu, 40%-Zn	2	500	1000	-	3	3	-390 (381)	-180 (192)	-132 (97)	-52 (61)	Defect free	[141]	

## 8. Polymers

Polymeric materials are generally characterised by different properties than metallic materials. Although the FSW method was initially dedicated to metal bonding, with the increasing use of polymers in various industries, it has been successfully used to join also this group of materials. The research on the friction stir welding of polymeric materials conducted so far focuses mainly on joining of polyethylene (PE) [164–169], high-density polyethylene (HDPE) [166,170–172], polyamide Nylon 6 [173–175], acrylonitrile butadiene styrene (ABS) [176–179], polyvinyl chloride (PVC) [171], polypropylene (PP) [180,181], and polyethylene terephthalate glycol (PETG) [182].

Using conventional tools for friction stir welding of polymers is the easiest but not the most effective approach, which will be concluded later. Panneerselvam et al. [183] successfully butt-joined 10 mm polypropylene plates using the FSW method, but for some pin geometries, the insufficient material softening; the tool damage or the blowhole defects were observed in the joint line. Design of experiments analysis (DOE) was used for modelling and analysing the influence of the process parameters [184]. The analysis of the obtained results allowed the authors to conclude that insufficient heat on the retreating side did not allow for proper mixing of the material in this zone and increased the probability of weld defects. The same conclusions were presented by Simoes et al. [185]. The morphology of the polymethyl methacrylate joints welded by the FSW method was analysed, and it was claimed that the advancing side of the welds performs almost the same transparency as the base material, while in the retreating side, the insufficient stirring and voids were observed. The studies conducted so far allow the conclusion that low heat conductivity of polymeric materials is not favourable for an efficient FSW process. Sufficient softening and plasticization of the material that is not in direct contact with the tool is difficult to achieve. In the literature, approaches can be found related to the application of an additional heating system that would compensate for heat deficiencies related to low thermal conductivity and friction coefficient of polymer materials. Squeo et al. [186] friction stir welded 3 mm polyethylene sheets using a pin previously heated with a hot air gun. This solution was not considered reliable due to the rapid cooling of the tool. Another approach was to use a hot plate between the CNC table and the components. The plate was heated up to 150 °C and ensured high quality of joints, while the biggest disadvantage of this method was low repeatability during the process. Arbegast [187] proposed a model of the FSW joint that describes the conditions of the process and a mechanism of creating weld defects. The theory also confirms that volumetric defects are likely to be observed on the retreating side of the weld.

The FSW method using a conventional tool to perform the welding process usually does not bring the expected results, and the properties of the welds are relatively low. In order to minimize the risk of weld defects and increase the efficiency of the process, a modification of the FSW method—stationary shoulder friction stir welding (SSFSW)—is used. The mechanism of the SSFSW process consists of a rotating pin that runs in a non-rotating shoulder element sliding on the material surface during welding. The stationary shoulder, usually called a shoe, minimizes the risk of the plasticized weld material being expelled from the weld seam [181]. The literature review on the SSFSW method can lead to the conclusion that this modification should be used for joining polymers in order to obtain non-defects and high mechanical properties welds [168,176,182,188]. Rezgui et al. [188] applied the SSFSW method with a wooden stationary shoulder to weld 15 mm thick HDPE. The temperature detected during the process was in a range from 120 to 180 °C, which means that the material reached its melting point, and the process did not have a solid-state nature. Other studies also confirm that friction stir welding of polymers is not a solid-state process, unlike the FSW of metals [185,189]. In order to obtain better results from the SSFSW method, a tool called “hot shoe” was developed and patented by Nelson et al. [190]. The aluminum static shoulder with the polytetrafluoroethylene (PTFE) coating with a heater component inside of the shoe allows the attainment of the tensile strength of 75% of the base material of ABS. The concept of SSFSW with a hot shoe as a shoulder was also successfully used in the studies of Bagheri et al. [176], Banjare et al. [191], and Laieghi et al. [192].

Sahu et al. [180] successfully welded 6 mm polypropylene sheets using three pin geometries—cylindrical, square, and conical. Only cylindrical and square pins enabled the production of defect-free welds. The influence of the tool traverse speed and the tool rotational speed on the ultimate tensile strength was determined. It was observed that the UTS of the welds firstly increased with an increase in the tool rotational speed and then slowly decreased. The same dependence was observed for the tensile strength function of welds on the tool traverse speed. The same conclusions for both tool traverse and tool rotational speed were confirmed by Pirizadeh et al. [178] on the friction stir welded 5 mm thick ABS plates and Arici et al. [165] on double pass friction stir welded Nylon 6 plates, where the influence of the tool traverse speed on the UTS of the welds was measured. In the studies, it was concluded that the tilt angle of the tool equal to  $1^\circ$  results in better mechanical properties of the welds than the tilt angle of  $0^\circ$ . The studies of Youssif et al. [175] on 13 mm thick Nylon 6 plates proved that the UTS of the welds decreases with an increase of the tool traverse speed. The same dependence was observed for the UTS as a function of the tool rotational speed. The same conclusions were presented in the studies of Zafar et al. [174] on 16 mm Nylon 6 plates. In the studies of Bagheri et al. [176] on 5 mm thick ABS plates, the UTS always increased with the increase of the tool rotational speed for all of the values of applied tool traverse speed. The maximum value of UTS reached almost 90% of the value for the base material.

Table 6 summarizes the best process parameters applied during the friction stir welding of polymeric materials and presents the mechanical properties of welds and parent material if given by the authors.

Table 6. FSW of polymers—process parameters and mechanical properties of the joints.

Material	Plate Thickness [mm]	Process Parameters					Weld Properties					Reference
		v [mm/min]	$\omega$ [rpm]	Tool Shape	Pin D/d Ratio	Tilt Angle [°]	UTS [MPa]	Yield Strength [MPa]	Hardness of the Stir Zone [HV]	Elongation [%]	Defects	
Polyethylene (PE)	5	25	1000	Cylindrical pin with no threads	3.2	1	19.30 (20.00)	-	-	-	-	[165]
Polypropylene (PP)	6	15	750	Square pin with no threads	2	1	19.74 (33)	-	-	-	Peeling defects	[180]
Polyvinyl chloride (PVC)	5	10	1800	Right-hand screw pin	-4.2	0	23.5 (66.5)	-	-	-	Around 78% of base material	[171]
Nylon 6	10	10	1000	Left handed threaded cylindrical pin	4	-	34.8 (73.4)	-	-	-	64 SD (shore-D hardness) (70 SD)	[173]
Nylon 6	13	10	1250	Right handed threaded cylindrical pin	-	-	25.75 (54)	-	-	8.7 (43)	-	[175]
Nylon 6	16	25	300	Right-hand threaded pin	2.4	0	27.22 (85)	-	-	-	Lack of bonding, minor weld defects at the bottom	[174]
Polyamide 6 (PA6)	5	40	440	Right-hand screw pin	-4.2	0	30 (67.1)	-	-	-	60% of base material	[171]
Polyamide (nylon 66)	8	42	1570	Smooth cylindrical pin	4	-	8.51 (15.57)	-	-	-	-	[193]
Acrylonitrile Butadiene Styrene (ABS)	5	20	1600	Right-hand threaded cylindrical pin	1.7	-	32.62 (36.76)	-	-	-	-	[176]
Acrylonitrile Butadiene Styrene (ABS) (double side welded)	5	40	400	Smooth cylindrical pin, flat shoulders surfaces	-	-	15.58 (34.14)	-	-	-	-	[178]
Acrylonitrile Butadiene Styrene (ABS) (double side welded)	5	40	400	Smooth convex pin, flat shoulders surfaces	-	-	20.70 (34.14)	-	-	-	-	[178]
Acrylonitrile Butadiene Styrene (ABS)	6	200	1500	Conical threaded pin	-	-	30.6 (40.5)	-	-	-	Defect free	[179]

Table 6. Cont.

Material	Plate Thickness [mm]	Process Parameters				Weld Properties						
		v [mm/min]	$\omega$ [rpm]	Tool Shape	Pin D/d Ratio	Tilt Angle [°]	UTS [MPa]	Yield Strength [MPa]	Hardness of the Stir Zone [HV]	Elongation [%]	Defects	Reference
Acrylonitrile Butadiene Styrene (ABS)	8	16	1400	Cylindrical with no threads	3.3	1	41.42 (41.80)	-	-	-	-	[177]
Acrylonitrile Butadiene Styrene (ABS)	8	25	900	Conical with no threads	3.3	2	41.95 (41.80)	-	-	-	-	[177]
High-density polyethylene (HDPE)	4	115	3000	-	3	2	19.4 (22.5)	-	-	-	-	[166]
High-density polyethylene (HDPE)	5	15	1240	Right-hand screw pin	-4.2	0	22.3 (31.9)	-	Above 90% of base material	-	No significant defects	[171]

## 9. Composites

Polymer matrix composites (PMCs) and metal matrix composites (MMCs), especially aluminum matrix composites (AMCs), replace metals and their alloys and polymers in many industries, as the mechanical properties of such materials can be controlled by the proper selections of the filler properties. High temperature during conventional welding methods of metal matrix composites can lead to degradation of the microstructure of the composite, which leads to deterioration of mechanical properties of the joint. As an example, the process of formation of a brittle  $Al_4C_3$  phase during conventional welding of a SiC-reinforced aluminum matrix composite can be presented [60]. Phase changes might be avoided by using shorter thermal cycles or lower heat input. During the FSW process, the temperature of the components to be joined is also increased, but it is relatively lower than that during conventional welding processes, and this problem is reduced. The problems that might occur during the FSW of composites include, beyond in the case of MMCs, the possibility of forming the brittle phases, which results in deterioration of strength, the formation of clusters of reinforcement particles, or change of particles' configuration due to the plastic deformation and applied forces and temperature [194,195].

In the FSW process of composites, in addition to the standard process parameters such as the rotational and traverse speed of the tool and the tilt angle of the tool, the shape of the tool itself also has a significant impact on the properties of the joints. Vijay and Murugan [196] used three pin shapes to friction stir weld Al/TiB<sub>2</sub>/10 composite—square, hexagonal, and octagon. Using the untampered square pin resulted in obtaining the maximum tensile strength of the joint equal to 99.47% of the base material. The authors explained that by obtaining the highest ratio of static volume to dynamic volume of the plasticized material equal to 1.56 for the square pin, the best mechanical properties of the joints were achieved, while for hexagonal and octagon pins, the values were equal to 1.21 and 1.11, respectively. The same phenomenon was confirmed by Hassan et al. [197] in the study on aluminum matrix composite containing Mg, SiC, and graphite particles. The square head pin provided better mechanical properties of the joints than hexagonal and octagonal pins. Mahmoud et al. [198] used four different pin shapes—circular with and without threads, triangular, and square—to fabricate composite surface layers with SiC particles dispersed in A1050-H24 aluminum plates. It was reported that the square pin enabled the formation of the most homogeneous microstructure of the nugget zone.

Another aspect often discussed in the case of FSW of composites is the change of shape and size of the particle size of the composite reinforcement. The first reports in this area indicated the identical number of particles before and after the process, which implies that there is no particle breakage during the process [199–201]. However, other tests conducted prove that the breakdown of the reinforcing particles takes place in the nugget zone during the FSW process [202–206]. Baxter and Reynolds [202] reported that for the composite with 7079 aluminum matrix and SiC reinforcement, the number of SiC particles the number of particles doubled without changing their volume percentage, which means that the particle breakage takes place during the process. In the studies of Acharya et al. [207], the particle size of the SiC reinforcement in AA6092 in friction stir welded material zones was measured. In the nugget zone, thermo-mechanically affected zone, and the base materials the size of the particles was equal to 4.03, 4.99, and 7.92  $\mu\text{m}$ , respectively. Feng et al. [204,205], in the studies on Al2009-15vol% SiC composite, reported that the particle breakage takes place in the stir zone, and the particles are uniformly distributed. Moreover, it is generally observed that the matrix phase experienced a grain refinement due to the dynamic recrystallization resulting from the frictional heating [204–206].

Kumar et al. [208], in the studies on glass-filled Nylon 6 friction stir welded 5 mm thick plates, used different tool traverse and tool rotational speed, and the values of the tilt angle were equal to 0, 1, and 2°. It was observed that the highest ultimate tensile strength and the elongation were obtained for the joints with the highest tilt angle. The UTS of the joints increased with an increase of the tool rotational speed and decreased as a function of the tool traverse speed. In the studies of Bhushan et al. [209] on the AA6082/SiC/10p 6 mm thick plates, the lowest tilt angle of 1° and the highest tool rotational speed resulted in the highest UTS and elongation. Jafrey et al. [210] reported that for 5 mm thick

plates of PP/C30B/EA nanocomposite, the highest tool traverse speed resulted in the highest UTS of the joints. Liu et al. [211] and Wang et al. [212], in their studies on AC4A/SiC/30p and 2009Al-T4/SiC/17p, respectively, also reported that the elongation and the UTS of the joints increase when the tool traverse speed increases. Mozammil et al. [213], in the studies on Al-4.5% Cu/TiB<sub>2</sub>/2.5 p plates with thickness of 6 mm, noted that the highest tool traverse speed of 26 mm/min and the highest tool rotational speed of 931 rpm resulted in the highest UTS for all the joints fabricated with three tool shoulder geometries—full flat, 1 mm flat shoulder and 7° concave, and 2 mm flat and 7° concave. Among them, the tool with 1 mm flat shoulder and 7° concave provided the best mechanical properties of the joints. Vijayavel et al. [117] investigated the influence of the D/d ratio on the mechanical properties of the FSW welds of LM25AA-5% SiC. Among the values from 2 to 4 in steps of 0.5, the D/d ratio equal to 3 resulted in the highest UTS, hardness, and elongation of the welds. The UTS value of such a joint reached 123% of that for the base material.

Table 7 summarizes the process parameters and weld properties for composites, considering in brackets the properties of the parent material if given by the authors.

Table 7. FSW of composites—process parameters and mechanical properties of the joints.

Material	Process Parameters					Weld Properties					Reference	
	Plate Thickness [mm]	v [mm/min]	$\omega$ [rpm]	Tool Shape	Pin D/d Ratio	Tilt Angle [°]	UTS [MPa]	Yield Strength [MPa]	Hardness of the Stir-Zone [HV]	Elongation [%]		Defects
Al-4.5%Cu/TB2/2.5p	6	26	931	Full flat shoulder surface, cylindrical pin with no threads	~2.9	2	190.39 (no inf about parent material)	-	69.86	16.875	-	[213]
Al-4.5%Cu/TB2/2.5p	6	26	931	1 mm flat shoulder and 7° concave, cylindrical pin with no threads	~2.9	2	198.62	-	57.63	18.825	-	[213]
Al-4.5%Cu/TB2/2.5p	6	26	931	2 mm flat shoulder and 7° concave, cylindrical pin with no threads	~2.9	2	191.39	-	60.76	17.050	-	[213]
AA6061/SiC (10wt%)/fly ash (7.5 wt%)	6	60	1200	Square profile pin	-	2	-	-	~130 (102)	-	No major defects	[214]
AA2124/SiC/2.5p-T4	3	40	1120	Cylindrical left-handed screwed pin	3.3	2	366 (454)	-	170 (185)	1.4 (2.4)	-	[215]
AA6092/SiC/17.5p	6	120	1500	Taper cylindrical pin	3	2	347 (415)	290 (360)	140 (157)	5.46 (7.76)	No major defects	[208,216]
ACHA + 30vol%SiCp	5	150	2000	Columnar pin with right-handed threads	2.3	3	140 (163)	-	-	0.33	Defect free	[211]
17vol%SiCp/2009Al-T4	3	800	1000	Threaded conical pin	2.8	-	501 (514)	341 (344)	-	3.5 (4.0)	No defects	[212]
17vol%SiCp/AA2009	3	50	1000	Cylindrical pin	2.8	-	443 (581)	278 (508)	-	4.7 (4.3)	No defects	[217]
AA2124/SiC/2.5p-T4	3	45	900	-	3	2	355.15 (454)	-	-	-	Flash defects on the surface	[218]
25%SiC/2124Al	8	15	400	Tapered conical pin	3.5	1.5	359 (372)	-	-	-	Small voids	[219]
AA6061-10%SiCp	6	45	1100	Threaded cylindrical pin	3	-	206 (278)	126 (200)	95 (105)	6.5 (8.0)	No defects	[220]
15vol%SiCp/2009Al	6	100	800	Conical pin	2.5	-	441 (537)	306 (343)	-	5.4 (10.1)	No defects	[221]
AA6092/SiC/17.5p-T6	3.1	100	1500	Flat edge featureless concave shoulder and M6 threaded cylindrical pin with a domed end	-	2	314 (420)	220 (370)	-	5 (3.5)	-	[222]



Table 7. Cont.

Material	Plate Thickness [mm]	Process Parameters					Weld Properties					Reference	
		v [mm/min]	$\omega$ [rpm]	Tool Shape	Pin D/d Ratio	Tilt Angle [°]	UTS [MPa]	Yield Strength [MPa]	Hardness of the Stir-Zone [HV]	Elongation [%]	Defects		
AA6082SiC/10p	6	100	1800	Cylindrical	2.5	1	359	-	-	-	-	-	[209]
LM25AA-5%SiCp	12	40	1000	Plain taper pin	3	-	192 (155)	-	~105 (68)	7.2 (2)	-	-	[116]
PP/C30B/EA nanocomposite	5	18	-	Square pin with no threads	1	-	13.533 (25.08)	-	-	-	-	-	[210]
PP/C30B/EA nanocomposite	5	18	-	Cylindrical pin with no threads	1	-	16.300 (25.08)	-	-	-	-	-	[210]
PP/C30B/EA nanocomposite	5	18	-	Triangle pin with no threads	1	-	13.500 (25.08)	-	-	-	-	-	[210]
Glass-filled Nylon 6	5	12	600	Cylindrical pin with cylindrical shank	3	2	36.51 (86.01)	-	-	7.35 (13.68)	-	Defect free	[208]

## 10. Dissimilar Materials

Joining of dissimilar materials is essential in applications that require different material properties in the same component, i.e., joining different aluminum alloys to other metals allows reducing weight [223]. However, FSW of different metals is very challenging due to the huge differences in mechanical and metallurgical properties of dissimilar materials [224,225]. Welding of dissimilar materials in the context of FSW may also refer to joining the same material family but different alloys or grades, or the same material but with different thickness of components. Recently, the FSW method has been successfully and progressively applied to weld dissimilar alloys because of its technical benefits and cost-effectiveness. Comprehensive analysis of material flow during the FSW process of dissimilar materials, studies on mechanical properties of joints, and selection of process parameters are necessary before applying the method in constructional applications [226,227]. One of the key parameters, besides the geometry of the tool and its rotational and traverse speed, is the offset of the tool toward one side. It should be noted that it is difficult to predict the amount of heat generated, material flow, and mechanical properties of dissimilar joints using theoretical analysis [228].

The FSW method allows for avoiding problems that occur during fusion welding. For instance, arc welding, laser beams, and electron beams might cause the formation of coarse grains or brittle intermetallic compounds in the dissimilar aluminum/magnesium joints [229,230]. The proper selection of welding parameters using the FSW method is extremely difficult in the case of aluminum–magnesium welding due to the possibility of liquid formation resulting from the relatively low eutectic temperature (437 and 450 °C) in the binary Al-Mg phase diagram [231]. This phenomenon may, as in the case of fusion welding techniques, result in the formation of intermetallic compounds. Abdollahzadeh et al. [232] improved the microstructural characteristics by using a zinc interlayer in the magnesium and aluminum butt joints. Intermetallic formation of Al-Mg was avoided. The most common phases in the stirred zone were both Mg-Zn and Mg-Al-Zn intermetallic compounds, as well as Al solid solution and residual Zn. It is also difficult to obtain aluminum to copper welds using FSW. The brittle intermetallic compounds such as AlCu, Al<sub>2</sub>Cu, and Al<sub>9</sub>Cu<sub>4</sub> are easy to create in such joints [224,233,234]. Zhang et al. [235] proposed the underwater process environment to minimize this problem.

Movement of the material around the pin during FSW of dissimilar materials affects the creation of the bond formation and material interlocking mechanism. It improves the mechanical properties of the weld and increases its strength. This phenomenon was reported for Al-Mg [236], Al-Cu [237], Mg-steel, and Al-steel [238] welds. The phenomenon of material interlocking depends on the characteristic of the complex material flow and depends mostly on the geometry of tool and the positioning of components to be welded. The mechanical interlocking occurs only in a stir zone, and it is an effect of the rotational movement of the tool. The phenomenon of interlocking is also observed in explosive welding where a periodic structure can be distinguished, but this organised structure is not observed in the case of friction stir welding [239].

As established by Fu et al. [240], the heat generated during the FSW process mostly derives from the friction ( $E_f$ ), the viscous dissipation ( $E_v$ ), and the plastic deformations at the interface between tool and components ( $E_d$ ). Zettler et al. [241], in the studies on dissimilar FSW of AZ31 and AA6040 alloys, reported that at the boundary between magnesium alloy and the tool, the frictional coefficient is lower than that on the aluminum alloy and the tool boundary. It was recommended to give tool offset toward aluminum to provide greater contact between the tool and the aluminum to increase the contributions of  $E_f$  and  $E_v$  during the friction stir welding process. This phenomenon can be explained by referring to the crystal structures of these materials. In the case of aluminum with its face-centred cubic structure (FCC) and twelve slip systems, better deformability is observed in comparison to the hexagonal close-packed structure (HCP) with three slip systems of magnesium. It promotes higher heat input through  $E_v$  and  $E_d$  during the FSW of aluminum than of magnesium [223,240]. These types of phenomena have a significant impact during the FSW of dissimilar materials; therefore, an important process parameter in such cases is also the tool offset.

In the studies of Jamshidi et al. [31] two aluminum alloys were used to fabricate friction stir welded dissimilar joints—AA6061-T6 and AA5086-O. For the case with AA6061-T6 plate on the advancing side and AA5086-O plate on the retreating side, better UTS and yield strength of the joint were observed, but the values of the reverse configuration were only slightly worse. Moreover, for both cases, it was observed that the highest tool traverse speed of 150 mm/min and the lowest tool rotational speed of 840 rpm resulted in the best mechanical properties of the joints. Kasai et al. [242] fabricated three dissimilar material joints—on the advancing side, low carbon steel plates were used, while on the retreating side, pure magnesium, AZ31, and AZ61 plates, respectively, were used. The highest UTS was noted for the joint with low carbon and AZ61, and it was observed that the UTS of steel/magnesium joints increases with the increase of Al content in the magnesium alloy. The reason for this phenomenon is simple—for all the used magnesium components, the UTS of the base material also increases with the increase in aluminum content in the material. In the studies of Zettler et al. [241], the dissimilar joints of Al6040-T6 and AZ31 were fabricated using the FSW method. The UTS of the joint of the configuration with aluminum alloy on the retreating side was about 50% higher than for the joint with reverse configuration. Peel et al. [243] used AA5083 and AA6082 aluminum alloys to fabricate dissimilar joints. It was observed that for both material configurations, the highest UTS was achieved when the tool traverse speed and the tool rotational speed were the highest and equal to 300 mm/min and 840 rpm, respectively. Furthermore, the joints with AA5083 plate on the advancing side exhibit higher UTS than for the reverse configuration, and for all the joints, no defects were observed. Similar studies were conducted by Khodir et al. [244]. The dissimilar welds of AA2024-T3 and AA7075-T6 were fabricated with both plates configurations. The welds with AA2024-T3 plate on the advancing side exhibit better mechanical properties, such as the UTS, the yield strength, and the elongation. Avinash et al. [245], in studies on AA2024-T3 on the advancing side and AA7075-T6 on the retreating side joints, reported that applying the lowest tool traverse speed of 80 mm/min and the highest tool rotational speed of 1400 rpm resulted in the highest UTS of the joint. Palanivel et al. [246] investigated the influence of the tool geometry on the UTS of dissimilar AA6351-T6 on the advancing side and AA5083-H111 on retreating side joints. Five different pins were used: Straight square, straight octagon, straight hexagon, tapered octagon, and tapered square. Among them, the straight square pin enabled the production of defect-free joints with the highest UTS, while all the welds fabricated with tapered octagon and tapered square pins exhibit tunnel defects along the joint line. Malarvizhi et al. [247] studied the influence of the D/d ratio of the tool on dissimilar AZ31B-O/AA6061-T6 joints. For the tapered smooth pin, the D/d ratios from 2 to 4 in steps of 0.5 were investigated. It was reported that the value equal to 3.5 resulted in the highest UTS, yield strength, and elongation of the produced joints.

Table 8 summarizes the studied results of research on welds from dissimilar materials. Table 8 includes the materials used for advancing and retreating side of the welds, process parameters, welds properties, and the properties of base materials if given by the authors.

**Table 8.** FSW of dissimilar materials—process parameters and mechanical properties of the joints.

Material		Process Parameters						Weld Properties				Reference	
Advancing Side	Retreating Side	Plate Thickness [mm]	v [mm/min]	$\omega$ [rpm]	Tool Shape	Pin D/d Ratio	Tilt Angle [°]	UTS [MPa]	Yield Strength [MPa]	Hardness of the Stir Zone [HV]	Elongation [%]	Defects	Reference
AA2024-T3	AA7075-T6	3	102	1200	Cylindrical threaded pin	3	-	423 (416 for AA2024-T3 and 593 for AA7075-T6)	290.0 (327 for AA2024-T3 and 498 for AA7075-T6)	14.9 (29.5 for AA2024-T3 and 17.7 for AA7075-T6)	-	-	[244]
AA2024-T6	AA7075-T6	5	12	1200	Flat shoulder and smooth cylindrical pin	3	-	356 (416 for AA2024-T6 and 485 for AA7075-T6)	-	-	-	Defect free	[116]
AA5052	AA6061	-	28	710	Cylindrical pin with two threads	3	-	180	-	82	10.6	-	[248]
AA5083	AA6082	3	300	840	Conical surface of the shoulder, threaded cylindrical pin	3	2	241	-	-	3.05	-	[243]
AA5086-O	AA6061-T6	5	150	840	Tapered pin with 3 threads and concave shoulder surface	3.3	-	221 (253 for AA5086-O; 315 for AA6061-T6)	136 (112 for AA5086-O; 278 for AA6061-T6)	-	-	-	[31]
AA6061-T6	AA5086-O	5	150	840	Tapered pin with 3 threads and concave shoulder surface	3.3	-	224 (315 for AA6061-T6; 253 for AA5086-O)	139 (278 for AA6061-T6; 112 for AA5086-O)	-	-	-	[31]
AA6082	AA5083	3	200	840	Conical surface of the shoulder, threaded cylindrical pin	3	2	227	-	-	2.67	-	[243]
AA6351-T6	AA5083-H111	6	60	950	Flat shoulder surface, straight square pin with no threads	3	0	273 (AA6351-T6; 310 for AA5083H111; 308)	-	-	-	No defects	[246]
AA7075-T6	AA2024-T3	6.5 (AA7075-T6); 5 (AA2024-T3)	80	1400	Square pin	-	-	261	-	-	-	Defect-free	[245]
AA7075-T6	AA2024-T3	3	102	1200	Cylindrical threaded pin	3	-	381 (593 for AA7075-T6 and 416 for AA2024-T3)	280.0 (498 for AA7075-T6 and 327 for AA2024-T3)	9.0 (17.7 for AA7075-T6 and 29.5 for AA2024-T3)	-	-	[244]

Table 8. Cont.

Material		Process Parameters				Weld Properties				Reference			
Advancing Side	Retreating Side	Plate Thickness [mm]	v [mm/min]	$\omega$ [rpm]	Tool Shape	Pin D/d Ratio	Tilt Angle [°]	UTS [MPa]	Yield Strength [MPa]	Hardness of the Stir Zone [HV]	Elongation [%]	Defects	Reference
S137	304 austenitic stainless steel	3	50	600	-	2.9	3	494 (446 for S137 and 679 for 304 steel)	290 (305 for S137 and 287 for 304 steel)	240 (120 for S137 and 180 for 304 steel)	28 (42 for S137 and 111 for 304 steel)	No macro defects	[249]
S152 mild steel	AA5186	3	56	355	M3 threaded pin	6	3	246 (520 for AA5186)	-	-	-	No defects	[250]
Low carbon steel	Pure Mg	2	100	1000	Cylindrical with no threads	3	3	~70 (316 for low carbon steel and 170 for pure Mg)	-	-	-	-	[242]
Low carbon steel	AZ31	2	100	500	Cylindrical with no threads	3	3	~165 (316 for low carbon steel and 260 for AZ31)	-	-	-	-	[242]
Low carbon steel	AZ61	2	100	750	Cylindrical with no threads	3	3	~220 (316 for low carbon steel and 280 for AZ61)	-	-	-	-	[242]
AZ31	AA6040-T61	2	225	1400	Threaded tapered pin	2.6	2.5	189 (228-238 for AZ31 and 175-205 for AA6040-T61)	-	-	-	-	[241]
AA6040-T61	AZ31	2	200	1400	Threaded tapered pin	2.6	2.5	127 (175-205 for AA6040-T61 and 228-238 for AZ31)	-	-	-	-	[241]
AA5052-H	AZ31B	3	200	1000	-	3	3	147 (244 for AA5052-H and 241 for AZ31B)	64.0 (181 for AA5052-H and 200 for AZ31B)	-	3.4 (18.0 for AA5052-H and 21.6 for AZ31B)	No defects	[251]
AA6061	AZ31	3	40	1000	Concave shoulder and cylindrical pin	5	2.5	178 (295 for 6061 Al and 235 for AZ31)	170 (235 for 6061 Al and 130 for AZ31)	-	2.4 (12.5 for 6061 Al and 18.7 for AZ31)	Defect free	[252]
AZ31B-0	AA6061-T6	6	20	400	Tapered smooth pin	3.5	-	192 (216 for AZ31B-0 and 311 for AA6061-T6)	153 (175 for AZ31B-0 and 280 for AA6061-T6)	-	10 (15 for AZ31B-0 and 20 for AA6061-T6)	Defect free	[247]

Table 8. Cont.

Material		Process Parameters					Weld Properties						
Advancing Side	Retreating Side	Plate Thickness [mm]	v [mm/min]	$\omega$ [rpm]	Tool Shape	Pin D/d Ratio	Tilt Angle [°]	UTS [MPa]	Yield Strength [MPa]	Hardness of the Stir Zone [HV]	Elongation [%]	Defects	Reference
AZ31B	AA1100	3	20	570	Cylindrical threaded pin	3.6	-	122 (228 for AZ31B; 175 AA1100)	101 (145 AZ31B; 105 AA1100)	-	9 (17 AZ31B; 11 AA1100)	-	[253]
SS400 mild steel	AZ31B-O	2	100	1250	Unthreaded cylindrical pin	5	-	178.5 (455 for SS400; 257 AZ31B-O)	-	-	~2.7 (39 for SS400 and 23.3 for AZ31B-O)	-	[254]
304L stainless steel	Pure Cu	3	31.5	1500	Taper pin	-	2	173.05 (574 for 304L; 227 for copper)	-	-	8.22 (51 for 304L; 23 for copper)	-	[255]
Pure Cu	AA1050	6	63	1400	-	-	-	88.466 (91% of AA1050)	-	-	-	-	[256]
Pure Cu	AA1060	5	100	600	Cylindrical pin	~3.3	-	110	-	-	-	Defect free	[257]

## 11. Conclusions and Future Challenges

Over the past two decades, FSW technology has developed significantly, and it is widely used to combine not only aluminum and other light metals but also titanium, steel, composites, and polymers. The above literature review has extensively discussed the current state of knowledge and addressed the most common problems arising in the process of welding different groups of materials. The analysis of material characteristics and the correct selection of parameters for a particular material is crucial for effective welding.

Despite numerous studies on the selection of suitable process parameters such as tool traverse speed and tool rotational speed, tool geometry, tilt angle, and tool offset, there is still a need for process optimization. It should not be forgotten that in addition to the main process parameters, consideration should be given to factors such as plunged depth, axial force, and tool material. In addition, the material flow mechanism needs to be standardized, especially when welding dissimilar materials with different mechanical properties. Optimization of process parameters should be based on the characteristics of the materials being processed. Appropriate tool geometry and its material selection should also be preceded by a material analysis. In the case of aluminum or copper welding, the problem of material wear is not as important as in the case of titanium or steel. For these materials, specially designed materials are used, most often composite materials, which allow minimizing the process of material wear. Titanium welding requires a tool with an uncomplicated geometry, while for light alloys, a more developed tool geometry is required. SSFSW technology is becoming increasingly important for polymer welding, while traditional FSW technique might be problematic with a conventional tool, it usually does not bring the expected results, and the properties of the welds are relatively low. Despite extensive knowledge of the welding of aluminum and its alloys, the problem of the welding of dissimilar materials still remains. The most recent reports indicate the use of an interlayer or water environment to minimize the risk of unwanted intermetallic compounds.

The environmental friendliness and cost-effectiveness of this method make its use increasingly widespread in many industries, but further work is needed to optimise this process to unify the conclusions about the impact of individual parameters on the properties of the resulting welds. It is also necessary to work on further improving the geometry of the tool and the proper selection of its material in order to minimize the wear process. For the development of friction stir welding technique, it is important to control tool wear state in the real time of the process in order to ensure the highest possible process repeatability. The tool life can be effectively predicted by implementing the numerical simulation of the interaction between the component's material and the tool. The material flow is the crucial phenomenon during FSW, and it still requires more understanding. There is a need for concerted research efforts towards the computer simulations of the process, which will help develop understanding of the mechanism of material flow and heat generation. Due to the wide application of FSW technology in the marine industry, special attention should be paid to the electrochemical properties of the produced welds. The current state of the art is poor in this type of research. Future studies should focus on the influence of particular process parameters not only on the mechanical properties of welds intended for the marine industry, but also on their corrosion properties.

**Author Contributions:** Conceptualization: A.L. and M.S.; formal analysis: M.S.; investigation: A.L.; writing—original draft preparation: A.L. All authors have read and agreed to the published version of the manuscript.

**Funding:** This research received no external funding.

**Conflicts of Interest:** The authors declare no conflict of interest.

## References

1. Arunprasad, R.V.; Surendhiran, G.; Ragul, M.; Soundararajan, T.; Moutheepan, S.; Boopathi, S. Review on Friction Stir Welding Process. *Int. J. Appl. Eng. Res. ISSN* **2018**, *13*, 5750–5758.

2. Kossakowski, P.; Wciślik, W.; Bakalarz, M. Macrostructural Analysis of Friction Stir Welding (FSW) Joints. *J. Chem. Inf. Model.* **2018**, *1*, 1689–1699. [CrossRef]
3. Kah, P.; Rajan, R.; Martikainen, J.; Suoranta, R. Investigation of weld defects in friction-stir welding and fusion welding of aluminum alloys. *Int. J. Mech. Mater. Eng.* **2015**, *10*, 26. [CrossRef]
4. Safeen, M.W.; Spena, P.R. Main issues in quality of friction stir welding joints of aluminum alloy and steel sheets. *Metals* **2019**, *9*, 610. [CrossRef]
5. Pasha, A.; Reddy, R.P.; Ahmad Khan, I. Influence of Process and Tool Parameters on Friction Stir Welding—Overview. *Int. J. Appl. Eng. Technol.* **2014**, *4*, 54–69.
6. Sato, Y.S.; Urata, M.; Kokawa, H. Parameters controlling microstructure and hardness during friction-stir welding of precipitation-hardenable aluminum alloy 6063. *Metall. Mater. Trans. A* **2002**, *33*, 625–635. [CrossRef]
7. Colligan, K.J. *The Friction Stir Welding Process: An Overview*; Woodhead Publishing Limited: Cambridge, UK, 2009.
8. Raweni, A.; Majstorović, V.; Sedmak, A.; Tadić, S.; Kirin, S. Optimization of AA5083 friction stir welding parameters using taguchi method. *Teh. Vjesn.* **2018**, *25*, 861–866. [CrossRef]
9. Micari, F.; Buffa, G.; Pellegrino, S.; Fratini, L. Friction Stir Welding as an effective alternative technique for light structural alloys mixed joints. *Procedia Eng.* **2014**, *81*, 74–83. [CrossRef]
10. Nandan, R.; DebRoy, T.; Bhadeshia, H.K.D.H. Recent advances in friction-stir welding—Process, weldment structure and properties. *Prog. Mater. Sci.* **2008**, *53*, 980–1023. [CrossRef]
11. Wang, W.; Deng, D.; Mao, Z.; Tong, Y.; Ran, Y. Influence of tool rotation rates on temperature profiles and mechanical properties of friction stir welded AZ31 magnesium alloy. *Int. J. Adv. Manuf. Technol.* **2017**, *88*, 2191–2200. [CrossRef]
12. Mishra, A. Friction Stir Welding of Aerospace Alloys. *Int. J. Res. Appl. Sci. Eng. Technol.* **2019**, *7*, 863–870. [CrossRef]
13. Singh, I.; Cheema, G.S.; Kang, A.S. An experimental approach to study the effect of welding parameters on similar friction stir welded joints of AZ31B-O Mg alloy. *Procedia Eng.* **2014**, *97*, 837–846. [CrossRef]
14. Gesella, G.; Czechowski, M. The application of friction stir welding (FSW) of aluminum alloys in shipbuilding and railway industry. *J. KONES* **2017**, *24*, 85–90. [CrossRef]
15. Kawasaki, T.; Makino, T.; Masai, K.; Ohba, H.; Ina, Y.; Ezumi, M. Application of friction stir welding to construction of railway vehicles. *JSME Int. J. Ser. A Solid Mech. Mater. Eng.* **2004**, *47*, 502–511. [CrossRef]
16. Singh, K.; Singh, G.; Singh, H. Investigation of microstructure and mechanical properties of friction stir welded AZ61 magnesium alloy joint. *J. Magnes. Alloy.* **2018**, *6*, 292–298. [CrossRef]
17. Sevel, P.; Jaiganesh, V. An detailed examination on the future prospects of friction stir welding—a green technology. In Proceedings of the Second International Conference on Advances in Industrial Engineering Applications (ICAIEA 2014), Chennai, India, 6–8 January 2014; pp. 275–280.
18. Grimm, A.; Schulze, S.; Silva, A.; Göbel, G.; Standfuss, J.; Brenner, B.; Beyer, E.; Füssel, U. Friction Stir welding of Light Metals for Industrial Applications. *Mater. Today Proc.* **2015**, *2*, S169–S178. [CrossRef]
19. Singarapu, U.; Adepu, K.; Arumalle, S.R. Influence of tool material and rotational speed on mechanical properties of friction stir welded AZ31B magnesium alloy. *J. Magnes. Alloy.* **2015**, *3*, 335–344. [CrossRef]
20. Magalhães, V.M.; Leitão, C.; Rodrigues, D.M. Friction stir welding industrialisation and research status. *Sci. Technol. Weld. Join.* **2018**, *23*, 400–409. [CrossRef]
21. Rhodes, C.G.; Mahoney, M.W.; Bingel, W.H.; Spurling, R.A.; Bampton, C.C. Effects of friction stir welding on microstructure of 7075 aluminum. *Scr. Mater.* **1997**, *36*, 69–75. [CrossRef]
22. Liu, G.; Murr, L.E.; Niou, C.S.; McClure, J.C.; Vega, F.R. Microstructural aspects of the friction-stir welding of 6061-T6 aluminum. *Scr. Mater.* **1997**, *37*, 355–361. [CrossRef]
23. Sato, Y.; Kokawa, H.; Enomoto, M.; Jogan, S. Microstructural evolution of 6063 aluminum during friction-stir welding. *Metall. Mater. Trans. A Phys. Metall. Mater. Sci.* **1999**, *30*, 2429–2437. [CrossRef]
24. Jata, K.V.; Sankaran, K.K.; Ruschau, J.J. Friction-stir welding effects on microstructure and fatigue of aluminum alloy 7050-T7451. *Metall. Mater. Trans. A Phys. Metall. Mater. Sci.* **2000**, *31*, 2181–2192. [CrossRef]
25. Heinz, B.; Skrotzki, B. Characterization of a friction-stir-welded aluminum alloy 6013. *Metall. Mater. Trans. B Process Metall. Mater. Process. Sci.* **2002**, *33*, 489–498. [CrossRef]
26. Colligan, K.J. *Failure Mechanisms of Advanced Welding Processes*; Woodhead Publishing Limited: Cambridge, UK, 2010; pp. 137–163.



27. Woo, W.; Balogh, L.; Ungár, T.; Choo, H.; Feng, Z. Grain structure and dislocation density measurements in a friction-stir welded aluminum alloy using X-ray peak profile analysis. *Mater. Sci. Eng. A* **2008**, *498*, 308–313. [CrossRef]
28. Tasi, P.; Hajro, I.; Hodži, D.; Dobraš, D. Energy Efficient Welding Technology: Fsw. In Proceedings of the 11th International Conference on Accomplishments in Electrical and Mechanical Engineering and Information Technology, 30 May–1 June 2013; pp. 429–442.
29. Sivaraj, P.; Kanagarajan, D.; Balasubramanian, V. Effect of post weld heat treatment on tensile properties and microstructure characteristics of friction stir welded armour grade AA7075-T651 aluminum alloy. *Def. Technol.* **2014**, *10*, 1–8. [CrossRef]
30. Surendrababu, P.; Gopala Krishna, A.; Srinivasa Rao, C. Material Flow Behaviour in Friction Stir Welding Process-A Critical Review on Process Parameters and Modeling Methodologies. *Int. J. Emerg. Technol. Adv. Eng.* **2013**, *3*, 219–225.
31. Jamshidi Aval, H.; Serajzadeh, S.; Kokabi, A.H. Evolution of microstructures and mechanical properties in similar and dissimilar friction stir welding of AA5086 and AA6061. *Mater. Sci. Eng. A* **2011**, *528*, 8071–8083. [CrossRef]
32. Mishra, R.S.; Ma, Z.Y. Friction Stir Welding and Processing. *Mater. Sci. Eng.: R: Rep.* **2005**, *50*, 1–78. [CrossRef]
33. Hussain, A.K.; Azam, S.; Quadri, P. Evaluation of Parameters of Friction Stir Welding for Aluminum Aa6351 Alloy. *Int. J. Eng. Sci. Technol.* **2010**, *2*, 5977–5984.
34. Patel, A.R.; Kotadiya, D.J.; Kapopara, J.M.; Dalwadi, C.G.; Patel, N.P.; Rana, H.G. Investigation of Mechanical Properties for Hybrid Joint of Aluminum to Polymer using Friction Stir Welding (FSW). *Mater. Today Proc.* **2018**, *5*, 4242–4249. [CrossRef]
35. Liu, F.C.; Liao, J.; Nakata, K. Joining of metal to plastic using friction lap welding. *Mater. Des.* **2014**, *54*, 236–244. [CrossRef]
36. Patel, A.R.; Dalwadi, C.G.; Rana, H.G. A Review: Dissimilar Material Joining of Metal to Polymer using Friction Stir Welding (FSW). *IJSTE-Int. J. Sci. Technol. Eng.* **2016**, *2*, 702–706.
37. Murr, L.E.; Li, Y.; Trillo, E.; McClure, J.C. Fundamental Issues and Industrial Applications of Friction-Stir Welding. *Mater. Technol.* **2000**, *15*, 37–48. [CrossRef]
38. Threadgill, P.L.; Johnson, R. The Potential for Friction Stir Welding in Oil and Gas Applications. In Proceedings of the Fourteenth International Offshore Polar Engineering Conference, Toulon, France, 23–28 May 2004.
39. Shtrikman, M.M. Current state and development of friction stir welding Part 3. Industrial application of friction stir welding. *Weld. Int.* **2008**, *22*, 806–815. [CrossRef]
40. Thomas, W.M.; Nicholas, E.D. Friction stir welding for the transportation industries. *Mater. Des.* **1997**, *18*, 269–273. [CrossRef]
41. Tang, W.; Guo, X.; McClure, J.C.; Murr, L.E.; Nunes, A. Heat input and temperature distribution in friction stir welding. *J. Mater. Process. Manuf. Sci.* **1998**, *7*, 163–172. [CrossRef]
42. Mahoney, M.W.; Rhodes, C.G.; Flintoff, J.G.; Spurling, R.A.; Bingel, W.H. Properties of friction-stir-welded 7075 T651 aluminum. *Metall. Mater. Trans. A Phys. Metall. Mater. Sci.* **1998**, *29*, 1955–1964. [CrossRef]
43. Reynolds, A.P.; Lockwood, W.D.; Seidel, T.U. Processing-property correlation in friction stir welds. *Mater. Sci. Forum* **2000**, *331*, 1719–1724. [CrossRef]
44. Colegrove, P.A.; Shercliff, H.R. Experimental and numerical analysis of aluminum alloy 7075-T7351 friction stir welds. *Sci. Technol. Weld. Join.* **2003**, *8*, 360–368. [CrossRef]
45. Sato, Y.S.; Kokawa, H.; Ikeda, K.; Enomoto, M.; Jogan, S.; Hashimoto, T. Microtexture in the friction-stir weld of an aluminum alloy. *Metall. Mater. Trans. A Phys. Metall. Mater. Sci.* **2001**, *32*, 941–948. [CrossRef]
46. Krasnowski, K.; Sedek, P.; Lomozik, M.; Pietras, A. Impact of selected FSW process parameters on mechanical properties of 6082-T6 aluminum alloy butt joints. *Arch. Metall. Mater.* **2011**, *56*, 965–973. [CrossRef]
47. Srinivasa Rao, M.S.; Ravi Kumar, B.V.R.; Manzoor Hussain, M. Experimental study on the effect of welding parameters and tool pin profiles on the IS:65032 aluminum alloy FSW joints. *Mater. Today Proc.* **2017**, *4*, 1394–1404. [CrossRef]
48. Emamian, S.; Awang, M.; Hussai, P.; Meyghani, B.; Zafar, A. Influences of tool pin profile on the friction stir welding of AA6061. *ARPN J. Eng. Appl. Sci.* **2016**, *11*, 12258–12261.
49. Rajendran, C.; Srinivasan, K.; Balasubramanian, V.; Balaji, H.; Selvaraj, P. Effect of tool tilt angle on strength and microstructural characteristics of friction stir welded lap joints of AA2014-T6 aluminum alloy. *Trans. Nonferrous Met. Soc. China* **2019**, *29*, 1824–1835. [CrossRef]

50. Barlas, Z.; Ozsarac, U. Effects of FSW parameters on joint properties of AlMg3 Alloy. *Weld. J.* **2012**, *91*, 16S–22S.
51. Peel, M.; Steuwer, A.; Preuss, M.; Withers, P.J. Microstructure, mechanical properties and residual stresses as a function of welding speed in aluminum AA5083 friction stir welds. *Acta Mater.* **2003**, *51*, 4791–4801. [CrossRef]
52. Khan, N.Z.; Khan, Z.A.; Siddiquee, A.N. Effect of Shoulder Diameter to Pin Diameter (D/d) Ratio on Tensile Strength of Friction Stir Welded 6063 Aluminum Alloy. *Mater. Today Proc.* **2015**, *2*, 1450–1457. [CrossRef]
53. Peng, P.; Wang, K.; Wang, W.; Huang, L.; Qiao, K.; Che, Q.; Xi, X.; Zhang, B.; Cai, J. High-performance aluminum foam sandwich prepared through friction stir welding. *Mater. Lett.* **2019**, *236*, 295–298. [CrossRef]
54. Basic, M.; Kozuh, Z.; Klobcar, D.; Samardzic, I. Friction Stir Welding (FSW) of Aluminum Foam Sandwich Panels. *Metallurgija* **2016**, *55*, 473–476.
55. Yoo, J.T.; Yoon, J.H.; Min, K.J.; Lee, H.S. Effect of Friction Stir Welding Process Parameters on Mechanical Properties and Macro Structure of Al-Li Alloy. *Procedia Manuf.* **2015**, *2*, 325–330. [CrossRef]
56. Lim, S.; Kim, S.; Lee, C.G.; Kim, S. Tensile behavior of friction-stir-welded A356-T6/Al 6061-T651 bi-alloy plate. *Metall. Mater. Trans. A Phys. Metall. Mater. Sci.* **2004**, *35*, 2837–2843. [CrossRef]
57. Sayer, S.; Ceyhan, V.; Tezcan, Ö. The influence of friction stir welding parameters on the mechanical properties and low cycle fatigue in AA 6063 (AlMgSi0.5) alloy. *Kov. Mater.* **2008**, *46*, 157–164.
58. Sato, Y.S.; Kokawa, H. Distribution of tensile property and microstructure in friction stir weld of 6063 aluminum. *Metall. Mater. Trans. A Phys. Metall. Mater. Sci.* **2001**, *32*, 3023–3031. [CrossRef]
59. Boonchouytan, W.; Ratanawilai, T.; Muangjunburee, P. Effect of pre/post heat treatment on the friction stir welded SSM 356 aluminum alloys. *Adv. Mater. Res.* **2012**, *32*, 1139–1146. [CrossRef]
60. Çam, G. Friction stir welded structural materials: Beyond Al-alloys. *Int. Mater. Rev.* **2011**, *56*, 1–48. [CrossRef]
61. Singh, K.; Singh, G.; Singh, H. Review on friction stir welding of magnesium alloys. *J. Magnes. Alloy.* **2018**, *6*, 399–416. [CrossRef]
62. Dargusch, M.S.; Bowles, A.L.; Pettersen, K.; Bakke, P.; Dunlop, G.L. The effect of silicon content on the microstructure and creep behavior in die-cast magnesium AS alloys. *Metall. Mater. Trans. A Phys. Metall. Mater. Sci.* **2004**, *35*, 1905–1909. [CrossRef]
63. You, S.; Huang, Y.; Kainer, K.U.; Hort, N. Recent research and developments on wrought magnesium alloys. *J. Magnes. Alloy.* **2017**, *5*, 239–253. [CrossRef]
64. Froes, F.H.; Eliezer, D.; Aghion, E. The Science, Technology, and Applications of Magnesium. *J. Miner. Met. Mater. Soc.* **1998**, *50*, 30–34. [CrossRef]
65. Xin, R.; Liu, D.; Li, B.; Sun, L.; Zhou, Z.; Liu, Q. Mechanisms of fracture and inhomogeneous deformation on transverse tensile test of friction-stir-processed AZ31 Mg alloy. *Mater. Sci. Eng. A* **2013**, *565*, 333–341. [CrossRef]
66. Shang, Q.; Ni, D.R.; Xue, P.; Xiao, B.L.; Ma, Z.Y. Evolution of local texture and its effect on mechanical properties and fracture behavior of friction stir welded joint of extruded Mg-3Al-1Zn alloy. *Mater. Charact.* **2017**, *128*, 14–22. [CrossRef]
67. Yang, J.; Xiao, B.L.; Wang, D.; Ma, Z.Y. Effects of heat input on tensile properties and fracture behavior of friction stir welded Mg-3Al-1Zn alloy. *Mater. Sci. Eng. A* **2010**, *527*, 708–714. [CrossRef]
68. Commin, L.; Dumont, M.; Rotinat, R.; Pierron, F.; Masse, J.E.; Barrallier, L. Influence of the microstructural changes and induced residual stresses on tensile properties of wrought magnesium alloy friction stir welds. *Mater. Sci. Eng. A* **2012**, *551*, 288–292. [CrossRef]
69. Lim, S.; Kim, S.; Lee, C.G.; Yim, C.D.; Kim, S.J. Tensile behavior of friction-stir-welded AZ31-H24 Mg alloy. *Metall. Mater. Trans. A Phys. Metall. Mater. Sci.* **2005**, *36*, 1609–1612. [CrossRef]
70. Lee, W.B.; Yeon, Y.M.; Jung, S.B. Joint properties of friction stir welded AZ31B-H24 magnesium alloy. *Mater. Sci. Technol.* **2003**, *19*, 785–790. [CrossRef]
71. Kumar, R.; Pragash, M.S.; Varghese, S. Optimizing the process parameters of FSW on AZ31B Mg alloy by Taguchi-grey method. *Middle East J. Sci. Res.* **2013**, *15*, 161–167. [CrossRef]
72. Han, J.; Chen, J.; Peng, L.; Tan, S.; Wu, Y.; Zheng, F.; Yi, H. Microstructure, texture and mechanical properties of friction stir processed Mg-14Gd alloys. *Mater. Des.* **2017**, *130*, 90–102. [CrossRef]
73. Sahu, P.K.; Pal, S. Effect of FSW parameters on microstructure and mechanical properties of AM20 welds. *Mater. Manuf. Process.* **2018**, *33*, 288–298. [CrossRef]
74. Sevvel, P.; Jaiganesh, V. Characterization of mechanical properties and microstructural analysis of friction stir welded AZ31B Mg alloy thorough optimized process parameters. *Procedia Eng.* **2014**, *97*, 741–751. [CrossRef]

75. Pareek, M.; Polar, A.; Rumiche, F.; Indacochea, J.E. Metallurgical evaluation of AZ31B-H24 magnesium alloy friction stir welds. *J. Mater. Eng. Perform.* **2007**, *16*, 655–662. [CrossRef]
76. Esparza, J.A.; Davis, W.C.; Murr, L.E. Microstructure-property studies in friction-stir welded, thixomolded magnesium alloy AM60. *J. Mater. Sci.* **2003**, *38*, 941–952. [CrossRef]
77. Park, S.H.C.; Sato, Y.S.; Kokawa, H. Effect of micro-texture on fracture location in friction stir weld of Mg alloy AZ61 during tensile test. *Scr. Mater.* **2003**, *49*, 161–166. [CrossRef]
78. Xie, G.M.; Ma, Z.Y.; Geng, L.; Chen, R.S. Microstructural evolution and mechanical properties of friction stir welded Mg-Zn-Y-Zr alloy. *Mater. Sci. Eng. A* **2007**, *471*, 63–68. [CrossRef]
79. Zhang, D.; Suzuki, M.; Maruyama, K. Microstructural evolution of a heat-resistant magnesium alloy due to friction stir welding. *Scr. Mater.* **2005**, *52*, 899–903. [CrossRef]
80. Xunhong, W.; Kuaishu, W. Microstructure and properties of friction stir butt-welded AZ31 magnesium alloy. *Mater. Sci. Eng. A* **2006**, *431*, 114–117. [CrossRef]
81. Ugender, S.; Kumar, A.; Reddy, A.S. Microstructure and Mechanical Properties of AZ31B Magnesium Alloy by Friction Stir Welding. *Procedia Mater. Sci.* **2014**, *6*, 1600–1609. [CrossRef]
82. Padmanaban, G.; Balasubramanian, V. Selection of FSW tool pin profile, shoulder diameter and material for joining AZ31B magnesium alloy-An experimental approach. *Mater. Des.* **2009**, *30*, 2647–2656. [CrossRef]
83. Afrin, N.; Chen, D.L.; Cao, X.; Jahazi, M. Strain hardening behavior of a friction stir welded magnesium alloy. *Scr. Mater.* **2007**, *57*, 1004–1007. [CrossRef]
84. Patel, N.; Bhatt, K.D.; Mehta, V. Influence of Tool Pin Profile and Welding Parameter on Tensile Strength of Magnesium Alloy AZ91 During FSW. *Procedia Technol.* **2016**, *23*, 558–565. [CrossRef]
85. Chai, F.; Zhang, D.; Li, Y. Microstructures and tensile properties of submerged friction stir processed AZ91 magnesium alloy. *J. Magnes. Alloy.* **2015**, *3*, 203–209. [CrossRef]
86. Kadigithala, N.K.; Vanitha, C. Effects of welding speeds on the microstructural and mechanical properties of AZ91D Mg alloy by friction stir welding. *Int. J. Struct. Integr.* **2020**, *11*, 769–782. [CrossRef]
87. Kouadri-Henni, A.; Barrallier, L. Mechanical properties, microstructure and crystallographic texture of magnesium AZ91-D alloy welded by friction stir welding (FSW). *Metall. Mater. Trans. A Phys. Metall. Mater. Sci.* **2014**, *45*, 4983–4996. [CrossRef]
88. Wang, K.S.; Shen, Y.; Yang, X.R.; Wang, X.H.; Xu, K.W. Evaluation of Microstructure and Mechanical Property of FSW Welded MB3 Magnesium Alloy. *J. Iron Steel Res. Int.* **2006**, *13*, 75–78. [CrossRef]
89. Weng, F.; Liu, Y.; Chew, Y.; Lee, B.Y.; Ng, F.L.; Bi, G. Double-side friction stir welding of thick magnesium alloy: Microstructure and mechanical properties. *Sci. Technol. Weld. Join.* **2020**, *25*, 359–368. [CrossRef]
90. Reynolds, A.P.; Tang, W.; Posada, M.; DeLoach, J. Friction stir welding of DH36 steel. *Sci. Technol. Weld. Join.* **2003**, *8*, 455–461. [CrossRef]
91. Sorensen, C.; Nelson, T. Friction stir welding of ferrous and nickel alloys. *Fri. Stir Weld. Process.* **2007**, 111–121. Available online: [https://www.researchgate.net/publication/267856005\\_Friction\\_Stir\\_Welding\\_of\\_Ferrous\\_and\\_Nickel\\_Alloys](https://www.researchgate.net/publication/267856005_Friction_Stir_Welding_of_Ferrous_and_Nickel_Alloys) (accessed on 17 February 2020).
92. Perrett, J.; Martin, J.; Peterson, J.; Steel, R.; Packer, S. *Friction Stir Welding of Industrial Steels*; The Minerals, Metals & Materials Society: Pittsburgh, PA, USA, 2011; pp. 65–72.
93. Cater, S.; Martin, J.; Galloway, A.; McPherson, N. Comparison between Friction Stir and Submerged Arc Welding Applied to Joining DH36 and E36 Shipbuilding Steel. In *Friction Stir Welding and Processing VII*; Springer Nature: Berlin, Germany, 2013; pp. 49–58.
94. Thomas, W.M.; Threadgill, P.L.; Nicholas, E.D. Feasibility of friction stir welding steel. *Sci. Technol. Weld. Join.* **1999**, *4*, 365–372. [CrossRef]
95. Lienert, T.J.; Lippold, J.C. Improved weldability diagram for pulsed laser welded austenitic stainless steels. *Sci. Technol. Weld. Join.* **2003**, *8*, 1–9. [CrossRef]
96. Fujii, H.; Cui, L.; Tsuji, N.; Maeda, M.; Nakata, K.; Nogi, K. Friction stir welding of carbon steels. *Mater. Sci. Eng. A* **2006**, *429*, 50–57. [CrossRef]
97. Cui, L.; Fujii, H.; Tsuji, N.; Nogi, K. Friction stir welding of a high carbon steel. *Scr. Mater.* **2007**, *56*, 637–640. [CrossRef]
98. Saeid, T.; Abdollah-zadeh, A.; Assadi, H.; Malek Ghaini, F. Effect of friction stir welding speed on the microstructure and mechanical properties of a duplex stainless steel. *Mater. Sci. Eng. A* **2008**, *496*, 262–268. [CrossRef]

99. Ghosh, M.; Kumar, K.; Mishra, R.S. Analysis of microstructural evolution during friction stir welding of ultrahigh-strength steel. *Scr. Mater.* **2010**, *63*, 851–854. [CrossRef]
100. Miura, T.; Ueji, R.; Fujii, H.; Komine, H.; Yanagimoto, J. Phase transformation behavior of Cr-Mo steel during FSW. *Mater. Des.* **2016**, *90*, 915–921. [CrossRef]
101. Fujii, H.; Ueji, R.; Morisada, Y.; Tanigawa, H. High strength and ductility of friction-stir-welded steel joints due to mechanically stabilized metastable austenite. *Scr. Mater.* **2014**, *70*, 39–42. [CrossRef]
102. Mahoney, M.; Nelson, T.; Sorenson, C.; Packer, S. Friction stir welding of ferrous alloys: Current status. *Mater. Sci. Forum* **2010**, *638–642*, 41–46. [CrossRef]
103. Miura, T.; Ueji, R.; Morisada, Y.; Fujii, H. Enhanced tensile properties of Fe-Ni-C steel resulting from stabilization of austenite by friction stir welding. *J. Mater. Process. Technol.* **2015**, *216*, 216–222. [CrossRef]
104. Fujii, H.; Cui, L.; Nakata, K.; Nogi, K. Mechanical properties of friction stir welded carbon steel joints-Friction stir welding with and without transformation. *Weld. World* **2008**, *52*, 75–81. [CrossRef]
105. Meshram, M.P.; Kodli, B.K.; Dey, S.R. Mechanical Properties and Microstructural Characterization of Friction Stir Welded AISI 316 Austenitic Stainless Steel. *Procedia Mater. Sci.* **2014**, *5*, 2376–2381. [CrossRef]
106. Maltin, C.A.; Nolton, L.J.; Scott, J.L.; Toumpis, A.I.; Galloway, A.M. The potential adaptation of stationary shoulder friction stir welding technology to steel. *Mater. Des.* **2014**, *64*, 614–624. [CrossRef]
107. Bhadeshia, H.K.D.H.; Debroy, T. Critical assessment: Friction stir welding of steels. *Sci. Technol. Weld. Join.* **2009**, *14*, 193–196. [CrossRef]
108. Ragu Nathan, S.; Balasubramanian, V.; Malarvizhi, S.; Rao, A.G. Effect of welding processes on mechanical and microstructural characteristics of high strength low alloy naval grade steel joints. *Def. Technol.* **2015**, *11*, 308–317. [CrossRef]
109. Sabooni, S.; Karimzadeh, F.; Enayati, M.H.; Ngan, A.H.W.; Jabbari, H. *Gas Tungsten arc Welding and Friction Stir Welding of Ultrafine Grained AISI 304L Stainless Steel: Microstructural and Mechanical Behavior Characterization*; Elsevier B.V.: Amsterdam, The Netherlands, 2015; Volume 109, ISBN 8415683111.
110. Meshram, M.P.; Kodli, B.K.; Dey, S.R. Friction Stir Welding of Austenitic Stainless Steel by PCBN Tool and its Joint Analyses. *Procedia Mater. Sci.* **2014**, *6*, 135–139. [CrossRef]
111. Lakshminarayanan, A.K.; Balasubramanian, V.; Salahuddin, M. Microstructure, tensile and impact toughness properties of friction stir welded mild steel. *J. Iron Steel Res. Int.* **2010**, *17*, 68–74. [CrossRef]
112. Li, H.B.; Jiang, Z.H.; Feng, H.; Zhang, S.C.; Li, L.; Han, P.D.; Misra, R.D.K.; Li, J.Z. Microstructure, mechanical and corrosion properties of friction stir welded high nitrogen nickel-free austenitic stainless steel. *Mater. Des.* **2015**, *84*, 291–299. [CrossRef]
113. Wang, D.; Ni, D.R.; Xiao, B.L.; Ma, Z.Y.; Wang, W.; Yang, K. Microstructural evolution and mechanical properties of friction stir welded joint of Fe-Cr-Mn-Mo-N austenite stainless steel. *Mater. Des.* **2014**, *64*, 355–359. [CrossRef]
114. Du, D.; Fu, R.; Li, Y.; Jing, L.; Ren, Y.; Yang, K. Gradient characteristics and strength matching in friction stir welded joints of Fe-18Cr-16Mn-2Mo-0.85N austenitic stainless steel. *Mater. Sci. Eng. A* **2014**, *616*, 246–251. [CrossRef]
115. Kiese, J.; Siemers, C.; Schmidt, C. *A New Class of Oxidation-Resistant, Microstructural-Stabilized and Cold-Workable Titanium Alloys for Exhaust Applications*; The Minerals, Metals & Materials Society: Pittsburgh, PA, USA, 2016; pp. 733–737. ISBN 9781119293668.
116. Saravanan, V.; Rajakumar, S.; Banerjee, N.; Amuthakkannan, R. Effect of shoulder diameter to pin diameter ratio on microstructure and mechanical properties of dissimilar friction stir welded AA2024-T6 and AA7075-T6 aluminum alloy joints. *Int. J. Adv. Manuf. Technol.* **2016**, *87*, 3637–3645. [CrossRef]
117. Vijayavel, P.; Balasubramanian, V.; Sundaram, S. Effect of shoulder diameter to pin diameter (D/d) ratio on tensile strength and ductility of friction stir processed LM25AA-5% SiCp metal matrix composites. *Mater. Des.* **2014**, *57*, 1–9. [CrossRef]
118. Pasta, S.; Reynolds, A.P. Residual stress effects on fatigue crack growth in a Ti-6Al-4V friction stir weld. *Fatigue Fract. Eng. Mater. Struct.* **2008**, *31*, 569–580. [CrossRef]
119. Lee, W.B.; Lee, C.Y.; Chang, W.S.; Yeon, Y.M.; Jung, S.B. Microstructural investigation of friction stir welded pure titanium. *Mater. Lett.* **2005**, *59*, 3315–3318. [CrossRef]
120. Zhang, Y.; Sato, Y.S.; Kokawa, H.; Park, S.H.C.; Hirano, S. Microstructural characteristics and mechanical properties of Ti-6Al-4V friction stir welds. *Mater. Sci. Eng. A* **2008**, *485*, 448–455. [CrossRef]

121. Mironov, S.; Sato, Y.S.; Kokawa, H. Development of grain structure during friction stir welding of pure titanium. *Acta Mater.* **2009**, *57*, 4519–4528. [CrossRef]
122. Knipling, K.E.; Fonda, R.W. Texture development in the stir zone of near- $\alpha$  titanium friction stir welds. *Scr. Mater.* **2009**, *60*, 1097–1100. [CrossRef]
123. Pilchak, A.L.; Juhas, M.C.; Williams, J.C. Microstructural changes due to friction stir processing of investment-cast Ti-6Al-4V. *Metall. Mater. Trans. A Phys. Metall. Mater. Sci.* **2007**, *38*, 401–408. [CrossRef]
124. Rai, R.; De, A.; Bhadeshia, H.K.D.H.; DebRoy, T. Review: Friction stir welding tools. *Sci. Technol. Weld. Join.* **2011**, *16*, 325–342. [CrossRef]
125. Gangwar, K.; Mamidala, R.; Sanders, D.G. Friction stir welding of near  $\alpha$  and  $\alpha + \beta$  titanium alloys: Metallurgical and mechanical characterization. *Metals* **2017**, *7*, 565. [CrossRef]
126. Fonda, R.W.; Bingert, J.F. Texture variations in an aluminum friction stir weld. *Scr. Mater.* **2007**, *57*, 1052–1055. [CrossRef]
127. Gangwar, K.; Ramulu, M. Friction stir welding of titanium alloys: A review. *Mater. Des.* **2018**, *141*, 230–255. [CrossRef]
128. Kulkarni, N.; Ramulu, M. Experimental and Numerical Analysis of Mechanical Behavior in Friction Stir Welded Different Titanium Alloys. In Proceedings of the ASME 2014 International Mechanical Engineering Congress and Exposition, Montreal, QC, Canada, 14–20 November 2014; pp. 1–8.
129. Su, J.; Wang, J.; Mishra, R.S.; Xu, R.; Baumann, J.A. Microstructure and mechanical properties of a friction stir processed Ti-6Al-4V alloy. *Mater. Sci. Eng. A* **2013**, *573*, 67–74. [CrossRef]
130. Mashinini, P.M.; Hattingh, D.G.; Lombard, H. Mechanical Properties and Microstructure of Friction Stir and Laser Beam Welded 3mm Ti6Al4V Alloy. In Proceedings of the World Congress on Engineering, London, UK, 29 June–1 July 2016.
131. Fujii, H.; Sun, Y.; Kato, H.; Nakata, K. Investigation of welding parameter dependent microstructure and mechanical properties in friction stir welded pure Ti joints. *Mater. Sci. Eng. A* **2019**, *527*, 3386–3391. [CrossRef]
132. Edwards, P.; Ramulu, M. Identification of process parameters for friction stir welding Ti-6Al-4V. *J. Eng. Mater. Technol. Trans. ASME* **2010**, *132*, 031006. [CrossRef]
133. Steuwer, A.; Hattingh, D.G.; James, M.N.; Singh, U.; Buslaps, T. Residual stresses, microstructure and tensile properties in Ti-6Al-4V friction stir welds. *Sci. Technol. Weld. Join.* **2012**, *17*, 525–533. [CrossRef]
134. Edwards, P.; Ramulu, M. Fracture toughness and fatigue crack growth in Ti-6Al-4V friction stir welds. *Fatigue Fract. Eng. Mater. Struct.* **2015**, *38*, 970–982. [CrossRef]
135. Liu, H.J.; Zhou, L. Microstructural zones and tensile characteristics of friction stir welded joint of TC4 titanium alloy. *Trans. Nonferrous Met. Soc. China* **2010**, *20*, 1873–1878. [CrossRef]
136. Ebrahimi, M.; Par, M.A. Twenty-year uninterrupted endeavor of friction stir processing by focusing on copper and its alloys. *J. Alloy. Compd.* **2019**, *781*, 1074–1090. [CrossRef]
137. Cederqvist, L.; Sorensen, C.D.; Reynolds, A.P.; Öberg, T. Improved process stability during friction stir welding of 5 cm thick copper canisters through shoulder geometry and parameter studies. *Sci. Technol. Weld. Join.* **2009**, *14*, 178–184. [CrossRef]
138. Cederqvist, L.; Öberg, T. Reliability study of friction stir welded copper canisters containing Sweden's nuclear waste. *Reliab. Eng. Syst. Saf.* **2008**, *93*, 1491–1499. [CrossRef]
139. Cartigueyen, S.; Mahadevan, K. Role of Friction Stir Processing on Copper and Copper based Particle Reinforced Composites—A Review. *J. Mater. Sci. Surf. Eng.* **2015**, *2*, 133–145.
140. Nakata, K. Friction stir welding of copper and copper alloys. *Weld. Int.* **2010**, *55*, 37–41. [CrossRef]
141. Park, H.S.; Kimura, T.; Murakami, T.; Nagano, Y.; Nakata, K.; Ushio, M. Microstructures and mechanical properties of friction stir welds of 60% Cu-40% Zn copper alloy. *Mater. Sci. Eng. A* **2004**, *371*, 160–169. [CrossRef]
142. Çam, G.; Serindağ, H.T.; Çakan, A.; Mistikoglu, S.; Yavuz, H. The effect of weld parameters on friction stir welding of brass plates. *Materwiss. Werksttech.* **2008**, *39*, 394–399. [CrossRef]
143. Machniewicz, T.; Nosal, P.; Korbela, A.; Hebda, M. Effect of FSW Traverse Speed on Mechanical Properties of Copper Plate Joints. *Materials* **2020**, *13*, 1937. [CrossRef]
144. Lee, W.B.; Jung, S.B. The joint properties of copper by friction stir welding. *Mater. Lett.* **2004**, *58*, 1041–1046. [CrossRef]

145. Xue, P.; Xie, G.M.; Xiao, B.L.; Ma, Z.Y.; Geng, L. Effect of heat input conditions on microstructure and mechanical properties of friction-stir-welded pure copper. *Metall. Mater. Trans. A Phys. Metall. Mater. Sci.* **2010**, *41*, 2010–2021. [CrossRef]
146. Khodaverdizadeh, H.; Mahmoudi, A.; Heidarzadeh, A.; Nazari, E. Effect of friction stir welding (FSW) parameters on strain hardening behavior of pure copper joints. *Mater. Des.* **2012**, *35*, 330–334. [CrossRef]
147. Serio, L.M.; Palumbo, D.; De Filippis, L.A.C.; Galietti, U.; Ludovico, A.D. Effect of friction stir process parameters on the mechanical and thermal behavior of 5754-H111 aluminum plates. *Materials* **2016**, *9*, 122. [CrossRef]
148. Costa, J.D.; Ferreira, J.A.M.; Borrego, L.P.; Abreu, L.P. Fatigue behaviour of AA6082 friction stir welds under variable loadings. *Int. J. Fatigue* **2012**, *37*, 8–16. [CrossRef]
149. Salahi, S.; Yapici, G.G. Fatigue Behavior of Friction Stir Welded Joints of Pure Copper with Ultra-fine Grains. *Procedia Mater. Sci.* **2015**, *11*, 74–78. [CrossRef]
150. Surekha, K.; Els-Botes, A. Development of high strength, high conductivity copper by friction stir processing. *Mater. Des.* **2011**, *32*, 911–916. [CrossRef]
151. Liu, H.J.; Shen, J.J.; Huang, Y.X.; Kuang, L.Y.; Liu, C.; Li, C. Effect of tool rotation rate on microstructure and mechanical properties of friction stir welded copper. *Sci. Technol. Weld. Join.* **2009**, *14*, 577–583. [CrossRef]
152. Sahlot, P.; Singh, A.K.; Badheka, V.J.; Arora, A. Friction Stir Welding of Copper: Numerical Modeling and Validation. *Trans. Indian Inst. Met.* **2019**, *72*, 1339–1347. [CrossRef]
153. Xie, G.M.; Ma, Z.Y.; Geng, L. Development of a fine-grained microstructure and the properties of a nugget zone in friction stir welded pure copper. *Scr. Mater.* **2007**, *57*, 73–76. [CrossRef]
154. Cartigueyen, S.; Mahadevan, K. Influence of rotational speed on the formation of friction stir processed zone in pure copper at low-heat input conditions. *J. Manuf. Process.* **2015**, *18*, 124–130. [CrossRef]
155. Cartigueyen, S.; Mahadevan, K. Study of friction stir processed zone under different tool pin profiles in pure copper. *IOSR J. Mech. Civ. Eng.* **2014**, *11*, 6–12. [CrossRef]
156. Ethiraj, N.; Sivabalan, T.; Meikeerthy, S.; Kumar, K.L.V.R.; Chaithanya, G.; Reddy, G.P.K. Comparative study on conventional and underwater friction stir welding of copper plates. In Proceedings of the Int. Conf. Mater. Manuf. Mach. 2019, Sibiu, Romania, 5–7 June 2019; Volume 2128, p. 30003. [CrossRef]
157. Sakthivel, T.; Mukhopadhyay, J. Microstructure and mechanical properties of friction stir welded copper. *J. Mater. Sci.* **2007**, *42*, 8126–8129. [CrossRef]
158. Lin, J.W.; Chang, H.C.; Wu, M.H. Comparison of mechanical properties of pure copper welded using friction stir welding and tungsten inert gas welding. *J. Manuf. Process.* **2014**, *16*, 296–304. [CrossRef]
159. Raju, L.S.; Kumar, A.; Prasad, S.R. Microstructure and mechanical properties of friction stir welded pure copper. *Appl. Mech. Mater.* **2014**, *592–594*, 499–503. [CrossRef]
160. Nagabharam, P.; Srikanth Rao, D.; Manoj Kumar, J.; Gopikrishna, N. Investigation of Mechanical Properties of Friction Stir Welded pure Copper Plates. *Mater. Today Proc.* **2018**, *5*, 1264–1270. [CrossRef]
161. Nia, A.A.; Shirazi, A. Effects of different friction stir welding conditions on the microstructure and mechanical properties of copper plates. *Int. J. Miner. Metall. Mater.* **2016**, *23*, 799–809. [CrossRef]
162. Barmouz, M.; Givi, M.K.B.; Jafari, J. Evaluation of tensile deformation properties of friction stir processed pure copper: Effect of processing parameters and pass number. *J. Mater. Eng. Perform.* **2014**, *23*, 101–107. [CrossRef]
163. Rao, A.N.; Naik, L.S.; Srinivas, C. Evaluation and Impacts of Tool Profile and Rotational Speed on Mechanical Properties of Friction Stir Welded Copper 2200 Alloy. *Mater. Today Proc.* **2017**, *4*, 1225–1229. [CrossRef]
164. Gao, J.; Shen, Y.; Zhang, J.; Xu, H. Submerged friction stir weld of polyethylene sheets. *J. Appl. Polym. Sci.* **2014**, *131*, 1–8. [CrossRef]
165. Arici, A.; Sinmaz, T. Effects of double passes of the tool on friction stir welding of polyethylene. *J. Mater. Sci.* **2005**, *40*, 3313–3316. [CrossRef]
166. Bozkurt, Y. The optimization of friction stir welding process parameters to achieve maximum tensile strength in polyethylene sheets. *Mater. Des.* **2012**, *35*, 440–445. [CrossRef]
167. Aydin, M. Effects of welding parameters and pre-heating on the friction stir welding of UHMW-polyethylene. *Polym.-Plast. Technol. Eng.* **2010**, *49*, 595–601. [CrossRef]
168. Mostafapour, A.; Azarsa, E. A study on the role of processing parameters in joining polyethylene sheets via heat assisted friction stir welding: Investigating microstructure, tensile and flexural properties. *Int. J. Phys. Sci.* **2012**, *7*, 647–654. [CrossRef]

169. Saeedy, S.; Besharati, M.K. Investigation of the effects of critical process parameters of friction stir welding of polyethyleneg. *Proc. Inst. Mech. Eng. Part B J. Eng. Manuf.* **2011**, *225*, 1305–1310. [CrossRef]
170. Mishra, D.; Sahu, S.K.; Mahto, R.P.; Pal, S.K. *Strengthening and Joining by Plastic Deformation*; Springer: Singapore, 2019; ISBN 978-981-13-0377-7.
171. Inaniwa, S.; Kurabe, Y.; Miyashita, Y.; Hori, H. Application of friction stir welding for several plastic materials. In *Proceedings of the 1st International Joint Symposium on Joining and Welding, Osaka, Japan, 6–8 November 2013*; Woodhead Publishing Limited: Cambridge, UK, 2013; Volume 2, pp. 137–142.
172. Rezgui, M.-A.; Trabelsi, A.-C.; Ayadi, M.; Hamrouni, K. Optimization of Friction Stir Welding Process of High Density Polyethylene. *Int. J. Prod. Qual. Eng.* **2011**, *2*, 55–61.
173. Panneerselvam, K.; Lenin, K. Joining of Nylon 6 plate by friction stir welding process using threaded pin profile. *Mater. Des.* **2014**, *53*, 302–307. [CrossRef]
174. Zafar, A.; Awang, M.; Khan, S.R.; Emamian, S. Investigating friction stir welding on thick nylon 6 plates. *Weld. J.* **2016**, *95*, 210s–218s.
175. Khaliel Youssif, M.S.; El-Sayed, M.A.; Khoureshid, A.E.F.M. Influence of critical process parameters on the quality of friction stir welded nylon 6. *Int. Rev. Mech. Eng.* **2016**, *10*, 501–507. [CrossRef]
176. Bagheri, A.; Azdast, T.; Doniavi, A. An experimental study on mechanical properties of friction stir welded ABS sheets. *Mater. Des.* **2013**, *43*, 402–409. [CrossRef]
177. Sadeghian, N.; Besharati Givi, M.K. Experimental optimization of the mechanical properties of friction stir welded Acrylonitrile Butadiene Styrene sheets. *Mater. Des.* **2015**, *67*, 145–153. [CrossRef]
178. Pirizadeh, M.; Azdast, T.; Rash Ahmadi, S.; Mamaghani Shishavan, S.; Bagheri, A. Friction stir welding of thermoplastics using a newly designed tool. *Mater. Des.* **2014**, *54*, 342–347. [CrossRef]
179. Mendes, N.; Loureiro, A.; Martins, C.; Neto, P.; Pires, J.N. Morphology and strength of acrylonitrile butadiene styrene welds performed by robotic friction stir welding. *Mater. Des.* **2014**, *64*, 81–90. [CrossRef]
180. Sahu, S.K.; Mishra, D.; Mahto, R.P.; Sharma, V.M.; Pal, S.K.; Pal, K.; Banerjee, S.; Dash, P. Friction stir welding of polypropylene sheet. *Eng. Sci. Technol. Int. J.* **2018**, *21*, 245–254. [CrossRef]
181. Kiss, Z.; Czirány, T. Microscopic analysis of the morphology of seams in friction stir welded polypropylene. *Express Polym. Lett.* **2012**, *6*, 54–62. [CrossRef]
182. Kiss, Z.; Czirány, T. Effect of Welding Parameters on the Heat Affected Zone and the Mechanical Properties of Friction Stir Welded Poly(ethylene-terephthalate-glycol). *J. Appl. Polym. Sci.* **2012**, *125*, 2231–2238. [CrossRef]
183. Panneerselvam, K.; Lenin, K. Investigation on effect of tool forces and joint defects during FSW of polypropylene plate. *Procedia Eng.* **2012**, *38*, 3927–3940. [CrossRef]
184. Panneerselvam, K.; Lenin, K. Effects and Defects of the Polypropylene Plate for Different Parameters in Friction Stir Welding Process. *Int. J. Res. Eng. Technol.* **2013**, *2*, 143–152. [CrossRef]
185. Simoes, F.; Rodrigues, D.M. Material flow and thermo-mechanical conditions during Friction Stir Welding of polymers: Literature review, experimental results and empirical analysis. *Mater. Des.* **2014**, *59*, 344–351. [CrossRef]
186. Squeo, E.A.; Bruno, G.; Guglielmotti, A.; Quadrini, F. Friction Stir Welding of Polyethylene Sheets. The Annals of “Dunarea de Jos” University of Galati Fascicle V. 2009, pp. 241–246. Available online: [https://www.researchgate.net/publication/267842113\\_Friction\\_stir\\_welding\\_of\\_polyethylene\\_sheets](https://www.researchgate.net/publication/267842113_Friction_stir_welding_of_polyethylene_sheets) (accessed on 24 August 2020).
187. Arbogast, W.J. A flow-partitioned deformation zone model for defect formation during friction stir welding. *Scr. Mater.* **2008**, *58*, 372–376. [CrossRef]
188. Rezgui, M.A.; Ayadi, M.; Cherouat, A.; Hamrouni, K.; Zghal, A.; Bejaoui, S. Application of Taguchi approach to optimize friction stir welding parameters of polyethylene. *EPJ Web Conf.* **2010**, *6*, 1–8. [CrossRef]
189. Strand, S.R. Effects of Friction Stir Welding on Polymer Microstructure. Master’s Thesis, Ira A. Fulton College of Engineering and Technology, Tempe, AZ, USA, February 2004.
190. Nelson, T.W.; Sorensen, C.D.; John, C.J. Friction Stir Welding of Polymeric Materials. U.S. Patent 681,163,2B2, 2 November 2009.
191. Banjare, P.N.; Sahlot, P.; Arora, A. An assisted heating tool design for FSW of thermoplastics. *J. Mater. Process. Technol.* **2016**, *239*, 83–91. [CrossRef]
192. Laieghi, H.; Alipour, S.; Mostafapour, A. Heat-assisted friction stir welding of polymeric nanocomposite. *Sci. Technol. Weld. Join.* **2020**, *25*, 56–65. [CrossRef]

193. Husain, I.M.; Salim, R.K.; Azdast, T.; Hasanifard, S.; Shishavan, S.M.; Lee, R.E. Mechanical properties of friction-stir-welded polyamide sheets. *Int. J. Mech. Mater. Eng.* **2015**, *10*, 18. [CrossRef]
194. Leng, X.; Yang, W.; Zhang, J.; Ma, X.; Zhao, W.; Yan, J. Designing high-performance composite joints close to parent materials of aluminum matrix composites. *arXiv* **2017**, *34*, 660–663.
195. Hall, I.W.; Kyono, T.; Diwanji, A. On the fibre/matrix interface in boron/aluminum metal matrix composites. *J. Mater. Sci.* **1987**, *22*, 1743–1748. [CrossRef]
196. Vijay, S.J.; Murugan, N. Influence of tool pin profile on the metallurgical and mechanical properties of friction stir welded Al-10wt.% TiB2 metal matrix composite. *Mater. Des.* **2010**, *31*, 3585–3589. [CrossRef]
197. Hassan, A.M.; Qasim, T.; Ghaitan, A. Effect of pin profile on friction stir welded aluminum matrix composites. *Mater. Manuf. Process.* **2012**, *27*, 1397–1401. [CrossRef]
198. Mahmoud, E.R.I.; Takahashi, M.; Shibayanagi, T.; Ikeuchi, K. Effect of friction stir processing tool probe on fabrication of SiC particle reinforced composite on aluminum surface. *Sci. Technol. Weld. Join.* **2009**, *14*, 413–425. [CrossRef]
199. Cavaliere, P.; Cerri, E.; Marzoli, L.; Dos Santos, J. Friction stir welding of ceramic particle reinforced aluminum based metal matrix composites. *Appl. Compos. Mater.* **2004**, *11*, 247–258. [CrossRef]
200. Marzoli, L.M.; Strombeck, A.V.; Dos Santos, J.F.; Gambaro, C.; Volpone, L.M. Friction stir welding of an AA6061/Al<sub>2</sub>O<sub>3</sub>/20p reinforced alloy. *Compos. Sci. Technol.* **2006**, *66*, 363–371. [CrossRef]
201. Prado, R.A.; Murr, L.E.; Shindo, D.J.; Soto, K.F. Tool wear in the friction-stir welding of aluminum alloy 6061 + 20% Al<sub>2</sub>O<sub>3</sub>: A preliminary study. *Scr. Mater.* **2001**, *45*, 75–80. [CrossRef]
202. Baxter, S.C.; Reynolds, A.P. Characterization of Reinforcing Particle Size Distribution in a Friction Stir Welded Al-SiC Extrusion. In *Proceedings of the Lightweight Alloys for Aerospace Application*; Jata, K., Lee, E., Frazier, W., Kim, N.J., Eds.; The Minerals, Metals & Materials Society: Pittsburgh, PA, USA, 2001; pp. 283–294.
203. Mahoney, M.W.; Harrigan, W.; Wert, J.A. Friction Stir Welding SiC Discontinuously Reinforced Aluminium. In *Proceedings of the 7th Int. Conf. Joints in Aluminum*, Cambridge, UK, 15–17 April 1998; pp. 231–236.
204. Feng, A.H.; Ma, Z.Y. Formation of Cu<sub>2</sub>FeAl<sub>7</sub> phase in friction-stir-welded SiCp/Al-Cu-Mg composite. *Scr. Mater.* **2007**, *57*, 1113–1116. [CrossRef]
205. Feng, A.H.; Xiao, B.L.; Ma, Z.Y. Effect of microstructural evolution on mechanical properties of friction stir welded AA2009/SiCp composite. *Compos. Sci. Technol.* **2008**, *68*, 2141–2148. [CrossRef]
206. Ceschini, L.; Boromei, I.; Minak, G.; Morri, A.; Tarterini, F. Microstructure, tensile and fatigue properties of AA6061/20 vol.%Al<sub>2</sub>O<sub>3</sub>p friction stir welded joints. *Compos. Part A Appl. Sci. Manuf.* **2007**, *38*, 1200–1210. [CrossRef]
207. Acharya, U.; Roy, B.S.; Saha, S.C. Torque and force perspectives on particle size and its effect on mechanical property of friction stir welded AA6092/17.5SiC p -T6 composite joints. *J. Manuf. Process.* **2019**, *38*, 113–121. [CrossRef]
208. Kumar, S.; Medhi, T.; Roy, B.S. *Friction Stir Welding of Thermoplastic Composites*; Springer: Singapore, 2019; ISBN 978-981-13-6412-9.
209. Bhushan, R.K.; Sharma, D. Optimization of FSW parameters for maximum UTS of AA6082/SiC/10 P composites. *Adv. Compos. Lett.* **2019**, *28*, 96369351986770. [CrossRef]
210. Jafrey, D.D.; Panneerselvam, K. Study on Tensile Strength, Impact Strength and Analytical Model for Heat Generation in Friction Vibration Joining of Polymeric Nanocomposite Joints Daniel. *Polym. Eng. Sci.* **2016**, *57*, 495–504. [CrossRef]
211. Liu, H.; Hu, Y.; Zhao, Y.; Fujii, H. Microstructure and mechanical properties of friction stir welded AC4A+30vol.%SiCp composite. *Mater. Des.* **2015**, *65*, 395–400. [CrossRef]
212. Wang, D.; Wang, Q.Z.; Xiao, B.L.; Ma, Z.Y. Achieving friction stir welded SiCp/Al-Cu-Mg composite joint of nearly equal strength to base material at high welding speed. *Mater. Sci. Eng. A* **2014**, *589*, 271–274. [CrossRef]
213. Mozammil, S.; Karloopia, J.; Verma, R.; Jha, P.K. Mechanical response of friction stir butt weld Al-4.5%Cu/TiB<sub>2</sub>/2.5p in situ composite: Statistical modelling and optimization. *J. Alloy. Compd.* **2020**, *826*, 154184. [CrossRef]
214. Narendranath, S.; Chakradhar, D. Effect of FSW on microstructure and hardness of AA6061/SiC/fly ash MMCs. *Mater. Today Proc.* **2018**, *5*, 17866–17872. [CrossRef]
215. Bozkurt, Y.; Uzun, H.; Salman, S. Microstructure and mechanical properties of friction stir welded particulate reinforced AA2124/SiC/25p-T4 composite. *J. Compos. Mater.* **2011**, *45*, 2237–2245. [CrossRef]



216. Acharya, U.; Saha Roy, B.; Chandra Saha, S. A Study of Tool Wear and its Effect on the Mechanical Properties of Friction Stir Welded AA6092/17.5 Sicp Composite Material Joint. *Mater. Today Proc.* **2018**, *5*, 20371–20379. [CrossRef]
217. Ni, D.R.; Chen, D.L.; Xiao, B.L.; Wang, D.; Ma, Z.Y. Residual stresses and high cycle fatigue properties of friction stir welded SiCp/AA2009 composites. *Int. J. Fatigue* **2013**, *55*, 64–73. [CrossRef]
218. Bozkurt, Y.; Boumerzoug, Z. Tool material effect on the friction stir butt welding of AA2124-T4 Alloy Matrix MMC. *J. Mater. Res. Technol.* **2018**, *7*, 29–38. [CrossRef]
219. Fernández, R.; Ibáñez, J.; Cioffi, F.; Verdera, D.; González-Doncel, G. Friction stir welding of 25%SiC/2124Al composite with optimal mechanical properties and minimal tool wear. *Sci. Technol. Weld. Join.* **2017**, *22*, 526–535. [CrossRef]
220. Periyasamy, P.; Mohan, B.; Balasubramanian, V. Effect of heat input on mechanical and metallurgical properties of friction stir welded AA6061-10% SiCp MMCs. *J. Mater. Eng. Perform.* **2012**, *21*, 2417–2428. [CrossRef]
221. Wang, D.; Xiao, B.L.; Wang, Q.Z.; Ma, Z.Y. Evolution of the Microstructure and Strength in the Nugget Zone of Friction Stir Welded SiCp/Al-Cu-Mg Composite. *J. Mater. Sci. Technol.* **2014**, *30*, 54–60. [CrossRef]
222. Salih, O.S.; Ou, H.; Wei, X.; Sun, W. Microstructure and mechanical properties of friction stir welded AA6092/SiC metal matrix composite. *Mater. Sci. Eng. A* **2019**, *742*, 78–88. [CrossRef]
223. Firouzdar, V.; Kou, S. Al-to-Mg friction stir welding: Effect of material position, travel speed, and rotation speed. *Metall. Mater. Trans. A Phys. Metall. Mater. Sci.* **2010**, *41*, 2914–2935. [CrossRef]
224. Mehta, K.P.; Badheka, V.J. A review on dissimilar friction stir welding of copper to aluminum: Process, properties, and variants. *Mater. Manuf. Process.* **2016**, *31*, 233–254. [CrossRef]
225. Miles, M.P.; Melton, D.W.; Nelson, T.W. Formability of friction-stir-welded dissimilar-aluminum-alloy sheets. *Metall. Mater. Trans. A Phys. Metall. Mater. Sci.* **2005**, *36*, 3335–3342. [CrossRef]
226. Simar, A.; Jonckheere, C.; Deplus, K.; Pardoën, T.; De Meester, B. Comparing similar and dissimilar friction stir welds of 2017-6005A aluminum alloys. *Sci. Technol. Weld. Join.* **2010**, *15*, 254–259. [CrossRef]
227. Ipekoglu, G.; Cam, G. Effects of initial temper condition and postweld heat treatment on the properties of dissimilar friction-stir-welded joints between AA7075 and AA6061 aluminum alloys. *Metall. Mater. Trans. A Phys. Metall. Mater. Sci.* **2014**, *45*, 3074–3087. [CrossRef]
228. Ahmadnia, M.; Shahraki, S.; Kamarposhti, M.A. Experimental studies on optimized mechanical properties while dissimilar joining AA6061 and AA5010 in a friction stir welding process. *Int. J. Adv. Manuf. Technol.* **2016**, *87*, 2337–2352. [CrossRef]
229. Sato, Y.S.; Park, S.H.C.; Michiuchi, M.; Kokawa, H. Constitutional liquation during dissimilar friction stir welding of Al and Mg alloys. *Scr. Mater.* **2004**, *50*, 1233–1236. [CrossRef]
230. Yan, J.; Xu, Z.; Li, Z.; Li, L.; Yang, S. Microstructure characteristics and performance of dissimilar welds between magnesium alloy and aluminum formed by friction stirring. *Scr. Mater.* **2005**, *53*, 585–589. [CrossRef]
231. Firouzdar, V.; Kou, S. Formation of liquid and intermetallics in Al-to-Mg friction stir welding. *Metall. Mater. Trans. A Phys. Metall. Mater. Sci.* **2010**, *41*, 3238–3251. [CrossRef]
232. Abdollahzadeh, A.; Shokuhfar, A.; Cabrera, J.M.; Zhilyaev, A.P.; Omidvar, H. The effect of changing chemical composition in dissimilar Mg/Al friction stir welded butt joints using zinc interlayer. *J. Manuf. Process.* **2018**, *34*, 18–30. [CrossRef]
233. Ouyang, J.; Yarrapareddy, E.; Kovacevic, R. Microstructural evolution in the friction stir welded 6061 aluminum alloy (T6-temper condition) to copper. *J. Mater. Process. Technol.* **2006**, *172*, 110–122. [CrossRef]
234. Xue, P.; Xiao, B.L.; Ma, Z.Y. Effect of interfacial microstructure evolution on mechanical properties and fracture behavior of friction-stir-welded Al-Cu joints. *Metall. Mater. Trans. A* **2015**, *46*, 3091–3103. [CrossRef]
235. Zhang, J.; Shen, Y.; Yao, X.; Xu, H.; Li, B. Investigation on dissimilar underwater friction stir lap welding of 6061-T6 aluminum alloy to pure copper. *Mater. Des.* **2014**, *64*, 74–80. [CrossRef]
236. Venkateswaran, P.; Reynolds, A.P. Factors affecting the properties of Friction Stir Welds between aluminum and magnesium alloys. *Mater. Sci. Eng. A* **2012**, *545*, 26–37. [CrossRef]
237. Zhao, Y.Y.; Li, D.; Zhang, Y.S. Effect of welding energy on interface zone of Al-Cu ultrasonic welded joint. *Sci. Technol. Weld. Join.* **2013**, *18*, 354–360. [CrossRef]
238. Liyanage, T.; Kilbourne, J.; Gerlich, A.P.; North, T.H. Joint formation in dissimilar Al alloy/steel and Mg alloy/steel friction stir spot welds. *Sci. Technol. Weld. Join.* **2009**, *14*, 500–508. [CrossRef]

239. Lancaster, J.F. *Metallurgy of Welding*; Woodhead Publishing Limited: Cambridge, UK, 1999; ISBN 978-1-85573-428-9.
240. Fu, B.; Qin, G.; Li, F.; Meng, X.; Zhang, J.; Wu, C. Friction stir welding process of dissimilar metals of 6061-T6 aluminum alloy to AZ31B magnesium alloy. *J. Mater. Process. Technol.* **2015**, *218*, 38–47. [CrossRef]
241. Zettler, R.; Da Silva, A.A.M.; Rodrigues, S.; Blanco, A.; Dos Santos, J.F. Dissimilar Al to Mg alloy friction stir welds. *Adv. Eng. Mater.* **2006**, *8*, 415–421. [CrossRef]
242. Kasai, H.; Morisada, Y.; Fujii, H. Dissimilar FSW of immiscible materials: Steel/magnesium. *Mater. Sci. Eng. A* **2015**, *624*, 250–255. [CrossRef]
243. Peel, M.J.; Steuwer, A.; Withers, P.J.; Dickerson, T.; Shi, Q.; Shercliff, H. Dissimilar friction stir welds in AA5083-AA6082. Part I: Process parameter effects on thermal history and weld properties. *Metall. Mater. Trans. A Phys. Metall. Mater. Sci.* **2006**, *37*, 2183–2193. [CrossRef]
244. Khodir, S.A.; Shibayanagi, T. Friction stir welding of dissimilar AA2024 and AA7075 aluminum alloys. *Mater. Sci. Eng. B Solid-State Mater. Adv. Technol.* **2008**, *148*, 82–87. [CrossRef]
245. Avinash, P.; Manikandan, M.; Arivazhagan, N.; Devendranath, R.K.; Narayanan, S. Friction stir welded butt joints of AA2024 T3 and AA7075 T6 aluminum alloys. *Procedia Eng.* **2014**, *75*, 98–102. [CrossRef]
246. Palanivel, R.; Koshy Mathews, P.; Murugan, N.; Dinaharan, I. Effect of tool rotational speed and pin profile on microstructure and tensile strength of dissimilar friction stir welded AA5083-H111 and AA6351-T6 aluminum alloys. *Mater. Des.* **2012**, *40*, 7–16. [CrossRef]
247. Malarvizhi, S.; Balasubramanian, V. Influences of tool shoulder diameter to plate thickness ratio (D/T) on stir zone formation and tensile properties of friction stir welded dissimilar joints of AA6061 aluminum-AZ31B magnesium alloys. *Mater. Des.* **2012**, *40*, 453–460. [CrossRef]
248. RajKumar, V.; VenkateshKannan, M.; Sadeesh, P.; Arivazhagan, N.; Devendranath Ramkumar, K. Studies on effect of tool design and welding parameters on the friction stir welding of dissimilar aluminum alloys AA 5052-AA 6061. *Procedia Eng.* **2014**, *75*, 93–97. [CrossRef]
249. Jafarzadegan, M.; Abdollah-zadeh, A.; Feng, A.H.; Saeid, T.; Shen, J.; Assadi, H. Microstructure and Mechanical Properties of a Dissimilar Friction Stir Weld between Austenitic Stainless Steel and Low Carbon Steel. *J. Mater. Sci. Technol.* **2013**, *29*, 367–372. [CrossRef]
250. Dehghani, M.; Amadeh, A.; Akbari Mousavi, S.A.A. Investigations on the effects of friction stir welding parameters on intermetallic and defect formation in joining aluminum alloy to mild steel. *Mater. Des.* **2013**, *49*, 433–441. [CrossRef]
251. Morishige, T.; Kawaguchi, A.; Tsujikawa, M.; Hino, M.; Hirata, T.; Higashi, K. Dissimilar welding of Al and Mg alloys by FSW. *Mater. Trans.* **2008**, *49*, 1129–1131. [CrossRef]
252. Masoudian, A.; Tahaei, A.; Shakiba, A.; Sharifianjazi, F.; Mohandesi, J.A. Microstructure and mechanical properties of friction stir weld of dissimilar AZ31-O magnesium alloy to 6061-T6 aluminum alloy. *Trans. Nonferrous Met. Soc. China* **2014**, *24*, 1317–1322. [CrossRef]
253. Azizieh, M.; Sadeghi Alavijeh, A.; Abbasi, M.; Balak, Z.; Kim, H.S. Mechanical properties and microstructural evaluation of AA1100 to AZ31 dissimilar friction stir welds. *Mater. Chem. Phys.* **2016**, *170*, 251–260. [CrossRef]
254. Abe, Y.; Watanabe, T.; Tanabe, H.; Kagiya, K. Dissimilar metal joining of magnesium alloy to steel by FSW. *Adv. Mater. Res.* **2007**, *15–17*, 393–397. [CrossRef]
255. Joshi, G.R.; Badheka, V.J. Microstructures and Properties of Copper to Stainless Steel Joints by Hybrid FSW. *Metallogr. Microstruct. Anal.* **2017**, *6*, 470–480. [CrossRef]
256. Shankar, S.; Chattopadhyaya, S. Friction stir welding of commercially pure copper and 1050 aluminum alloys. *Mater. Today Proc.* **2019**, *25*, 664–667. [CrossRef]
257. Xue, P.; Ni, D.R.; Wang, D.; Xiao, B.L.; Ma, Z.Y. Effect of friction stir welding parameters on the microstructure and mechanical properties of the dissimilar Al-Cu joints. *Mater. Sci. Eng. A* **2011**, *528*, 4683–4689. [CrossRef]

**Publisher's Note:** MDPI stays neutral with regard to jurisdictional claims in published maps and institutional affiliations.



© 2020 by the authors. Licensee MDPI, Basel, Switzerland. This article is an open access article distributed under the terms and conditions of the Creative Commons Attribution (CC BY) license (<http://creativecommons.org/licenses/by/4.0/>).

### **7.3. [P3] Temperature evolution, material flow and resulting mechanical properties as a function of tool geometry during Friction Stir Welding of AA6082.**

**Laska A.\***, Sadeghi B., Sadeghian B., Taherizadeh A., Szkodo M., Cavaliere P., Temperature evolution, material flow and resulting mechanical properties as a function of tool geometry during Friction Stir Welding of AA6082. Major Revision (II round of Under Review after Major Revision status) in Journal of Materials Engineering and Performance (IF = 2.036, 70 points of the Polish Ministry of Science and Higher Education)

#### 7.3.1. Declaration of the contribution of the doctoral candidate

My contribution to the preparation of this publication included the development of the research methodology and the design and fabrication of the FSW tool in two different geometries. In addition, I analyzed the results of computer simulations. I acquired the studied material and produced samples of AA6082 aluminum alloy using the FSW method. I conducted macro- and microstructural observations, hardness measurements on the cross-sections of the produced joints, and carried out static tensile testing and SEM observations of the fractures. I analyzed the obtained research results. I conducted a discussion in the manuscript. I prepared figures and tables. In addition, I prepared the manuscript for publication and functioned as a correspondence author.

.....  
Aleksandra Laska



### 7.3.2. Content of the publication

#### **Temperature evolution, material flow and resulting mechanical properties as a function of tool geometry during Friction Stir Welding of AA6082**

Aleksandra Laska<sup>1\*</sup>, Behzad Sadeghi<sup>2</sup>, Behzad Sadeghian<sup>3</sup>, Aboozar Taherizadeh<sup>3</sup>, Marek Szkodo<sup>1</sup>, Pasquale Cavaliere<sup>2</sup>

<sup>1</sup> Faculty of Mechanical Engineering and Ship Technology, Gdansk University of Technology, 4 Narutowicza 11/12, 80-233 Gdańsk, Poland; aleksandra.laska@pg.edu.pl; mszkodo@pg.edu.pl

<sup>2</sup> Department of Innovation Engineering, University of Salento, Via per Arnesano, 73100 Lecce, Italy; b.sadeghi2020@gmail.com; pasquale.cavaliere@unisalento.it

<sup>3</sup> Department of Materials Engineering, Isfahan University of Technology, Isfahan 8415683111, Iran; behzadsadeghian91@gmail.com; a.taheri@iut.ac.ir

\* Corresponding author: aleksandra.laska@pg.edu.pl

**Abstract:** The Friction Stir Welding (FSW) process was simulated for joining AA6082 aluminum alloy using two different tool geometries – with a tapered cylindrical pin (simple pin) and with a hexagonal pin with grooves (complex pin). The analysis of the simulations performed was discussed in terms of temperature evolution during the process, total heat input, residual stresses and material flow. Simulations revealed that a 5% higher temperature, equal to maximum 406 °C, was provided when using the complex pin than with the simple pin. Higher temperature and higher shear stresses during the welding with the complex pin caused the introduction of higher residual stresses in the weld. Experimental results on the produced welds allowed observation of the microstructure of the joints, hardness tests in cross sections and tensile strength tests. Due to the higher temperature during the process with the complex pin and the more efficient recrystallization process, grain refinement in the SZ was more pronounced. The average grain size in the stir zone for the weld produced with the complex pin was equal to  $10.770 \pm 1.386 \mu\text{m}$ , and in the case of the simple pin  $14.321 \pm 1.319 \mu\text{m}$ . The presented hardness profiles showed that the weld produced with a complex pin had higher hardness in the stir zone, which is consistent with the Hall-Petch relationship. The obtained UTS values corresponded to the joint efficiency of  $72.5 \pm 4.9 \%$  and  $55.8 \pm 8.6 \%$  for the weld produced with the complex pin and the simple pin, respectively.

**Keywords:** Friction Stir Welding; Aluminum Alloys; Computational Fluid Dynamics; Mechanical Properties; Microstructure; COMSOL.

#### **1. Introduction**

Friction Stir Welding (FSW) is a method gaining increasing interest, especially for joining light metals such as aluminum and its alloys. Patented in 1991, the method is based on joining materials by plasticizing and mixing them in the weld zone by using a non-consumable tool (Ref 1). The tool consists of two integral parts - a pin and a shoulder. During the process, the tool performs both rotational and traverse motions. The tool shoulder is in constant contact with the surface of the components in contact with each other. The friction generated by the movement of the tool is transformed into heat, which leads to the plasticization of the material (Ref 2). At the same time, the pin performing rotational motion mixes the material, and the tool moves in a traverse motion along the weld line (Ref 3). The most important process parameters include the tool's tilt

angle, traverse and rotational speed, as well as the geometry of the tool (Ref 4). Properly selected process parameters, by ensuring optimum temperature and proper mixing of the weld material, allow to obtain sound joints characterized by low residual stresses, high mechanical and electrochemical properties (Ref 5,6).

Among the greatest advantages of the FSW method is the ability to join materials presenting low weldability (Ref 7). Such materials include aluminum alloys from all groups, including the 6xxx group. Due to their properties such as low density, relatively high strength and corrosion resistance, as well as its low price, it is a good competitor to steel for, for example, train car structures (Ref 8). However, problems in joining aluminum require the development of a method of successive joining of this alloy (Ref 9). An excellent solution is the FSW method. The main problems arising from the welding of aluminum alloys by conventional methods are their extreme susceptibility to solidification cracking and porosity associated with the change of state (Ref 10,11). Therefore, using a solid-state joining process such as FSW eliminates this problem.

Due to the complexity of the mixing process during the welding, the limitations of the equipment, and possible uncertainties due to the experimental procedures, advanced investigations of the thermal process by the real experiments are still challenging. In addition, conducting actual experiments involves a considerable financial effort, and therefore present trends are shifting toward computer simulations. On the contrary, numerical modeling of FSW is a demanding process actually, mainly due to material assumptions and boundary conditions.

One of the most widely adopted approaches of the numerical simulations of the FSW is computational fluid dynamics (CFD). Seidel and Reynolds (Ref 12) presented a two-dimensional model coupled with a thermal model. This model was created by assuming laminar, viscous and non-Newtonian flow around the pin. They showed that the transport of material mainly occurs in retreat side. Bendzszak et al. (Ref 13), in practical research, obtained the viscosity of aluminum alloy as a function of strain rate and temperature. Ulysse (Ref 14) obtained the influence of speed parameters on temperature and forces during FSW by constructing a three-dimensional viscoplastic model. Colegrove et al. (Ref 15,16) studied the temperature distribution and material flow during welding of aluminum alloys by developing 3D numerical simulations with the CFD approach by the use of different tool geometries – smooth and threaded tool. Nandan et al. (Ref 17–19) analyzed the heat transfer, plastic flow and the effect of material flow rates during FSW for aluminum alloy, stainless steel and mild steel. In these researches they considered the non-Newtonian viscosity as a function of temperature and strain rate. Kim et al. (Ref 20), using the finite volume method (FVM), investigated the temperature distribution and material flow during friction stir welding of 5083 aluminum alloy. They showed that the CFD method is more effective than other proposed methods such as ALE, although it cannot investigate the phenomenon of material hardening (Ref 21). Hasan et al. (Ref 22) applied a CFD model to predict tool wear during the FSW of AISI 304 austenitic stainless steel. The influence of tool geometry in the FSW process has been widely analyzed by conducting computer simulations, especially CFD method, by Ji et al. (Ref 23), Zhang et al. (Ref 24), Hirasawa et al. (Ref 25) and Yu et al. (Ref 26). However, the current state of the art is deficient in analyzing the effect of tool geometry on the properties of AA6082 aluminum alloy welds.

The following work analyzes the effect of tool geometry on the properties of AA6082 joints produced by the FSW process. Based on computer simulations performed, the contributions of temperature, total heat input, residual stresses and material flow were discussed. In addition, the effects of these factors on the microstructure, hardness and tensile strength of the resulting welds were determined through performed experiments.

## **2. Experimental procedure**

### **2.1 FSW procedure**

The material used in this study was AA6082 aluminum alloy, solution heat-treated and artificially aged to T651 condition. The rolled sheets of 3 mm in thickness were used to perform Friction Stir Welding process.



To determine the chemical composition of the chosen material the X-ray energy dispersive spectrometer (EDS) (Edax Inc., Mahwah, NJ, USA) was applied. The results are given in Table 1.

Table 1. Chemical composition of AA6082.

Chemical composition [wt.%]									
	Zn	Mg	Cr	Ti	Fe	Si	Cu	Mn	Al
<b>AA6082</b>	0.20	1.03	0.25	0.10	0.50	0.90	0.10	0.42	Balance

The welding process was conducted on a conventional milling machine (FU251, Friedrich Engels Kazanluk, Bulgaria). To establish the influence of the tool geometry on the properties of resulting welds, two different tools were chosen. The shoulder geometry was in both cases identical. The two tools differed in the shape and dimensions of the pins. The exact geometries of the tools with the tapered cylindrical pin and the hexagonal pin with grooves are presented in Fig. (1). The material of the pins was 73MoV52 tool steel and the shoulder was made of X210Cr12 tool steel. The hardness values of the pin and the shoulder were equal to 58 and 61 HRC, respectively (Wilson Mechanical Instrument Co. Inc., USA). The employed tool traverse speed was 250 mm/min, the tool rotational speed was 1000 rpm and the tool tilt angle was 2°. The proposed welding parameters were based on previous experience with the friction stir welding of AA6082 alloy (Ref 27).

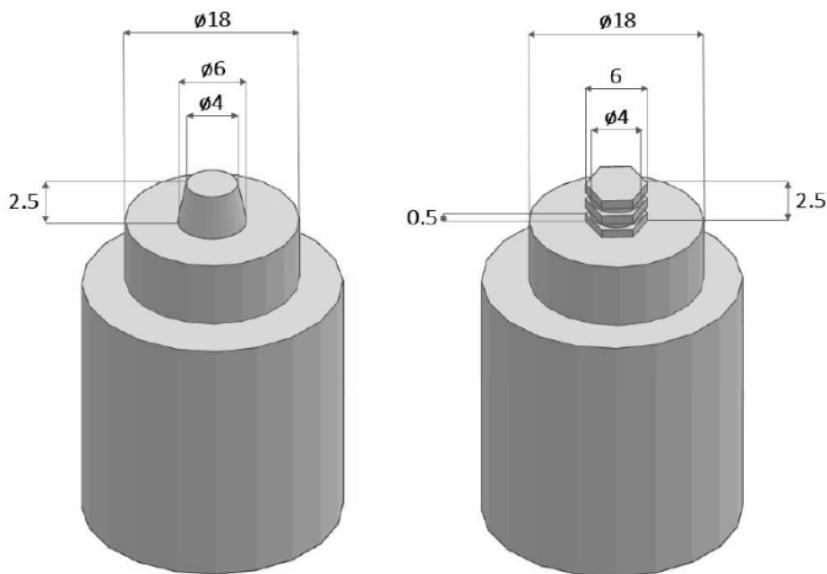


Fig. 1 Schematic illustration of the geometry of the tool used for FSW of AA6082

## 2.2 Modelling

In this research, in order to simulate the heat generated in the tool/ workpiece interface, the steady state solution was used. In this model, the tool was placed in the center of the part and the temperature distribution model was considered based on the steady state heat transfer equation, considering the translational motion, according to Eq. (1) (Ref 18,28).

$$\rho C_p U(\nabla T) = \nabla(k\nabla T) + \dot{Q} \quad (1)$$

3

Where,  $\rho$  is the density,  $C_p$  is the heat capacity,  $k$  is the heat transfer coefficient and  $Q$  is the heat generated. In this particular model, the material heat transfer properties was considered for aluminum 6082.

In order to predict the heat generated under the tool, the tangential velocity of each point of the tool on the workpiece was obtained from Eq. (2) according to Fig. (2 a),

$$V_{\theta} = (\omega r - U\psi \sin\theta) \quad (2)$$

where,  $r$  is the distance of each point from the tool to its center,  $U$  is the linear speed of the tool on the part and  $\omega$  is the rotational speed. Various parameters such as the difference of plastic deformation and shear force in advancing and retreating sides (AS and RS) affect the temperature asymmetry. In fact, considering the effect of AS and RS has an important role in the proper prediction of the model. Therefore,  $\psi$ , according to what was mentioned in the previous articles, is considered equal to 20 (Ref 29).

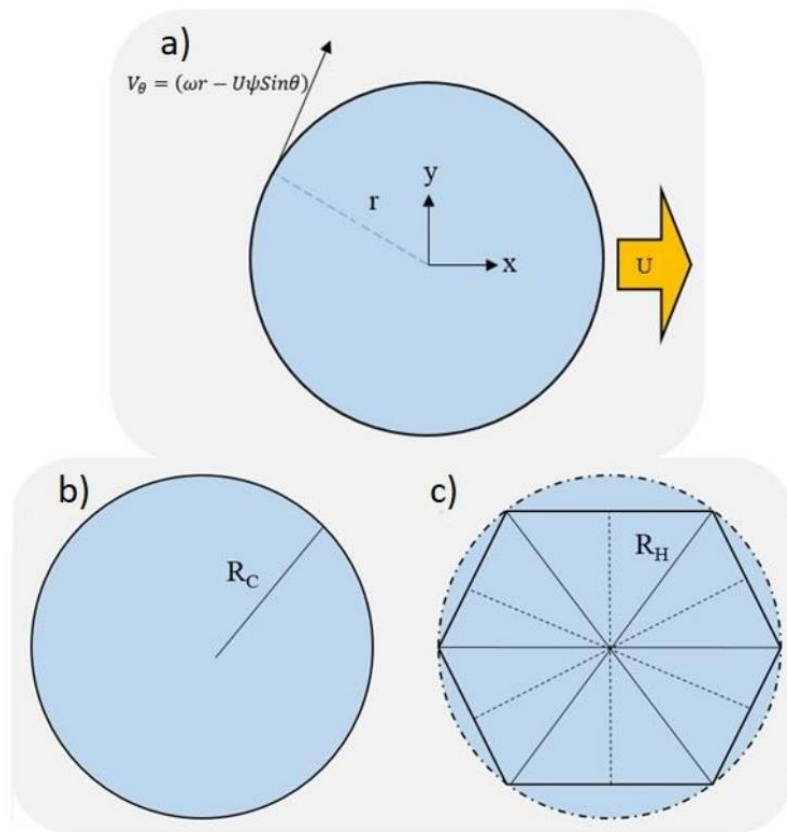


**Fig. 2** Schematic of tangential velocity model during FSW process (a), schematic of a circular pin (b) and a hexagonal pin (c) sections

The heat generated in the tool shoulder during the FSW process was obtained from Eq. (3) (Ref 17,29,30):

$$\dot{Q} = \gamma \cdot f \cdot F(\omega r - U\psi \sin\theta) \quad (3)$$



where,  $\gamma$  is a constant number and is considered equal to 1. Also, parameter  $f$  represents the heat ratio that enters the workpiece, because some heat is wasted by the thermal conduction of the tool. This ratio was obtained according to Eq. (4) by dividing the thermal parameters of the workpiece to the total thermal parameters.

$$f = \frac{\sqrt{(k\rho Cp)_\omega}}{\sqrt{(k\rho Cp)_\omega} + \sqrt{(k\rho Cp)_T}} \quad (4)$$

In this model, the heat generated was divided into two general parts: heat produced by friction and heat produced by plastic deformation, and this issue was considered in the models. Therefore,  $F$ , which is the total heat generated between the workpiece and the tool, was considered according to Eq. (5):

$$F = (1 - S)\tau\eta + S(\delta\tau\eta + (1 - \delta)\mu P_N) \quad (5)$$

where, the effect of sliding and sticking friction, as well as the effect of heat generated by plastic deformation during welding, has been determined. Here,  $P_N$  is the pressure resulting from the vertical force,  $\tau$  is the maximum shear yield stress,  $S$  is the slip parameter, according to Eq. (6), and  $\delta$  is the adhesion parameter, which is suggested 0.65 for aluminum alloys (Ref 30) and  $\mu$  is the friction coefficient, according to Eq. (7) (Ref 29).

$$S = 1 - \exp\left(-S_0 \frac{r\omega - \varphi U \cdot \sin(\theta)}{R_s \omega_0}\right) \quad (6)$$

$$\mu = \mu_0 \exp(-S(r\omega - \varphi U \cdot \sin(\theta))) \quad (7)$$

Eq. (8) shows the heat generated in the cylindrical parts of the pin and Eq. (9) shows the heat generated in the hexagonal parts, according to the Fig. (2 b and c). These equations are obtained from Waheed et al.'s work (Ref 31).

$$Q_{pin\_circle} = \int_0^{2\pi} \int_0^{R_c} \mu pr(\omega r - U\psi \sin(\theta)) dr d\theta \quad (8)$$

$$Q_{pin\_Hexagon} = \int_0^{2\pi} \int_0^{R_H} \mu pr(\omega r - U\psi \sin(\theta)) dr d\theta \quad (9)$$

$$- \int_0^{\frac{\pi}{6}} \int_0^{R_H} \mu pr(\omega r - U\psi \sin(\theta)) dr d\theta$$

Computational fluid dynamics (CFD) was applied to model the material flow during FSW process. To this purpose, the continuity equation for single-phase material was used according to Eq. (10) (Ref 32,33):

$$\nabla \cdot U = 0 \quad (10)$$

where,  $U$  is the material flow velocity. Also, the momentum equation according to the Navier-Stokes equation for single phase material in steady state solution was used as Eq. (11):

$$\rho U \cdot \nabla U = -\nabla p + \mu \nabla^2 U \quad (11)$$

where,  $\rho$  is the density,  $\mu$  is the non-Newtonian viscosity, and  $p$  is the fluid pressure. The energy equation is also the steady state heat transfer equation that was used in the thermal simulation previously and is used



as a coupled simulation with this model. Dynamic viscosity, which is a function of temperature and strain rate, was obtained from Eq. (12):

$$\mu = \frac{\sigma(T, \dot{\epsilon})}{3\dot{\epsilon}} \quad (12)$$

Where,  $\mu$  indicates viscosity,  $\sigma$  is the yield strength of the material, which itself follows the Eq. (13) and  $Z$  is the Zener-Holman parameter, according to the Eq. (14):

$$\sigma(T, \dot{\epsilon}) = \frac{1}{\alpha} \ln \left[ \left( \frac{Z(T, \dot{\epsilon})}{A} \right)^{\frac{-1}{n}} + \left[ 1 + \left( \frac{Z(T, \dot{\epsilon})}{A} \right)^{\frac{2}{n}} \right]^{1/2} \right] \quad (13)$$

$$Z(T, \dot{\epsilon}) = \dot{\epsilon} \exp\left(\frac{-Q}{RT}\right) \quad (14)$$

Strain and strain rate were also obtained from CFD solution according to the Eq. (15) and (16) (Ref 19).

$$\epsilon_{xy} = \frac{1}{2} \left( \frac{\partial U_y}{\partial x} + \frac{\partial U_x}{\partial y} \right) \quad (15)$$

$$\dot{\epsilon} = \left( \frac{2}{3} \epsilon_{xy} \dot{\epsilon}_{xy} \right)^{1/2} \quad (16)$$

In order to predict the residual thermal stress, a thermo-mechanical model was used. The strain was calculated according to Equation (9). However, the second part of this equation is applied because no other strain is assumed in this model except thermal strains. The thermal strain was calculated according to Equation (10) (Ref 34).

$$\epsilon = \epsilon^M + \epsilon^T \quad (17)$$

$$\epsilon^T = \alpha \Delta T \quad (18)$$

All stages of model construction, meshing and solving were accomplished by COMSOL Multiphysics version 5.3 software.

### 2.3 Materials characterization

After the welding process, the samples were cut in order to perform microstructure investigation, tensile and hardness tests. In order to perform the microstructure observations on the cross-sections, the specimens were cut in the size of 300x10 mm. The samples were wet ground to the final gradation of #4000 and polished with a 1 $\mu$ m diamond suspension. A double-stage etching was performed using Weck's etchant. Firstly, the metallographic samples were etched in a 2(wt)% NaOH solution for 60 s. Then, the samples were immersed for 10 s in a solution of 4 g KMnO<sub>4</sub>, 1 g NaOH and 100 mL of distilled water. The microstructural observations were performed using an optical microscope (BX51, OLYMPUS, Japan), in accordance to the ASTM E3 standard - Standard Guide for Preparation of Metallographic Specimens. The average grain size was calculated with the use of the linear intercept method, according to ASTM E112-13 standard - Standard Test Methods for Determining Average Grain Size.

The microhardness distributions measurements were performed on the cross-sections of the produced joints at the distance of 1.5 mm from the weld face. A Vickers microhardness tester (Future-Tech FM-800, Tokyo, Japan) with the load of 1 N was used.



The tensile properties of the produced welds were performed with a universal testing machine (Zwick/Roell 100, Germany). Three samples were tested in order to calculate their standard deviation. The geometry of the tensile sample is presented in Fig. (3). The fracture surfaces of the samples after the tensile tests were investigated by a high-resolution scanning electron microscope (SEM) (Phenom XL, Thermo Fisher Scientific, Netherlands) with a backscattered electron detector (BSE).

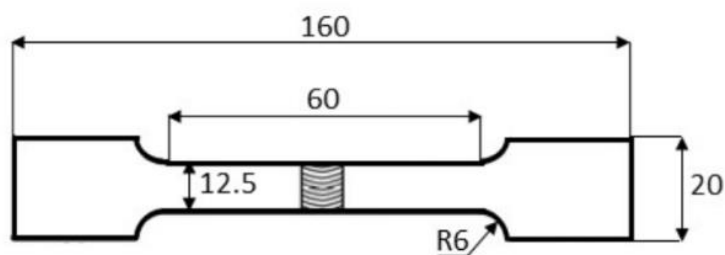


Fig. 3 Geometry of a tensile sample

### 3. Results and discussion

Figure (4 a and b) shows the three-dimensional and two-dimensional contour plot of the simulated temperature distribution during the FSW process with the hexagonal pin with grooves (complex pin). It can be seen that in the AS region, the temperature is higher than in the RS region. The thermal results are in good agreement with the model obtained from previous researches. The simulation results show that this model could be used to predict temperature profiles for other simulations. In addition, it can be seen that there is a clear asymmetry in the welding section, which indicates the existence of AS and RS regions.

It can be seen that the maximum temperature is below the tool. This is because the material in the top surface of the workpiece move parallel to the shoulder of the tool and therefore has a higher shear rate and more heat is generated. This result is in consistent with the results obtained in previous researches (Ref 18,29,32,35,36). On the other hand, the heat-affected zone (HAZ) is larger on the AS side. It can also be seen that the temperature around the pin and under the shoulder is higher, which indicates the heat-generating areas.

By observing Fig. (4 a and b), it can be seen that the temperature gradient is clearly higher in front of the tool than behind the tool. This phenomenon is mainly caused by the different heat transfer properties of the cool zone and the heated zone. Therefore, it is easy to conclude that the heat is transferred at a higher rate to the front and at a lower rate to the back of the tool.

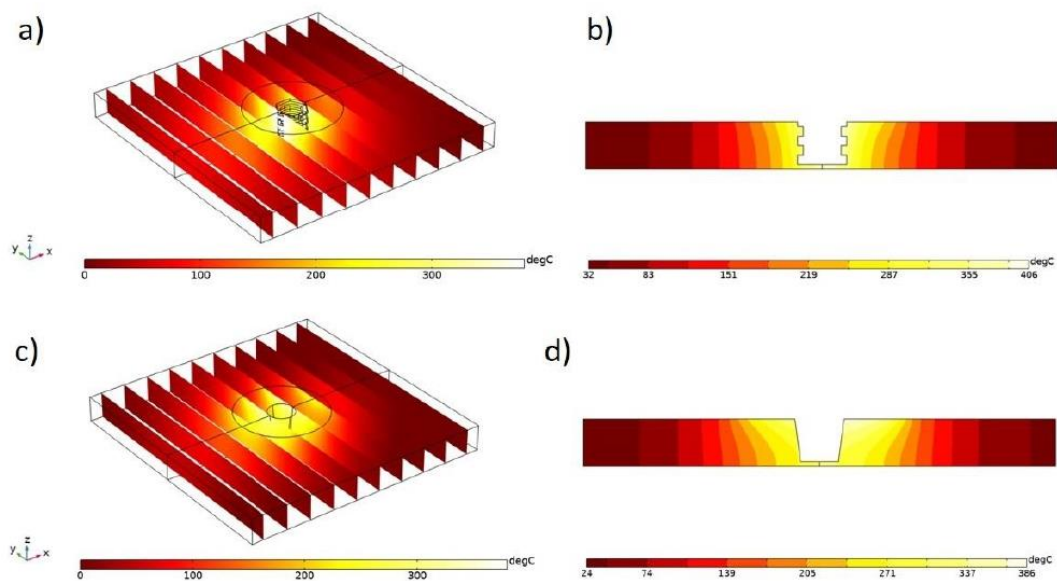


**Fig. 4** 3D (a) and 2D (b) plot of temperature distribution during FSW for a hexagonal pin and 3D (c) and 2D (d) plot of temperature distribution during FSW for a circular pin

Figure (4 c and d) shows the results of the thermal simulation of the FSW process of aluminum alloy 6082, with the tapered cylindrical pin (simple pin) and with the same welding conditions as before, in a 2D section and a 3D plot. By comparing the results of the simple pin and the previous state (complex pin), it can be seen that the maximum temperature produced by the complex pin is at least 5% higher. The reason for this is the presence of more shear stresses in the corners of the pin and the presence of more heat producing surfaces in this pin model.

By observing the three-dimensional plot of the heat generated by the pin, according to Fig. (5 a), it can be seen that the heat generated ( $W/m^2$ ) around the hexagonal region is higher than in the cylindrical region. The reason for this is in the geometric form and the compliance of the heat generated according to the equations mentioned in the previous section. In fact, the presence of many corners in the geometry of the hexagonal pin leads to higher shear stress and, therefore, higher heat generation. Additionally, the area of this zone is also effective on the heat generation in this solution. By comparing the results obtained from the heat generated around the simple pin, in comparison with the complex pin, according to Fig. (5 b), it can be seen that the heat generated by the complex pin is at least 20% higher than the simple pin, which is due to the presence of sharp corners of the complex pin. Therefore, this causes more heat generation due to shear stress in the specimen.

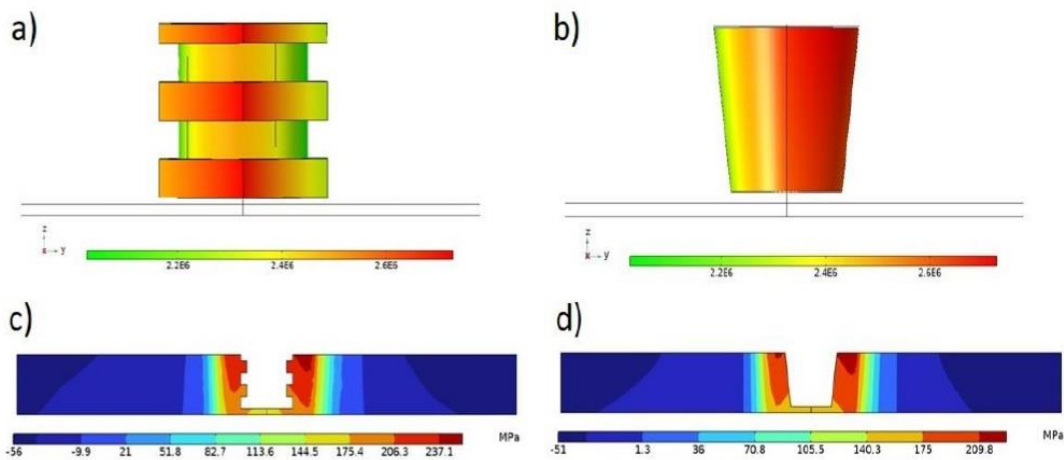


**Fig. 5** Simulated heat generated plot on a complex pin (a) and a simple pin (b), and residual thermal stresses in the cross section of the specimen during FSW with a complex pin (c) and a simple pin (d)

By using the results of temperature distribution and by performing the simulation in the transient state solution, based on the obtained results from steady state solution, the thermal residual stress distribution in the parts was obtained. Fig. (5 c) shows the distribution of residual thermal stress in the cross section of the weld produced with the complex pin. It should be noted that the obtained graph is in good agreement with previous researches (Ref 28,30,37,38). Since the residual thermal stresses are the result of thermal expansion and contraction of the material, by comparing the thermal results and the residual stress simulation results, it can be seen that due to the presence of a region with a maximum temperature in the middle line of welding, the stress in this region is higher and of course it is tensile. In the far areas and around the edge of the workpiece, the stress is compressive.

By comparing the thermal residual stress obtained from the FSW process with the complex pin in comparison with the simple pin, as shown in Fig. (5 d), it can be seen that the residual stress in the case of the simple pin is at least 13% lower than the complex case. The reason for this, as mentioned earlier, is the higher average temperature around the complex pin, due to higher shear stress than the simple pin. This causes the higher maximum temperature in the center line of the weld in the complex pin compared to the simple pin, and therefore the thermal residual stress increases.

Figure (6 a and b) shows the CFD simulation results, material flow velocity, of the FSW process. It can be seen that the maximum velocity of material flow is in the area below the surface of the tool shoulder. The reason for this is the higher temperature under the surface of the tool and the application of more shear stress from the tool in this area. High shear stress and temperature by softening the material and reducing the dynamic viscosity lead to the flow of the material in the direction of tool rotation. Especially in aluminum alloy, which properties are highly dependent on temperature and strain rate.



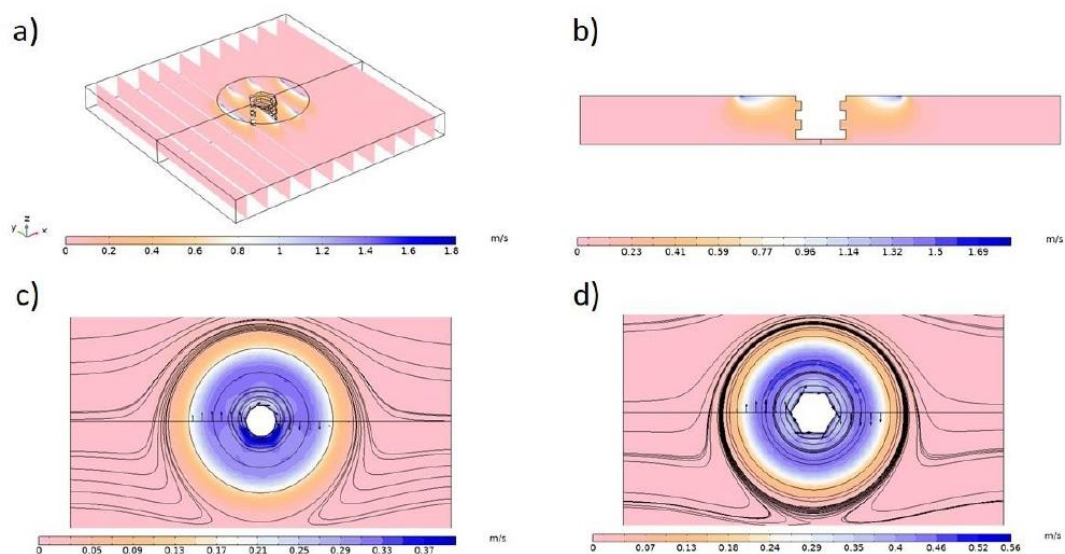


**Fig. 6** 3D (a) and 2D (b) plot of material flow velocity for a complex pin and 2D contour plot in the cross sections around the circular (c) and hexagonal (d) zone of the pin

Figure (6 c and d) shows the velocity of material flow and stream lines around the pin in two circular and hexagonal regions, both in the case of the hexagonal pin. As can be seen, the maximum velocity of the material flow around the hexagonal region is at least 40% higher than the circular one. The reason for this is the higher heat generated around the hexagonal area and also due to the higher shear stresses around the tool in this area, therefore, the dynamic viscosity of the material decreases and as a result, the flow rate increases.

It can be seen that there are flow separations around the hexagonal pin, which took on the hexagonal zone. The reason for these separations is the presence of deformation zones in the pin. These regions are less visible around the circular pin, however, around the circular pin in the RS region there are signs of flow separation, which, due to their polygonal shape, are caused by the flow created by the hexagonal pin at the top and bottom of this area.

By observing the stream lines, it can be seen that the lines around the edges parallel to the shoulder of the tool have more accumulation, this is actually the thermo-mechanically affected zone (TMAZ). In fact, the thermo-mechanical work is more due to the high temperature and strain rate in these areas. On the other hand, around the hexagonal pin, the stream lines have more density than in the circular area, which is because of the existence of shear stresses around the hexagonal pin.

By comparing the results of the material flow during the FSW process in the simple pin compared to the complex pin, according to Figure (7 a and b), it can be seen that the velocity of the material around the pin and under the shoulder of the tool is almost equal. In case of complex pin, according to Fig. (6 b), the flow velocity under the tool is much higher than around the pin. The reason for this is that the flow of the material is wrapped around the pin at different levels of the tool, but in a simple pin, due to the slope, the material finds a simpler flow around the pin, so it has a higher velocity.



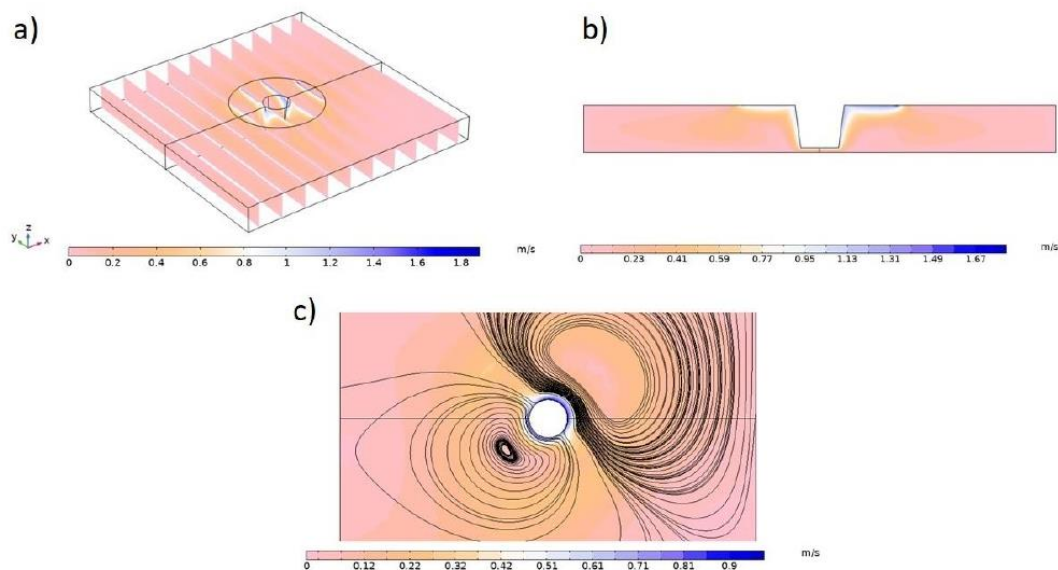


**Fig. 7** 3D (a) and 2D (b) plot of material flow velocity for a simple pin and 2D contour plot in the cross sections around the simple pin (c)

This issue can also be clearly seen in Fig. (7 c), as it can be seen that around the simple pin, in a section, the velocity of the material flow is very high, but in the distant areas, this speed is low. In comparison with Figure (5 c and d), which is related to the complex pin, it can be seen that, whether in the circular region or the hexagonal, the fluidity of the material around the pin is low and it is more in the distant regions. In fact, the presence of a slope in a simple pin causes more flow and the material has a higher flow around the pin. But the presence of different levels for material flow in the complex pin leads to the trapping of the material in one area and the flow around the pin is reduced. Therefore, due to the high shear rate generated by the shoulder of the tool, the velocity of the material increases in the distant areas.

Obviously, the thermomechanical behavior of the material during FSW strongly influences the final microstructural properties and mechanical performances of the welds.

Visual inspections were performed to determine the quality of the produced welds. Fig. (8) presents the images of the weld seam surfaces. In the produced welds, no serious defects like grooves or lacks of bonding were observed. Also, no material outflow was found. In the case of the sample produced with a tapered cylindrical pin (Fig. 8 a) some cavitation loses can be observed. It might be caused by insufficient plasticization of the material due to the lower heat input in the case of the simple pin. The performed computer simulations revealed that by applying the hexagonal pin with grooves, the amount of heat generated during the process is around 20% higher, when compared to the process with the use of tapered cylindrical pin (see Fig. (5 a and b)). This is due to the presence of sharp corners of the complex pin and it causes more heat generation due to shear stress in the specimen. It is claimed that the key factors determining the quality of the weld are adequate heat input and proper stirring of the plasticized material. Therefore, for the weld produced with the hexagonal pin, higher heat input and better plasticization and mixing of the material resulted in the formation of a non-defective weld seam.



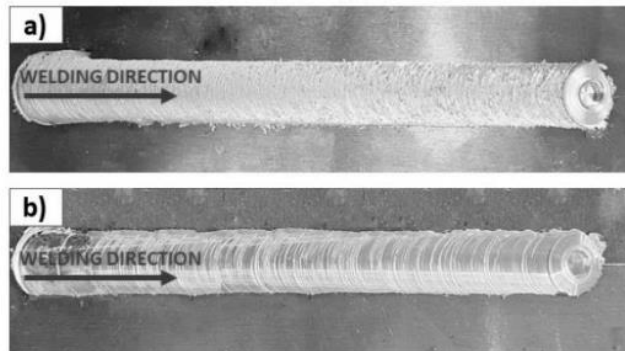


**Fig. 8** Friction stir welded samples produced with the tapered cylindrical pin (a) and the hexagonal pin with grooves (b)

In order to define the influence of the tool geometry on the grain structure of the joints, the macro- and microstructural observations were performed. Fig. (9) presents the macrostructure of the resulting welds and Fig. (10) illustrates the microstructure of the welds in different zones.

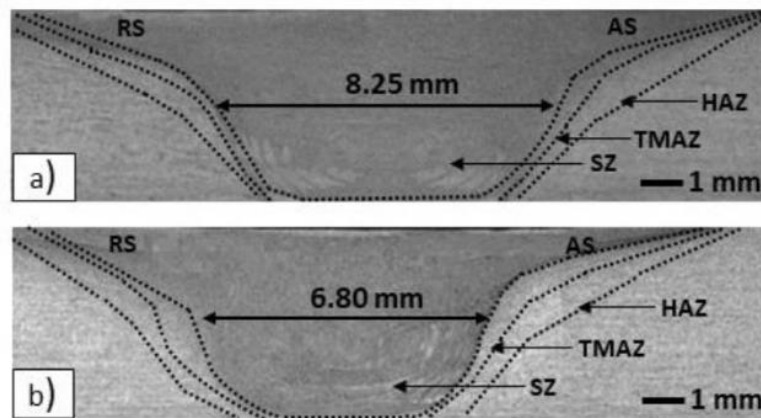


**Fig. 9** Macrostructure of the welds produced with the tapered cylindrical pin (a) and the hexagonal pin with grooves (b)

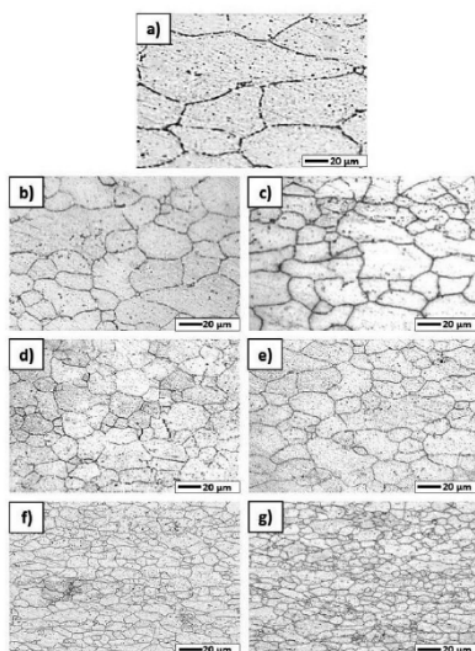


**Fig. 10** Microstructure of the base material AA6082 (a) and welds produced with the tapered cylindrical pin in the HAZ (b), TMAZ (d) and SZ (f) and the hexagonal pin with grooves in the HAZ (c), TMAZ (e) and SZ (g)

Based on the micro- and macrostructure observations it can be concluded that the geometry of the tool strongly influences the macrostructure of the weld. High temperatures, large deformations, strains, strain rate and the total heat input are the factors strongly dependent on the process parameters, including the tool geometry. In the case of the weld produced with the tapered cylindrical pin, the width of the stir zone (SZ) is larger. The width of the SZ measured in the center line of the cross-section was equal to 8.25 mm for the tapered cylindrical pin, and 6.80 mm in the case of the hexagonal pin with grooves. Despite the temperature being about 5% higher when using a complex pin compared to a straight pin and the greater total heat input, the mixing process differed between the two cases. CFD simulation results showed that mixing the plasticized material through the complex pin leads to the trapping of the material in some areas and the flow around the pin is reduced. With a simple pin, due to the slope, the material finds a simpler flow around the pin, so it has a higher velocity, which results in the wider stir zone area. However, higher temperature during the process with the complex pin and the larger total heat input resulted in a wider heat-affected zone (HAZ) comparing the weld produced with the simple pin. It should also be noted that the zone directly under the shoulder is of similar width in both cases, reflecting the geometry of the tool. Simulation results indicated that the material mixing velocity is the highest in this region. This is attributed to higher temperature below the tool surface and higher shear stress applied from the tool. High shear stress and temperature by softening the material and reducing dynamic viscosity lead to the increased flow of the material in the direction of tool rotation. Therefore, the micro- and macrostructure of the upper weld zone is primarily related to the impact of the tool shoulder during the process, rather than the pin itself.

Discussing the obtained pictures it can be noted that no internal defects typical of the FSW process were found. The asymmetries of the weld cross-sections can be clearly observed, indicating the advancing and retreating sides of the welds. The differences mainly relate to the size of the different zones, which is particularly evident in the HAZ. On the AS side, it is larger, which agrees with the results of the simulations performed (Fig. 4 b and d). Typically for a FSW joint, the weld nugget zone consists of a fine-grained structure formed by the recrystallization process in the stir zone (SZ), thermo-mechanically affected zone (TMAZ) and



heat-affected zone (HAZ). In the case of a complex tool, finer grains can be observed in the SZ. Computer simulations demonstrated that during the FSW process using a hexagonal pin with grooves, the maximum temperature in the stirring zone is at least 5% higher compared to a tapered cylindrical pin. Due to the higher heat input, the recrystallization process occurred more efficiently, resulting in a finer-grained microstructure. The average grain size in the SZ of the weld produced with the simple pin was equal to  $14.321 \pm 1.319 \mu\text{m}$ , and for the weld produced with the complex pin  $10.770 \pm 1.386 \mu\text{m}$ . According to the Hall-Petch relationship, smaller grain size affect the increase of the hardness of the material (Ref 39,40). Higher heat input during the FSW process results in greater grain refinement due to more efficient recrystallization, which enhances the strength of the SZ.

The microhardness profiles of the joints produced with the hexagonal pin with grooves and the tapered cylindrical pin tool are presented in Fig. (11).

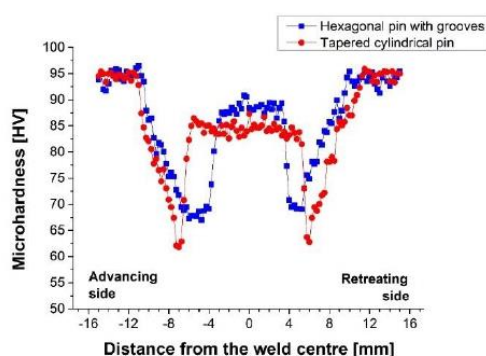


Fig. 11 Microhardness profiled of the FSW joints produced with different tools at the distance of 1.5 mm from the weld face

The microhardness of the base metal AA6082 was established as  $96 \pm 3.9 \text{ HV}$ . It should be noted that the reduction of the microhardness in the entire joint's cross-section can be observed. The highest reduction of the microhardness in both cases can be observed in the heat-affected zones. The lowest values of approximately 62 and 67 HV can be observed on the advancing side of the welds produced with the simple and complex pin, respectively. More significant decrease in hardness in the heat-affected zone on the advancing side is consistent with the results of the simulations performed, where greater heat input was observed on the advancing side for the process involving both tools (Fig. (4 a and b)). As the temperature in the HAZ increases, the process of dissolution of precipitates is intensified, leading to the decrease in strength in this zone. The heat input in the welding process is a crucial factor, as it causes the overaging of the strengthening phase and grain growth. For precipitation-strengthening alloys, such as AA6082, dissolution or coarsening of precipitates lead to drastic reduction in the hardness. For instance,  $\text{Mg}_2\text{Si}$  phases tend to coarsen and dissolve in the aluminum matrix when the temperature exceeds  $250 \text{ }^\circ\text{C}$  (Ref 41). Based on the conducted simulations, by analyzing temperature distribution during the process (Fig. (4 b and d)) it is evident that such temperatures were achieved in HAZ during welding. It should be also noted that the HAZ of HAZ/TMAZ interface is often the location of the failure during tensile tests (Ref 42–44). The results of the simulations clearly indicated the asymmetry of the process and the existence of advancing and retreating sides. Also, the microhardness profile confirms this theory, where different hardness values are observed in different zones on both sides of the weld, as well as their different sizes. The results of simulations indicated that the larger size of the HAZ is observed of the advancing side (Fig. (4 b and d)), which is also noticeable on the microhardness profiles, especially in the case of the weld produced with the complex pin. Also in this case, the location of the HAZ is closer to the weld center, which indicates a smaller size of the stir zone. These observations are in a good agreement with the macrostructural observations (Fig. (9)). In the case of the weld produced with a simple tool, the nugget zone is larger, which was also proved by macroscopic imaging (Fig.

(9)), but the maximum hardness observed is lower than that in the nugget zone of a weld produced with a complex tool. In the nugget zone of the weld produced with the complex tool, the geometry of the hexagonal pin lead to higher shear stress, and therefore, higher heat generation. The conducted simulations revealed that the maximum temperature in the stir zone of the weld produced with complex pin is 5% higher than in the case of the simple pin. It leads to more effective recrystallization process. Microscopic observations allowed to observe lower grain size in the nugget zone of the weld produced with the complex pin. The reduction of the grain size leads to the increase of the hardness, according to the Hall-Petch relationship (Ref 39,40,45). Also, this geometry of the tool promotes better plasticizing and mixing of the material in the nugget zone, leading to more uniform microstructure and reducing the risk of defects resulting from improper mixing of the material.

The produced joints, as well as the base metal were tensile tested on the universal testing machine. Fig. (12) presents the failure locations of the welded samples after tensile tests. Fig. (13) illustrates stress-strain curves for the investigated welds and the base material AA6082 (a) and their average ultimate tensile strength (UTS) values (b).



Fig. 12 Fracture locations of the welds produced with the tapered cylindrical pin (a) and the hexagonal pin with grooves (b)

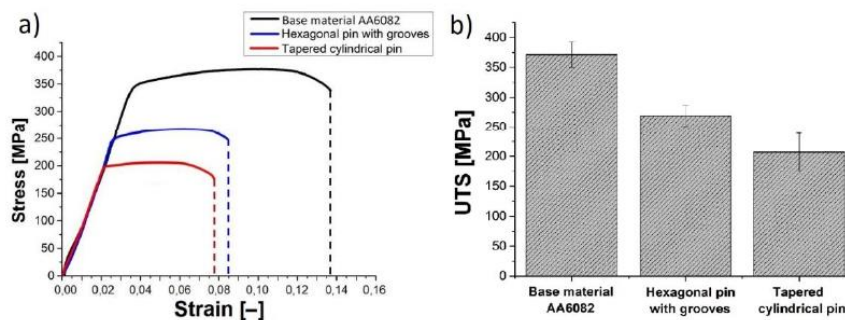
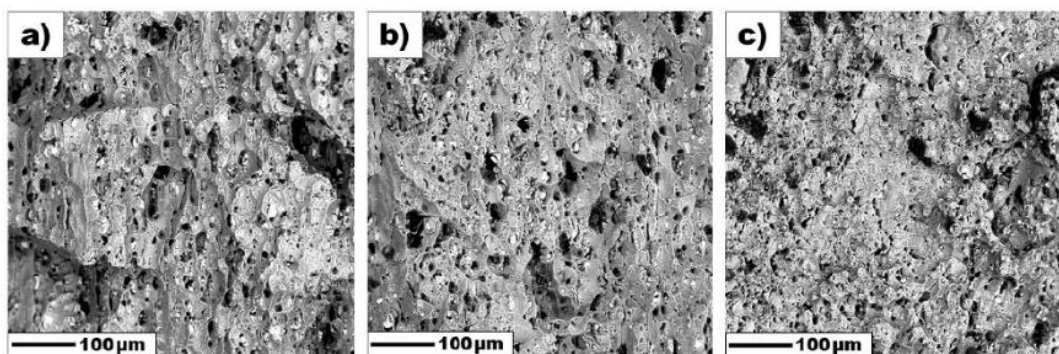


Fig. 13 Stress-strain curves for the produced FSW joints and the base material AA6082 (a) and their average UTS values (b)

The highest value of UTS was found for AA6082 base material equal to  $371 \pm 21$  MPa. In case of the welds, the values of  $269 \pm 18$  MPa and  $207 \pm 32$  MPa were noted for the joints produced with hexagonal pin with grooves and tapered cylindrical pin, respectively. It corresponds to the joint efficiency of  $72.5 \pm 4.9\%$  and  $55.8 \pm 8.6\%$ , respectively. In both of the cases, the location of the failure was detected in the HAZ on advancing side of the welds (Fig. (12)). These observations are consistent with the simulation studies and hardness observations. The lowest hardness was found in the HAZ on AS of the welds for both cases. Also, the larger HAZ was found on the AZ comparing to the HAZ on the RS of the welds. This is due to the increased heat input on the advancing side of the HAZ, as indicated by computer simulations, for both tool geometries. However, it should be noted that the results of computer simulations indicate that the highest thermal stresses of tensile nature, induced by the welding process, occur in the nugget zone. They are caused by the highest heat input in the mixing zone. However, recrystallization occurs in this zone, resulting in a reduction

in grain size and re-precipitation. In the HAZ, due to sufficient heat input, the precipitations dissolve or overaging occurs, where enlargement and roughening of pre-existing particles can be observed, and no recrystallization process occurs (Ref 46). For precipitation hardened alloys like AA6082, the presence of the precipitations is crucial to provide desired mechanical properties. Consequently, in the case of a precipitation hardened alloy such as AA6082, in addition to thermal stresses, the presence of fine precipitates uniformly dispersed in the matrix material, as is the case in the nugget zone, also plays a key role in ensuring adequate mechanical properties. These observations are in a good agreement with the studies of Pabandi et al. (Ref 47) where two precipitation hardened alloys of AA6061 and AA2024 were friction stir welded. Regardless of the positioning of the alloys on AS or RS, the failure location after tensile tests were noted in HAZ. The failure location in the HAZ was also noted by Fathi et al. (Ref 48) for AA6061, Liu et al. (Ref 49) for AA2219, Patel et al. (Ref 50) for AA6063 and Rajendran et al. (Ref 51) for AA2014.

The fractography pictures of the FSW joints and the base material are presented in Fig. (14). As presented before, the fracture of the tested FSW tensile samples located in the HAZ region close to the original joint line on the advancing side. In the case of both welded samples, the fracture surface is quite homogenous. No significant surface irregularities can be observed, due to the fact that both samples ruptured out in the heat-affected zone, where no mixing occurred. It is notable that in the case of welds, the material cracked simultaneously in multiple parallel planes, and the individual cracks are connected together by perpendicular interplanar cracks. Fig. (14 b and c) clearly present that the cracking proceeded in a ductile nature. The surface of the cracks consisted mainly of a large number of shallow and uniform dimples indicating mainly ductile behavior of the material. In the case of the base material (Fig. 14 a), the dominant mechanism was ductile cracking with several brittle precipitations present, around which local voids were formed. The fracture surface of the base material consisting of long and flat areas corresponds to the elongated grains revealed by microstructural observations (Fig. 10 a).



**Fig. 14** Fracture surface of the base material AA6082 (a) and the FSW joints produced with the tapered cylindrical pin (b) and hexagonal pin with grooves (c) subjected to tensile tests

#### 4. Conclusions

The present work focuses on simulation of Friction Stir Welding of AA6082 by applying different tool geometries. This study also presents experimental results that provide microstructural observations and determination of the mechanical properties of the resulting welds. On the base of the experimental and simulation analysis the following conclusions can be determined:

1. Computer simulations revealed that when welding with the tool with a hexagonal pin with grooves the maximum temperature is at least 5% higher than when welding with use of a tapered cylindrical pin with no grooves. The reason for this is the presence of more shear stresses in the corners of the pin and the presence of more heat producing surfaces in the hexagonal pin model. During the welding simulations a maximum temperature of 406 °C was noted for the welding with the complex pin.

2. The residual stresses introduced when using a simple pin are at least 13% lower than in the case of the complex pin. The reason for this is the higher average temperature around the complex pin due to higher shear stresses than in the simple pin. A higher maximum temperature at the weld centerline consequently increased the thermal residual stresses.
3. Material flow during the welding process was simulated and discussed. In the case of the complex pin, the maximum velocity of the material flow around the hexagonal region was at least 40% higher than the circular one, due to the higher heat generated around the hexagonal area, higher shear stresses, lower dynamic viscosity and as a result, higher flow rate. The presence of a slope in the simple pin affected the greater flow of the plasticized material.
4. In the produced welds, greater grain fineness was observed in the SZ as a result of applying the complex pin. In the case of the welds produced with the complex pin, the average grain size in the SZ was equal to  $10.770 \pm 1.386 \mu\text{m}$ , and in the case of the simple pin  $14.321 \pm 1.319 \mu\text{m}$ .
5. Hardness measurements revealed that the weld produced with the complex pin had a higher hardness in the SZ compared to the weld produced with the simple pin, which was consistent with the Hall-Petch relationship. The asymmetry of the hardness profile also indicates the existence of AS and RS.
6. Performed tensile tests revealed that the location of the lowest strength was the HAZ on the advancing side. This location was also characterized with the lowest hardness. The UTS of  $269 \pm 18 \text{ MPa}$  and  $207 \pm 32 \text{ MPa}$  were noted for the joints produced with hexagonal pin with grooves and tapered cylindrical pin, respectively. It corresponded to the joint efficiency of  $72.5 \pm 4.9 \%$  and  $55.8 \pm 8.6 \%$ , respectively.

#### References:

1. A. Laska and M. Szkodo, Manufacturing Parameters, Materials, and Welds Properties of Butt Friction Stir Welded Joints—Overview, *Materials (Basel)*, 2020, **13**, p 1–46.
2. A.R.S. Essa, M.M.Z. Ahmed, A.K.Y.A. Mohamed, and A.E. El-Nikhaily, An Analytical Model of Heat Generation for Eccentric Cylindrical Pin in Friction Stir Welding, *J. Mater. Res. Technol.*, Korea Institute of Oriental Medicine, 2016, **5**(3), p 234–240, doi:10.1016/j.jmrt.2015.11.009.
3. M. Ilangovan, S. Rajendra Boopathy, and V. Balasubramanian, Effect of Tool Pin Profile on Microstructure and Tensile Properties of Friction Stir Welded Dissimilar AA 6061–AA 5086 Aluminium Alloy Joints, *Def. Technol.*, Elsevier Ltd, 2015, **11**(2), p 174–184, doi:10.1016/j.dt.2015.01.004.
4. P. Cavaliere, Friction Stir Welding of Al Alloys: Analysis of Processing Parameters Affecting Mechanical Behavior, *Procedia CIRP*, Elsevier B.V., 2013, **11**, p 139–144, doi:10.1016/j.procir.2013.07.039.
5. A. Laska, M. Szkodo, Ł. Pawłowski, and G. Gajowiec, Corrosion Properties of Dissimilar AA6082/AA6060 Friction Stir Welded Butt Joints in Different NaCl Concentrations, *Int. J. Precis. Eng. Manuf. - Green Technol.*, 2022.
6. A. Laska, M. Szkodo, P. Cavaliere, D. Moszczyńska, and J. Mizera, Analysis of Residual Stresses and Dislocation Density of AA6082 Butt Welds Produced by Friction Stir Welding, *Metall. Mater. Trans. A*, 2022.
7. S. Lim, S. Kim, C.G. Lee, and S. Kim, Tensile Behavior of Friction-Stir-Welded Al 6061-T651, *Metall. Mater. Trans. A Phys. Metall. Mater. Sci.*, 2004, **35 A**(9), p 2829–2835.
8. A. Bandi and S.R. Bakshi, Effect of Pin Length and Rotation Speed on the Microstructure and Mechanical Properties of Friction Stir Welded Lap Joints of AZ31B-H24 Mg Alloy and AA6061-T6 Al Alloy, *Metall. Mater. Trans. A Phys. Metall. Mater. Sci.*, Springer US, 2020, **51**(12), p 6269–6282, doi:10.1007/s11661-020-06020-8.
9. A.H. Feng, D.L. Chen, and Z.Y. Ma, Microstructure and Cyclic Deformation Behavior of a Friction-Stir-

Welded 7075 Al Alloy, *Metall. Mater. Trans. A Phys. Metall. Mater. Sci.*, 2010, **41**(4), p 957–971.

10. A.H. Lotfi and S. Nourouzi, Effect of Welding Parameters on Microstructure, Thermal, and Mechanical Properties of Friction-Stir Welded Joints of Aa7075-T6 Aluminum Alloy, *Metall. Mater. Trans. A Phys. Metall. Mater. Sci.*, 2014, **45**(6), p 2792–2807.
11. G. Ipekoglu, S. Erim, and G. Cam, Investigation into the Influence of Post-Weld Heat Treatment on the Friction Stir Welded AA6061 Al-Alloy Plates with Different Temper Conditions, *Metall. Mater. Trans. A Phys. Metall. Mater. Sci.*, 2014, **45**(2), p 864–877.
12. T.U. Seidel and A.P. Reynolds, Visualization of the Material Flow in AA2195 Friction-Stir Welds Using a Marker Insert Technique, *Metall. Mater. Trans. A Phys. Metall. Mater. Sci.*, 2001, **32**(11), p 2879–2884.
13. G.J. Bendzsak, T.H. North, and C.B. Smith, “An Experimentally Validated 3D Model for Friction Stir Welding,” *Proceedings of the Second International Symposium of FSW, Gothenbutg*, 2000.
14. P. Ulysse, Three-Dimensional Modeling of the Friction Stir-Welding Process, *Int. J. Mach. Tools Manuf.*, 2002, **42**(14), p 1549–1557.
15. P.A. Colegrove and H.R. Shercliff, Experimental and Numerical Analysis of Aluminium Alloy 7075-T7351 Friction Stir Welds, *Sci. Technol. Weld. Join.*, 2003, **8**(5), p 360–368.
16. P.A. Colegrove and H.R. Shercliff, 3-Dimensional CFD Modelling of Flow Round a Threaded Friction Stir Welding Tool Profile, *J. Mater. Process. Technol.*, 2005, **169**(2), p 320–327.
17. R. Nandan, G.G. Roy, T.J. Lienert, and T. Debroy, Three-Dimensional Heat and Material Flow during Friction Stir Welding of Mild Steel, *Acta Mater.*, 2007, **55**(3), p 883–895.
18. R. Nandan, G.G. Roy, T.J. Lienert, and T. Debroy, Numerical Modelling of 3D Plastic Flow and Heat Transfer during Friction Stir Welding of Stainless Steel, *Sci. Technol. Weld. Join.*, 2006, **11**(5), p 526–537.
19. R. Nandan, G.G. Roy, and T. Debroy, Numerical Simulation of Three Dimensional Heat Transfer and Plastic Flow during Friction Stir Welding, *Metall. Mater. Trans. A Phys. Metall. Mater. Sci.*, 2006, **37**(4), p 1247–1259.
20. D. Kim, H. Badarinarayan, J.H. Kim, C. Kim, K. Okamoto, R.H. Wagoner, and K. Chung, Numerical Simulation of Friction Stir Butt Welding Process for AA5083-H18 Sheets, *Eur. J. Mech. A/Solids*, Elsevier Masson SAS, 2010, **29**(2), p 204–215, doi:10.1016/j.euromechsol.2009.10.006.
21. J.N. Reddy and D.K. Gartling, “The Finite Element Method in Heat Transfer and Fluid Dynamics,” CRC Press, 2010.
22. A.F. Hasan, C.J. Bennett, P.H. Shipway, S. Cater, and J. Martin, A Numerical Methodology for Predicting Tool Wear in Friction Stir Welding, *J. Mater. Process. Technol.*, Elsevier B.V., 2017, **241**, p 129–140, doi:10.1016/j.jmatprotec.2016.11.009.
23. S.D. Ji, Q.Y. Shi, L.G. Zhang, A.L. Zou, S.S. Gao, and L. V. Zan, Numerical Simulation of Material Flow Behavior of Friction Stir Welding Influenced by Rotational Tool Geometry, *Comput. Mater. Sci.*, 2012, **63**, p 218–226.
24. L. Zhang, S. Ji, G. Luan, C. Dong, and L. Fu, Friction Stir Welding of Al Alloy Thin Plate by Rotational Tool without Pin, *J. Mater. Sci. Technol.*, 2011, **27**(7), p 647–652.
25. S. Hirasawa, H. Badarinarayan, K. Okamoto, T. Tomimura, and T. Kawanami, Analysis of Effect of Tool Geometry on Plastic Flow during Friction Stir Spot Welding Using Particle Method, *J. Mater. Process. Technol.*, Elsevier B.V., 2010, **210**(11), p 1455–1463, doi:10.1016/j.jmatprotec.2010.04.003.



26. Z. Yu, W. Zhang, H. Choo, and Z. Feng, Transient Heat and Material Flow Modeling of Friction Stir Processing of Magnesium Alloy Using Threaded Tool, *Metall. Mater. Trans. A Phys. Metall. Mater. Sci.*, 2012, **43**(2), p 724–737.
27. A. Laska, M. Szkodo, D. Koszelow, and P. Cavaliere, Effect of Processing Parameters on Strength and Corrosion Resistance of Friction Stir-Welded AA6082, *Metals (Basel)*, 2022, **12**(192), p 1–16.
28. X.K. Zhu and Y.J. Chao, Numerical Simulation of Transient Temperature and Residual Stresses in Friction Stir Welding of 304L Stainless Steel, *J. Mater. Process. Technol.*, 2004, **146**(2), p 263–272.
29. A.R. Darvazi and M. Iranmanesh, Prediction of Asymmetric Transient Temperature and Longitudinal Residual Stress in Friction Stir Welding of 304L Stainless Steel, *Mater. Des.*, Elsevier Ltd, 2014, **55**, p 812–820, doi:10.1016/j.matdes.2013.10.030.
30. M.Z.H. Khandkar, J.A. Khan, A.P. Reynolds, and M.A. Sutton, Predicting Residual Thermal Stresses in Friction Stir Welded Metals, *J. Mater. Process. Technol.*, 2006, **174**(1–3), p 195–203.
31. M.A. Waheed, L.O. Jayesimi, S.O. Ismail, and O.U. Dairo, Modeling of Heat Generations for Different Tool Profiles in Friction Stir Welding: Study of Tool Geometry and Contact Conditions, *J. Appl. Comput. Mech.*, 2017, **3**(1), p 37–59.
32. Y. Zhu, G. Chen, Q. Chen, G. Zhang, and Q. Shi, Simulation of Material Plastic Flow Driven by Non-Uniform Friction Force during Friction Stir Welding and Related Defect Prediction, *Mater. Des.*, Elsevier Ltd, 2016, **108**, p 400–410, doi:10.1016/j.matdes.2016.06.119.
33. G.Q. Chen, Q.Y. Shi, Y.J. Li, Y.J. Sun, Q.L. Dai, J.Y. Jia, Y.C. Zhu, and J.J. Wu, Computational Fluid Dynamics Studies on Heat Generation during Friction Stir Welding of Aluminum Alloy, *Comput. Mater. Sci.*, Elsevier B.V., 2013, **79**, p 540–546, doi:10.1016/j.commatsci.2013.07.004.
34. M.M. El-Sayed, A.Y. Shash, and M. Abd-Rabou, Finite Element Modeling of Aluminum Alloy AA5083-O Friction Stir Welding Process, *J. Mater. Process. Technol.*, Elsevier, 2018, **252**(September 2017), p 13–24, doi:10.1016/j.jmatprotec.2017.09.008.
35. B. Sadeghian, A. Taherizadeh, M. Atapour, N. Saeidi, and A. Alhaji, Phase-Field Simulation of Microstructure Evolution during Friction Stir Welding of 304 Stainless Steel, *Mech. Mater.*, Elsevier Ltd, 2021, **163**(July), p 104076, doi:10.1016/j.mechmat.2021.104076.
36. B. Sadeghian, A. Taherizadeh, and M. Atapour, Simulation of Weld Morphology during Friction Stir Welding of Aluminum-Stainless Steel Joint, *J. Mater. Process. Technol.*, Elsevier, 2018, **259**(February), p 96–108, doi:10.1016/j.jmatprotec.2018.04.012.
37. M. Riahi and H. Nazari, Analysis of Transient Temperature and Residual Thermal Stresses in Friction Stir Welding of Aluminum Alloy 6061-T6 via Numerical Simulation, *Int. J. Adv. Manuf. Technol.*, 2011, **55**(1–4), p 143–152.
38. P. Poolperm, W. Nakkiew, and N. Naksuk, Finite Element Analysis of the Effect of Porosity on Residual Stress in 2024 Aluminium Alloy GTAW, *Mater. Res. Express*, IOP Publishing, 2020, **7**(5), p 56518, doi:10.1088/2053-1591/ab906a.
39. S.N. Naik and S.M. Walley, The Hall–Petch and Inverse Hall–Petch Relations and the Hardness of Nanocrystalline Metals, *J. Mater. Sci.*, Springer US, 2020, **55**(7), p 2661–2681, doi:10.1007/s10853-019-04160-w.
40. K. Surekha and A. Els-Botes, Development of High Strength, High Conductivity Copper by Friction Stir Processing, *Mater. Des.*, Elsevier Ltd, 2011, **32**(2), p 911–916, doi:10.1016/j.matdes.2010.08.028.
41. C.B. Fuller and D.N. Seidman, Temporal Evolution of the Nanostructure of Al(Sc,Zr) Alloys: Part II-Coarsening of Al<sub>3</sub>(Sc<sub>1-x</sub>Zr<sub>x</sub>) Precipitates, *Acta Mater.*, 2005, **53**(20), p 5415–5428.



42. Z. Zhang, B.L. Xiao, and Z.Y. Ma, Effect of Welding Parameters on Microstructure and Mechanical Properties of Friction Stir Welded 2219Al-T6 Joints, *J. Mater. Sci.*, 2012, **47**(9), p 4075–4086.
43. R. Kosturek, J. Torzewski, M. Wachowski, and L. Śnieżek, Effect of Welding Parameters on Mechanical Properties and Microstructure of Friction Stir Welded AA7075-T651 Aluminum Alloy Butt Joints, *Materials (Basel)*, 2022, **15**(5950), p 1–15.
44. W. Wang, S. Zhang, K. Qiao, K. Wang, P. Peng, S. Yuan, S. Chen, T. Zhang, Q. Wang, T. Liu, and Q. Yang, Microstructure and Mechanical Properties of Friction Stir Welded Joint of TRIP Steel, *J. Manuf. Process.*, Elsevier, 2020, **56**(13), p 623–634, doi:10.1016/j.jmapro.2020.05.045.
45. N.K. Babu, K. Kallip, M. Leparoux, K.A. AlOgab, X. Maeder, and Y.A.R. Dasilva, Influence of Microstructure and Strengthening Mechanism of AlMg5-Al<sub>2</sub>O<sub>3</sub> Nanocomposites Prepared via Spark Plasma Sintering, *Mater. Des.*, Elsevier B.V., 2016, **95**, p 534–544, doi:10.1016/j.matdes.2016.01.138.
46. M.M. Krishnan, Overview of the Effect of Post Welded Heat Treatment on Friction Stir Welding Of Aluminum Alloys, *Int. J. Eng. Innov. Technol.*, 2013, **2**(9), p 76–80.
47. H.K. Pabandi, H.R. Jashnani, and M. Paidar, Effect of Precipitation Hardening Heat Treatment on Mechanical and Microstructure Features of Dissimilar Friction Stir Welded AA2024-T6 and AA6061-T6 Alloys, *J. Manuf. Process.*, The Society of Manufacturing Engineers, 2018, **31**(November 2017), p 214–220, doi:10.1016/j.jmapro.2017.11.019.
48. J. Fathi, P. Ebrahimzadeh, R. Farasati, and R. Teimouri, Friction Stir Welding of Aluminum 6061-T6 in Presence of Watercooling: Analyzing Mechanical Properties and Residual Stress Distribution, *Int. J. Light. Mater. Manuf.*, Elsevier Ltd, 2019, **2**(2), p 107–115, doi:10.1016/j.ijlmm.2019.04.007.
49. H.J. Liu, H.J. Zhang, Y.X. Huang, and L. Yu, Mechanical Properties of Underwater Friction Stir Welded 2219 Aluminum Alloy, *Trans. Nonferrous Met. Soc. China (English Ed.)*, The Nonferrous Metals Society of China, 2010, **20**(8), p 1387–1391, doi:10.1016/S1003-6326(09)60309-5.
50. V. Patel, J. De Backer, H. Hindsefelt, M. Igestrand, S. Azimi, J. Andersson, and J. Säll, High Speed Friction Stir Welding of AA6063-T6 Alloy in Lightweight Battery Trays for EV Industry: Influence of Tool Rotation Speeds, *Mater. Lett.*, 2022, **318**(March).
51. C. Rajendran, G. Parthiban, K. Pranav, and S.P. Nithi Balaji, Influence of Solution Treatment and Artificial Aging On Fracture Load of Friction Stir Welded Lap Joints of AA2014-T6, *IOP Conf. Ser. Mater. Sci. Eng.*, 2021, **1059**(1).

**Statements and Declarations:**

**Funding:** The authors declare that no funds, grants, or other support were received during the preparation of this manuscript.

**Data availability:** The datasets generated during and/or analysed during the current study are available from the corresponding author on reasonable request.

**Authors' contributions:** All authors contributed to the study conception and design. Material preparation, data collection and analysis were performed by all authors. The first draft of the manuscript was written by Aleksandra Laska, Behzad Sadeghi, Behzad Sadeghian, Aboozar Taherizadeh and Pasquale Cavaliere and all authors commented on previous versions of the manuscript. All authors read and approved the final manuscript.

**Competing Interests:** The authors have no relevant financial or non-financial interests to disclose.

#### **7.4. [P4] Effect of Processing Parameters on Strength and Corrosion Resistance of Friction Stir-Welded AA6082.**

**Laska A.**, Szkodo M., Koszlow D., Cavaliere P.\*, Effect of Processing Parameters on Strength and Corrosion Resistance of Friction Stir-Welded AA6082. *Metals*. 12(2), 192; 2022. doi:10.3390/met12020192. (IF = 2.695, 70 points of the Polish Ministry of Science and Higher Education)

##### 7.4.1. Declaration of the contribution of the doctoral candidate

My contribution to the preparation of the manuscript was the preparation of the literature review and the acquisition of the study material. I developed the methodology of the experiments. I fabricated AA6082 aluminum alloy specimens by the FSW method using two different rotational speeds, two traverse speeds, and two tool tilt angles. I conducted a visual inspection and microscopic examination. I examined the microhardness of the samples on cross-sections. I performed potentiodynamic tests and Tafel extrapolation. I analyzed the obtained research results. I conducted a discussion in the manuscript. I prepared figures and tables and drafted the entire manuscript. I prepared responses to reviewers.

My percentage contribution to the preparation of the manuscript was equal to 60 %.

.....  
Aleksandra Laska





Article

## Effect of Processing Parameters on Strength and Corrosion Resistance of Friction Stir-Welded AA6082

Aleksandra Laska <sup>1</sup>, Marek Szkodo <sup>1</sup>, Damian Koszelow <sup>2</sup> and Pasquale Cavaliere <sup>3,\*</sup>

- <sup>1</sup> Faculty of Mechanical Engineering and Ship Technology, Gdansk University of Technology, Narutowicza 11/12, 80-233 Gdansk, Poland; aleksandra.laska@pg.edu.pl (A.L.); mskzodo@pg.edu.pl (M.S.)
- <sup>2</sup> Faculty of Electronics, Telecommunications and Informatics, Gdansk University of Technology, Narutowicza 11/12, 80-233 Gdansk, Poland; damian.koszelow@pg.edu.pl
- <sup>3</sup> Department of Innovation Engineering, University of Salento, Via per Amesano, 73100 Lecce, Italy
- \* Correspondence: pasquale.cavaliere@unisalento.it

**Abstract:** The friction stir welding method is increasingly attracting interest in the railway sector due to its environmental friendliness, low cost, and ease of producing high-quality joints. Using aluminum alloys reduces the weight of structures, increasing their payload and reducing fuel consumption and running costs. The following paper presents studies on the microstructure, strength, and corrosion resistance of AA6082 aluminum alloy sheets joined via friction stir welding. The sheets were joined by employing two different traverse speeds (200 and 250 mm/min), two different rotational speeds (1000 and 1250 rpm), and two different tool tilt angles (0° and 2°). It was observed that the use of the inclined tool provides finer microstructure in the nugget zone, higher value of microhardness, and better corrosion resistance, compared to the tilt angle equal to 0°. By increasing the value of revolutionary pitch, finer grains are observed in the nugget zone and the measured hardness is higher. It was also observed that the change in process parameters strongly influences the radius of the nugget zone and the potentiodynamic properties of the friction stir-welded material. The joints produced with the tool tilt angle equal to 2°, the tool traverse speed of 200 mm/min, and its rotational speed of 1250 rpm revealed the highest hardness in the nugget zone (about 92% of the base material). Moreover, the finest grain size in the nugget with the average value of  $9.8 \pm 1.5 \mu\text{m}$  was found. The lowest corrosion current density equal to  $16.029 \mu\text{A cm}^{-2}$  was noted for the sample with the highest strength, which also provides its good corrosion resistance.

**Keywords:** friction stir welding; aluminum alloy; mechanical properties; corrosion; potentiodynamic behavior



**Citation:** Laska, A.; Szkodo, M.; Koszelow, D.; Cavaliere, P. Effect of Processing Parameters on Strength and Corrosion Resistance of Friction Stir-Welded AA6082. *Metals* **2022**, *12*, 192. <https://doi.org/10.3390/met12020192>

Academic Editor: Byeong Choon Goo

Received: 30 December 2021  
Accepted: 19 January 2022  
Published: 20 January 2022

**Publisher's Note:** MDPI stays neutral with regard to jurisdictional claims in published maps and institutional affiliations.



**Copyright:** © 2022 by the authors. Licensee MDPI, Basel, Switzerland. This article is an open access article distributed under the terms and conditions of the Creative Commons Attribution (CC BY) license (<https://creativecommons.org/licenses/by/4.0/>).

### 1. Introduction

Friction stir welding (FSW) is a solid-state joining technique developed three decades ago at The Welding Institute of the United Kingdom [1]. During the process, a specially designed non-consumable tool, consisting of a pin and a shoulder rotates and moves along the weld line, while inserted between the contact line of two sheets to be joined. The friction generated by the contact of the rotating shoulder with the component surface generates intense heating always well below the melting point of the joined materials [2]. As the solid-state nature of the process is retained, the maximum temperature can approach up to 0.95 of the melting temperature  $T_M$ , depending on the process parameters, tool geometry, and material to be friction stir welded [3,4]. The plasticized material undergoes severe plastic deformations and its flow around the pin produces complex patterns from the advancing side, where the rotational direction and the welding direction are the same, to the retreating side, where the directions are opposite. Generally, FSW does not produce symmetric deformation with respect to the center line of the advancing tool. When a clockwise direction rotation is employed the less resistant area is the one on the advancing side of the tool [5].

Aluminum alloys, belonging to the 6xxx series, are among the most employed materials for transportation, aerospace, and marine industries. They are characterized by silicon and magnesium elements added to induce intense second phases precipitation during thermo-mechanical treatments [6–8]. Owing to their stiffness, aluminum alloys can reduce the weight of structures by up to three times compared to steel structures. This aspect is crucial in transportation applications [9,10]. Using aluminum in train carriage bodies reduces the weight and energy amount that is needed to accelerate and decelerate them. Owing to this feature, the payload of vehicles can be increased, which leads to reduced fuel consumption and lower machine running costs [11]. According to The Welding Institute of the United Kingdom, there is an increasing number of railway sector companies applying the FSW method in the vehicle constructions. Many international companies leading the rail industry use the FSW method to create many series of trains and vehicles serving subway lines around the world [12].

6082 aluminum alloy has the highest strength of 6000 series in plate form [13–15]. It shows excellent machinability, good welding performances, and high corrosion resistance [16]. AA6082 alloy is widely used in the high-speed train industry, such as profiles and carriage components [17,18]. Conventional welding methods might lead to the formation of defects due to the change of state, such as poor solidification and porosity in the nugget zone. FSW allows to improve the weld quality and is widely used in joining AA6082 alloy [19–22]. Fewer scientific evidence are present in the literature on the effect of processing parameters on the electrochemical behavior of friction stir-welded AA6082 sheets. Gharavi et al. [23] investigated the electrochemical properties of AA6061-T6 alloy butt welds. It was revealed that the friction stir welds produced with the tool traverse speed of 60 mm/min, tool rotational speed equal to 1000 rpm, and tool tilt angle of 3° showed lower electrochemical properties in 3.5 (wt)% NaCl solution compared to the base material. The intergranular corrosion type was dominant, with a small number of pits observed on the weld surface. On the other hand, Padovani et al. [24] noted that the pitting corrosion occurs on the friction stir welds and the base materials of AA2024 T351 and AA7449-T7951, but the weld region exhibited higher susceptibility to corrosion losses compared to the base material after the exposure to 0.1 M NaCl solution. In the studies of Ales et al. [25] the AA2024-T4 butt weld was produced with a tool traverse speed of 100 mm/min, tool rotational speed of 1000 rpm, and tool tilt angle 2°. It was noted that the most serious corrosion losses occurred in the weld nugget zone while exposed to 3.5 (wt)% NaCl solution. In the studies, also the finest microstructure of the nugget zone was found, and a significant drop of the hardness in the thermo-mechanically affected zone was noted. No influence of the process parameters on the properties of the joints was investigated.

As general behavior, tool shoulder and pin geometries and types have a large influence on the microstructural and mechanical properties of FSWed joints [26]. In [27], Rambabu et al. developed a mathematical model for a friction stir-welded AA2219 aluminum alloy sample immersed in 3.5 (wt)% NaCl solution. The influence of process parameters on the electrochemical properties of the samples was investigated. It was revealed that the shape of the pin has also a crucial effect on the friction stir-welded structure and the corrosion properties. The best quality was attained with a hexagonal pin shape. For a hexagonal pin shape, the highest hardness was noted for AA6082-T6 friction stir welds, produced with different welding speed values by Patil et al. [28]. This is generally due to the fact that, by employing such a hexagonal shape, it is demonstrated that the material mixing is optimized during welding. This is mainly due to the phenomenon of reprecipitation because of the increased heating due to the complex geometry [29].

The purpose of this study was to analyze the effect of friction stir welding parameters such as tool traverse speed, tool rotational speed and its tilt angle on microstructure, hardness and electrochemical properties of AA6082 friction stir welds by employing a special designed hexagonal pin tool.

## 2. Materials and Methods

Base material AA6082 aluminum alloy, solution heat-treated and artificially aged to T651 condition, was used for the above studies. The chemical composition of the chosen alloy was determined by the X-ray energy-dispersive spectrometer (EDS) (Edax Inc., Mahwah, NJ, USA) and is shown in Table 1.

**Table 1.** Chemical composition of AA6082.

	Chemical Composition [wt%]								
	Zn	Mg	Cr	Ti	Fe	Si	Cu	Mn	Al
AA6082	0.20	1.03	0.25	0.10	0.50	0.90	0.10	0.42	Balance

About 3-mm-thick plates were used to perform the friction stir welding process on a conventional milling machine (FU251, Friedrich Engels Kazanluk, Bulgaria). Figure 1 depicts the tool adopted for studies. The tool of 18 mm shoulder diameter, with the distance across flats of the hexagonal pin was equal to 6 mm and the pin length equal to 2.5 mm was used to produce the butt welds. The shoulder plunge depth was equal to 0.3 mm. The hexagonal pin with grooves was made of 73MoV52 steel and the shoulder material was X210Cr12 steel. The measured hardness of the pin and the shoulder were equal to 58 and 61 HRC (Wilson Mechanical Instrument Co. Inc., New York, NY, USA), respectively. Based on an extensive literature review, published in [2], the following process parameters were selected for the studies: the FSW process was performed at two different travel speeds: 200 and 250 mm/min, two different rotational speeds: 1000 and 1250 rpm, and two different tilt angles: 0° and 2°. The tilt direction of the tool was opposite to the direction of its traverse motion. The designation of the samples is shown in Table 2. The revolutionary pitch values, defined as the tool rotational speed divided by the tool traverse speed, are also presented in Table 2.

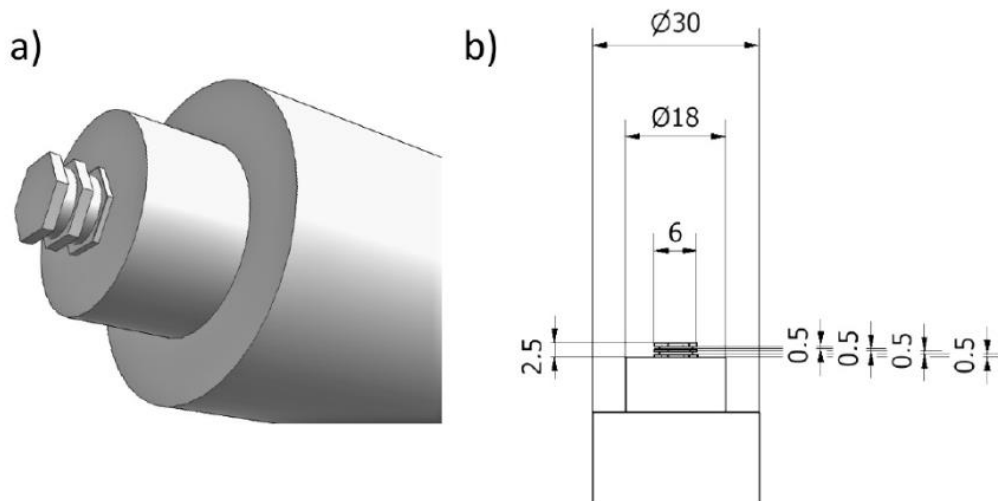


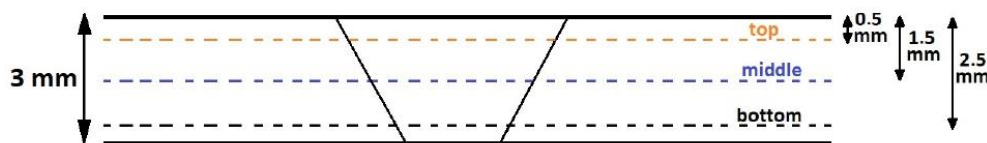
**Figure 1.** Schematic illustration of the geometry of the tool used for FSW of AA6082 (a) with its dimensions (b).



**Table 2.** Designation of the samples, corresponding process parameters and revolutionary pitch values.

Sample	Tool Rotational Speed [rpm]	Tool Travel Speed [mm/min]	Tool Tilt Angle [°]	Revolutionary Pitch [rot/min]
FSW1	1000	200	0	5
FSW2	1000	250	0	4
FSW3	1250	200	0	6.25
FSW4	1250	250	0	5
FSW5	1000	200	2	5
FSW6	1000	250	2	4
FSW7	1250	200	2	6.25
FSW8	1250	250	2	5

To determine the microstructure of the produced friction stir welds, the samples were wet ground to the final gradation #4000 and polished with a 1  $\mu\text{m}$  diamond suspension. The microstructure was analyzed by employing Keller's etchant (95 mL H<sub>2</sub>O, 2.5 mL HNO<sub>3</sub>, 1.5 mL HCl, 1 mL HF). For microstructure observations the double-staged etching in Weck's etchant was performed. At the first stage, the samples were etched in a solution of 2 (wt)% NaOH for 1 min. Then, the samples were immersed in a reagent containing 4 g KMnO<sub>4</sub>, 1 g NaOH, and 100 mL H<sub>2</sub>O. The microstructure of the samples was observed by an optical microscope (BX51, OLYMPUS, Tokyo, Japan). To calculate the average grain size in the nugget zone, ten measurements were performed. The microhardness measurements were performed using a Vickers microhardness tester (Future-Tech FM-800, Tokyo, Japan) with the load of 2 N. Figure 2 presents the locations of the microhardness measurements on the cross-sections of all the samples.

**Figure 2.** Hardness measurement locations on the cross-sections of the friction stir-welded samples.

Electrochemical measurements were performed according to the ASTM G5-94 "Standard reference test method for making potentiostatic and potentiodynamic anodic polarization measurements". Potentiostat/galvanostat (Atlas 0531, Atlas Sollich, Rebiechowo, Poland) was used for the tests in 3.5 (wt)% NaCl (99.8% purity, CHEMPUR, Piekary Śląskie, Poland) solution at the controlled temperature of 20 °C. Samples of the area of 1 cm<sup>2</sup> taken from the nugget zone and AA6082 as received material were studied. A three-electrode system containing a platinum electrode as a counter electrode, a saturated calomel electrode as a reference, and an aluminum sample as a working electrode was used. The open circuit potential (OCP) within 60 min initiated the measurements. The potentiodynamic method was used to obtain the corrosion curves for the potential range  $-2/+1$  V with a potential scan rate equal to 1 mV/s. To determine the values of the corrosive potential ( $E_{\text{corr}}$ ) and the corrosion current density ( $i_{\text{corr}}$ ) the Tafel extrapolation method was adopted using AtlasLab (Atlas Sollich, Rebiechowo, Poland) software (ATLAS 0532 Electrochemical unit and Impedance Analyser). After the corrosion studies the surfaces of all the friction stir-welded samples and the base material were observed using a high resolution scanning electron microscope (SEM) (Phenom XL, Thermo Fisher Scientific, Breda, Netherlands) with a backscattered electron detector (BSE).

### 3. Results and Discussion

The results of visual testing of the produced friction stir welds are presented in Figure 3. The pictures present the area containing the exact nugget zone cutout location for electrochemical testing. It was observed that the top surfaces exhibit no serious imperfections

like grooves or lack of bonding. A very little material outflow on the retreating side was noticed on samples FSW1–FSW4 (Figure 3a–d). No visible differences were detected on the top surface of all the produced friction stir welds.

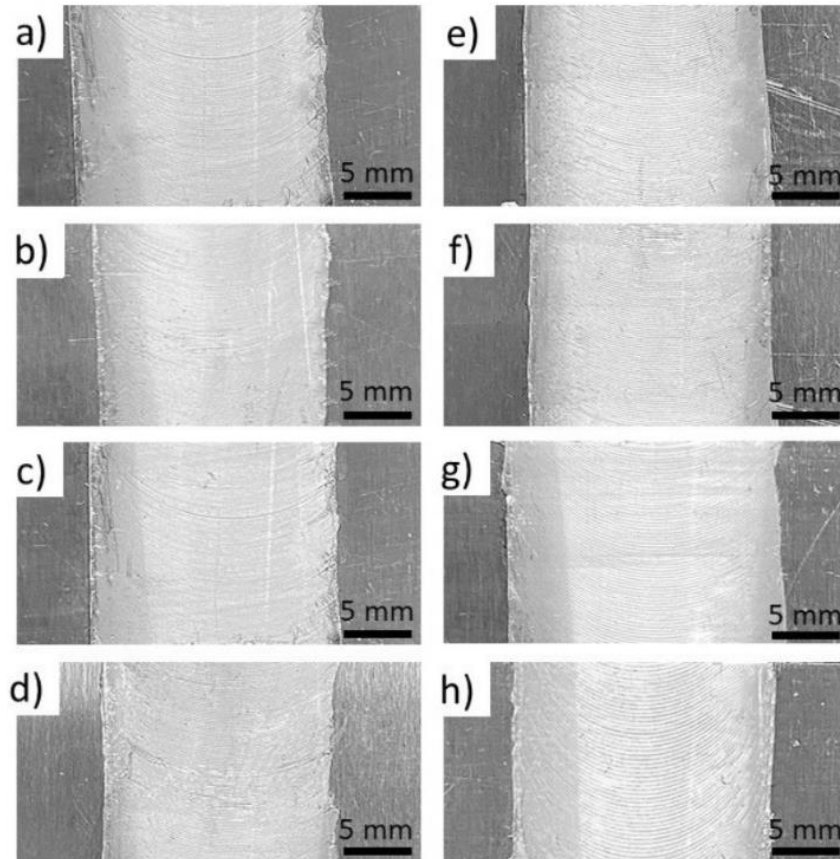


**Figure 3.** Top view of the friction stir welds surface—FSW1 (a), FSW2 (b), FSW3 (c), FSW4 (d), FSW5 (e), FSW6 (f), FSW7 (g) and FSW8 (h).

The macro and microstructure of one, representative friction stir weld (FSW7) is shown in Figure 4. The macroscopic evaluation (Figure 4a) allowed to observe the characteristic shape of the nugget zone, resulting from the movement of the pin between the sheets. The microscopic observations provided more information regarding the microstructure of the friction stir welds. Four characteristic zones for FSWs were recognized. Microstructure evolution during the process depends on the temperature and strain endured by welded material. High temperature changes, observed in the weld nugget zone (WN), as well as thermo-mechanically affected zone (TMAZ) and heat-affected zone (HAZ) result in characteristic microstructures. The weld nugget zone, where the plastic deformation and temperature are the highest is characterized by the finest structure, due to the dynamic recrystallization process. Figure 4b presents the nugget zone microstructure of the FSW 7 sample. Process parameters such as traverse and rotational speed and tool tilt angle have a significant influence on the final microstructure, due to the different heat input. The average grain sizes in the WN zone for all samples tested are shown in Table 3. A thermo-mechanically affected zone (Figure 4c) also experiences high temperature and

mechanical deformation due to the movement of the pin, but no recrystallization is observed. The heat affected zone (Figure 4d) is only affected by thermal evolution, and with increasing the distance from the nugget zone, the base metal (BM) is retrieved (Figure 4e). In the base metal the observed elongated grains are the result of the sheet preparation process by rolling.

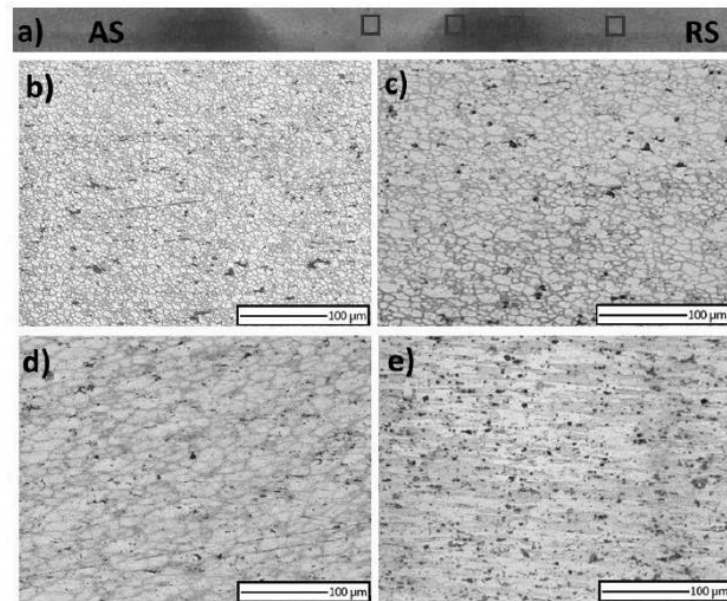


**Figure 4.** Macrostructure of FSW7 sample with the locations of microscopic observations (a) and its microstructures observed in the nugget zone (b), thermo-mechanically affected zone (c), heat-affected zone (d), and the microstructure of the base metal (e).

**Table 3.** Grain size in the nugget zone of all the produced friction stir welds.

	FSW1	FSW2	FSW3	FSW4	FSW5	FSW6	FSW7	FSW8
Grain Size in the Weld Nugget [ $\mu\text{m}$ ]	$13.5 \pm 2.1$	$17.3 \pm 1.5$	$12.8 \pm 1.5$	$14.9 \pm 1.1$	$10.3 \pm 1.8$	$15.9 \pm 2.0$	$9.8 \pm 1.5$	$12.7 \pm 1.2$

Figure 5 presents the relationship between the average grain size in the nugget zone of all the tested samples and the revolutionary pitch. It can be clearly observed that with increasing the revolutionary pitch, the average grain size in the nugget zone is decreased, for both applied tool tilt angles. The increase of the revolutionary pitch results in the increased heat input, which provides finer microstructure in such friction stir welds. Moreover, the use of an inclined tool influences the microstructure of the nugget zone. In the case of the welds produced with the tool tilt angle equal to  $2^\circ$ , the average grain size was lower than for the samples produced with non-tilted tool, for all the revolutionary pitch values. There are plenty of papers considering the heat input in the context of the inclination of the tool during the FSW process. Dialami et al. [30] studied the effect of the tool tilt angle on the heat generation and the material flow. It was assumed that an inclined tool increases stresses and the temperature during the process as well as strengthens the material stirring and facilitates the material flow behind the tool. Krishna et al. [31] observed that the heat input during the FSW process is not a uniform function of the tool tilt angle, but in general inclined function provides higher heat input and better plasticizing of the material to be

welded. Analysis of Meshram et al. [32] shows that the tool tilt angle of 2° provides the highest temperature of both advancing and retreating sides of the friction stir weld and thus proper plasticizing, mixing, and recrystallization are achieved.

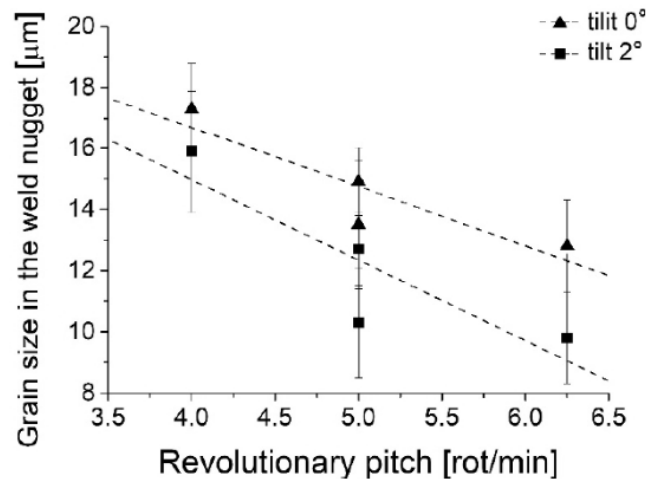


Figure 5. Average grain size in the nugget zone as a function of revolutionary pitch.

Figure 6 presents the Vickers microhardness profiles measured in different locations on the cross-sections of the friction stir welds. The microhardness of the base material was about 100 HV. Friction stir welding of precipitation hardenable alloys, among them AA6082 aluminum alloy, results in the inhomogeneous hardness distribution leading to the formation of a softened area. The dissolution of the strengthening particles in the aluminum matrix and the decrease of the dislocation density causes the decrease of the hardness in the thermo-mechanically affected zone (TMAZ) and heat-affected zone (HAZ) [33–35]. In all the cases, the minimum hardness was observed in the heat-affected zone, while in the nugget zone a recovered hardness was noted. Due to the fine microstructure of the nugget zone, the increase in the hardness can be explained by the Hall-Petch relationship, which indicates the increase of the hardness as the grain size decreases [36]. The Hall-Petch equation can be expressed as:

$$\sigma = \sigma_0 + kd^{-1/2} \quad (1)$$

where  $\sigma$  is the yield stress,  $\sigma_0$  is the resistance to the dislocation motion in the grain interior,  $k$  is a measure of the local stress needed to initiate plastic flow at grain boundaries, and  $d$  is a grain size [37]. In the case of the hardness, the Equation (1) can be presented as:

$$H = H_0 + k'd^{-1/2} \quad (2)$$

where  $H$  is the hardness of the material,  $H_0$  and  $k'$  are empirical constants [38]. The highest hardness of the nugget zone of about 92 HV was noted for FSW7 samples. Moreover, the smallest grain size was observed for this sample, which is in agreement with the Hall-Petch relationship.

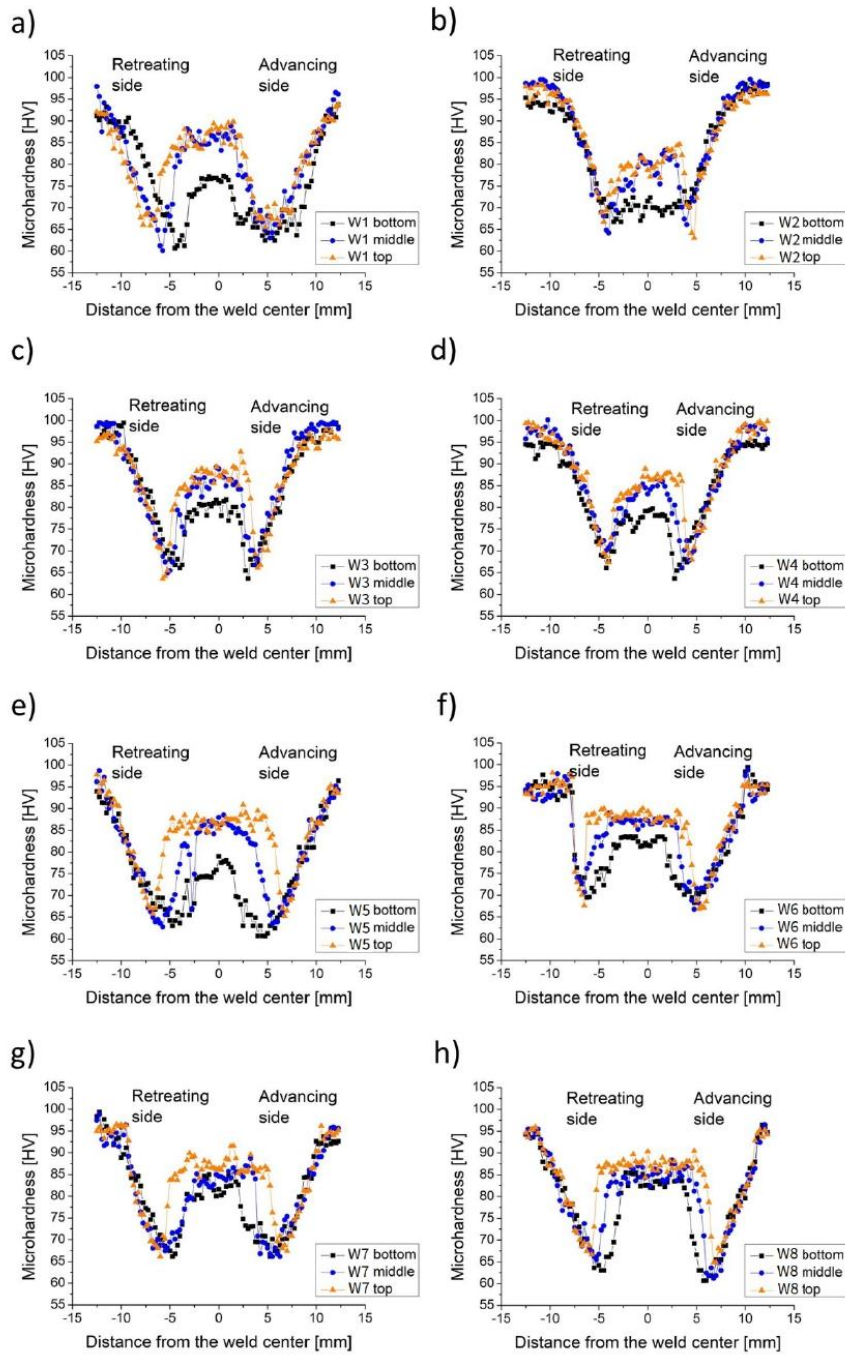
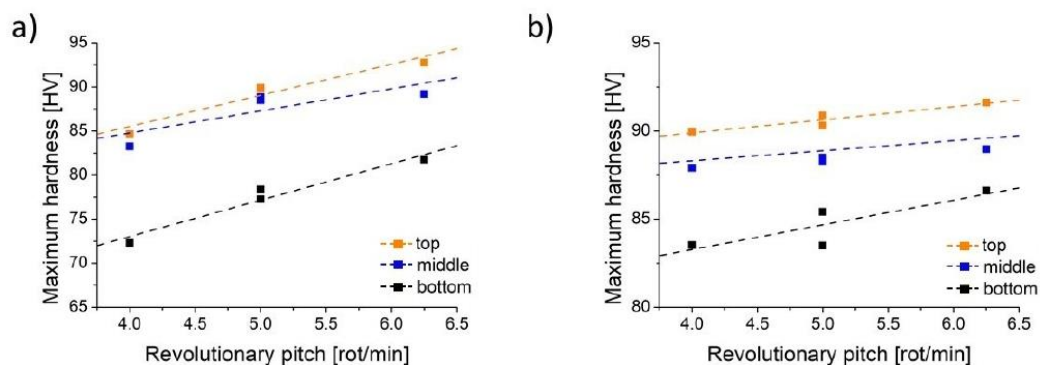


Figure 6. Microhardness profiles of the studied joints in the top, middle and bottom of the cross-sections—FSW1 (a), FSW2 (b), FSW3 (c), FSW4 (d), FSW5 (e), FSW6 (f), FSW7 (g), FSW8 (h).



The characteristic for the cross-sections of FSW joints hardness distribution is often reported in the case of aluminum alloys [39–44].

The summary of the main observations regarding the hardness profiles behavior is shown in Figure 7. It presents the correlation of the maximum hardness observed in the cross-sections of the nugget zone and the revolutionary pitch for the friction stir welds produced with the tool tilt angle of  $0^\circ$  (a) and  $2^\circ$  (b). In the case of  $0^\circ$  tool tilt angle, the observed values of hardness were lower than the ones observed in the case of the samples FSW5–FSW8. Clearly, in all the cases the lowest values were noted in the bottom of all the friction stir welds, while the highest were observed in the top of the samples. The top of the friction stir welds experienced the most significant heating due to the contact with the tool shoulder and the frictional heating, resulting in the finest microstructure and the highest microhardness. Among all the welds, the maximum hardness, reaching approximately 92% of the base material, was observed for the samples with the revolutionary pitch value equal to 6.25, for both applied the tool tilt angle values. As the revolutionary pitch increases, the heat input and the temperature during the process also increase. It can allow observing the most effective dynamic recrystallization. It can be also observed that for the samples produced with the highest revolutionary pitch the finest microstructure of the nugget zone was found. By decreasing the revolutionary pitch, the improper plastic flow might be observed and not sufficient dynamic recrystallization process can be noted. However, for further increase of the revolutionary pitch, the mixed material can be extremely softened and subjected to the grain growth, which would result in the significant decrease of the hardness in the nugget zone [45].



**Figure 7.** Maximum hardness of the nugget zone as a function of the revolutionary pitch—relationship for the friction stir welds produced with the tilt angle  $0^\circ$  (a) and  $2^\circ$  (b).

The radius of the nugget zone in the exact locations of the cross-sections of the friction stir welds as a function of the revolutionary pitch is presented in Figure 8. It can be clearly seen that in all the cases the highest values were observed in the top of the samples and the lowest in the bottom, which reflects the characteristic shape of the weld nugget [46–48]. It can be observed that with an increase of the revolutionary pitch, also the radius of the nugget zone increases. It is also attributed to the increase of the heat input during the process, as the revolutionary pitch is higher. In this case, the zone interested by the continuous dynamic recrystallization increases in dimensions and consequently the measured radius increases showing a larger zone of increased hardness with respect to TMAZ and HAZ.



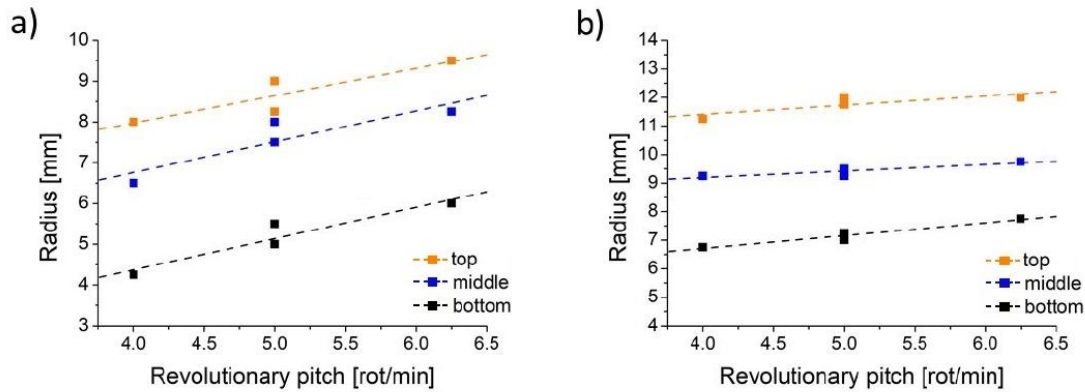


**Figure 8.** Radius of the nugget zone as a function of revolutionary pitch—relationship for the friction stir welds produced with the tilt angle 0° (a) and 2° (b).

Figure 9 presents the radius of the weld nugget in the function of the distance from the top of the friction stir weld for the samples with the revolutionary pitch equal to 4—FSW2 and FSW6 (for the tilt angle 0° and 2°, respectively) (a), and for the samples FSW3 and FSW7 (for the tilt angle 0° and 2°)—for the revolutionary pitch equal to 6.25 (b). These relationships clearly indicate that the use of an inclined tool increases the weld nugget zone for the entire cross-section of the specimen for both revolutionary pitch values analyzed. The same relationship was also observed for samples for which the revolutionary pitch value was 5. It can also be clearly noted that the radius of the weld nugget decreases with the increase of the distance from the top surface, which reflects the shape of the weld nugget.

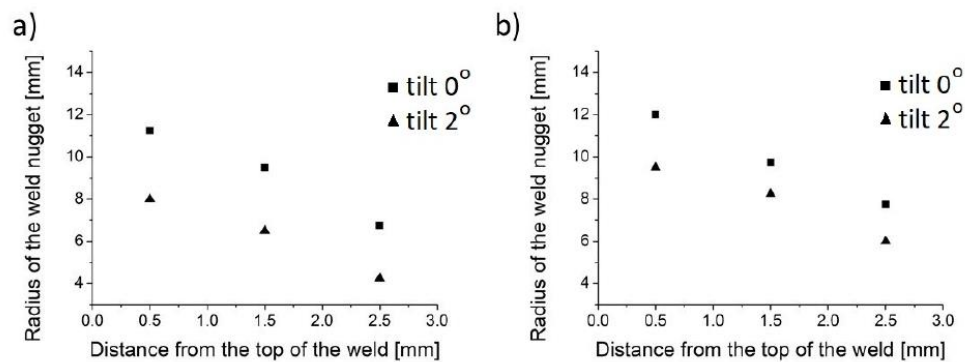


**Figure 9.** Radius of the weld nugget as a function of the distance from the top of the friction stir welds for the samples with the revolutionary pitch of 4 (a) and 6.25 (b).

Potentiodynamic studies are one of the basic tests to determine the properties of the produced friction stir welds. Their resistance to corrosion is of crucial importance not only in structures intended for marine vehicles, since even small corrosion losses caused by the influence of the environment may influence a significant decrease of the material strength. The potentiodynamic studies were initiated with the open circuit potential (OCP) measurements for 60 min. After the stability of OCP was achieved, all the samples exhibited similar values and further potentiodynamic studies were performed. Based on the Tafel extrapolation method on the obtained potentiodynamic curves, the corrosive potential

( $E_{\text{corr}}$ ) and the corrosion current density ( $i_{\text{corr}}$ ) values were collected. Table 4 contains the OCP,  $E_{\text{corr}}$ , and  $i_{\text{corr}}$  values for all the tested samples.

**Table 4.** Open circuit potential (OCP), corrosion potential ( $E_{\text{corr}}$ ), and current density ( $i_{\text{corr}}$ ) for the produced samples.

	FSW1	FSW2	FSW3	FSW4	FSW5	FSW6	FSW7	FSW8	AA6082
OCP [V]	−0.713 ± 0.036	−0.712 ± 0.036	−0.724 ± 0.036	−0.714 ± 0.036	−0.710 ± 0.035	−0.712 ± 0.036	−0.691 ± 0.035	−0.709 ± 0.035	−0.716 ± 0.036
$E_{\text{corr}}$ [V]	−0.682 ± 0.034	−0.680 ± 0.034	−0.684 ± 0.034	−0.676 ± 0.034	−0.654 ± 0.033	−0.648 ± 0.032	−0.649 ± 0.032	−0.659 ± 0.033	−0.686 ± 0.034
$i_{\text{corr}}$ [ $\mu\text{A}\cdot\text{cm}^{-2}$ ]	22.898 ± 1.145	23.907 ± 1.195	17.303 ± 0.865	20.809 ± 1.040	19.208 ± 0.960	19.128 ± 0.956	16.029 ± 0.801	18.895 ± 0.945	42.564 ± 2.128

It can be observed that the corrosion potential shifts from the minimum of  $-0.686$  V for AA6082 sample to the maximum of  $-0.648$  V for FSW6 sample. It should be noted that an increase in corrosion potential occurred for all welded samples, with the group of samples joined at tool tilt angle  $0^\circ$  (FSW1–FSW4) recording a smaller shift value. The FSW5–FSW8 specimens produced at a tool tilt angle of  $2^\circ$  showed the greatest shift in corrosion potential toward positive values. The movement to more positive values indicates that the corrosion resistance of the friction stir-welded samples was improved. The highest corrosion current density, which means the lowest corrosion resistance, was observed on AA6082 base metal sample and the value was equal to  $42.564 \mu\text{A cm}^{-2}$ . Almost two times lower values of  $i_{\text{corr}}$  were observed in the case of all the friction stir-welded samples, with the lowest value of  $16.029 \mu\text{A cm}^{-2}$  for FSW7 sample. Improvement of the corrosion resistance due to the FSW process was also observed by Qin et al. [49]. The 2A14-T6 aluminum alloy friction stir welds after electrochemical measurements in ex-foliation corrosion solution performed greatly improved corrosion resistance. Zucchi et al. [50] studied the pitting and stress corrosion cracking resistance of FSW AA5083 joints in 3.5% NaCl + 0.3 g/L  $\text{H}_2\text{O}_2$  and in ex-foliation solutions. In both cases, it was revealed that friction stir welds performed higher pitting and exfoliation corrosion resistance in comparison to the base material. The electrochemical studies on AA7022 FSW joints in  $\text{Na}_2\text{SO}_4$  + dilute  $\text{H}_2\text{SO}_4$  solution were performed by Wang et al. [51]. It was noted that the corrosion process in the base material was far greater than in the case of the friction stir welds under different process parameters. Monetta et al. [52] studied the corrosion resistance of AA6056 friction stir welds during the natural exposure in 3.5 (wt)% NaCl solution. It was revealed that the corrosion properties are strongly dependent on the process parameters. For relatively high welding speed, the pitting attack is more diffused and the pits penetration is less severe in the case of the nugget zone. For the FSW joints produced with lower welding speed the opposite observations were noted. The corrosion process was more pronounced within the nugget zone in comparison with the base material AA6056. In the studies of Padovani et al. [24] it was reported that FSW of AA2024 and AA7449 displayed greater susceptibility to pitting corrosion in the weld area after exposure to 0.1 M NaCl solution.

Figure 10a presents the potentiodynamic polarization curves for all the tested samples, while Figure 10b depicts the potentiodynamic polarization curves for the base material, FSW3 and FSW7, representing the friction stir welds with the lowest corrosion current density for the groups of the friction stir welds produced with the tilt angle of  $0^\circ$  and  $2^\circ$ , respectively.

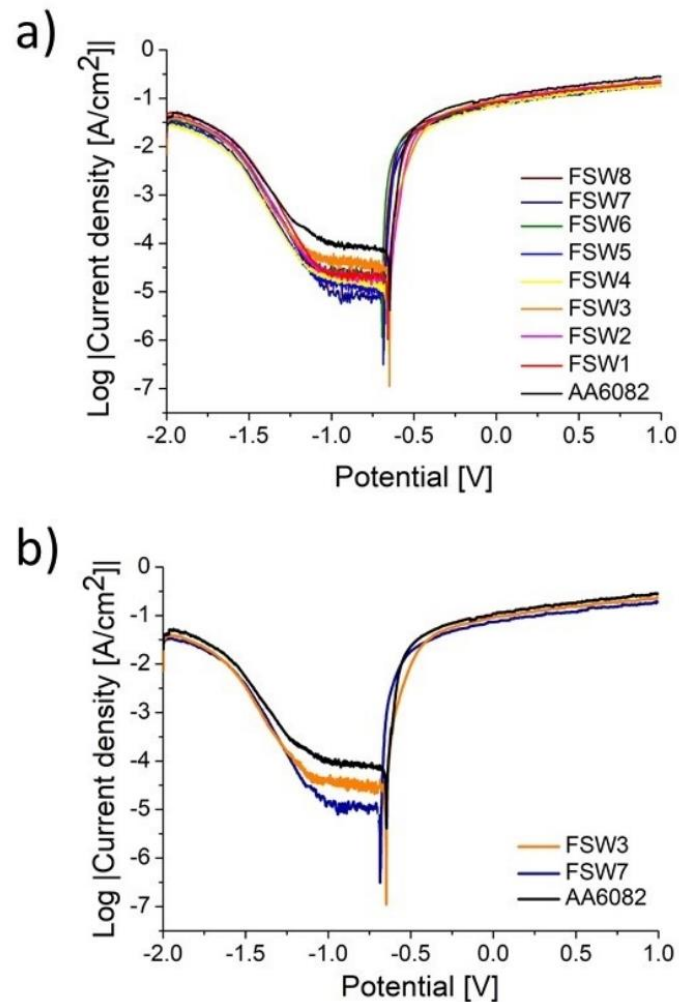


**Figure 10.** Potentiodynamic polarization curves for all the tested samples (a) and for AA6082 aluminum alloy, the FSW3 and FSW7 samples (b).

It was observed that, in general, the friction stir welds produced with the tool tilt angle of  $0^\circ$  (FSW1–FSW4) exhibited higher  $i_{\text{corr}}$  values compared to the welds produced with the same tool traverse speed and tool rotational speed, but with a tilt angle equal to  $2^\circ$ . These observations can be noted from the relationship of the corrosion current resistance as a function of revolutionary pitch presented in Figure 11. The trend line for the samples produced with the tilt angle of  $0^\circ$  remains above the trend line for the friction stir welds produced with the tilt angle equal to  $2^\circ$ . It can be also observed that with an increase of revolutionary pitch, the corrosion current density decreases, and the corrosion resistance increases. The corrosion susceptibility of the studied samples is highly influenced by their microstructure. Ralston et al. [53] reported that in a neutral NaCl environment, the corrosion rate has a tendency to decrease with a reduction of a grain size of pure aluminum. It was suggested that the fine grain microstructure might have more reactive surface to the formation of the protective oxide layer. Moreover, in the studies of Song et al. [54] it was revealed that by providing finer grained structure, the pitting

resistance of pure Al is increased, which is attributed to a denser oxide film on the surface of the samples. It should be also noted that FSW process changes not only the microstructure of the friction stir welds, but also has an influence on residual stresses and precipitation distribution, which may have an impact on electrochemical response as well.

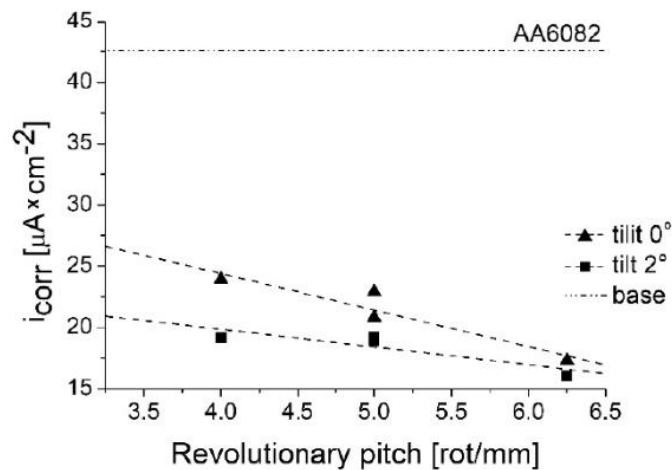


**Figure 11.** The relationship between corrosion current density and revolutionary pitch for all the tested samples.

Figure 12 presents the surfaces of the selected samples—FSW3, FSW7, and the base material AA6082. It can be observed that the base material (Figure 12c), thermally and mechanically unaffected during the movement of the tool exhibits the most serious corrosion losses on the surface. In Figure 12a,b, the characteristic shape of the top surface of the weld nugget is visible. A stepped structure is an effect of simultaneous rotation and traverse movement of a tool. It is observed that more significant corrosion losses are located on the top zone of the stepped surface. It can be explained by the corrosion propagation location at the edges of this structure. The passive layer at this location experiences a triaxial stress state, thus facilitating its delamination and corrosion propagation. A significant surface porosity can be observed on the surface of FSW3 sample. SEM images indicate that the lowest corrosion degradation can be observed on the sample FSW7, produced with a tool tilt angle of 2 and with the revolutionary pitch equal to 6.25. Although microscopic observations do not allow quantification of the amount of corrosion loss, a significantly higher degradation of the AA6082 base material was observed compared to all friction stir welds produced. Furthermore, it was noted that the samples produced at the tilt angle of 2° (FSW5–FSW8) exhibited less intense material degradation, which agrees with the results of the electrochemical tests where these samples were characterized by lower corrosion current density values.

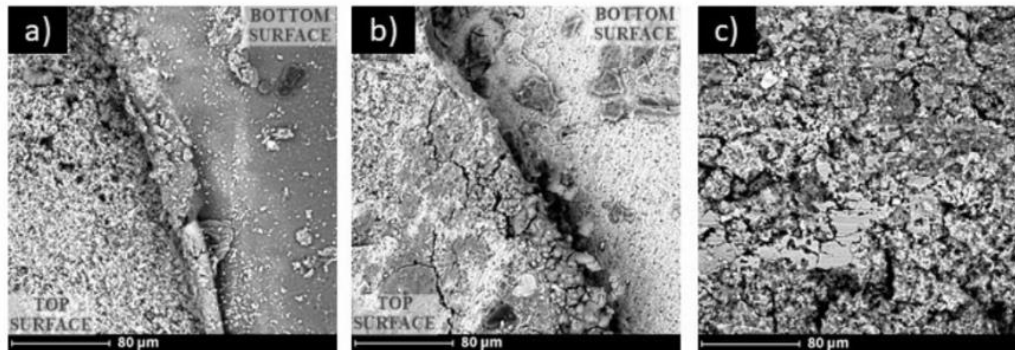


**Figure 12.** SEM images of the surface of the weld nugget of FSW3 (a), FSW7 (b) and AA6082 base material (c).

#### 4. Conclusions

The above studies were conducted to investigate the microstructure, hardness, and electrochemical properties of friction stir-welded AA6082. For this purpose, two different rotational speeds (1000 and 1250 rpm), two different traverse speeds (200 and 250 mm/min), and two different tool tilt angles ( $0^\circ$  and  $2^\circ$ ) were used. The obtained results allowed to draw the following conclusions:

1. Process parameters such as: tool traverse speed, tool tilt angle have an influence on the grain size of the nugget zone. Using a non-inclined tool results in a larger average grain size in the weld nugget zone (12.8–17.3  $\mu\text{m}$ ) than when using a tool tilt angle of  $2^\circ$  (9.8–15.9  $\mu\text{m}$ ). Furthermore, the average grain size decreases with an increase of a revolutionary pitch due to the increased heat input. The smallest grain size equal to  $9.8 \pm 1.5 \mu\text{m}$  was noted for a friction stir weld produced with a tool tilt angle  $2^\circ$ , tool traverse speed 200 mm/min, and tool rotational speed 1250 rpm.
2. The hardness measurements on the cross-sections of the friction stir welds revealed that higher hardness of the nugget zone was observed in the friction stir welds produced with an inclined tool. As the revolutionary pitch increases, the maximum hardness also increases in all the cases. The maximum hardness reached 92% of the hardness of the base material for the sample produced with the revolutionary pitch equal to 6.25 and tool tilt angle  $2^\circ$ . It was observed that with an increase of the revolutionary pitch, the radius of the nugget zone also increases.
3. Potentiodynamic studies showed that the friction stir welding process improves corrosion properties of AA6082 welds in 3.5 (wt)% NaCl solution. Using a tool tilt angle equal to  $2^\circ$  provided lower corrosion current density in the conducted tests. The best resistance ( $16.029 \pm 0.801 \mu\text{A cm}^{-2}$ ) was observed for the friction stir weld produced with the highest revolutionary pitch.

**Author Contributions:** Conceptualization, A.L. and M.S.; methodology, A.L.; validation, A.L., M.S. and P.C.; formal analysis, M.S., and P.C.; investigation, A.L., and D.K.; writing—original draft preparation, A.L.; writing—review and editing, P.C., and M.S.; visualization, A.L.; supervision, M.S., and P.C. All authors have read and agreed to the published version of the manuscript.

**Funding:** This research received no external funding.

**Institutional Review Board Statement:** Not applicable.

**Informed Consent Statement:** Not applicable.

**Data Availability Statement:** Not applicable.

**Conflicts of Interest:** The authors declare no conflict of interest.

## References

1. Thomas, W.M.W.; Norris, I.; Nicholas, E.D.; Needham, J.C.; Murch, M.G.; Temple-Smith, P.; Dawes, C.J. Friction Stir Welding Process Developments and Variant Techniques. International Patent Application No. PCT/GB92/02203 and GB Patent Application No. 9125978.8. 1991. Available online: [https://www.scirp.org/\(S\(lz5mqp453ed%20snp55rrgjt55\)\)/reference/referencespapers.aspx?referenceid=2200506](https://www.scirp.org/(S(lz5mqp453ed%20snp55rrgjt55))/reference/referencespapers.aspx?referenceid=2200506) (accessed on 29 December 2021).
2. Laska, A.; Szkodo, M. Manufacturing Parameters, Materials, and Welds Properties of Butt Friction Stir Welded Joints—Overview. *Materials* **2020**, *13*, 4940. [CrossRef] [PubMed]
3. Sato, Y.S.; Urata, M.; Kokawa, H. Parameters controlling microstructure and hardness during friction-stir welding of precipitation-hardenable aluminum alloy 6063. *Metall. Mater. Trans. A* **2002**, *33*, 625–635. [CrossRef]
4. Ma, Z.Y.; Feng, A.H.; Chen, D.L.; Shen, J. Recent Advances in Friction Stir Welding/Processing of Aluminum Alloys: Microstructural Evolution and Mechanical Properties. *Crit. Rev. Solid State Mater. Sci.* **2018**, *43*, 269–333. [CrossRef]
5. Cavaliere, P.; Rossi, G.L.; Di Sante, R.; Moretti, M. Thermoelasticity for the evaluation of fatigue behavior of 7005/Al2O3/10p metal matrix composite sheets joined by FSW. *Int. J. Fatigue* **2008**, *30*, 198–206. [CrossRef]
6. Dursun, T.; Soutis, C. Recent developments in advanced aircraft aluminium alloys. *Mater. Des.* **2014**, *56*, 862–871. [CrossRef]
7. Hirsch, J. Aluminium in innovative light-weight car design. *Mater. Trans.* **2011**, *52*, 818–824. [CrossRef]
8. Ertuğ, B.; Kumruoğlu, C. 5083 type Al-Mg and 6082 type Al-Mg-Si alloys for ship building. *Am. J. Eng. Res.* **2015**, *4*, 146–150.
9. Ancona, A.; Daurelio, G.; De Filippis, L.A.C.; Ludovico, A.D.; Spera, A.M. CO<sub>2</sub> Laser Welding of Aluminium Shipbuilding Industry Alloys: AA 5083, AA 5383, AA 5059, and AA 6082. In Proceedings of the XIV International Symposium on Gas Flow, Chemical Lasers, and High-Power Lasers, Wrocław, Poland, 25–30 August 2002; pp. 577–587.
10. Thomas, W.M.; Nicholas, E.D. Friction stir welding for the transportation industries. *Mater. Des.* **1997**, *18*, 269–273. [CrossRef]
11. Kawasaki, T.; Makino, T.; Masai, K.; Ohba, H.; Ina, Y.; Ezumi, M. Application of friction stir welding to construction of railway vehicles. *JSME Int. J. Ser. A Solid Mech. Mater. Eng.* **2004**, *47*, 502–511. [CrossRef]
12. Davenport, A.J.; Kallee, S.W.; Wylde, G.J. Creating a Stir in the Rail Industry. Available online: <https://www.twi-global.com/technical-knowledge/published-papers/creating-a-stir-in-the-rail-industry-november-2001> (accessed on 29 December 2021).
13. Prabhukhot, A.R. Effect of Heat Treatment on Hardness and Corrosion Behavior of 6082-T6 Aluminium Alloy in Artificial Sea Water. *Rev. Matéria* **2015**, *3*, 544–549. [CrossRef]
14. Singh, G.; Kumar, S.; Singh, A. Influence of Current on Microstructure and Hardness of Butt Welding Aluminium AA 6082 Using GTAW Process. *Int. J. Res. Mech. Eng. Technol.* **2013**, *3*, 143–146.
15. Koprivica, A.; Bajić, D.; Šibalić, N.; Vukčević, M. Analysis of welding of aluminium alloy AA6082-T6 by TIG, MIG and FSW processes from technological and economic aspect. *Mach. Technol. Mater.* **2020**, *5*, 194–198.
16. Ericsson, M.; Sandström, R. Influence of welding speed on the fatigue of friction stir welds, and comparison with MIG and TIG. *Int. J. Fatigue* **2003**, *25*, 1379–1387. [CrossRef]
17. Hoyos, E.; Escobar, S.; De Backer, J.; Martin, J.; Palacio, M. Manufacturing concept and prototype for train component using the fsw process. *J. Manuf. Mater. Process.* **2021**, *5*, 19. [CrossRef]
18. Liu, Q.; Han, R.; Gao, Y.; Ke, L. Numerical investigation on thermo-mechanical and material flow characteristics in friction stir welding for aluminium profile joint. *Int. J. Adv. Manuf. Technol.* **2021**, *114*, 2457–2469. [CrossRef]
19. Baratzadeh, F.; Boldsai Khan, E.; Nair, R.; Burford, D.; Lankarani, H. Investigation of mechanical properties of AA6082-T6/AA6063-T6 friction stir lap welds. *J. Adv. Join. Process.* **2020**, *1*, 100011. [CrossRef]
20. Varma, K.V.K.; Baig, I.; Kumar, B.V.R.R.; Ramana, M.V. Effect of friction stir welding parameters on tool geometry and metallurgical properties of AA 6082-T6 weldments at different weld zones. *Mater. Today Proc.* **2021**, *45*, 3195–3200. [CrossRef]
21. Maciel, R.; Bento, T.; Braga, D.F.O.; da Silva, L.F.M.; Moreira, P.M.G.P.; Infante, V. Fatigue properties of combined friction stir and adhesively bonded AA6082-T6 overlap joints. *Fatigue Fract. Eng. Mater. Struct.* **2020**, *43*, 2169–2180. [CrossRef]
22. Leal, R.M.; Galv, I. Recent Developments in Non-Conventional Welding of Materials. *Materials* **2022**, *15*, 171. [CrossRef]
23. Gharavi, F.; Matori, K.A.; Yunus, R.; Othman, N.K.; Fadaeifard, F. Corrosion evaluation of friction stir welded lap joints of AA6061-T6 aluminum alloy. *Trans. Nonferrous Met. Soc. China Engl. Ed.* **2016**, *26*, 684–696. [CrossRef]
24. Padovani, C.G.; Davenport, A.J.; Connolly, B.J.; Williams, S.W.; Groso, A.; Stampanoni, M.; Bellucci, F. Corrosion and Protection of friction stir welds in aerospace aluminium alloys. *La Metall. Ital.* **2008**, *100*, 29–42.
25. Ales, S.K.; Wang, L. Effects of Friction Stir Welding on Corrosion Behaviors of AA2024-T4 Aluminum Alloy. *MATEC Web Conf.* **2017**, *109*, 02003. [CrossRef]
26. Scialpi, A.; De Filippis, L.A.C.; Cavaliere, P. Influence of shoulder geometry on microstructure and mechanical properties of friction stir welded 6082 aluminium alloy. *Mater. Des.* **2007**, *28*, 1124–1129. [CrossRef]
27. Rambabu, G.; Balaji Naik, D.; Venkata Rao, C.H.; Srinivasa Rao, K.; Madhusudan Reddy, G. Optimization of friction stir welding parameters for improved corrosion resistance of AA2219 aluminum alloy joints. *Def. Technol.* **2015**, *11*, 330–337. [CrossRef]
28. Patil, H.S.; Soman, S.N. Effect of tool geometry and welding speed on mechanical properties and microstructure of friction stir welded joints of Aluminium alloys AA6082-T6. *Arch. Mech. Eng.* **2014**, *61*, 455–468. [CrossRef]
29. Naumov, A.; Rylkov, E.; Polyakov, P.; Isupov, F.; Rudskoy, A.; Aoh, J.N.; Popovich, A.; Panchenko, O. Effect of different tool probe profiles on material flow of al-mg-cu alloy joined by friction stir welding. *Materials* **2021**, *14*, 6296. [CrossRef] [PubMed]
30. Dialami, N.; Cervera, M.; Chiumenti, M. Effect of the tool tilt angle on the heat generation and the material flow in friction stir welding. *Metals* **2019**, *9*, 28. [CrossRef]

31. Krishna, G.G.; Reddy, P.R.; Hussain, M.M. Effect of Tool Tilt Angle on Aluminum 2014 Friction Stir Welds. *Glob. J. Res. Eng.* **2014**, *14*, 61–70.
32. Meshram, S.D.; Madhusudhan Reddy, G. Influence of tool tilt angle on material flow and defect generation in friction stir welding of AA2219. *Def. Sci. J.* **2018**, *68*, 512–518. [CrossRef]
33. Baghdadi, A.H.; Sajuri, Z.; Omar, M.Z.; Rajabi, A. Friction stir welding parameters: Impact of abnormal grain growth during post-weld heat treatment on mechanical properties of Al–Mg–Si welded joints. *Metals* **2020**, *10*, 1607. [CrossRef]
34. Huang, Y.; Meng, X.; Zhang, Y.; Cao, J.; Feng, J. Micro friction stir welding of ultra-thin Al-6061 sheets. *J. Mater. Process. Technol.* **2017**, *250*, 313–319. [CrossRef]
35. Huang, Y.; Meng, X.; Lv, Z.; Huang, T.; Zhang, Y.; Cao, J.; Zhou, L.; Feng, J. Microstructures and mechanical properties of micro friction stir welding ( $\mu$ FSW) of 6061-T4 aluminum alloy. *J. Mater. Res. Technol.* **2019**, *8*, 1084–1091. [CrossRef]
36. Naik, S.N.; Walley, S.M. The Hall–Petch and inverse Hall–Petch relations and the hardness of nanocrystalline metals. *J. Mater. Sci.* **2020**, *55*, 2661–2681. [CrossRef]
37. Song, Y.; Yeon, J.; Na, B. Numerical simulations of the hall-petch relationship in aluminium using gradient-enhanced plasticity model. *Adv. Civ. Eng.* **2019**, *2019*, 7356581. [CrossRef]
38. Facchini, D. Biomedical nanocrystalline metals and alloys: Structure, properties and applications. *Nanomedicine Technol. Appl.* **2012**, *1*, 36–67. [CrossRef]
39. Morozova, I.; Obrosof, A.; Naumov, A.; Królicka, A.; Golubev, I.; Bokov, D.O.; Doynov, N.; Weiß, S.; Michailov, V. Impact of impulses on microstructural evolution and mechanical performance of al-mg-si alloy joined by impulse friction stir welding. *Materials* **2021**, *14*, 347. [CrossRef]
40. Abbas, A.A.; Abdulkadhum, H.H. Effect of Shoulder–Workpiece Interference Depth on the Quality of Friction Stir Welding of AA7075-T6 Aluminium Alloy. *Assoc. Arab Univ. J. Eng. Sci.* **2019**, *26*, 150–159. [CrossRef]
41. Dawood, H.I.; Mohammed, K.S.; Rajab, M.Y. Advantages of the green solid state FSW over the conventional GMAW process. *Adv. Mater. Sci. Eng.* **2014**, *2014*, 105713. [CrossRef]
42. Pastor, A.; Svoboda, H.G. Time-evolution of Heat Affected Zone (HAZ) of Friction Stir Welds of AA7075-T651. *J. Mater. Phys. Chem.* **2013**, *1*, 58–64. [CrossRef]
43. Rodríguez, A.; Calleja, A.; López de Lacalle, L.N.; Pereira, O.; González, H.; Urbikain, G.; Laye, J. Burnishing of FSWAluminum Al-Cu-Li components. *Metals* **2019**, *9*, 260. [CrossRef]
44. Wahid, M.A.; Khan, Z.A.; Siddiquee, A.N. Review on underwater friction stir welding: A variant of friction stir welding with great potential of improving joint properties. *Trans. Nonferrous Met. Soc. China Engl. Ed.* **2018**, *28*, 193–219. [CrossRef]
45. Cavaliere, P.; Squillace, A.; Panella, F. Effect of welding parameters on mechanical and microstructural properties of AA6082 joints produced by friction stir welding. *J. Mater. Process. Technol.* **2008**, *200*, 364–372. [CrossRef]
46. Ahmed, M.M.Z.; Abdelazem, K.A.; El-Sayed Seleman, M.M.; Alzahrani, B.; Touileb, K.; Jouini, N.; El-Batanony, I.G.; Abd El-Aziz, H.M. Friction stir welding of 2205 duplex stainless steel: Feasibility of butt joint groove filling in comparison to gas tungsten arc welding. *Materials* **2021**, *14*, 4597. [CrossRef] [PubMed]
47. Krasnowski, K.; Sedek, P.; Lomozik, M.; Pietras, A. Impact of selected FSW process parameters on mechanical properties of 6082-T6 aluminium alloy butt joints. *Arch. Metall. Mater.* **2011**, *56*, 965–973. [CrossRef]
48. Aldanondo, E.; Vivas, J.; Alvarez, P.; Hurtado, I. Effect of Tool Geometry and Welding Parameters on Friction Stir Welded Lap Joint Formation with AA2099-T83 and AA2060-T8E30 Aluminium Alloys. *Metals* **2020**, *10*, 872. [CrossRef]
49. Qin, H.L.; Zhang, H.; Sun, D.T.; Zhuang, Q.Y. Corrosion behavior of the friction-stir-welded joints of 2A14-T6 aluminum alloy. *Int. J. Miner. Metall. Mater.* **2015**, *22*, 627–638. [CrossRef]
50. Zucchi, F.; Trabanelli, G.; Grassi, V. Pitting and stress corrosion cracking resistance of friction stir welded AA 5083. *Werkstoffe und Korrosion* **2001**, *52*, 853–859. [CrossRef]
51. Wang, H.F.; Wang, J.L.; Song, W.W.; Zuo, D.W.; Shao, D.L. Analysis on the corrosion performance of friction stir welding joint of 7022 aluminum alloy. *Int. J. Electrochem. Sci.* **2016**, *11*, 6933–6942. [CrossRef]
52. Monetta, T.; Montuori, M.; Squillace, A.; Bellucci, F. The Effect of Heat Treatment and Welding Parameters on the Corrosion Behaviour of a Friction Stir Welded 6056 Aluminium Alloy. *Adv. Mater. Res.* **2008**, *38*, 285–297. [CrossRef]
53. Ralston, K.D.; Fabijanic, D.; Birbilis, N. Effect of grain size on corrosion of high purity aluminium. *Electrochim. Acta* **2011**, *56*, 1729–1736. [CrossRef]
54. Song, D.; Ma, A.; Jiang, J.; Lin, P.; Yang, D. Corrosion behavior of ultra-fine grained industrial pure Al fabricated by ECAP. *Trans. Nonferrous Met. Soc. China Engl. Ed.* **2009**, *19*, 1065–1070. [CrossRef]



## **7.5. [P5] Analysis of Residual Stresses and Dislocation Density of AA6082 Butt Welds Produced by Friction Stir Welding.**

**Laska A.\***, Szkodo M., Cavaliere P., Moszczyńska D., Mizera J., Analysis of Residual Stresses and Dislocation Density of AA6082 Butt Welds Produced by Friction Stir Welding. Metallurgical and Materials Transactions A – Physical Metallurgy and Materials Science. 54, 211-225; 2023. doi:10.1007/s11661-022-06862-4. (IF = 2.726, 200 points of the Polish Ministry of Science and Higher Education)

### 7.5.1. Declaration of the contribution of the doctoral candidate

My contribution to the preparation of the manuscript consisted of preparing the literature review and obtaining the research material. I developed the methodology for the experiments. I fabricated AA6082 aluminum alloy specimens by FSW using two different rotational speeds, two traverse speeds, and two tool tilt angles. I conducted macroscopic observations. I analyzed the XRD diffractograms. I performed indentation studies. I made calculations of residual stresses, dislocation density, and dislocation mobility. I analyzed the obtained experimental results. I conducted a discussion in the manuscript. I prepared figures and tables and drafted the manuscript. I prepared responses to the reviewers and functioned as a correspondence author.

My percentage contribution to the preparation of the manuscript was equal to 60 %

.....  
Aleksandra Laska

## Analysis of Residual Stresses and Dislocation Density of AA6082 Butt Welds Produced by Friction Stir Welding



ALEKSANDRA LASKA, MAREK SZKODO, PASQUALE CAVALIERE,  
DOROTA MOSZCZYŃSKA, and JAROSŁAW MIZERA

The Friction Stir Welding (FSW) method was employed to join AA6082 sheets. The welds were produced with different tool traverse speed (200 and 250 mm/min), rotational speed (1000 and 1250 RPM) and tool tilt angle (0 and 2 deg). Based on the analysis of XRD patterns, the total precipitation volume fractions in the nugget zones and the base material were calculated. The FSW process resulted in a reduction in the fraction of precipitates up to 64 pct compared to the parent material. Based on the Williamson–Hall analysis and indentation tests, the residual stresses were calculated. The highest tensile residual stresses of  $-89.09 \pm 6.19$  MPa were observed for the base material, and the welding process reduced the residual stresses. The calculated dislocation density in the parent material AA6082 was equal to  $8.225 \times 10^{13} \text{ m}^{-2}$ , while in the welds a decrease was observed up to the value of  $1.419 \times 10^{13} \text{ m}^{-2}$ . In addition, the FSW process changed the nature of dislocations with edge-type dislocations dominating, while screw dominating character of dislocations were prevalent in the parent material. The mobility of dislocations in the studied welds was higher and reached the value of  $16.78 \times 10^{-7} \frac{\text{m}}{\text{s}}$ , while the dislocation mobility in the parent material was equal to  $3.19 \times 10^{-7} \frac{\text{m}}{\text{s}}$ . Process parameters during welding have a crucial effect on the amount of heat and strains introduced during the process, and thus influence the residual stresses, dislocation density and mobility, which might have a fundamental impact on the properties of the produced welds.

<https://doi.org/10.1007/s11661-022-06862-4>  
© The Author(s) 2022

### I. INTRODUCTION

FRICION Stir Welding (FSW), patented exactly 3 decades ago, is one of the most developed methods of joining materials. The process is based on the plasticizing of the material in the weld zone and mixing it to join the components.<sup>[1]</sup> For this purpose, a specially designed tool consisting of two essential parts—a pin and a shoulder is used. The tool, set in a rotary motion and placed between components in contact with each other, moves along the weld line. The most important role of the shoulder is to generate heat that plasticizes the

material through between its surface and the work-piece.<sup>[2]</sup> The pin, meanwhile, mixes the plasticized material, creating the weld.<sup>[3]</sup> The most important process parameters include the tool's traverse and rotational speed, the geometry of the tool and tool tilt angle.<sup>[4]</sup>

The FSW process produces a fine-grained structure in the nugget zone as a result of dynamic recrystallization in the weld.<sup>[5–7]</sup> Numbers of studies have been conducted to investigate recrystallization phenomena during the FSW of aluminum alloys.<sup>[8–10]</sup> The microstructural evolution during the process depends mostly on the temperature and strain evolution having a significant influence on the mechanical and electrochemical properties of aluminum alloys.<sup>[11]</sup> Also, the precipitate dissolution and coarsening at high temperatures during the FSW process lead to significant changes in the properties of the welded samples.<sup>[12,13]</sup> Another factor that has a significant impact on material properties is the density and type of dislocations evolving during the process. To understand the microscopic process of plastic behavior of the material, studies of dislocation density and mobility are necessary. Dislocation density and the velocity of dislocations influence the mechanical

ALEKSANDRA LASKA and MAREK SZKODO are with the Faculty of Mechanical Engineering and Ship Technology, Gdańsk University of Technology, Narutowicza 11/12, 80-233 Gdańsk, Poland. Contact e-mail: [aleksandra.laska@pg.edu.pl](mailto:aleksandra.laska@pg.edu.pl) PASQUALE CAVALIERE is with the Department of Innovation Engineering, University of Salento, Via per Arnesano, 73100 Lecce, Italy. DOROTA MOSZCZYŃSKA and JAROSŁAW MIZERA Faculty of Materials Science and Engineering, Warsaw University of Technology, Woloska 141, 02-507 Warsaw, Poland.  
Manuscript submitted July 13, 2022; accepted October 14, 2022.

METALLURGICAL AND MATERIALS TRANSACTIONS A

Published online: 09 November 2022

properties and the hardness of the material.<sup>[14]</sup> Lower dislocation mobility and high dislocation density result in an enhanced strength of the material.<sup>[15]</sup> Dislocation density is closely related to the straining resulting from severe plastic deformation and recrystallization during the friction stir welding process.<sup>[16,17]</sup> Woo *et al.*<sup>[18]</sup> noted that for FSW AA6061-T6 aluminum joints the dynamic recrystallized zone of the weld exhibits a low dislocation density compared to the parent material. In other studies by Woo *et al.*,<sup>[19]</sup> an increase in the dislocation density in the nugget zone was revealed in FSW AA6061-T6 joints. In Reference [20], Yuzbekova *et al.* noted an increase in the dislocation density in FSWed AA5024 aluminum alloy, compared to the base metal. Lee *et al.*<sup>[21]</sup> found lower dislocation density in the weld nugget of friction stir welded copper. In the study, it was also concluded that the hardness of the weld strongly depends on the dislocation density, rather than the grain size. The limited number of studies conducted in this area and the above assumption keep the topic addressed timely and relevant to the assessment of the strength of the joint.

Residual stress is another factor strongly affecting the mechanical properties of the welds. Residual stresses in the joints have a significant influence on its fatigue properties, and consequently on the lifetime of the welded component.<sup>[22]</sup> Tensile residual stresses, unlike compressive residual stresses, increase the negative effect of the environment. Residual stresses present in material might induce environmentally assisted cracking, as well as increased fatigue crack initiation susceptibility.<sup>[23]</sup> Moreover, the significant intensification of stress corrosion cracking can be observed at tensile residual stresses.<sup>[24]</sup> During the FSW process, the material in the nugget zone is both tensiled and compressed by friction and, at the same time, is exposed to the thermal compressive stresses due to the heat input.<sup>[25]</sup> Also, the corrosion resistance of materials may depend on the residual stresses and dislocations present in the material.<sup>[26,27]</sup> In the studies of Peel *et al.*<sup>[28]</sup> synchrotron analysis of residual stresses in AA5083 FSWed joints revealed the tension character of stresses in both parallel and perpendicular directions to the tool traverse direction. Also, the tool traverse speed strongly influences residual stresses due to the heat input and the increase of stresses is a result of a steeper thermal gradient during welding, while higher traverse speeds are applied. John *et al.*<sup>[29]</sup> investigated the effect of residual stresses on the fatigue crack growth in FSWed AA7050 alloy. It was revealed that even low residual stresses induced in the welds during the process resulted in significantly affected fatigue crack growth. In the studies of Steuwer *et al.*<sup>[30]</sup>, the significant tensile residual stresses were found in the region around the weld line of dissimilar AA5083/AA6082 friction stir welded joints. Also, it was revealed that both tool rotational speed and traverse speed influence the residual stresses formation. In the welds produced by Zhang *et al.*,<sup>[31]</sup> the residual stresses observed in 5A06 aluminum alloy and pure copper dissimilar welds were too high to achieve sound and reliable joints.

The Williamson–Hall analysis is a procedure that allows to calculate the crystallite size and residual stresses in the materials derived from X-ray diffraction patterns, whereas the dislocation density and its type can be calculated using the modified Williamson–Hall method.<sup>[32]</sup> Although many papers discussed the mechanical and electrochemical properties of friction stir welded AA6082 joints, a very limited number of studies is available on residual stresses and dislocation densities in the welds. The literature review still does not allow determining the effect of specific FSW process parameters on the residual stresses and dislocation densities in the welds.

The purpose of this study was to analyze the effect of friction stir welding parameters such as tool traverse speed, tool rotational speed and its tilt angle on residual stresses, dislocation density and dislocations mobility in the weld nugget of AA6082 aluminum alloy.

## II. METHODOLOGY

### A. Friction Stir Welding

The material under investigation was AA6082 aluminum alloy, solution heat-treated and artificially aged to T651 condition. The rolled sheets of 3 mm in thickness were used to perform the FSW process. The X-ray energy dispersive spectrometer (EDS) (Edax Inc., Mahwah, NJ) was used to determine the chemical composition of the chosen material. The results are shown in Table I.

The FSW process was performed on a conventional milling machine (FU251, Friedrich Engels Kazanluk, Bulgaria). For the present studies, a hexagonal pin tool was adopted to produce butt welds. Figure 1 depicts the schematic illustration of the tool. The shoulder diameter was equal to 18 mm, the distance across the flats of the hexagonal pin was equal to 6 mm and the pin length was set to 2.5 mm. The shoulder plunge depth of 0.3 mm was adopted. The material of the hexagonal pin was 73MoV52 steel and the shoulder was made of X210Cr12 steel. The hardness of the pin and the shoulder was measured (Wilson Mechanical Instrument Co. Inc.) and was equal to 58 and 61 HRC, respectively. The range of parameters was selected to produce welds without apparent defects and material discontinuities. The employed tool traverse speed values were 200 and 250 mm/min, the tool rotational speed values 1000 and 1250 rpm and the tool tilt angles 0 and 2 deg. The designations of the samples are shown in Table II. In the table, the revolutionary pitch values, defined as the tool rotational speed divided by the traverse speed for all the samples were also presented. For further testing, the specimens were cut from the nugget zone and the native material.

### B. Material Characterization

The metallography techniques were used to reveal the macrostructures of the welds. The samples were wet ground to the final gradation of #2000 and the polished



Table I. Chemical Composition of AA6082

	Chemical composition [Weight Percent]								
	Zn	Mg	Cr	Ti	Fe	Si	Cu	Mn	Al
AA6082	0.20	1.03	0.25	0.10	0.50	0.90	0.10	0.42	balance

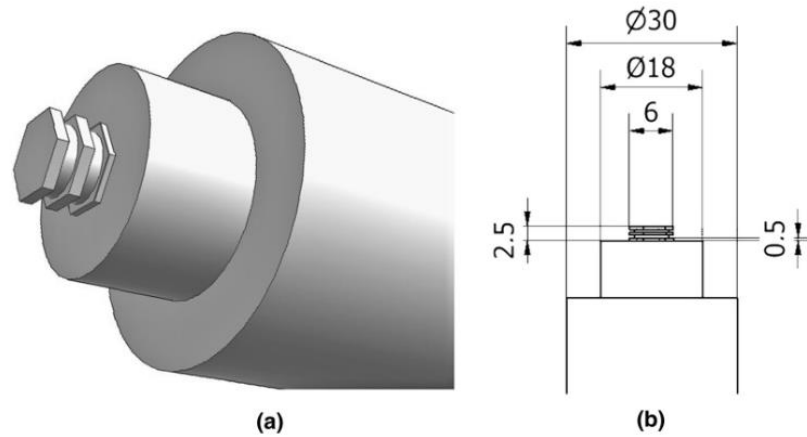


Fig. 1—Schematic illustration of the geometry of the tool used for FSW of AA6082.

Table II. Designations of the Samples

Sample	Tool Rotational Speed [RPM]	Tool Traverse Speed [mm/min]	Tool Tilt Angle [°]	Revolutionary Pitch [rot/mm]
FSW1	1000	200	0	5
FSW2	1000	250	0	4
FSW3	1250	200	0	6.25
FSW4	1250	250	0	5
FSW5	1000	200	2	5
FSW6	1000	250	2	4
FSW7	1250	200	2	6.25
FSW8	1250	250	2	5

using 1  $\mu\text{m}$  diamond suspension. The polished samples were etched in a reagent consisting 1 mL HF, 1 mL HCl, 2 mL  $\text{HNO}_3$  and 96 mL  $\text{H}_2\text{O}$  for 15 seconds. The microstructure at the cross-section of one selected weld (FSW2) was characterized by the electron backscattered diffraction (EBSD) method using a scanning electron microscope (SEM) (Hitachi SU-70, Japan). The sample for these measurements was prepared by argon ion polishing at 5 kV using Hitachi IM4000 Ion Milling System (Hitachi, Japan). The EBSD maps were taken on every zone with an acceleration voltage of 20 kV using a step size of 0.2  $\mu\text{m}$ . The collected data were examined using the HKL Channel 5 (Oxford Instruments, United Kingdom) software.

The X-ray diffraction method (XRD) (Philips X'Pert Pro, Netherlands) was used via diffractometer with Cu K $\alpha$  radiation with a wavelength  $\lambda = 0.15418$  nm operated at 30 kV and 50 mA. The diffraction patterns were collected using Bragg-Brentano geometry over  $2\theta$  range from 20 to 90 deg with a 0.02 deg step size. To evaluate and correct the instrumental broadening effect a silicon standard was used. The Rietveld refinement method was applied for a quantitative phase analysis based on the XRD patterns using MAUD software. Mathematical procedures implemented in the Rietveld refinement approach are described in detail in the literature.<sup>[33]</sup> The Williamson-Hall analysis was used to calculate the crystallite size and microstrain in the parent material

and the weld nuggets, whereas the modified Williamson–Hall analysis was applied to estimate the dislocation density. The hardness tests of the material were performed with a NanoTest Vantage nanoindenter (Nanotest Vantage, Micro Materials, United Kingdom) with a diamond Berkovich indenter. The tests were performed to determine the quantitative residual stresses in the examined samples, considering the strains calculated by the Williamson–Hall analysis and the Young’s modulus obtained from the indentation tests. The samples were subjected to 10 measurements with identical parameters. The maximum force was set up at 5N, the loading and unloading time was equal to 20 seconds and the dwell period at maximum load was 5 seconds. During the measurements, the load-depth curves were recorded. Microhardness ( $H$ ), reduced Young’s modulus ( $E_R$ ) and Young’s modulus ( $E$ ) were measured using the Oliver–Pharr method. For calculating Young’s modulus from reduced Young’s modulus, a Poisson’s ratio equal to 0.33<sup>[34]</sup> was assumed for the analyzed samples.

### III. RESULTS AND DISCUSSION

#### A. Macro- and Microstructure

Friction stir welding results in high temperatures during the process, large deformations, strains and strain rate. Figure 2 presents the macroscopic overview of the produce welds. In all the cases, a typical basin shape of the weld nugget can be observed. The uppermost part of the weld nugget is obviously wider due to the direct stirring by the tool shoulder.<sup>[35]</sup> No obvious defects were observed in the cross-sections of the joints, indicating a proper selection of the welding parameters. Moreover, a characteristic structure called “onion rings” can be observed as incomplete half elliptical banded patterns stacked into several layers. A formation of the onion ring pattern is an effect of downward and upward flow of the plasticized material around the pin while mixing. The width of the mixing zone was measured the mid-thickness of the cross-sections. It is worth to observe marginal differences in the width of the mixing zone for different process parameters. The welds produced with the tool tilt angle of 0° are characterized by slightly lower width of the stir zone. Also, for the welds produced with the tool traverse speed of 200 mm/min, the width is larger than in the case for the welds produced with the same tool tilt angle and the rotational speed, but with the tool traverse speed of 250 mm/min. This is due to the greater heat input both when the tool traverse speed is reduced and when the tool is tilted.<sup>[36,37]</sup>

High strains and heat input affect the microstructure evolution not only in the mixing zone, but also in the zones not in direct contact with the tool. Accordingly, besides the base material (BM), three zones characteristic of the FSW process can be distinguished. The nugget zone (NZ) is the area experienced by direct interactions with a tool. Extreme strain and high heat input result in a dynamic recrystallization process in this area. Due to that fact, the microstructure is very fine

with equiaxed well-dispersed grains. The resulting grain size strongly depends on the thermal cycle and stirring actions. In the thermo-mechanically affected zone (TMAZ) the material is plastically deformed from shear induced by the tool and is exposed to temperature increase. The plastic deformation degree depends mostly on the exact location within the zone, with higher deformations closer to the nugget. Due to insufficient heat input, no dynamic recrystallization occurs in TMAZ. As the distance from NZ increases, the degree of plastic deformation is reduced. The heat-affected zone (HAZ) experiences only the thermal energy of the process. In the precipitation strengthened alloys, such as AA6082, the HAZ is characterized by the overaging process of the precipitates, which is a result of the drastic reduction of the mechanical properties in this zone. Determination of the boundary between HAZ and BM might be difficult based on microstructure observations. Figure 3 shows the EBSD maps with the unit triangle of the stereographic projection which displays the color code for the direction of the plane normal of the map in the crystal axes. The EBSD measurements were performed for one selected weld (FSW2) in all four zones. In the base metal of AA6082 elongated grains can be observed which is a result of the rolling of the sheets. The microstructure of HAZ exhibits slightly elongated grains, with an emerging equiaxed shape. It should be noted that the structure in HAZ is more fine-grained, compared to the native material. The shape of the grains in the TMAZ does not reflect the elongated grains observed in the parent material. Also moving nearer to the nugget zone, the material experienced higher temperatures and deformation, so the partial recrystallization process was more clearly observed, resulting in more significant grain refinement closer to the nugget zone. This can be observed on the right side of Figure 3(c). In the weld nugget, newly formed grains with regular shape and very fine structure are observed. Due to the dynamic recrystallization process, the initial inhomogeneous microstructure is replaced by the fine-grain microstructure. The nugget zone clearly exhibits the increase of  $\langle 111 \rangle$  orientation. This phenomenon is the result of intense shear deformation by tool movement during the process. In<sup>[38]</sup> it was observed that at high strains, the  $\langle 111 \rangle$  texture might form in fcc crystals.

#### B. Precipitation Fraction Analysis

Figure 4 presents the XRD diffraction patterns for all the tested samples. The main peaks originating from the pure aluminum with their Miller indexes are distinguished. In Figure 5 the XRD diffraction patterns of the base material and one, representative weld are presented with the peaks corresponding to the phases of the main alloying elements. In all the diffractograms, the peaks originating from the phases of Mg, Mn, Si and Fe alloying elements were visible under magnifications.

Table III presents the type and volume of precipitation and pure aluminum fractions identified on the XRD patterns. The quantitative phase analysis was performed using Rietveld refinement of the XRD patterns. The

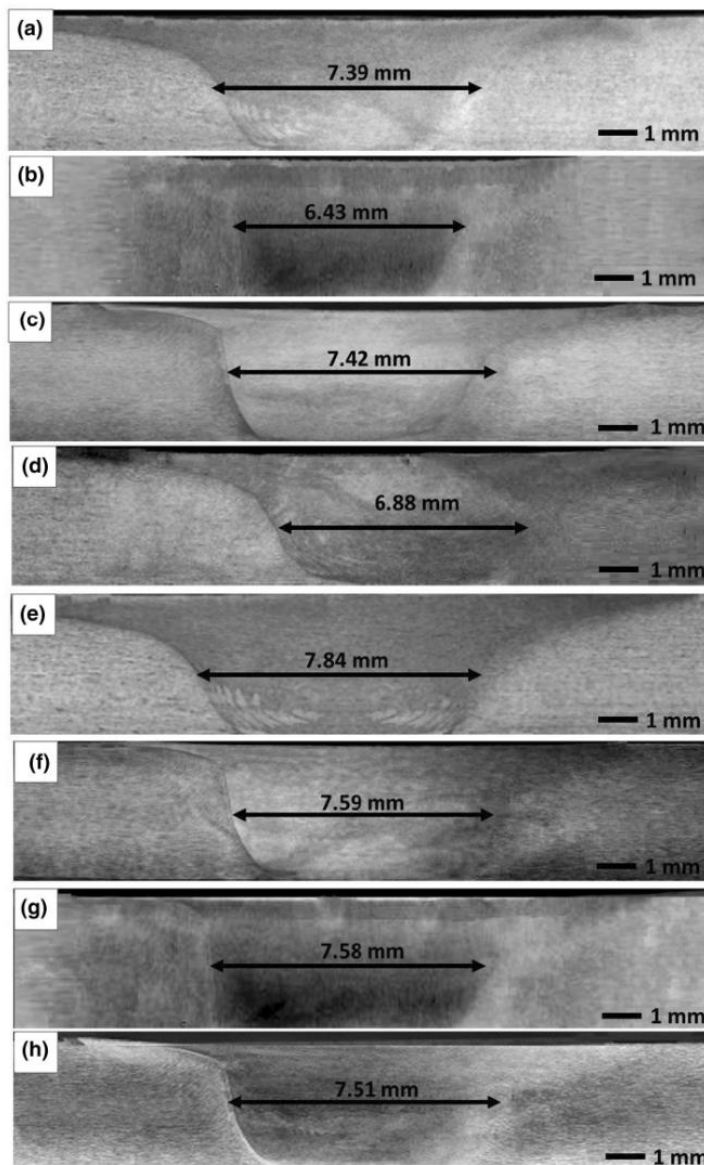


Fig. 2—Macrostructure of the produced welds—FSW1 (a), FSW2 (b), FSW3 (c), FSW4 (d), FSW5 (e), FSW6 (f), FSW7 (g) and FSW8 (h).

calculated goodness of fit values ranged from approximately 1.5 to 2.2 for all the samples, indicating very good agreement with the XRD patterns. The calculations show that the FSW process considerably reduces the precipitation content. The heat generated during the process, as well as the peak temperature, causes the dissolution of precipitates in the aluminum matrix.

Aluminum alloys containing Mg and Si as the main alloying elements are precipitation hardening alloys. Small particles of precipitates strengthen the material by inhibiting the dislocation movement in the metal crystal structure.<sup>[39]</sup> The dissolution of the precipitations leads to a noticeable decrease in the hardness and strength. In the studies of Rao *et al.*,<sup>[40]</sup> the dissolution of the

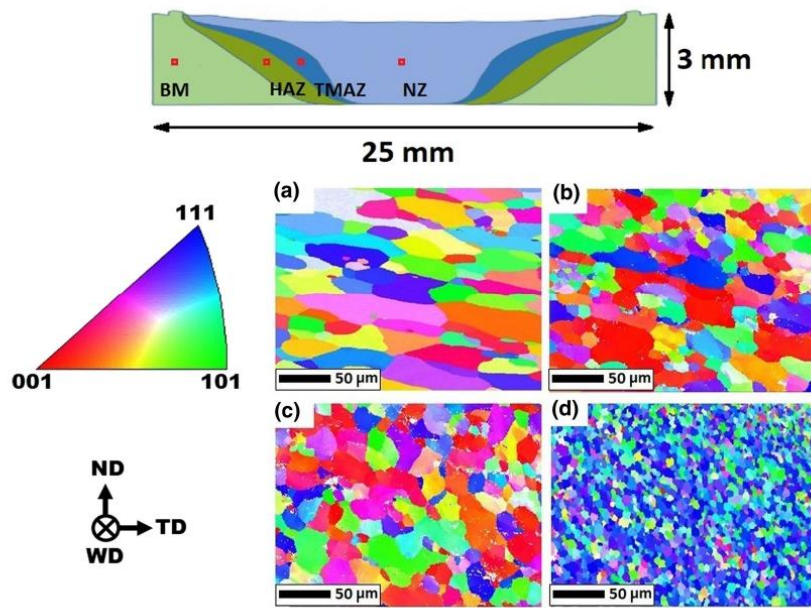


Fig. 3—EBSD maps of a selected FSW2 joint—base material AA6082 (a), heat-affected zone (b), thermo-mechanically affected zone (c) and weld nugget (d). Welding direction (WD), transverse direction (TD) and normal direction (ND) are also illustrated. The locations for the EBSD test in different zones of the FSW2 sample are also depicted.

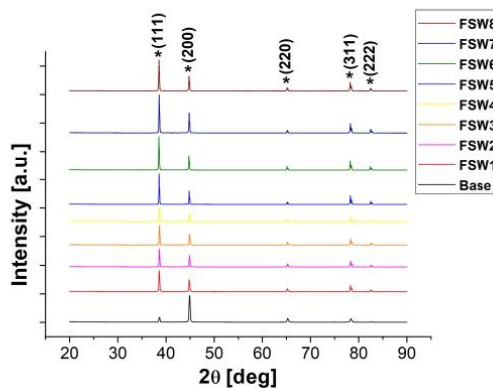


Fig. 4—Diffraction patterns for all the tested samples.

precipitates in AA2219 aluminum alloy during the FSW process was investigated. It was revealed that using a hexagonal pin might lead to the dissolution of 91 pct of precipitates. Simultaneously, the use of a hexagonal pin provides advanced material mixing, which leads to the recrystallization in the weld zone and the formation of a fine-grained structure. Thus, in these studies the use of a hexagonal pin resulted in an increase of the hardness of the nugget zone, compared to other pin shapes, although the precipitation dissolution was the highest.

Proper mixing of the material in the weld zone during the FSW process and grain recrystallization is the basic condition for maintaining the appropriate strength of the joints. Simultaneously, the dissolution of precipitates by increasing the temperature in the process reduces the strength in the case of precipitation hardening alloys, such as AA6082.

Figure 6 presents the relationship of the total precipitation volume fraction with a respect to the revolutionary pitch for both applied tilt angles. It should be noted that using the tilt angle equal to 2 deg results in more significant precipitate dissolution, while using the non-inclined tool results in the reduction of the precipitation dissolution. For the revolutionary pitch of 4 and the tilt of 0 deg, the precipitation fraction was reduced by 48 pct compared to the base material. The maximum reduction of the precipitation fraction (almost 64 pct of reduction comparing to the base material), was noted for the revolutionary pitch equal to 6.25 and the tool tilt angle of 2 deg. While increasing the revolutionary pitch, the heat input during the welding is also increased and the precipitation dissolution is higher, which leads to the reduction of their fraction. Also, by applying the inclined tool, the heat input during the process is increased, compared to the use of the non-inclined tool. The use of an inclined tool during the FSW process increases stress on the leading edge of the tool and on the surface of the component to be welded and thus, improves the frictional heating. This leads to an increase in the temperature, which affects the more efficient

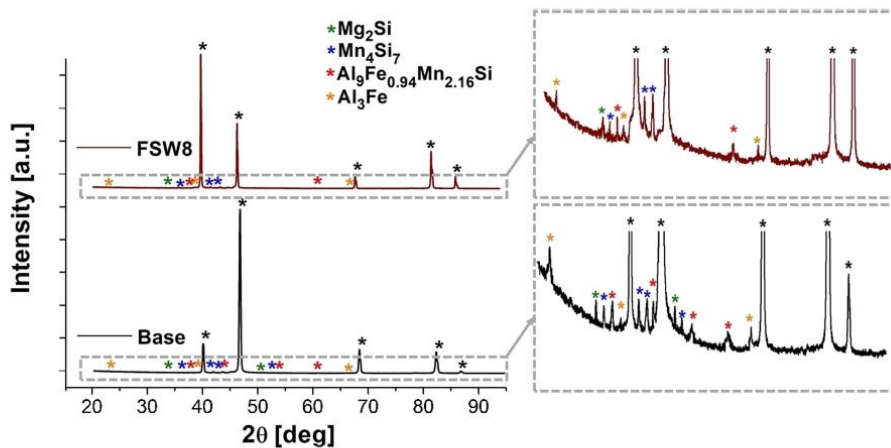


Fig. 5—Diffraction patterns of AA6082 base material and one selected weld (FSW8) with identified peaks originating from pure aluminum and phases of main alloying elements.

Table III. Type and Volume Fraction of the Precipitates Based on the XRD Patterns

	FSW1	FSW2	FSW3	FSW4	FSW5	FSW6	FSW7	FSW8	Base
Mg <sub>2</sub> Si Percent	0.209	0.208	0.206	0.201	0.178	0.189	0.169	0.222	0.832
Mn <sub>4</sub> Si <sub>7</sub> Percent	0.718	0.743	0.642	0.753	0.637	0.759	0.477	0.761	0.802
Al <sub>9</sub> Fe <sub>0.94</sub> Mn <sub>2.16</sub> Si Percent	0.393	0.371	0.264	0.302	0.207	0.290	0.261	0.214	0.597
Al <sub>3</sub> Fe Percent	0.466	0.529	0.394	0.385	0.448	0.315	0.378	0.349	1.326
Precipitations Fraction Percent	1.786	1.851	1.506	1.641	1.470	1.553	1.285	1.546	3.557
Al Fraction Percent	98.214	98.149	98.494	98.359	98.530	98.447	98.715	98.454	96.443

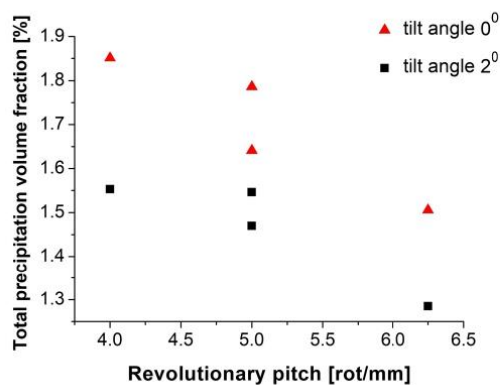


Fig. 6—Total precipitation volume fraction as a function of the revolutionary pitch for the samples produced with the tool tilt angle 0 deg (FSW1-FSW4) and 2 deg (FSW5-FSW8).

dissolution of precipitates and reduces their fraction. There are several studies on the heat input with the respect to the tool tilt angle during the FSW process. In the studies of Dialami *et al.*,<sup>[36]</sup> it was revealed that using

the inclined tool results in the increase of the temperature during the process and enhances the material stirring. Krishna *et al.*<sup>[41]</sup> noted that the heat input during welding is a non-uniform function of the tilt angle, but the use of the inclined tool results in higher heat input and better plasticizing of the material. Also, Meshram *et al.*<sup>[42]</sup> observed that when a tool tilt angle of 2 deg is set during the FSW process, the highest temperature is noted on both advancing and retreating sides. Figure 6 shows that for the welds produced with the tool tilt angle of 0 deg higher values of precipitation fractions are observed for all the studied revolutionary pitch values, compared to the welds produced with the inclined tool.

### C. Residual Stresses

A peak broadening on an XRD diffraction pattern is caused by the deviation from the ideal crystal lattice. The method that allows to distinguish the different contributions of that broadening is the Williamson–Hall analysis. This method assumes that a peak profile is a convolution of the profiles resulting from microstrains and crystallite size contributions<sup>[43]</sup>.



$$\beta_T = \beta_D + \beta_\varepsilon, \quad [1]$$

where  $\beta_T$  is a total broadening,  $\beta_D$  is a broadening resulting from the crystallite size and  $\beta_\varepsilon$ —from the microstrains.

The Scherrer equation presumes that the broadening due to the crystallite size can be presented as follows:

$$\beta_D = \frac{a_s \cdot \lambda}{L \cdot \cos\theta}, \quad [2]$$

where  $a_s$  is a Scherrer constant that depends on the crystal size distribution and its shape (here assumed to be equal to 1),<sup>[44]</sup>  $\lambda$  is the length of electron beam wave (here equal to 0.15418 nm) and  $L$  is the crystallite size that represents a crystallite portion with the same crystallographic orientation such as sub-grains (in nm).<sup>[45]</sup>

Also, the broadening due to the microstrains is defined as:

$$\beta_\varepsilon = 4\varepsilon \tan\theta, \quad [3]$$

where  $\varepsilon$  is the microstrain.

The Williamson–Hall equation, assuming the presented equations, can be defined as:

$$B = \frac{a_s \cdot \lambda}{L \cdot \cos\theta} + 4\varepsilon \tan\theta. \quad [4]$$

Or, while multiplied by  $\cos\theta$ , takes a form of a linear function:

$$B \cos\theta = \frac{a_s \cdot \lambda}{L} + 4\varepsilon \sin\theta. \quad [5]$$

Figure 7 depicts the plot of  $B \cos\theta$  vs.  $\sin\theta$ . Also, the approximations to the linear functions were calculated for the obtained values. Based on the constants of the linear functions, according to the Eq. [5] the crystallite size and microstrains were calculated. The obtained values are presented in Table IV. In order to calculate residual stresses ( $\sigma_R$ ) present in the material, the indentation tests were performed. Figure 8 presents

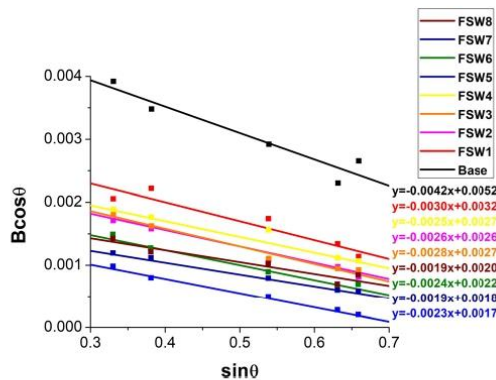


Fig. 7—Plots of  $B \cos\theta$  vs.  $\sin\theta$  for all the tested samples.

hysteresis plots of load-deformation during the tests for all the samples. The Young's modulus, calculated from the obtained values of reduced Young's modulus, as well as microhardness values are also presented in Table IV.

It can be clearly observed that the FSW process results in the increase of the crystallite size. By applying the tilt angle of 2 deg the increment is higher than in the case of the use of the non-tilted tool. The FSW method results in a large strain in the metal matrix during welding. The heat input and, consequently, the increase of the temperature in the weld nugget results in the recrystallization and grain refinement and, simultaneously, the increase in the size of crystallites. By applying the inclined tool, the heat input is higher<sup>[36, 42]</sup> and the crystallite size increment is greater. In all the cases, the Williamson–Hall analysis revealed that the strains present in the material are below zero, which indicates their tensile nature. The calculations of residual stresses show that the base material exhibit the lowest value. It means that in the case of the AA6082 alloy, the greatest tensile nature is observed. Also in the case of all the welds, the tensile residual stresses are observed, but the values are closer to zero. Residual stresses in friction stir welded joints are the result of complex interactions during the process, including thermal, mechanical and metallurgical phenomena. Indentation tests revealed that in the nugget zone of all the produced welds the hardness values were lower than in the case of the base material. High heat input and temperature peak during the process lead to the dissolution of precipitates in the aluminum matrix, as is shown in Table III. A decrease in the amount of precipitates, which in the case of precipitation-hardened alloys inhibit the movement of dislocations in the metal crystal structure, has a direct effect on the decrease in hardness, which can be seen in the results of indentation tests.

#### D. Dislocation Density and Mobility

The modified Williamson–Hall (MWH) analysis is a method that allows the dislocation density measurements based on XRD diffraction patterns. XRD diffraction patterns of all the tested samples with a horizontal axis determined as a diffraction vector  $K$  are presented in Figure 9. The diffraction vector can be calculated as:

$$K = \frac{2 \sin\theta}{\lambda}. \quad [6]$$

The modified Williamson–Hall equation can be expressed as follows:

$$\Delta K \cong \frac{a_s}{L} + bM \sqrt{\frac{\pi}{2} \rho (K \bar{C})^2}, \quad [7]$$

where  $\Delta K$  is defined as a peak width,  $b$  is a magnitude of the Burgers vector,  $M$  is a dislocation distribution parameter,  $\rho$  is a dislocation density and  $\bar{C}$  is a scaling parameter called the average contrast factor of dislocations.<sup>[46]</sup> Equation [7] is a linear function  $\Delta K =$

Table IV. Results Obtained from the Williamson–Hall Analysis and Indentation Tests

	$L$ [nm]	$\varepsilon$ [-]	$E$ [GPa]	$\sigma_R$ [MPa]	$H$ [GPa]
Base	29.62	- 0.00105	84.85 ± 5.90	- 89.09 ± 6.19	1.19 ± 0.11
FSW1	48.00	- 0.00074	82.44 ± 5.75	- 61.00 ± 4.25	1.08 ± 0.07
FSW2	58.38	- 0.00064	80.23 ± 10.97	- 51.35 ± 7.02	1.00 ± 0.09
FSW3	57.20	- 0.00069	81.18 ± 7.09	- 56.01 ± 4.89	1.11 ± 0.08
FSW4	56.43	- 0.00061	80.34 ± 6.06	- 49.01 ± 3.70	1.05 ± 0.06
FSW5	90.27	- 0.00057	80.48 ± 5.11	- 45.88 ± 2.91	1.07 ± 0.07
FSW6	68.79	- 0.00061	80.27 ± 5.38	- 48.97 ± 3.28	1.05 ± 0.10
FSW7	83.54	- 0.00048	82.30 ± 4.89	- 39.50 ± 2.35	1.04 ± 0.08
FSW8	77.09	- 0.00046	80.59 ± 6.40	- 37.07 ± 2.94	1.10 ± 0.04

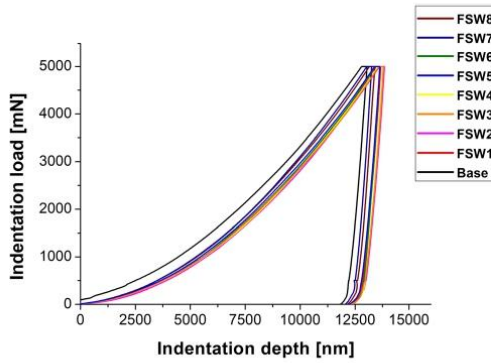


Fig. 8—Load-deformation hysteresis plots obtained during indentation tests.

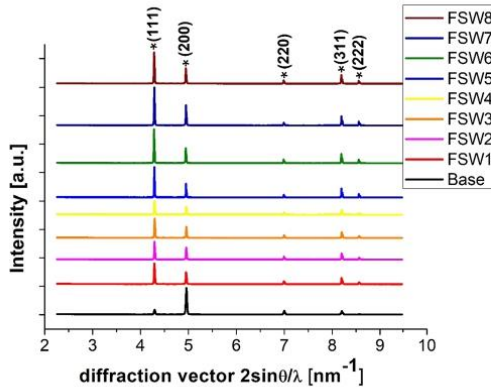


Fig. 9—Diffraction patterns for all the tested samples with a horizontal axis based on the diffraction vector  $K$ .

$f(KC^{-1/2})$ . The dislocation contrast factor is a function of Miller indexes and is given by:

$$\bar{C} = \bar{C}_{h00}(1 - qH^2), \quad [8]$$

where  $q$  is a dimensionless parameter that is dependent on the edge or screw character of dislocations and  $H$  is defined as:

$$H^2 = \frac{h^2l^2 + h^2k^2 + k^2l^2}{(h^2 + k^2 + l^2)}, \quad [9]$$

and  $\bar{C}_{h00}$ , is a factor of the average contrast of dislocations for  $\{h00\}$  reflections. It can be calculated by the dislocations contrast factor for the  $\{h00\}$  reflections of the pure screw and pure edge dislocation. For pure edge and pure screw dislocations, the dislocation contrast factor  $C_{h00}$  can be calculated as:

$$C_{h00i} = a_i^{C_{h00}} \left[ 1 - \exp\left(\frac{-A}{b_i^{C_{h00}}}\right) \right] + c_i^{C_{h00}} A + d_i^{C_{h00}}. \quad [10]$$

Here  $a_i^{C_{h00}}$ ,  $b_i^{C_{h00}}$ ,  $c_i^{C_{h00}}$  and  $d_i^{C_{h00}}$  are parameters determined by the elastic constants of the material. The values used for the calculations are presented in Table V. According to<sup>[47]</sup>  $A$  is the elastic anisotropy parameter defined as:

$$A = \frac{2c_{44}}{c_{11} - c_{12}}. \quad [11]$$

For the following calculations the values of  $c_{44}$ ,  $c_{11}$  and  $c_{12}$  were equal to  $2.83 \cdot 10^{10}$ ,  $10.73 \cdot 10^{10}$  and  $6.08 \cdot 10^{10} \frac{N}{m^2}$ , according to Vallin *et al.*<sup>[48]</sup> Substitution of these values gives the elastic anisotropy parameter  $A$  equal to 1.217.

To calculate parameter  $q$ , Eqs. [7] and [8] should be combined obtaining:

$$\frac{(\Delta K - \alpha)^2}{K^2} \cong \beta^2 \bar{C}_{h00}(1 - qH^2), \quad [12]$$

where  $\alpha = \frac{a_0}{L}$  and  $\beta = bM\left(\frac{\pi\rho}{2}\right)^{1/2}$ . The experimental value of  $q$  is determined by imposing the linear function  $\frac{(\Delta K - \alpha)^2}{K^2} = f(K^2)$ . The inverse value of  $q$  is obtained as the intercept of the extrapolated function with the

Table V. Parameters Needed to Calculate  $C_{h00}$  and  $q_i^{th}$  for Aluminum in fcc Crystal

	Parameter $q_i^{th}$ [47]				Factor $C_{h00}$ [47]			
	$a_i^q$	$b_i^q$	$c_i^q$	$d_i^q$	$a^{Ch00}_i$	$b^{Ch00}_i$	$c^{Ch00}_i$	$d^{Ch00}_i$
Screw	5.4252	0.7196	0.0690	- 3.1970	0.1740	1.9522	0.0293	0.0662
Edge*[49]	5.9049	0.8046	0.0826	- 4.374	0.2468	2.1880	0.0186	0.0731

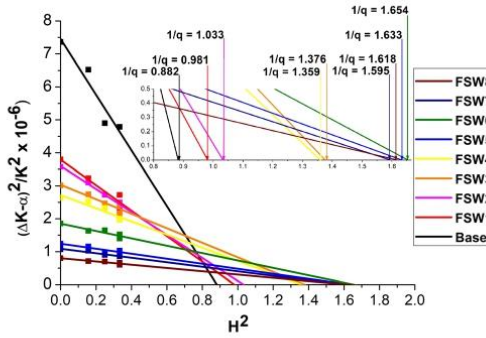


Fig. 10—Plot of Eq. [12] for all the tested samples. The intersect on the  $H^2$  gives  $1/q$ .

horizontal axis. Figure 10 presents the plot of Eq. [12] and the values of  $1/q$ .

Based on the calculated values of  $q$ , the fraction of screw and edge character dislocations can be calculated

$$f^{edge} = \frac{q_{screw}^{th} - q}{q_{screw}^{th} - q_{edge}^{th}} = 1 - f^{screw} \quad [13]$$

Here  $f^{edge}$  and  $f^{screw}$  mean the fractions of each type of dislocations. To make these calculations, the theoretical values of  $q$  for the pure screw ( $q_{screw}^{th}$ ) and pure edge ( $q_{edge}^{th}$ ) dislocations are needed. These values can be determined based on Eq. [14]:

$$q_i^{th} = a_i^q \left[ 1 - \exp\left(\frac{-A}{b_i^q}\right) \right] + c_i^q A + d_i^q \quad [14]$$

The elastic anisotropy parameter  $A$  was calculated according to Eq. [11], while  $a_i^q$ ,  $b_i^q$ ,  $c_i^q$  and  $d_i^q$  are values depending on the elastic constants and dislocations slip systems activated in crystals. The parameters needed to determine  $q_i^{th}$  values are presented in Table V.

Table VI presents the calculated values of  $q_{screw}^{th}$  and  $q_{edge}^{th}$ , as well as the fractions of screw and edge type dislocations determined using Eq. [13]. Also  $C_{h00screw}$ ,  $C_{h00edge}$  and  $C_{h00average}$  values are presented in Table VI.

After calculations of the  $q$  value for all the tested samples, the dislocation contrast value  $C^-$  is calculated according to Eq. [8]. Figure 11 presents the MWH equations plots for all the samples with the approximations to the linear functions. The results show that for all the welded samples the line broadening  $\Delta K$  is less significant in each  $(h k l)$  peak than in the case of AA6082 parent material. Based on the slope of the straight lines the dislocation densities were calculated, taking the  $M$  parameter equal to 2 and the Burgers vector equal to 0.286 nm.<sup>[50]</sup> The values of dislocation densities for all the tested samples are presented in Table VII.

Due to the severe plastic deformations during the friction stir welding and recrystallization process, the dislocation density is closely related to the straining.<sup>[18]</sup> The modified Williamson–Hall analysis revealed that the highest dislocation density was found for the base material AA6082 and was equal to  $8.225 \times 10^{13} \text{ m}^{-2}$ . The FSW process results in a decrease in dislocation

Table VI. The Theoretical Values of  $q$  for Screw and Edge Dislocations, the Fraction of Screw and Edge Dislocations, the Theoretical Value of Dislocation Contrast for Screw and Edge Dislocations, and the Average Dislocation Contrast Factor for the  $\{h00\}$  Reflections for All the Tested Samples

	$q_{screw}^{th}$	$q_{edge}^{th}$	$f^{screw}$	$f^{edge}$	$C_{h00screw}$	$C_{h00edge}$	$C_{h00average}$
base	1.313	0.331	0.818	0.182	0.183	0.200	0.186
FSW1	1.313	0.331	0.662	0.338	0.183	0.200	0.188
FSW2	1.313	0.331	0.649	0.351	0.183	0.200	0.189
FSW3	1.313	0.331	0.403	0.597	0.183	0.200	0.193
FSW4	1.313	0.331	0.412	0.588	0.183	0.200	0.193
FSW5	1.313	0.331	0.287	0.713	0.183	0.200	0.195
FSW6	1.313	0.331	0.279	0.721	0.183	0.200	0.195
FSW7	1.313	0.331	0.302	0.698	0.183	0.200	0.195
FSW8	1.313	0.331	0.293	0.707	0.183	0.200	0.195

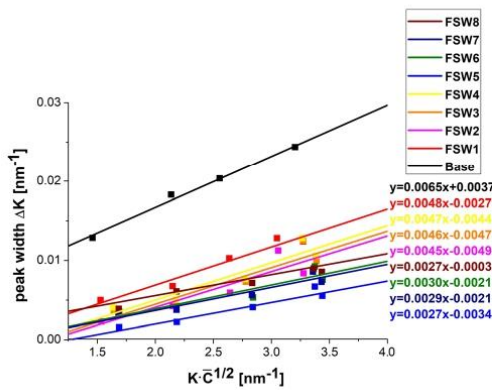


Fig. 11—The modified Williamson–Hall plot for welded samples and the parent material AA6082.

density. The analysis showed that using an inclined tool and thus increasing the amount of heat input causes a more intense decrease in dislocation density up to a value of  $1.419 \times 10^{13} \text{ m}^{-2}$  for FSW5 and FSW8 samples. In the studies of Woo *et al.*,<sup>[18]</sup> it was also noted that friction stir-welded AA6061 alloy performs lower dislocation density compared to the base material in the form of as-received rolled aluminum plate. It was revealed that lower dislocation density in the nugget zone results in a high strain hardening capacity and exponent during tensile plastic deformation. In the base metal region, where the dislocation density was higher, lower strain hardening and poor ductility were found. Valvi *et al.*<sup>[51]</sup> proposed the evaluation of the dislocation density in similar AA6061 and dissimilar AA6061/AA5086 weld zones during FSW. The proposed analysis was a function of grain size and depends on strain rate, strain and temperature. It was revealed that using the analytical model gives accurate predictions and the results obtained are consistent with the studied on the welds of Woo *et al.*<sup>[18]</sup>

To calculate the mobility of the dislocations ( $v$ ), the creep of the material during the dwell time in indentation tests was studied. Figure 12 presents the relationship of strain and time. The Orowan Eq. [15] allows to calculate the dislocation velocity based on the formula:<sup>[52]</sup>

$$\frac{d\epsilon}{dt} = \dot{\epsilon} = b \cdot \rho \cdot v, \quad [15]$$

where  $\dot{\epsilon}$  is a strain derivative. To calculate this value, the stabilized fragment of the creep was approximated to the linear function. The Orowan equation can be converted to:

$$v = \frac{\dot{\epsilon}}{b \cdot \rho}. \quad [16]$$

The results of the analysis strain–time relationship are presented in Table VIII.

Table VII. Dislocation Density for All the Tested Samples Calculated from the Modified Williamson–Hall Analysis

	FSW1	FSW2	FSW3	FSW4	FSW5	FSW6	FSW7	FSW8
Base								
$\rho \text{ [m}^{-2}\text{]}$	$4.485 \times 10^{13}$	$3.942 \times 10^{13}$	$4.119 \times 10^{13}$	$4.300 \times 10^{13}$	$1.419 \times 10^{13}$	$1.752 \times 10^{13}$	$1.637 \times 10^{13}$	$1.419 \times 10^{13}$

The results of the calculations based on the Orowan equations clearly indicate that the FSW process influences the dislocation mobility. The calculated velocities are higher in the case of samples welded with the tool tilt angle of 2 deg (FSW5-FSW8) than for the ones produced with the tool tilt angle equal to 0 deg (FSW1-FSW4). It should be emphasized that dislocation mobility and velocity control the mechanical behavior of the material, and the strength has a tendency to decrease as the velocity of dislocations increases. The Williamson–Hall analysis also revealed that the FSW process changes the nature of the dislocations. The native material is dominated by screw character of dislocations, accounting for almost 82 pct. An increase in edge-type dislocations was observed in all welds, up to values above 72 pct for the FSW6 sample. It should also be noted that the use of an inclined tool increases the proportion of character of dislocations from edge to screw type. This is attributed to the strains introduced into the material in various processes, such as FSW. Also, the use of an inclined tool in friction stir welding increases the strain in the material during the process. It is believed that as a result of relatively small deformations, the constriction required for cross-slip begins to become difficult, resulting in edge dislocations becoming more mobile. It leads to their annihilation while leaving screw-like dislocations. Consequently, screw character of dislocations dominate in the rolled parent material. While increasing strains, which can be observed in the FSW process, the character of dislocations changes from screw to edge. Providing greater deformation, thermally activated recovery processes result in increased annihilation of dislocations, which

is suggested as cross-slip of screws. Consequently, the fraction of screw type dislocations decreases, which implies an increase in the fraction of edge character of dislocations. These observations are in agreement with the studies of Teena Mouni *et al.*<sup>[53]</sup> on type 304 steel subjected to different strain levels. Also, Schaffler *et al.*<sup>[54]</sup> observed the increase of the fraction of edge dislocations under high strains in 99.9 pct Cu. On the contrary, at small strains, the dominance of the character of screw dislocations was noted, with only 10 pct of all dislocations characterized by edge character. These results are in good correspondence with the present studies. Simm<sup>[55]</sup> in the studies on compression tested 304 type steel attributed the observed decrease in  $q$ , therefore, an increase in the fraction of edge dislocations, to activation of secondary slip systems.

The increase in the proportion of edge dislocations also affects their mobility. It is believed that an increase in edge-type dislocation density and a decrease in the density of screw character dislocations lead to the increase in dislocation mobility. This results in the material softening due to the particles cut and loop, as well as the increase in lattice straining. There are plenty of studies on dislocation velocity proving that dislocations with edge character domination have higher mobility than screw dislocations.<sup>[56, 57]</sup> In the studies on the FSW samples, it can be clearly seen, that by welding AA6082, the character of dislocations changes with an increase of the fraction of edge domination dislocations and thus their mobility increases, which might strongly affect the mechanical properties of the welds. Also, during the process, the precipitations dissolve and thus, the inhibition of the dislocation movement is weakened. A low number of dislocations and their high mobility, due to the precipitation dissolution and the increase of edge character of dislocations, decreases the strength of the material. Figure 13 presents the relationship of the dislocation density quotient to its mobility as a function of the revolutionary pitch for welds produced with the tool tilt angle of 0 deg (a) and 2 deg (b). The more dislocations with low mobility present in the materials, the higher strength is expected. It is clearly seen that with an increase of revolutionary pitch and thus the higher heat input, the value of this quotient is lower. Also, by using the inclined tool and increasing the heat input, the values of the quotients are lower than in the case of the non-inclined tool. Higher strains introduced in the material during welding with the inclined tool resulted in a formation of edge dislocations, characterized by higher mobility. It means that heat input and temperature peak is the main reason for decreasing the precipitation fraction and dislocation density. The reduction of the screw dominating type

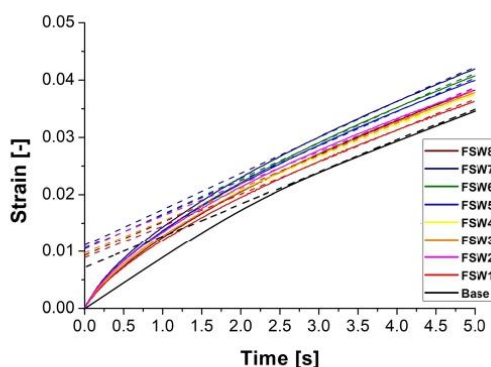


Fig. 12—Strain–time diagram for the dwell period during indentation tests.

Table VIII. Dislocation Mobility of the Tested Samples Based on the Indentation Tests

	Base	FSW1	FSW2	FSW3	FSW4	FSW5	FSW6	FSW7	FSW8
$v \left[ \frac{\text{m}}{\text{s}} \right]$	$3.19 \times 10^{-7}$	$4.69 \times 10^{-7}$	$4.84 \times 10^{-7}$	$4.37 \times 10^{-7}$	$4.54 \times 10^{-7}$	$13.46 \times 10^{-7}$	$16.78 \times 10^{-7}$	$12.38 \times 10^{-7}$	$13.54 \times 10^{-7}$

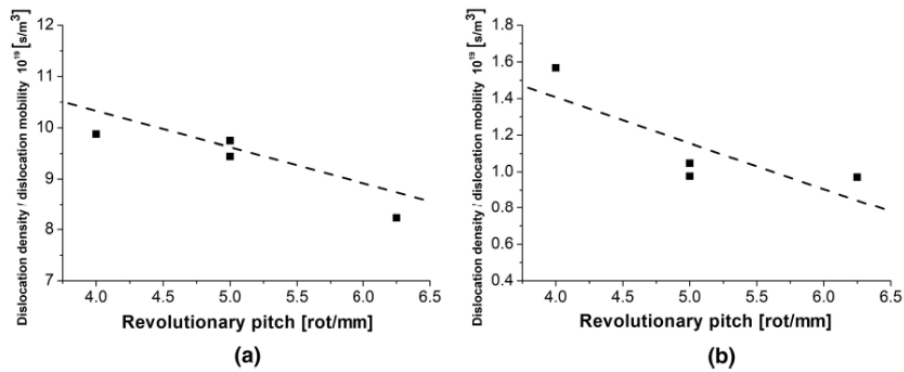


Fig. 13—The quotient of dislocation density and their mobility as a function of the revolutionary pitch for the welds produced with the tool tilt angle of 0 deg (a) and 2 deg (b).

dislocations fraction and, at the same time, the increase of the edge-type dislocation fractions are mostly influenced by the strains introduced in the material by the inclined tool. The decrease of precipitation fractions, as well as the change of the dislocations character, influenced the dislocation mobility. These relationships are clearly visible by analyzing the relationships based on revolutionary pitch, as well as comparing the values for the inclined and non-inclined tools.

#### IV. CONCLUSIONS

The present study focuses on the residual stresses, dislocation mobility and density of friction stir welded AA6082 aluminum alloy under different process parameters. The following conclusions can be drawn from the systematic research:

1. AA6082 aluminum alloy sheets were successfully welded using the FSW method with the tool with a hexagonal pin. Process parameters such as tool traverse speed of 200 and 250 mm/min, tool rotational speed of 1000 and 1250 RPM and tool tilt angle of 0 deg and 2 deg allowed to produce defect-free welds.
2. Typical microstructure containing elongated base material grains and fine grain weld nugget was observed by the EBSD method. Also, typical zones such as HAZ and TMAZ were found on the EBSD map.
3. Precipitation volume fractions in the nugget zones of all produced welds were calculated based on XRD patterns and Rietveld refinement. It was noted that a more significant reduction of precipitation fraction can be observed for the welds produced with a tool tilt angle of 2 deg, compared to the welds produced with a non-inclined tool. The precipitation volume fraction of the base metal was equal to 3.557 pct and the FSW process resulted in a reduction of up to 1.285 pct. Due to the higher heat input during the process with the inclined tool,

this effect was magnified. A revolutionary pitch parameter was introduced to determine the number of revolutions of the tool per 1 mm of its feed. As the value of revolutionary pitch and thus the amount of heat input increases, the precipitate volume fraction decreases due to an increase in their solubility. The maximum reduction of the precipitate volume fraction equal to 64 pct compared to the base material was found for the weld produced with the tool traverse speed of 200 mm/min, tool rotational speed of 1250 RPM and the tool tilt angle of 2 deg

4. The Williamson–Hall analysis was used to calculate residual strains. In addition, the indentation tests conducted allowed the calculation of residual stresses. Higher tensile residual stresses of  $-89.09 \pm 6.19$  MPa were observed in the parent material. The FSW process resulted in a reduction of the residual stresses up to  $-37.07 \pm 2.94$  MPa, which was particularly observed in the welds produced with the inclined tool.
5. The modified Williamson–Hall analysis was used to calculate the density and type of dislocation. The FSW process results in an increase in the fraction of dislocation of edge character dominating that had higher mobility. The sample produced with the tool rotational speed of 1000 RPM, tool traverse speed of 200 mm/min and the inclined tool was characterized by the dominance of edge character of dislocations of 71.3 pct while in the base material this value was equal to 18.2 pct. The change of the dislocation character influenced the dislocation mobility and it differed from  $3.19 \times 10^{-7}$  m/s for the base metal to  $16.78 \times 10^{-7}$  m/s for the weld produced with the tool rotational speed of 1000 RPM, traverse speed of 250 mm/min and the tool tilt angle of 2 deg.
6. Based on the calculations performed, the dislocation density was found to decrease for FSW welds up to the value of  $1.419 \times 10^{13} \frac{1}{\text{m}^2}$ . The dislocation



density of the base metals was equal to  $8.225 \times 10^{13} \frac{1}{\text{m}^2}$ .

7. A parameter for the density of dislocations divided by their mobility was introduced. A linear decreasing relationship was observed between this parameter and the value of revolutionary pitch for both tool tilt angles. As the density of dislocations increases and their mobility decreases, higher weld strength is expected. Based on the analysis, the introduction of less heat was found to be more favorable. Also, the lower heat input during the process results in reduced dissolution of precipitates, which in the case of precipitate-strengthened alloys such as AA6082 is crucial with regard to their strength.

#### CONFLICT OF INTEREST

The authors declare that they have no conflict of interest.

#### OPEN ACCESS

This article is licensed under a Creative Commons Attribution 4.0 International License, which permits use, sharing, adaptation, distribution and reproduction in any medium or format, as long as you give appropriate credit to the original author(s) and the source, provide a link to the Creative Commons licence, and indicate if changes were made. The images or other third party material in this article are included in the article's Creative Commons licence, unless indicated otherwise in a credit line to the material. If material is not included in the article's Creative Commons licence and your intended use is not permitted by statutory regulation or exceeds the permitted use, you will need to obtain permission directly from the copyright holder. To view a copy of this licence, visit <http://creativecommons.org/licenses/by/4.0/>.

#### REFERENCES

1. A. Laska and M. Szkodo: *Materials (Basel)*, 2020, vol. 13, pp. 1–46.
2. A.R.S. Essa, M.M.Z. Ahmed, A.K.Y.A. Mohamed, and A.E. El-Nikhaily: *J. Mater. Res. Technol.*, 2016, vol. 5, pp. 234–40.
3. M. Ilangoan, S.R. Boopathy, and V. Balasubramanian: *Def. Technol.*, 2015, vol. 11, pp. 174–84.
4. P. Cavaliere: *Procedia CIRP*, 2013, vol. 11, pp. 139–44.
5. S. Mabuwa and V. Msomi: *J. Mater. Res. Technol.*, 2020, vol. 9, pp. 9632–44.
6. A. Tamadon, D.J. Pons, K. Sued, and D. Clucas: *Metals (Basel)*, 2018, vol. 8, pp. 1–20.
7. F. Baratzadeh, E. Boldsai Khan, R. Nair, D. Burford, and H. Lankarani: *J. Adv. Join. Process.*, 2020, vol. 1, pp. 1–7.
8. P. Asadi, M.K.B. Givi, and M. Akbari: *Int. J. Adv. Manuf. Technol.*, 2016, vol. 83, pp. 301–11.
9. O. Barooni, M. Abbasi, M. Givi, and B. Bagheri: *Int. J. Adv. Manuf. Technol.*, 2017, vol. 93, pp. 4371–78.
10. N.M. Daniolos and D.I. Pantelis: *Int. J. Adv. Manuf. Technol.*, 2017, vol. 88, pp. 2497–2505.
11. A. Laska, M. Szkodo, D. Koszelow, and P. Cavaliere: *Metals (Basel)*, 2022, vol. 12, pp. 1–6.
12. A.H. Feng, B.L. Xiao, and Z.Y. Ma: *Compos. Sci. Technol.*, 2008, vol. 68, pp. 2141148.
13. J.F. dos Santos, P. Staron, T. Fischer, J.D. Robson, A. Kostka, P. Colegrove, H. Wang, J. Hilgert, L. Bergmann, L.L. Hütsch, N. Huber, and A. Schreyer: *Acta Mater.*, 2018, vol. 148, pp. 163–72.
14. P. Thirathipiwat, G. Song, J. Bednarcik, U. Kühn, T. Gemming, K. Nielsch, and J. Han: *Prog. Nat. Sci. Mater. Int.*, 2020, vol. 30, pp. 545–51.
15. Z. Zhuang, Z. Liu, and Y. Cui: *Dislocation Mechanism-Based Crystal Plasticity Theory and Computation at the Micron and Submicron Scale*, Elsevier Inc., 2019.
16. P.B. Prangnell and C.P. Heason: *Acta Mater.*, 2005, vol. 53, pp. 3179–92.
17. Z. Gao, J. Feng, Z. Wang, J. Niu, and C. Sommitsch: *Metals (Basel)*, DOI:<https://doi.org/10.3390/met9060672>.
18. W. Woo, L. Balogh, T. Ungár, H. Choo, and Z. Feng: *Mater. Sci. Eng. A*, 2008, vol. 498, pp. 308–13.
19. W. Woo, T. Ungár, Z. Feng, E. Kenik, and B. Clausen: *Metall. Mater. Trans. A*, 2010, vol. 41, pp. 1210–16.
20. D. Yuzbekova, V. Kulitskiy, A. Mogucheva, and R. Kaibyshev: *Mater. Sci. Forum*, 2017, vol. 879, pp. 2249–54.
21. W.B. Lee and S.B. Jung: *Mater. Lett.*, 2004, vol. 58, pp. 1041–46.
22. J. Altenkirch, A. Steuwer, M.J. Peel, P.J. Withers, S.W. Williams, and M. Poad: *Metall. Mater. Trans. A*, 2008, vol. 39, pp. 3246–59.
23. Y. Lin: *Recent Advances in Structural Integrity Analysis - Proceedings of the International Congress (APCF/SIF-2014)*, Woodhead Publishing, 2014.
24. W. Chen, G. Van Boven, and R. Rogge: *Acta Mater.*, 2007, vol. 55, pp. 43–53.
25. T. Li, Q.Y. Shi, and H.K. Li: *Sci. Technol. Weld. Join.*, 2007, vol. 12, pp. 664–70.
26. L.Y. Bai, L. Gao, and K.B. Jiang: *IOP Conf. Ser. Mater. Sci. Eng.*, 2018, vol. 21, pp. 1–10.
27. A. Laska, M. Szkodo, L. Pawłowski, and G. Gajowiec: *Int. J. Precis. Eng. Manuf. Green Technol.*, <https://doi.org/10.1007/s40684-022-00441-z>.
28. M. Peel, A. Steuwer, M. Preuss, and P.J. Withers: *Acta Mater.*, 2003, vol. 51, pp. 4791–4801.
29. R. John, K.V. Jata, and K. Sadananda: *Int. J. Fatigue*, 2003, vol. 25, pp. 939–48.
30. A. Steuwer, M.J. Peel, and P.J. Withers: *Mater. Sci. Eng. A*, 2006, vol. 441, pp. 187–96.
31. C. Zhang and A.A. Shirzadi: *Sci. Technol. Weld. Join.*, 2018, vol. 23, pp. 394–99.
32. M. Szkodo, A. Bień, and A. Stanisławska: *Int. J. Precis. Eng. Manuf. - Green Technol.*, 2022, vol. 9, pp. 175–90.
33. R.A. Young: *The Rietveld Method*, International Union of Crystallography, 1995.
34. M.D. Sandar and S. Yavasvi: *Int. J.*, 2017, vol. 3, pp. 39–47.
35. A. Abdollahzadeh, B. Bagheri, M. Abbasi, A.H. Kokabi, and A.O. Moghaddam: *J. Mater. Eng. Perform.*, 2021, vol. 30, pp. 1110–27.
36. N. Dialami, M. Cervera, and M. Chiumenti: *Metals (Basel)*, 2019, vol. 9, pp. 1–7.
37. B. Bagheri, M. Abbasi, and M. Dadaei: *J. Mater. Eng. Perform.*, 2020, vol. 29, pp. 1165–75.
38. J. Chen, W. Yan, C.X. Liu, R.G. Ding, and X.H. Fan: *Mater. Charact.*, 2011, vol. 62, pp. 237–42.
39. A. Lehtinen, L. Laurson, F. Granberg, K. Nordlund, and M.J. Alava: *Sci. Rep.*, 2018, vol. 8, pp. 1–2.
40. C.V. Rao, G.M. Reddy, and K.S. Rao: *Def. Technol.*, 2015, vol. 11, pp. 197–208.
41. G.G. Krishna, P.R. Reddy, and M.M. Hussain: *Glob. J. Res. Eng.*, 2014, vol. 14, pp. 61–70.
42. S.D. Meshram and G.M. Reddy: *Def. Sci. J.*, 2018, vol. 68, pp. 512–18.
43. G.K. Williamson and W.H. Hall: *Acta Metall.*, 1953, vol. 1, pp. 22–31.
44. P. Scherrer: Bestimmung Der Inneren Struktur Und Der Größe von Kolloidteilchen Mittels Röntgenstrahlen, in *Kolloidchemie Ein Lehrbuch*. R. Zsigmondy, ed., Springer, Berlin, 1912.
45. M.S. Khoshkhoo, S. Scudino, J. Thomas, K.B. Surreddi, and J. Eckert: *J. Alloys Compd.*, 2011, vol. 509, pp. S343-47.

46. F. HajyAkbar, J. Sietsma, A.J. Böttger, and M.J. Santofimia: *Mater. Sci. Eng. A*, 2015, vol. 639, pp. 208–18.
47. T. Ungár, I. Dragomir, A. Révész, and A. Borbély: *J. Appl. Crystallogr.*, 1999, vol. 32, pp. 992–1002.
48. J. Vallin, M. Mongy, K. Salama, and O. Beckman: *J. Appl. Phys.*, 1964, vol. 35, pp. 1825–26.
49. S.S. Bargujer, N.M. Suri, and R.M. Belokar: *Def. Sci. J.*, 2015, vol. 65, pp. 500–07.
50. W.J. Poole and D.J. Lloyd: *Proc. 9th Int. Conf. Alum. Alloy.*, 2004, pp. 939–45.
51. S.R. Valvi, A. Krishnan, S. Das, and R.G. Narayanan: *Int. J. Mater. Form.*, 2016, vol. 9, pp. 115–29.
52. U. Messerschmidt, B.V. Petukhov, M. Bartsch, C. Dietzsch, B. Geyer, D. Häussler, L. Ledig, M. Feuerbacher, P. Schall, and K. Urban: *Mater. Sci. Eng. A*, 2001, vol. 319–321, pp. 107–10.
53. C.T. Mouni, M.S.R.C.S.K. Albert, C.R. Das, P.K. Parida, and A. Sagdeo: *Mater. Sci. Eng. A*, 2021, vol. 826, p. 141960.
54. E. Schafner, M. Zehetbauer, and T. Ungár: *Mater. Sci. Eng. A*, 2001, vol. 319–321, pp. 220–23.
55. T.H. Simm: *Crystals*, 2018, vol. 8, pp. 1–32.
56. B. Chen, S. Li, H. Zong, X. Ding, J. Sun, and E. Ma: *Proc. Natl. Acad. Sci.*, 2020, vol. 117, pp. 16199–61206.
57. S. Starikov and V. Tseplyaev: *Comput. Mater. Sci.*, 2020, vol. 179, pp. 1–4.

**Publisher's Note** Springer Nature remains neutral with regard to jurisdictional claims in published maps and institutional affiliations.





## **7.6. [P6] Corrosion Properties of Dissimilar AA6082/AA6060 Friction Stir Welded Butt Joints in Different NaCl concentrations.**

**Laska A.\***, Szkodo M., Pawłowski Ł., Gajowiec G., Corrosion Properties of Dissimilar AA6082/AA6060 Friction Stir Welded Butt Joints in Different NaCl concentrations. *International Journal of Precision Engineering and Manufacturing – Green Technology*. 10, 457-477; 2023. doi: 10.1007/s40684-022-00441-z. (IF = 4.66, 200 points of the Polish Ministry of Science and Higher Education)

### 7.6.1. Declaration of the contribution of the doctoral candidate

My contribution to the preparation of the manuscript consisted of preparing the literature review and obtaining the research material. I developed the methodology for the experiments. I fabricated AA6082/AA6060 aluminum alloy joints by the FSW method using two different traverse speeds. I conducted macro- and microscopic observations. I analyzed the XRD diffractograms. I performed indentation studies. I made calculations of residual stresses, dislocation density, and dislocation mobility. I performed potentiodynamic studies. I analyzed the obtained experimental results. I conducted a discussion in the manuscript. I prepared figures and tables and drafted the manuscript. I prepared responses to the reviewers and functioned as a correspondence author.

My percentage contribution to the preparation of the manuscript was equal to 55 %.

.....  
Aleksandra Laska



## Corrosion Properties of Dissimilar AA6082/AA6060 Friction Stir Welded Butt Joints in Different NaCl Concentrations

Aleksandra Laska<sup>1</sup> · Marek Szkodo<sup>1</sup> · Łukasz Pawłowski<sup>1</sup> · Grzegorz Gajowiec<sup>1</sup>Received: 19 April 2021 / Revised: 3 March 2022 / Accepted: 16 April 2022 / Published online: 7 June 2022  
© The Author(s), under exclusive licence to Korean Society for Precision Engineering 2022

### Abstract

A solid-state friction stir welding method which is increasingly used in the marine and shipbuilding industry, has been developed to produce welds with high mechanical properties. In seawater, the oxide layer of aluminium is attacked by  $\text{Cl}^-$  ions resulting in its disruption and formation of pitting corrosion. It is particularly important to determine the electrochemical properties of the produced welds and to evaluate the effect of welding parameters on these properties. The following paper presents a study on the corrosion properties of welds of dissimilar aluminium alloys, AA6082 and AA6060, produced for two different tool traverse speeds of 160 and 200 mm/min, with consideration of the size of crystallites and residual stresses in the samples, determined by Williamson-Hall analysis and micro-indentation tests. The results revealed that the size of the crystallites in the welds was larger compared to the base materials and the friction stir welding process generated residual compressive stresses. Furthermore, the welds exhibited higher corrosion resistance compared to the parent materials. Scanning electron microscope observations indicated that the preferred locations of corrosion propagation for welds are the edges on the joint line formed by the combination of rotational and linear motion of the tool.

**Keywords** Friction stir welding · Aluminium alloy · Residual stress · Williamson-Hall analysis · Corrosion · Electrochemical impedance spectroscopy

### 1 Introduction

Aluminium and its alloys are widely used in many sectors of industry. Due to sufficient corrosion resistance and good mechanical properties, this group of materials is widely used in the maritime and shipbuilding industry [1]. Because of the susceptibility to plastic processing of aluminium and its alloys, it is possible to obtain structures with adequate mechanical strength, reducing the weight of the construction by up to three times in comparison with steel constructions [1]. This feature is extremely important for the shipbuilding industry because it allows increasing the payload of ships and reduces fuel consumption for lighter structures. In addition, the high strength-to-weight ratio of aluminium alloys contributes to the excellent manoeuvrability and stability of floating objects. 6xxx series aluminium alloys, which

contain magnesium and silicon as principal alloying elements, are one of the most popular alloys used in aerospace, transportation, and marine industries [2–5].

In seawater,  $\text{Cl}^-$  ions attack oxide film protecting aluminium alloys. The breakdown of the oxide protective nanolayer results in pitting corrosion [6]. Deep pits created on the surface of aluminium components are widely observed when they are exposed to the sea water environment. Depending on the concentration of chloride anions in the solution, pitting corrosion can occur at different rates [7, 8]. The average salinity of the world's marine waters is determined at 35‰ [9]. Studies conducted so far determine the corrosion properties of aluminium in such salinity [6, 10–12]. However, there are water reservoirs with different salinity levels. The average salinity of the Baltic Sea is 7‰, so it is significantly lower than the world average [13, 14]. There is, therefore, a supposition that the corrosion in such an environment will occur at a different rate. However, the current literature review does not allow to confirm this hypothesis.

Friction Stir Welding (FSW) is a modern method of joining materials, invented at The Welding Institute in London (TWI) and patented by Thomas et al. almost three decades

✉ Aleksandra Laska  
aleksandra.laska@pg.edu.pl

<sup>1</sup> Faculty of Mechanical Engineering and Ship Technology, Gdansk University of Technology, Narutowicza, 11/12, 80-233 Gdansk, Poland



ago [15]. It is a solid-state joining method that uses a specially designed non-consumable rotating tool to move along the contact line of the components to be welded. The tool consists of a pin plunged between the components and a shoulder that provides the friction between the tool and the workpiece. The contact friction generates thermal energy. The heated material is plasticised and extruded around the pin [16]. Since the melting point is not reached during the process, problems associated with the changes in the volume and gas solubility are eliminated [17–19]. The FSW method allows producing butt, corner, lap, t-joints and other types of welds [20–22]. The most important process parameters include a tool geometry, a tool rotational speed, a tool traverse speed and a tilt angle [23–26]. FSW method is considered as an eco-friendly technology. Since no melting point is reached during the process, less energy is consumed compared to fusion welding techniques. Besides, the emission of CO<sub>2</sub> into the atmosphere can be significantly limited [27]. Controlling the process is relatively easy, and by setting optimal parameters, the necessary non-destructive testing can be subsequently minimized. Pollution generated by atomized gases for visual and magnetic inspections and radiation exposure for X-ray examinations are reduced. In addition, post-weld heat treatment is not required when optimal parameters are set [27–29]. This results in the reduction of CO<sub>2</sub> emissions, energy consumption and other pollutants emitted into the atmosphere.

The current literature review does not allow to determine significant correlations between particular parameters of FSW welding and electrochemical properties of the resulting welds. Qin et al. [30] studied the corrosion behaviour of the 1A14-T6 friction stir welded butt joint in the solution consisting 4 mol NaCl, 0.5 mol KNO<sub>3</sub> and 0.1 mol HNO<sub>3</sub>. The joint was produced at a traverse speed of 50 mm/min, a tool rotational speed 800 rpm and a tilt angle equal to 3°. It was noticed that the joint was more resistant to exfoliation corrosion compared to the base material. In the studies of Gharavi et al. [31] AA6061-T6 FSW lap joints were tested for their electrochemical properties. The lap joint produced at the traverse speed equal to 60 mm/min, the rotational speed of 1000 rpm and the tilt angle of 3° exhibited a poorer corrosion resistance than that for the parent alloy in the solution of 3.5(wt)% NaCl. Ales et al. [32] prepared the FSW butt joints of AA2024-T4 alloy with the following process parameters: the tool traverse speed 100 mm/min, the tool rotational speed 1000 rpm, the tilt angle 2°. In the 3.5(wt)%

NaCl solution it was observed that the most serious corrosion occurs in the weld nugget region.

The aim of the following study was to determine electrochemical properties of friction stir welded dissimilar AA6060/AA6082 joints and both parent alloys in seawater. The current state of the art does not allow to determine the conclusions concerning the influence of the tool traverse speed on electrochemical properties of welds of AA6082 and AA6060 aluminium alloys. The paper presents the results of tests on FSW welds produced with a different tool traverse speed.

## 2 Materials and Methods

### 2.1 Friction Stir Welding

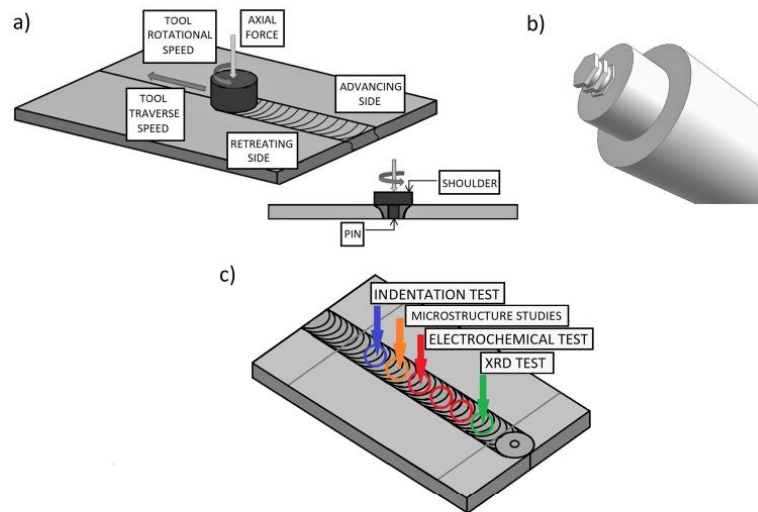
For this study AA6060 and AA6082 aluminium alloys were used. According to the producer, both alloys were solution heat-treated and artificially aged to T651 condition. The welds for the present studies were produced by the FSW method on 3 mm thick sheets. AA6082 alloy was kept on the advancing side and AA6060 on the retreating side of the welds. Chemical compositions of the chosen alloys were determined by the X-ray energy-dispersive spectrometer (EDS) (Edax Inc., Mahwah, NJ, USA) and are shown in Table 1.

The FSW welds were performed on a conventional milling machine (FU251, Friedrich Engels Kazanluk, Bulgaria). The butt welds were produced with a tool of 18 mm shoulder diameter, the distance across flats of the hexagonal pin was equal to 6 mm and the pin length was equal to 2.5 mm. The schematic illustration of the tool is shown in Fig. 1 b. The shoulder plunge depth was 0.3 mm. The hexagonal pin with grooves was made of 73MoV52 (carbon 0.77%, vanadium 0.25%, molybdenum 0.65%) steel and the shoulder material was X210Cr12 (carbon 2.20%, chromium 13.00%, tungsten 0.80%) steel. The measured hardness of the pin and the shoulder were equal to 58 and 61 HRC (Wilson Mechanical Instrument Co. Inc., USA), respectively. The tilt angle ( $\alpha$ ) and the tool rotational speed ( $\omega$ ) were kept constant and equal to 0° and 1250 rpm, respectively, while the welds were performed at two different traverse speeds:  $v = 160$  mm/min (W160) and 200 mm/min (W200). In accordance with the principles of the solid-state FSW method, the temperature was kept below the melting point during welding. The

**Table 1** Chemical composition of AA6082 and AA6060 alloys

	Chemical composition [%wt]								
	Zn	Mg	Cr	Ti	Fe	Si	Cu	Mn	Al
AA6060	0.15	0.58	0.05	0.10	0.25	0.44	0.10	0.10	Balance
AA6082	0.20	1.03	0.25	0.10	0.50	0.90	0.10	0.42	Balance

**Fig. 1** Schematic illustration of the FSW process (a), geometry of the tool used for FSW of AA6060/AA6082 (b) and location of the samples cut for the performed tests (c) (colour figure online)



schematic illustration of the FSW process and the tool geometry is shown in Fig. 1a, b. Figure 1c indicates the location of the samples cut for specific tests. Disk-shaped samples were cut from the weld nugget zone providing a sample area of  $1 \text{ cm}^2$ .

## 2.2 Material Characterization

To determine the grain size of the parent materials and welds, the samples were wet ground to the final gradation #4000 and polished using a  $1 \mu\text{m}$  diamond suspension. Double-stage etching in Weck's etchant was performed. Firstly, the samples were immersed in 2(wt)% NaOH solution in distilled water for 60 s. Next, the samples were etched in a reagent of 4 g  $\text{KMnO}_4$ , 1 g NaOH and 100 ml distilled water for 10 s. The microstructure observations were performed by an optical microscope (BX51, OLYMPUS, Tokyo, Japan). For electrochemical tests, samples of the parent material and the produced welds were cut out in the shape of discs with a working surface of  $1 \text{ cm}^2$ . The samples were cleaned and degreased with isopropanol (99.7% purity, POCH, Poland).

The X-ray diffraction method (XRD) (Philips X'Pert Pro, Netherlands) was applied via a diffractometer (with  $\text{Cu K}\alpha$  radiation  $\lambda = 0.15418 \text{ nm}$ ), operated at 30 kV and 50 mA. Bragg–Brentano focusing geometry was used collecting the diffraction patterns over the  $2\theta$  range from  $20^\circ$  to  $90^\circ$  with a step size of  $0.02^\circ$ . A silicon standard was used to evaluate and correct instrumental broadening effects. Williamson–Hall analysis was used to estimate the size of crystallites and micro-strains in both parent materials and welds. The hardness of the samples was measured by NanoTest Vantage

nanoindenter (NanoTest Vantage, Micro Materials, UK). A pyramidal Berkovich indenter was used for the tests. For each sample, 25 independent measurements were carried out with the maximum force of 10 N. The loading time was set up as 20 s, the unloading time 15 s and the dwell time at maximum force was equal to 5 s. The distance between the subsequent indents was equal to  $200 \mu\text{m}$ . The load–displacement curves were recorded based on the Olivier and Pharr method. From the obtained values of reduced Young's modulus, Young's modulus was calculated by considering the following values—Poisson's ratio of diamond equal to 0.07, Poisson's ratio of aluminium 0.3 [33]. Considering calculated from Williamson–Hall analysis values of micro-strains and modulus of elasticity calculated on basis of indentation tests, the quantitative residual stresses were determined.

## 2.3 Electrochemical Studies

Electrochemical measurements were performed using potentiostat/galvanostat (Atlas 0531, Atlas Sollich, Poland) in NaCl (99.8% purity, CHEMPUR, Poland) solutions of various concentrations: 0.2(wt)%, 0.7(wt)% and 1.2(wt)% at room temperature. The solutions were not aerated and their level of oxygen was about 24%, according to the analysis of Shatkay [34]. The pH of all prepared solutions kept neutral (PHT-200, Voltcraft, Germany). The designation of samples with applied parameters is shown in Table 2.

A three-electrode system with a platinum electrode as counter-electrode, saturated calomel electrode as reference electrode, and aluminium samples as working electrode was used. Measurements were initiated by determining the open



**Table 2** Designations of experiment samples with the applied process parameters

Sample	Material	Welding parameters	NaCl concentration (wt%)
AA6082 <sub>0,2</sub>	AA6082	–	0.2
AA6082 <sub>0,7</sub>	AA6082	–	0.7
AA6082 <sub>1,2</sub>	AA6082	–	1.2
AA6060 <sub>0,2</sub>	AA6060	–	0.2
AA6060 <sub>0,7</sub>	AA6060	–	0.7
AA6060 <sub>1,2</sub>	AA6060	–	1.2
W160 <sub>0,2</sub>	Weld AA6082/AA6060	v = 160 mm/min	0.2
W160 <sub>0,7</sub>	Weld AA6082/AA6060	ω = 1250 rpm	0.7
W160 <sub>1,2</sub>	Weld AA6082/AA6060	α = 0°	1.2
W200 <sub>0,2</sub>	Weld AA6082/AA6060	v = 200 mm/min	0.2
W200 <sub>0,7</sub>	Weld AA6082/AA6060	ω = 1250 rpm	0.7
W200 <sub>1,2</sub>	Weld AA6082/AA6060	α = 0°	1.2

circuit potential (OCP) within 60 min. Then electrochemical impedance spectroscopy (EIS) was conducted at frequencies in the range of 1 Hz–100 kHz with a signal of 10 mV amplitude, collecting 10 points per decade. The EIS spectra were obtained at the open circuit potential value. ZView (Scribner Associates Inc., USA) software was applied to fit the obtained EIS data. The  $\chi^2$  values, representing goodness of fit, were kept on the level of  $10^{-3}$  or lower to maintain the high reliability of the obtained results. Corrosion curves were determined using the potentiodynamic method for the potential range of  $-2/+1$  V with a potential scan rate of 1 mV/s. Tafel extrapolation method was adopted to determine the values of the corrosive potential ( $E_{\text{corr}}$ ) and the corrosion current density ( $i_{\text{corr}}$ ) using AtlasLab (Atlas Sollich, Poland) software. Before and after electrochemical studies the samples were weighed (Pioneer PA114CM/1, OHAUS, Greifensee, Switzerland) to determine the weight loss. The measurement results were collected at an accuracy of 0.0001 g.

#### 2.4 Surface Characterization

The surfaces of the samples before and after corrosion tests were examined using a high resolution scanning electron microscope (SEM JEOL JSM-7800 F, JEOL Ltd., Japan) with a BED detector at 5 kV acceleration voltage.

#### 2.5 Degradation Analysis

Material degradation tests were carried out by immersion of the samples in NaCl (99.8% purity, CHEMPUR, Poland) solutions with a mass concentrations of 3.5(wt)%.

The samples were kept for 168 h at room temperature. The weight loss of the samples after this time was investigated (Pioneer PA114CM/1, OHAUS, Greifensee, Switzerland). The measurement results were collected at an accuracy of 0.0001 g. The corrosion rate (CR) based on weight loss was calculated using a formula:

$$CR \left[ \frac{\text{mm}}{\text{year}} \right] = \text{weight loss} [g] \cdot \frac{1}{\text{metal density} \left[ \frac{\text{cm}^3}{g} \right]} \cdot \frac{1}{\text{exposed area} [\text{cm}^2]} \cdot 10 \left[ \frac{\text{mm}}{\text{cm}} \right] \cdot \frac{1}{\text{exposed time} [h]} \cdot 8760 \left[ \frac{h}{\text{year}} \right], \quad (1)$$

which can be simplified to:

$$CR \left[ \frac{\text{mm}}{\text{year}} \right] = \frac{\Delta m [g]}{d \left[ \frac{g}{\text{cm}^3} \right] \cdot S [\text{cm}^2] \cdot t [h]} \cdot 87600, \quad (2)$$

where  $\Delta m$  is a weight loss after the time of immersion,  $d$  is a density of the material,  $S$  is a surface area of the sample and  $t$  is the time of immersion. Densities of both aluminium alloys—AA6082 and AA6060, based on safety data sheets provided by the manufacturer, are equal to  $2.710 \text{ g/cm}^3$ . To calculate the standard deviation, the test was performed 3 times.

### 3 Results

Figure 2a, b shows metallographic cross-sections of W160 and W200 sample, respectively. In the cross-section of the specimen, typical FSW weld zones were distinguished—weld nugget, thermo-mechanically affected zone, heat-affected zone and base materials—AA6082 on the advancing side and AA6060 on the retreating side. In both macroscopic images of the cross-sections, the curvature of the top surface can be observed due to the tool shoulder plunge into the aluminium sheets during welding. A little material outflow, on both advancing and retreating side can be also observed. The microstructure of AA6082 and AA6060 parent materials, as well as W160 and W200 samples, is shown in Fig. 2c–f. By etching the samples, the grain size of the investigated materials could be determined. From the microscopic images it can be concluded that the weld nuggets are characterized by a more finely grained structure compared to both parent materials. Welds produced with tool traverse speeds of 160 mm/min and 200 mm/min show no significant differences in the grain size of the nugget zone. The formation of the fine-grained weld nugget (WN) is a result of the recrystallization process caused by intense plastic deformation and high heat input in this zone. The nugget experiences plastic deformations resulting from the interaction with the pin, while the



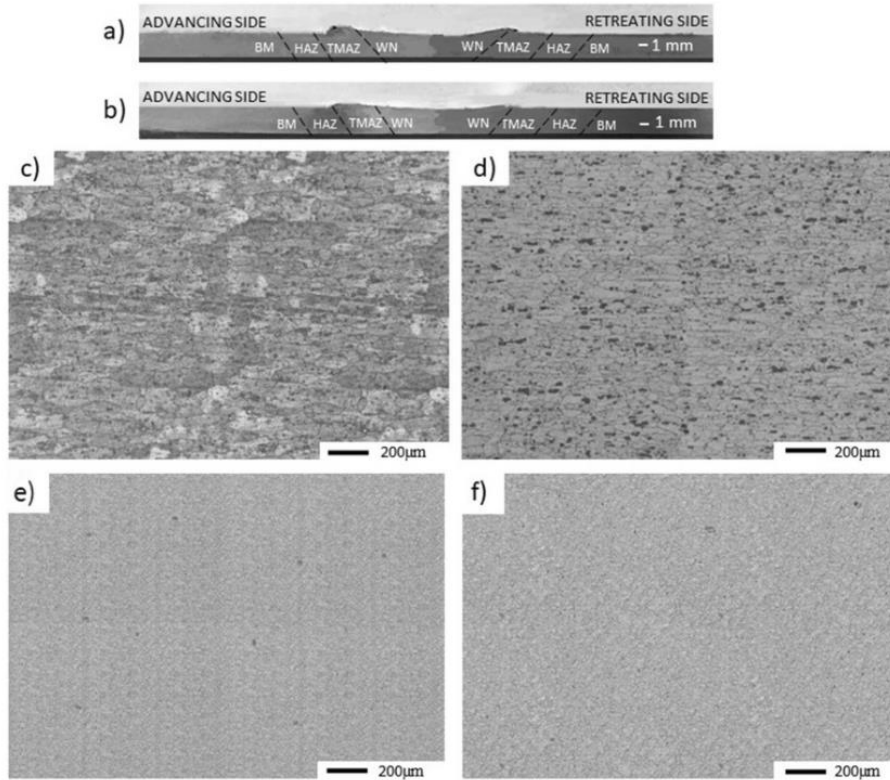


**Fig. 2** Metallographic cross-section of W160 (a) and W200 sample (b), optical micrographs of etched AA6082 (c) and AA6060 (d) parent materials and the weld nuggets of W160 (e) and W200 (f) samples (colour figure online)

frictional heating is mostly provided by the contact with the rotating shoulder. The existence of the unique zone between the base material and the heat-affected zone, called thermo-mechanically affected zone (TMAZ) is characteristic for FSW joints. Thermo-mechanically affected zone experiences both temperature and deformation, however, recrystallization cannot be observed in this zone due to insufficient deformation strain. The heat-affected zone (HAZ) is located beyond the TMAZ and experiences a thermal cycle. No plastic deformation occurs in the HAZ. The HAZ might experience a temperature rise above 250 °C for a heat-treatable aluminium alloy [35]. Although the HAZ retains the same grain structure as the parent material, the thermal exposure above 250 °C causes a significant effect on the precipitate structure. The HAZ is sufficiently heated during the process so it alters the properties of that material without any plastic deformation.

Figure 3 presents X-ray diffractograms obtained for AA6082, AA6060, W160 and W200 samples. The main

diffractograms can be indexed as originating from pure aluminium. In all the diffractograms also the peaks corresponding to phases with the main alloying elements (Mg, Mn, Si, Fe) can be observed. The diffractograms obtained for all samples also allowed the identification of aluminium oxide  $\alpha\text{-Al}_2\text{O}_3$  forming a passive layer on both the native materials and the welds tested. The oxide film of  $\alpha\text{-Al}_2\text{O}_3$  is generally reported to be present on the surface of aluminium alloys [36, 37]. The crystallite size and microstrain were estimated by the Williamson-Hall analysis for the peaks assigned to aluminium. The peaks assigned to the particular phases are in agreement with the studies of Khorsand et al. [38], Leszczyńska-Madej et al. [39] and Debih et al. [40].

The Williamson-Hall method assumes that the broadening of the peaks is due to the combination of crystallites size and microstrain [41]:

$$\beta_T = \beta_D + \beta_\epsilon, \quad (3)$$

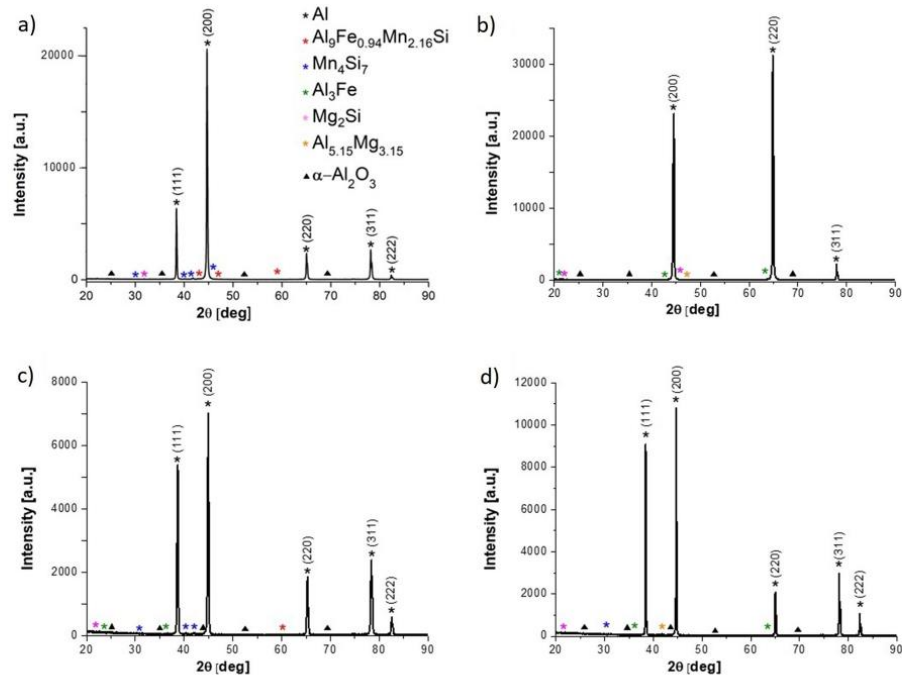


Fig. 3 XRD diffraction patterns for AA6082 (a) and AA6060 (b) base materials and W160 (c) and W200 (d) welds (colour figure online)

where  $\beta_T$  is the total broadening,  $\beta_D$  is the broadening due to the crystallite size and  $\beta_\varepsilon$  is the broadening resulting from strain.  $z$

From the Scherrer equation:

$$\beta_D = \frac{a_s \cdot \lambda}{L \cdot \cos\theta}, \quad (4)$$

where  $a_s$  is the Scherrer constant dependent on the shape of the crystal and the size distribution (here is assumed to be 1),  $\lambda$  is an electron beam wavelength (0.15418 nm) and  $L$  is a crystallite size represents a crystal portion with exactly the same crystallographic orientation such as sub-grains [42].

Similarly, the XRD peak broadening resulting to micro-strain is given as:

$$\beta_\varepsilon = 4 \varepsilon \tan\theta, \quad (5)$$

where  $\varepsilon$  is the strain.

Assuming Eqs. (3), (4) and (5) the Williamson-Hall equation can be presented as:

$$B = \frac{a_s \cdot \lambda}{L \cdot \cos\theta} + 4 \varepsilon \tan\theta, \quad (6)$$

Or, presented as a linear function:

$$B \cos\theta = \frac{a_s \cdot \lambda}{L} + 4 \varepsilon \sin\theta. \quad (7)$$

Plots of  $B \cos\theta$  vs.  $\sin\theta$  are presented in Fig. 4. Figure 4 contains the approximation of linear functions for points representing peaks in the diffraction patterns.

The results of plot analysis, containing microstrain values and crystallite size of all the samples are shown in Table 3. The indentation tests were performed in order to calculate the reduced modulus of elasticity and the microhardness for all the tested samples. Considering the calculated Young's modulus, the values of  $\sigma_R$  for all the samples are also presented in Table 3. It should be noted that the residual stresses for both parent materials were below zero, which indicates the tensile nature. For both of the welds, the residual compressive stresses were observed and higher crystallite size was found. During friction stir welding a large strain of the metal matrix is observed. In combination with high temperatures during the process dynamic recrystallization occurs in the weld nugget and, consequently, a reduction in the grain size with a simultaneous increase in the size of the crystallites can be observed.

The obtained load and unload curves for single indentation for each sample are shown in Fig. 5 a. Small deflections

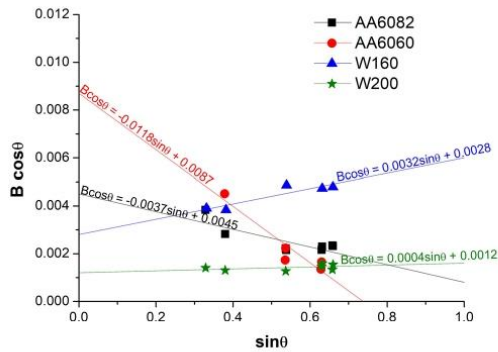


Fig. 4 Plots of  $B \cos\theta$  vs.  $\sin\theta$  for the parent materials and both welds (colour figure online)

observed on the deformation curves are caused by the temperature drift occurred with each measurement. Similar Young modulus values were observed for all the tested samples. It was evident that the welds performed higher microhardness than the parent materials. The difference in hardness between the native materials and the produced welds may be due to the difference in dislocation velocities in the materials tested. The nature of the collective motion of dislocation in the crystals controls the mechanical properties, such as the microhardness of materials. The dwell time period of the indentation test was analysed to determine dislocation density and its mobility. During the indentation experiment, once the maximum load of 10 N was reached, the indenter dwelt at the maximum load for a time of 5 s. During the dwell time, the material continued

to deform. The time-strain relationship during the dwell time is shown in Fig. 5b.

A significant increase in the hardness of metallic materials can be observed in indentation tests at low forces. It is referred to indentation size effect (ISE). The ISE is directly related to geometrically necessary dislocations (GNDs) in the material. The density of GNDs is proportional to the inverse of the indentation depth ( $h$ ). The density of GNDs is derived from the total line length  $k$  of the loop of dislocations required to form the shape of the conical indenter. These dislocations are geometrically necessary as they are introduced into the material to accommodate the indenter shape and thus provide the necessary lattice rotations. The complete line length is then divided by the hemispherical volume  $V$  defined by the contact radius  $a_c$ . The indentation depth is denoted by  $h$ ,  $b$  is the Burgers vector magnitude,  $V$  is the storage volume of the GNDs, and  $\delta$  is the angle between the surface and the indenter. Instead of using the volume defined by the contact radius as the storage volume of GNDs, the plastically deformed volume under the indenter is considered here. The plastic zone radius is denoted by  $a_{pz}$  and a factor  $f$  is assumed to connect  $a_c$  and  $a_{pz}$ . For most metallic materials, the plastic zone radius is larger than the contact radius, and  $f > 1$  [43]. The geometry of the cross-section of the specimen during the indentation test is shown in Fig. 6. The formula for the density of GNDs can be expressed as follows (8):

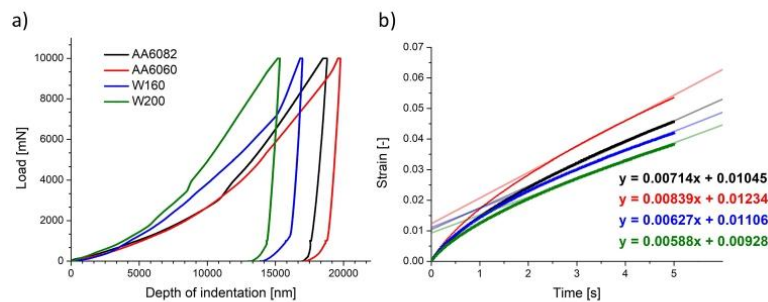
$$\rho_{\text{GND}} = \frac{3}{2} \cdot \frac{1}{f^3} \cdot \frac{\tan^2 \delta}{bh} \tag{8}$$

For a cone-shaped indenter, the plasticized zone is hemispherical in shape. Although the GNDs density described

Table 3 Crystallite size, microstrain, Young modulus, residual stress and microhardness in AA6082, AA6060, W160 and W200 samples

	L [nm]	$\varepsilon$ [-]	E [GPa]	$\sigma_R$ [MPa]	$H_{ISE}$ [GPa]
AA6082	34.2	- 0.00093	70.43 ± 4.56	- 65.500 ± 4.241	1.282 ± 0.157
AA6060	17.7	- 0.00295	75.22 ± 4.10	- 221.899 ± 12.095	1.065 ± 0.043
W160	55.0	0.0008	74.43 ± 5.15	59.544 ± 4.120	1.519 ± 0.161
W200	128.0	0.0001	71.42 ± 4.59	7.142 ± 0.459	1.580 ± 0.171

Fig. 5 Hysteresis plots of load-deformation for a single indentation measurement for the analysed samples (a) and strain-time diagram for dwell period (b) (colour figure online)





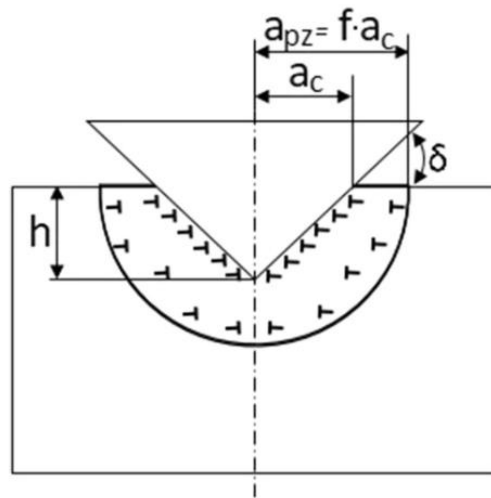


**Fig. 6** Geometry of the cross-section of the specimen during the indentation test (colour figure online)

above applies to the cone-shaped indenter, the same relationship between indenter displacement depth and GNDs density also exists for indenters of other shapes. For soft phases such as Al-based solid solution, the volume of the plasticized zone is much larger than the volume implied by the contact radius. For the purposes of our analysis, a factor of  $f=3$  can be assumed for the Berkovich indenter.

Apart from the density of GNDs and SSDs (statistically stored dislocations) the result of hardness measurement  $t$  is also affected by such factors as frictional stress of crystalline lattice  $H_{fr}$  or hardening of solid solution by dissolved alloy additives  $H_{ss}$ . The equation describing the influence of all the factors described above on the result of hardness measurement can be written as follows:

$$H_{ISE} = H_{fr} + H_{ss} + MC\alpha Gb \sqrt{\rho_{GND} + \rho_{SSD}}, \quad (9)$$

where  $M$  is the Taylor coefficient relating the shear stress to the normal stress in uniaxial deformation,  $C$  is the factor transferring the complex stress state under the indenter into a uniaxial stress state,  $a$  is a coefficient depending on the dislocation substructure,  $G$  is the transverse elastic modulus, and  $b$  is the magnitude of the Burgers vector. As a good first-order approximation, the coefficient  $C=3$  and the Taylor coefficient  $M=3$  [44]. Due to the complex stress field under the indenter, a constant value of  $a=0.5$  can be chosen for the dislocations GND and SSD. For Al, the Burgers vector is  $b=0.286$  nm and the transverse elastic modulus  $G=26$  GPa [45]. Dislocation hardening will only be considered in this

**Table 4** GNDs density, SSDs density and dislocation velocity of AA6082, AA6060, W160 and W200 samples

	$\rho_{GND} [\frac{1}{m^2}]$	$\rho_{SSD} [\frac{1}{m^2}]$	$v [\frac{m}{s}]$
AA6082	$2.421 \cdot 10^{12}$	$1.465 \cdot 10^{15}$	$1.704 \cdot 10^{-8}$
AA6060	$2.401 \cdot 10^{12}$	$1.011 \cdot 10^{15}$	$2.903 \cdot 10^{-8}$
W160	$2.964 \cdot 10^{12}$	$2.058 \cdot 10^{15}$	$1.065 \cdot 10^{-8}$
W200	$3.161 \cdot 10^{12}$	$2.226 \cdot 10^{15}$	$0.908 \cdot 10^{-8}$

analysis. In such a case, the relation describing the hardness including the scale effect can be written as follows:

$$H_{ISE} = MC\alpha Gb \sqrt{\rho_{GND} + \rho_{SSD}}, \quad (10)$$

In contrast, the relationship between macroscopic hardness  $H_0$  (without ISE scale effect) and dislocation density (SSD) can be described by Taylor's relation [46]:

$$H_0 = MC\alpha Gb \sqrt{\rho_{SSD}}. \quad (11)$$

To determine the dislocation density generated during the nanoindentation tests ( $\rho_{GND}$ ), use relation (8). For the Berkovich indenter, the angle  $\delta=24.7^\circ$  and the maximum indenter displacement depths  $h$  (for plastic deformation) are registered during nanoindentation tests [47]. The  $H_{ISE}$  hardness was also determined during the nanoindentation tests. To determine the dislocation densities ( $\rho_{SSD}$ ) generated during the FSW process with different parameters, the relation (10) is transformed as follows:

$$\rho_{SSD} = \frac{H_{ISE}^2}{(MC\alpha Gb)^2} - \rho_{GND}. \quad (12)$$

The Orowan Eq. (13) was used to calculate the dislocation velocity ( $v$ ) [48].

$$\frac{d\epsilon}{dt} = \dot{\epsilon} = b \cdot \rho_{SSD} \cdot v. \quad (13)$$

In order to calculate the strain derivative as a function of time, the stabilized fragment of the creep graph of the material during the period of the maximum force during the indentation test was approximated to a linear function. The formulas of the resulting linear functions are shown in Fig. 5b. Equation 13 can be converted to the:

$$v = \frac{\dot{\epsilon}}{b \cdot \rho_{SSD}}. \quad (14)$$

The results of the above analysis are presented in Table 4.

Figures 7a, 7c and 7e show the variation of the open circuit potential (OCP) as a function of time obtained for the samples immersed in NaCl solution with a mass concentration of 0.2, 0.7 and 1.2%, respectively. In the case of the lowest NaCl concentration, all metallic samples reached stability

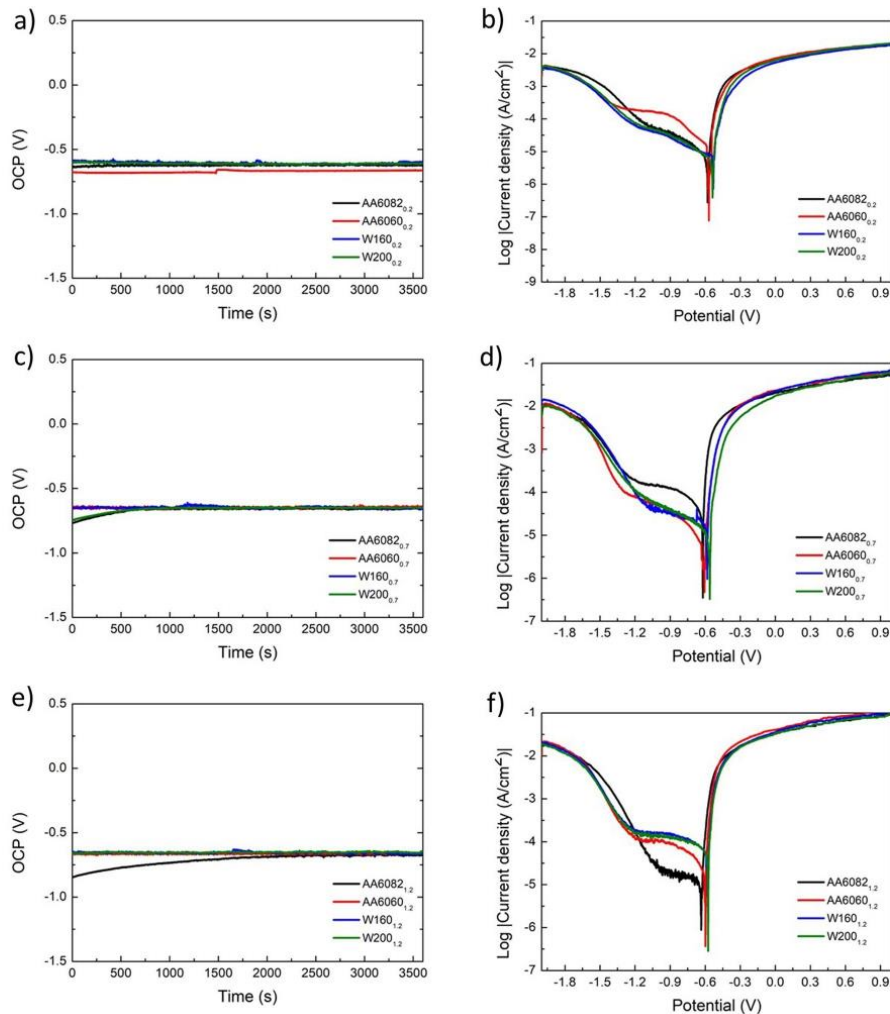


**Fig. 7** Open circuit potential (a, c, e) and potentiodynamic polarization curves (b, d, f) of AA6082, AA6060, W160 and W200 in NaCl solution with a concentration of 0.2(wt)% (a, b), 0.7(wt)% (c, d) and 1.2(wt)% (e, f) (colour figure online)

in relation to the electrolyte after a few seconds of immersion in the solution. The OCP values for all the prepared samples were similar. Although lower OCP values were noted for both parent materials in comparison to the both welds, the differences were not significant. For the samples immersed in a solution of 0.7(wt)% NaCl, the stabilization of the open circuit potential was achieved after a maximum of 700 s of immersion in the electrolyte. The achieved values of OCP for all the samples were similar and they differ in the range from  $-0.657$  V for AA6082 base material to  $-0.647$

for AA6060 base material. The corrosion resistance studies of aluminium alloys and welds in 1.2(wt)% NaCl solution were also initiated by measuring the open circuit potential in this medium. The circuit containing AA6060 alloy and both welds achieved stability almost immediately after being placed in the electrolyte, while the circuit containing the sample of AA6082 alloy submerged in 1.2(wt)% NaCl solution achieved stability after about 2200 s after immersion. After the stability was achieved, all circuits exhibited a similar OCP value. The lowest value of  $-0.674$  V was reported

for a circuit containing a sample of AA6082 alloy and the highest OCP value for a circuit with a weld produced at a tool traverse speed of 200 mm/min and this value was equal to  $-0.649$  V.

Based on the data from the potentiodynamic method, corrosion potential ( $E_{\text{corr}}$ ) and current density ( $i_{\text{corr}}$ ) of individual samples were determined on the basis of Tafel extrapolation for all NaCl concentrations. Table 5 contains the OCP,  $E_{\text{corr}}$  and  $i_{\text{corr}}$  values for the above tests.

Figures 7b, d, f present the potentiodynamic polarization curves obtained for the samples immersed in 0.2, 0.7 and 1.2(wt)% NaCl solution, respectively. In order to obtain a corrosion curve range that allows Tafel extrapolation to be performed, a test range of  $-2$  to  $1$  V potential was established. This range allows observation of both cathodic and anodic branches of the resulting polarization curve. The cathode branch of the polarization curves corresponds to the release of hydrogen, while the anode branch represents the dissolution of the substrate [49]. The  $E_{\text{corr}}$  values for both friction stir welded samples immersed in 0.2(wt)% NaCl electrolyte were higher and shifted towards positive values in comparison to AA6082 and AA60606 parent materials. The  $i_{\text{corr}}$  values for W160 and W200 samples were similar and lower in comparison to the both parent materials. It could be noted that both welds exhibited lower  $i_{\text{corr}}$  values and higher OCP values compared to both parent materials. The highest OCP values were noted for W160 and W200 samples, equal to  $-0.598$  and  $-0.608$  V, respectively. The highest  $i_{\text{corr}}$  values were observed for AA6082 and AA6060 alloys, 10.749 and 9.831  $\mu\text{A}\cdot\text{cm}^{-2}$ , respectively. In the case of the studies of corrosion resistance in 0.7(wt)% NaCl concentration, the lowest value of  $i_{\text{corr}}$  was observed for the weld produced at a tool traverse speed of 200 mm/min. The highest  $i_{\text{corr}}$  value was reported to AA6082 base metal. It is worth noting that the particular  $i_{\text{corr}}$  values for each type of the sample were

higher for 0.7(wt)% than for 0.2(wt)% NaCl concentration. Based on the potentiodynamic polarization curves values of the  $i_{\text{corr}}$  for all the samples indicate that the highest  $i_{\text{corr}}$  values were reported for the base materials, with AA6082 alloy having the value of 17.459  $\mu\text{A}\cdot\text{cm}^{-2}$ . In the case of the concentration of NaCl of 1.2(wt)%, as well as for 0.2(wt)% and 0.7(wt)% NaCl concentration, the lowest value of  $i_{\text{corr}}$  was achieved with a weld produced with a tool traverse speed of 200 mm/min. The trend of higher  $i_{\text{corr}}$  values for both parent materials compared to the welds is maintained, with the weld produced at the tool traverse speed of 200 mm/min exhibiting the lowest  $i_{\text{corr}}$  value for all investigated concentrations of NaCl. These observations were in accordance with the SEM images (Fig. 8), where the lowest corrosion degradation was observed for W200 samples immersed in different NaCl concentrations.

The results of SEM imaging of both base materials—AA6082 on the advancing side and AA6060 on the retreating side and the welds produced with a tool traverse speed of 160 mm/min and 200 mm/min are shown in Figs. 8a, b, c, d. The base metals, mechanically and thermally unaffected during the FSW process, exhibit a similar surface appearance. In the welds produced at different tool traverse speeds, a characteristic structure relating to the rotational movement of the tool was observed. No defects of the welds were observed as a result of the welding process. Figures 8a', b', c' and d' show scanning electron microscope images of all samples on which electrochemical tests were performed in 0.2(wt)% NaCl solution. The effects of electrochemical corrosion were observed on all the samples. SEM images indicate that the highest corrosion degradation was observed for a sample of AA6082 parent material (a'), while the smallest losses were observed for a weld produced at a tool traverse speed of 200 mm/min (d'). Although the degradation effects for both friction stir welded samples were not significant,

**Table 5** Open circuit potential (OCP), corrosion potential ( $E_{\text{corr}}$ ) and current density ( $i_{\text{corr}}$ ) for the prepared samples obtained after the tests in 0.2(wt)%, 0.7(wt)% and 1.2(wt)% NaCl solutions

Sample	AA6082 <sub>0,2</sub>	AA6060 <sub>0,2</sub>	W160 <sub>0,2</sub>	W200 <sub>0,2</sub>
OCP [V]	-0.626	-0.663	-0.598	-0.608
$E_{\text{corr}}$ [V]	-0.590	-0.557	-0.532	-0.541
$i_{\text{corr}}$ [ $\mu\text{A}\cdot\text{cm}^{-2}$ ]	10.749	9.831	8.162	8.006
Sample	AA6082 <sub>0,7</sub>	AA6060 <sub>0,7</sub>	W160 <sub>0,7</sub>	W200 <sub>0,7</sub>
OCP [V]	-0.657	-0.647	-0.653	-0.652
$E_{\text{corr}}$ [V]	-0.616	-0.611	-0.583	-0.561
$i_{\text{corr}}$ [ $\mu\text{A}\cdot\text{cm}^{-2}$ ]	13.381	11.107	9.983	9.426
Sample	AA6082 <sub>1,2</sub>	AA6060 <sub>1,2</sub>	W160 <sub>1,2</sub>	W200 <sub>1,2</sub>
OCP [V]	-0.674	-0.659	-0.661	-0.649
$E_{\text{corr}}$ [V]	-0.640	-0.599	-0.579	-0.576
$i_{\text{corr}}$ [ $\mu\text{A}\cdot\text{cm}^{-2}$ ]	17.459	16.755	15.458	13.426

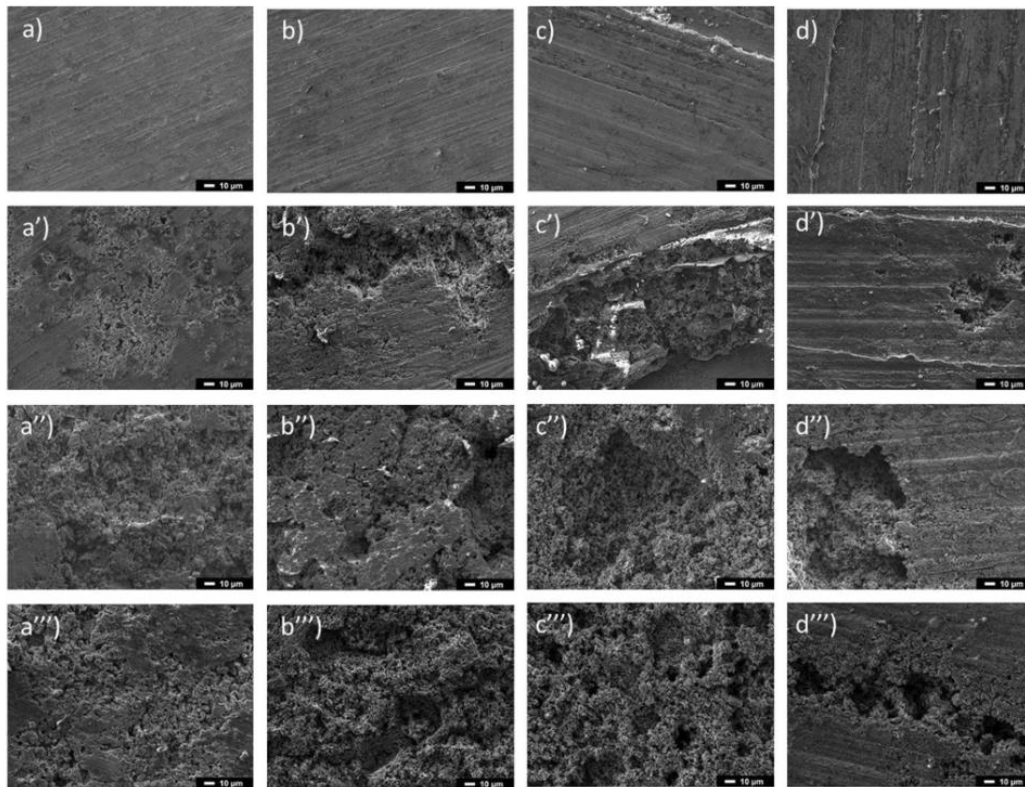


**Fig. 8** SEM images of the surface of AA6082 (a, a', a'', a'''), AA6060 (b, b', b'', b'''), W160 (c, c', c'', c''') and W200 (d, d', d'', d''') and 1.2(wt)% NaCl (a''', b''', c''', d'''). Magnification  $\times 500$  (colour figure online)

the material loss as a result of the corrosion process was observed in particular on edges of single strips associated with tool rotational movement. The results of observation of samples subjected to electrochemical tests at 0.7(wt)% NaCl concentration on the scanning electron microscope are presented in Figs. 8a'', b'', c'' and d''. A significant surface porosity was observed due to numerous losses caused by galvanic corrosion. Similarly, as for the results of electrochemical tests conducted in the medium of 0.2(wt)% NaCl concentrations, in both native materials pits covered a larger surface area compared to the welds. Figures 8 a''', b''', c''' and d''' show SEM images of the samples after electrochemical tests in 1.2(wt)% NaCl solution. The largest corrosion losses are exhibited by the AA6060 native material. Galvanic corrosion caused an increase in the porosity of the substrate and numerous losses were observed. Similar to the observations for lower NaCl concentrations, the corrosion losses for the welded samples are located mainly at the

edges resulting from tool movement. This phenomenon is particularly evident in Fig. 8d'''.

The obtained EIS experimental and simulated results are presented in Fig. 9. Table 6 summarizes the results of the simulations of EIS tests. Figure 9a illustrates the proposed equivalent electrical circuit model used for fitting the obtained experimental data. It is composed of  $R_s$  representing ohmic resistance of the electrolyte,  $CPE_1$  is a constant phase element representing the oxide layer on an aluminium alloy sample,  $R_2$ - $CPE_2$  loop which represents the charge transfer reaction resistance corresponding to the localised corrosion and the constant phase element of the double layer, added to the resistance of the native aluminium oxide layer ( $R_1$ ). A constant phase element (CPE) was used instead of an ideal capacitor due to the roughness and unevenness of the oxide layer and the bare sample surface. The same equivalent circuit was proposed in the studies of Yu et al. [50], Kwolek et al. [51], Popa et al. [52] and de Assis et al.

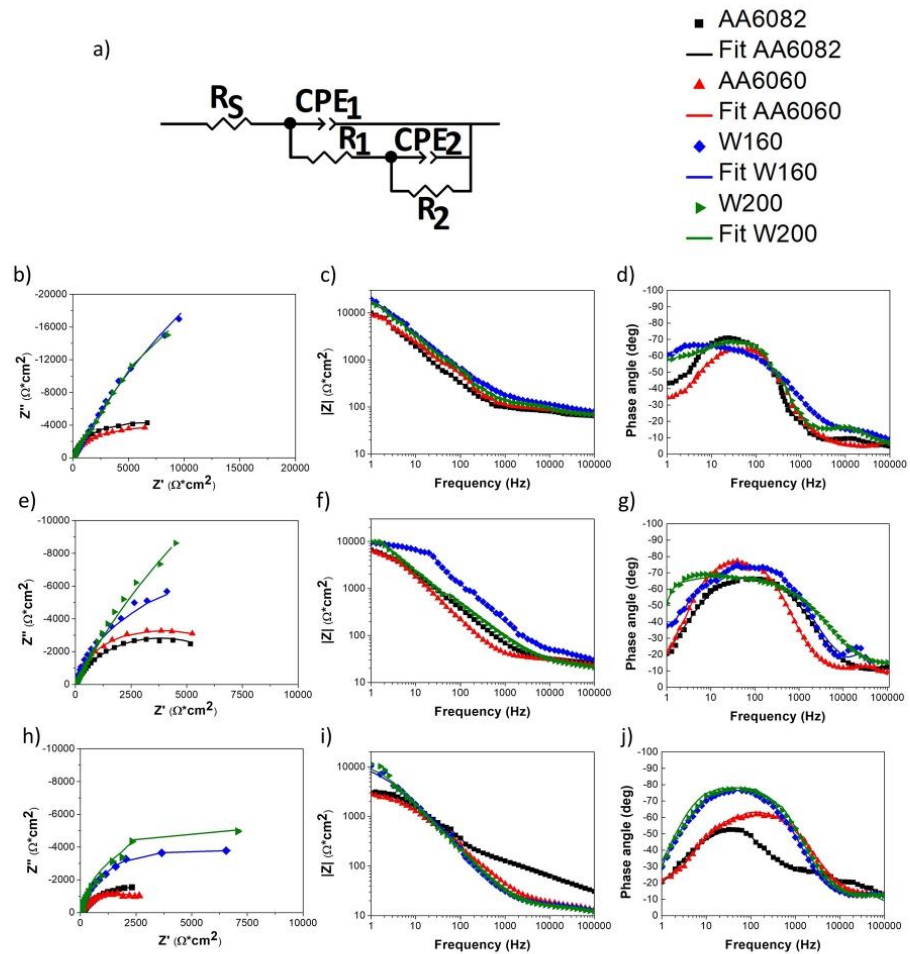


**Fig. 9** The equivalent circuit used to simulate experimental impedance data (a), experimental and fitted Nyquist graphs (b, e, h), Bode-Z graphs (c, f, i) and Bode-phase graphs (d, g, j) for the prepared

samples in the solution with 0.2(wt)% (b, c, d), 0.7(wt)% (e, f, g), 1.2(wt)% (h, i, j) NaCl concentration (colour figure online)

[53]. Figure 9b, e, h illustrate the obtained experimental and simulated Nyquist diagrams, Fig. 9c, f, i Bode-phase angle diagrams and Fig. 9d, g, j Bode-Z diagrams.

The Nyquist diagrams obtained for the samples immersed in the electrolyte of 0.2(wt)% NaCl concentration (Fig. 9b) consisted of quarter-round capacitive loops of all examined samples. It was clearly seen that the radius of quarter-round loops of W160 and W200 samples were significantly higher than the ratios of loops representing the AA6082 and AA6060 base material samples. According to the Bode-Z diagram (Fig. 9c), the impedances of

the W160 and W200 samples were higher than the impedance of both base metals throughout the whole analysed frequency range. It can be simplified that the impedance values taken by both welds were similar. The impedance values for both native materials were also similar. The Bode-phase angle (Fig. 9d) diagram allowed to note that a wider maximum existed for both W160 and W200 welds in comparison to both base alloys. The radius at the medium frequency capacitive loop was higher for both welds. From the simulation results, it can be seen that  $R_s$  values for all the examined samples were roughly the same, as the

**Table 6** Simulated parameters of EIS data in 0.2(wt)%, 0.7(wt)% and 1.2(wt)% solutions of NaCl for the proposed equivalent circuit model

	$R_s$ [ $\Omega\text{-cm}^2$ ]	$CPE_1\text{-T}$ [ $\mu\text{F}\text{-cm}^2$ ]	$CPE_1\text{-P}$	$R_1$ [ $\Omega\text{-cm}^2$ ]	$CPE_2\text{-T}$ [ $\mu\text{F}\text{-cm}^2$ ]	$CPE_2\text{-P}$	$R_2$ [ $\Omega\text{-cm}^2$ ]	$\chi^2$
AA6082 <sub>0,2</sub>	63.12	3.629	0.82	34.99	14.237	0.92	9184	0.00096164
AA6060 <sub>0,2</sub>	62.84	4.281	0.81	35.01	13.855	0.92	9333	0.00038292
W160 <sub>0,2</sub>	72.80	1.605	0.80	65.12	9.708	0.77	13,677	0.0013381
W200 <sub>0,2</sub>	65.25	1.914	0.83	66.69	10.887	0.86	19,668	0.00027963
AA6082 <sub>0,7</sub>	15.02	1.953	0.75	15.71	12.226	0.83	7577	0.00087268
AA6060 <sub>0,7</sub>	21.53	1.059	0.88	14.43	8.92	0.95	7126	0.00086053
W160 <sub>0,7</sub>	16.54	2.219	0.75	33.78	7.99	0.91	15,337	0.008496
W200 <sub>0,7</sub>	21.13	1.598	0.75	34.62	4.972	0.93	17,896	0.0043254
AA6082 <sub>1,2</sub>	12.66	29.754	0.55	15.77	13.728	0.81	5307	0.0015056
AA6060 <sub>1,2</sub>	9.734	19.945	0.67	10.49	13.219	0.84	3388	0.0020721
W160 <sub>1,2</sub>	10.67	2.015	0.89	7.63	13.925	0.91	9365	0.00081832
W200 <sub>1,2</sub>	11.69	4.745	0.98	10.38	21.648	0.68	11,494	0.008254

electrolytes of the same chemical composition were used. The resistances of the native aluminium oxide layer were markedly higher in the case of W160 and W200 samples, comparing to both base alloys. Also, the values of charge transfer reaction resistance of W160 and W200 samples were significantly higher in comparison to base materials.  $CPE_1\text{-T}$  values, which correspond to the capacitance of the oxide layers on aluminium alloy samples were significantly lower in the case of both welded samples. The same tendency was observed in the case of  $CPE_2\text{-T}$  values, which represented the constant phase element of the double layer.

For samples immersed in the 0.7(wt)% NaCl concentration electrolytes, the obtained Nyquist diagrams, shown in Fig. 9e, consists of the capacitive loops in the shape of quarter-round. It can be noted that the radii of loops representing W160 and W200 samples were higher than the radii of loops of AA6082 and AA6060 alloys. The loop of the joint friction stir welded with a tool traverse speed of 200 mm/min was bigger than the one of the weld produced with a tool traverse speed equal to 160 mm/min. Figure 9f shows Bode-Z graphs of all samples. At both higher and lower frequencies, the impedance value of the W160 sample was approximately the highest. The impedance values of the AA6060 sample were the lowest in almost the whole measurement frequency range. The widest maximum observed in the Bode-phase diagram (Fig. 9g) existed for the W200 sample, but the highest absolute value of phase angle around  $-80^\circ$  was noted for the W160 sample. The EIS simulation results indicate that each sample revealed lower a  $R_2$  value compared to the tests in 0.2(wt)% electrolyte. The base material samples exhibited similar  $R_2$  values, more than two times lower than the both W160 and W200 samples. Also, the resistance of the native aluminium oxide layer of both friction stir welded samples were more than two times higher compared to the base materials.

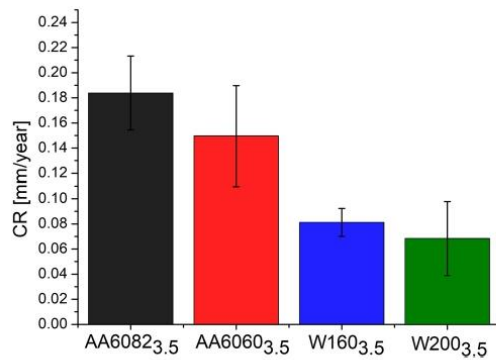
Figures 9h, i and j illustrate the obtained experimental and simulated EIS results for the samples in 1.2(wt)% NaCl environment. The loops in the Nyquist diagrams (Fig. 9h) representing W160 and W200 samples were characterized by the highest radii. Based on the Bode-Z diagram (Fig. 9i), the impedances of the W160 and W200 samples were higher in the lower frequency range, but for high frequencies, the highest impedance values were obtained for AA6082 base metal. It can be simplified that all the impedance values obtained for both welded samples were similar in all the frequency range. According to the Bode-phase diagram (Fig. 9j) the widest maxima existed for both friction stir welded samples. The obtained simulation values of the electrochemical impedance test on the samples immersed in 1.2(wt)% NaCl solution show that the resistance of the used solution differs from 9.73 to 12.66  $\Omega\text{-cm}^2$  and the obtained values were notably lower than for the electrolytes of lower concentrations. The resistance of the native aluminium oxide layer was the highest for the AA6082 sample and the lowest value was obtained for the W160 sample. The values of the charge transfer resistance corresponding to the localised corrosion were the highest for the friction stir welded samples and significantly lower in the case of base metal samples. The values of the constant phase element of the double layer of AA6082, AA6060 and W160 samples were similar, but the value corresponding to W200 sample was significantly higher. It should be marked that for the W200 the value of  $\chi^2$  was the highest, which means that the results obtained were subject to the greatest uncertainty.

To prove conclusions from the conducted electrochemical tests, the weight losses during the process for all of the samples in 0.2(wt)%, 0.7(wt)% and 1.2(wt)% NaCl concentrations were measured. The obtained results are presented in Table 7.

Furthermore, 3.5(wt)% NaCl solution was prepared to immerse the samples of base materials and both welds

**Table 7** Weight loss of the samples after the electrochemical tests in the solutions of 0.2%, 0.7% and 1.2% NaCl concentrations

NaCl concentration [wt%]	0.2	0.7	1.2
	Weight loss [g/cm <sup>2</sup> ]		
AA6082	0.0029	0.0148	0.0160
AA6060	0.0026	0.0139	0.0165
W160	0.0018	0.0059	0.0085
W200	0.0009	0.0043	0.0079

**Fig. 10** Corrosion rate for the samples of AA6082, AA6060, W160 and W200 immersed in 3.5(wt)% NaCl solution (colour figure online)

and check the weight loss after 168 h. On the basis of the obtained weight losses, the corrosion rate (CR) for 3.5(wt)% concentration was calculated using formula (1). The CR values are shown in the diagram in Fig. 10.

The data presented in the graph in Fig. 10 indicate that the CR of the welds was significantly lower than that of both parent materials. It should be noted that the specific values for both welds are similar, however, the CR for the W200 weld was slightly lower. According to the Polish standard PN-78/H-04608 [54] defining a 10-grade corrosion resistance scale, both native materials represent grade 6 of the corrosion resistance in the environment of 3.5(wt)% NaCl solution. At the same time, the welds exhibit grade 5. Furthermore, according to the designations used in the standard, it can be concluded that the welds are sufficiently resistant to corrosion, while both parent materials are characterized by a limited degree of corrosion resistance. Taking into account the data in Table 7, it can be seen that the tendency of weight loss in electrochemical tests was the same for all analysed NaCl concentrations (0.2(wt)%, 0.7(wt)% and 1.2(wt)%). The weight loss of both welds was much lower than the weight loss of both parent materials for all the conducted electrochemical and degradation tests. The highest weight

loss for all the tests carried out was observed for AA6082 parent material.

#### 4 Discussion

SEM observations of the samples revealed that the native material of both alloys corroded at a faster rate than FSW welds produced at 160 and 200 mm/min. The area covered by the corrosion process was larger for AA6082 and AA6060 alloys than for W160 and W200 samples. This relationship was already observed after electrochemical tests in a solution of 0.2(wt)% NaCl. The higher corrosion resistance of FSW welds was also observed for the study of Qin et al. [30] for 2A14-T6 aluminium alloy, Zucchi et al. [55] for AA5083 alloy, and Wang et al. [56] for AA7022 alloy. Corrosion in the case of FSW welds occurred mainly on the edges of the curves resulting from the combination of rotational and linear movements of the tool. This phenomenon was evident primarily for samples corroded in the electrolyte containing 1.2(wt)% NaCl (Fig. 8d'''). It seems that this effect may result from the triaxial stress state in these places in the passive layer. Such a state of stress reduces the resistance of the passive layer to delamination during corrosive processes under the stresses. On the other hand, on flat surfaces there is a uniaxial stress state, which increases the resistance of the passive layer to its delamination. It should be noted that for lower linear speed, while maintaining the same rotational speed, there will be more such edges. Thus, a sample produced at a lower tool linear velocity may be exposed to an intensification of corrosion phenomenon due to a higher number of regions that can be considered as corrosion propagation areas. Hence, in the case of the above studies, the weld produced at a linear speed of 160 mm/min may have been more exposed to corrosion than the sample produced at a tool linear speed of 200 mm/min. Although the microscopic studies indicate higher corrosion resistance of the welds, they were unable to determine the relationship of the effect of the weld surface geometry on the corrosion resistance of the welds, and thus the tool linear speed on the electrochemical properties of the welds. SEM observations of the samples allowed qualitative determination of the corrosion losses, and subsequent quantitative analysis of the corrosion degradation rate was determined by analysing the results obtained from electrochemical tests.

Investigation of the open circuit potential of the samples immersed in 0.2(wt)% NaCl solution revealed that the welded samples had the highest OCP values. The highest OCP value of  $-0.598$  V was observed for the sample welded with the tool traverse speed of 160 mm/min, which might indicate the highest corrosion resistance among all tested samples [57]. Also for the tests for an electrolyte with a concentration of 1.2(wt)% NaCl, the highest OCP value was

observed for the welded sample, but in the case of this sample, the tool traverse speed was equal to 200 mm/min. For studies with a concentration of 0.7(wt)%, no such relationship was observed. The highest OCP value was reported for the AA6060 parent material sample, but it should be noted that the individual OCP values for all samples differed by up to 0.010 V, so the trend was not clear. The individual OCP values for all the tested samples were approximated to the  $E_{\text{corr}}$  values for these samples [58]. It could be seen that the lowest  $i_{\text{corr}}$  values were noted for the friction stir welded samples produced with a tool traverse speed of 200 mm/min. However, the highest  $i_{\text{corr}}$  values were recorded for both parent materials. This relationship was evident for all NaCl concentrations. These results clearly indicate that the corrosion resistance of the welds was higher than that of the native materials, of which the weld produced with a tool traverse speed of 200 mm/min had the highest corrosion resistance. These relationships are illustrated in Fig. 11a. EIS investigations confirmed the potentiodynamic study results. The shape of the Nyquist diagrams shows that during

corrosion, the process of charge transfer through the electrolyte/electrode interface is slower than mass transfer and the ongoing reaction is irreversible. The rate of this reaction is related to the rate of charge transfer. The Nyquist plots also show that the imaginary component of impedance, at the same frequency, for both FSW joint is much smaller for all concentrations of  $\text{Cl}^-$  ions. This proves a much higher charge transfer resistance ( $R_1 + R_2$ ) and thus a lower corrosion rate of FSW joints compared to the corrosion rate of both aluminium alloys. Similarly, in the case of Bode diagrams, it can be noticed that the circuit impedance for FSW welds is higher, in almost all analysed cases, than for Al alloys. Since the circuit impedance at zero frequency is equal to the sum of the electrolyte resistance  $R_s$  and the charge transfer resistance ( $R_1 + R_2$ ), assuming that the electrolyte resistance is the same, the resistance to charge and mass transfer through the passive layer is much greater for FSW joints. Figure 11 b shows that the passive layer formed on FSW joints has much greater resistance to charge and mass transfer than the passive layers on aluminium alloy

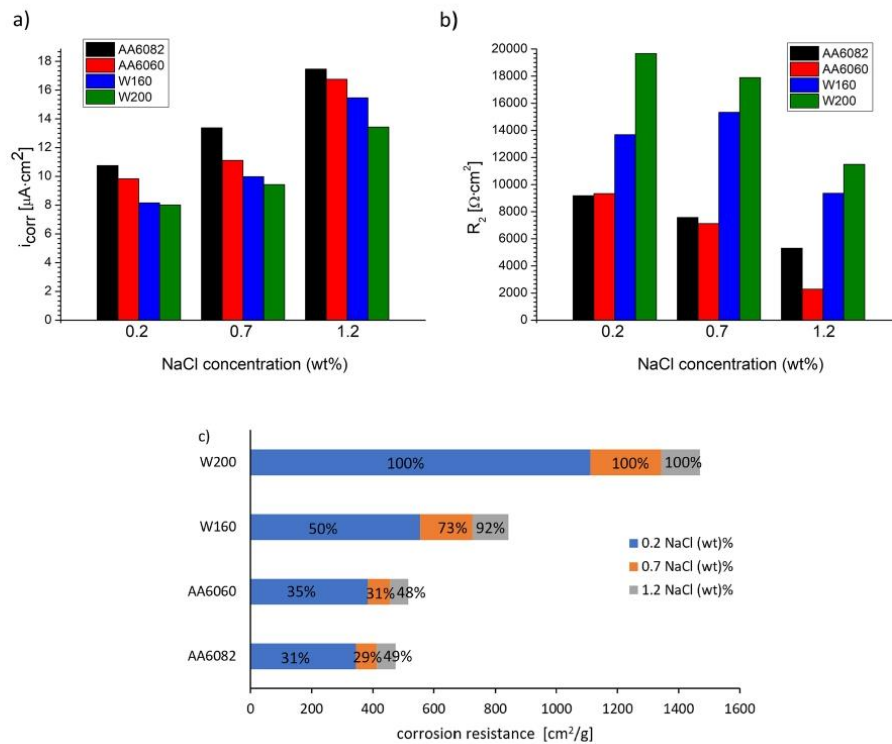


**Fig. 11**  $i_{\text{corr}}$  (a), the charge transfer resistance (b), and corrosion resistance calculated as the mass loss reciprocal of the AA6082, AA6060, W160 and W200 samples in different NaCl concentrations (c) (colour figure online)



sheets. This suggests that the passive layer at the FSW joints has less defective structure and is more homogeneous, thus constituting a greater barrier to Al ions passing into the aqueous NaCl solution. The corrosion resistance of all tested materials decreased with increasing NaCl concentration in the solution related to the increase of  $\text{Cl}^-$  ions, which caused the corrosion phenomenon attacking the surface of the samples (see Fig. 11c). However, as shown by the test results, the ranking of alloys and their joints in terms of their corrosion resistance, regardless of salinity, is as follows: W200  $\rightarrow$  W160A  $\rightarrow$  A6060  $\rightarrow$  AA6082. Weight loss studies after a degradation test in a solution of 3.5(wt)% confirmed the previous assumptions.

The corrosion resistance of metals could be related to the crystallite size, grain size, hardness and residual stresses in the material. The results of the Williamson-Hall analysis are presented as the graphs of  $i_{\text{corr}}(L)$ ,  $R_2(L)$ ,  $i_{\text{corr}}(\sigma_R)$  and  $R_2(\sigma_R)$  in Fig. 12. The obtained values were extrapolated to a linear function to determine the particular tendency.

The indentation measurements revealed that the welds performed a higher hardness than the native materials and reached  $1.580 \pm 0.171$  and  $1.519 \pm 0.161$  GPa for samples W200 and W160, respectively. Table 8 assumes the precipitation volume fraction identified on the XRD patterns. It should be noted that calculated values for both welded samples are lower in comparison to AA6082 parent material and higher than in case of AA6060 parent material. Indentation studies of the native materials indicated a higher hardness of the AA6082 alloy characterized by a higher volume fraction of precipitates compared to the AA6060 alloy. However, these tests also indicated higher hardness of both welds comparing to both native materials. A slightly lower hardness of  $1.519 \pm 0.161$  GPa was observed in the W160 weld, which also had a lower precipitate content. In precipitation-strengthened alloys, such as AA6060 and AA6082, the content of precipitates has a key effect on their strength. It can be observed in the case of AA6082 and AA6060 samples that higher precipitation volume fraction resulted in higher hardness of AA6082 alloy. However, it must be noted that the welds, in comparison to both parent materials, were characterized by a more fine-grained structure due to the recrystallization process. Also, analysis in accordance with Taylor and Orowan's theories has shown that welds exhibit higher dislocation densities and lower mobility of these dislocations, resulting in increased hardness in these samples.

The Williamson-Hall analysis revealed that the size of the crystallites increased due to the FSW process. In the studies of Woo et al. [59] it was reported that the AA6060-T6 weld and the native material showed no significant difference in crystallite size. In other studies of Woo et al. [60] the subgrain size before and after friction stir welding of AA6061 alloy was investigated. It was revealed that the subgrain size before the process was equal to 120 nm and after the process

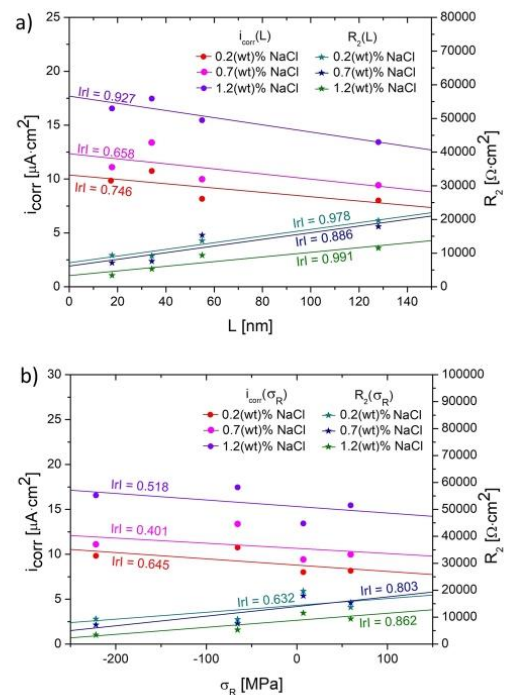


**Fig. 12** Relationship of corrosion current density and charge transfer resistance to crystallite size (a) and residual stress (b) in the material (colour figure online)

130 nm. Berezina et al. [61] observed that the Williamson-Hall-Unger analysis for the base material Al-Li-Cu-Sc-Zr alloy and FSWed sample indicated that depending on the regression profile (linear or parabolic) the calculated crystallite size is different. For the base material the value was equal to 118.9 nm, while for the weld nugget was equal to 193.18 and 70.86 nm in the case of the linear and parabolic regression, respectively. There are no extensive studies on the influence of the FSW process parameters on the crystallite size and this phenomena still needs to be explored.

As it can be seen in Fig. 12a, the crystallite growth leads to the increase of the corrosion resistance of the samples for all the investigated NaCl concentrations. In turn, the reduction in interatomic spacing due to compressive stresses on the surface can facilitate the growth and maintenance of the passivation layer. In the studies of Terasaki et al. [62] the residual stress distribution in FSW AA6063-T5 welds was investigated. The distribution of strain and residual stress in the weld is affected by the FSW welding load. The strain value is obtained by adding the positive strain value caused by the welding load to the negative strain value caused

**Table 8** Type and volume fraction of the precipitates identified on the XRD patterns

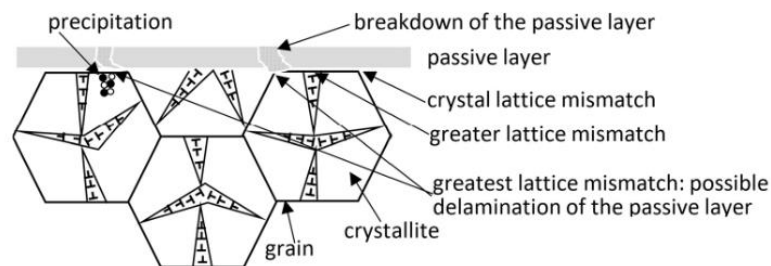
	Al <sub>9</sub> Fe <sub>0.94</sub> Mn <sub>2.16</sub> Si %	Mn <sub>4</sub> Si <sub>7</sub> %	Al <sub>3</sub> Fe %	Mg <sub>2</sub> Si %	Al <sub>5.15</sub> Mg <sub>3.15</sub> %	Precipita- tions frac- tion	Al. fraction
AA6082	1.146	0.700	–	0.144	–	1.99%	98.01%
AA6060	–	–	0.124	0.179	0.028	0.331%	99.669%
W160	0.104	0.365	0.335	0.241	–	1.045%	98.955%
W200	–	0.270	0.190	0.38	0.240	1.080%	98.920%

by the welding thermal cycle. Lim et al. [63] studied the residual stresses in the weld nugget of friction stir welded SUS 409 L stainless steel. It was revealed that the compressive residual stresses occurring in the nugget zone are the result of strong compression reaction by the tool shoulder. Residual tensile stresses can decrease the activation energy and surface atomic density simultaneously, thereby reducing corrosion resistance. The introduction of compressive residual stresses facilitates the formation of a passivation layer, thereby increasing corrosion resistance. The dependence of residual stress on corrosion current density ( $i_{\text{corr}}$ ) and charge transfer resistance ( $R_2$ ) is shown in Fig. 12 b. The corrosion current density was the lowest for sample W200, which was characterized by the presence of low compressive stresses. In the case of the sample welded with a tool traverse speed of 160 mm/min, the  $i_{\text{corr}}$  values were slightly higher. The native material samples AA6082 and AA6060 exhibited much lower corrosion resistance when subjected to tensile stresses. This is evidenced by higher  $i_{\text{corr}}$  values and lower  $R_2$  values for all analysed NaCl concentrations. These conclusions are consistent with the studies of Bai et al. [64] and Trdan et al. [65]. The relationships presented in the graphs in Fig. 12 were approximated to linear functions, and Pearson correlation coefficients (IrI) for all relationships indicate moderate to high fit to linear functions [66].

However, the above relationships between  $i_{\text{corr}}$  and  $R_2$  and the size of crystallites and residual stresses do not explain the ranking of corrosion resistance of the tested materials and FSW joints. The most corrosion-resistant W200 joint did not have the greatest residual compressive stresses and the largest crystallites. This is due to the fact that there is a

mismatch in the crystal lattice between the passive layer and the substrate. The passive layer for  $\alpha$ -Al<sub>2</sub>O<sub>3</sub> is a Hexagonal Close Packed (HCP) crystal structure and lattice constant  $a=0.4785$  nm and  $c=1.299$  nm [67], and aluminium crystallizes as Face Centered Cubic structure (FCC) with a lattice constant of  $a=0.4044$  nm [68]. In addition, the mismatch of the crystal lattice of the passive layer and the substrate increases in the places where crystallite boundaries, grain boundaries and precipitates reinforcing the aluminium solid solution occur. It seems that the crystallite boundaries have the least influence on these disturbances, while the grain boundaries and precipitation have the greatest influence (see Fig. 13). Table 8 summarizes the type and volume fraction of the precipitates identified on the XRD patterns.

As shown in Table 8, the smallest fraction of precipitates in the structure occurs for AA6060 alloy and the highest for AA6082 alloy. Both FSW joints have a similar and average fraction of precipitates concerning both aluminium alloys. Since both the FSW joints have a greater corrosion resistance than aluminium alloys, alone fraction of the precipitates cannot affect the corrosion resistance. AA6060 and AA6082 alloys were characterized by low corrosion resistance because their manufacturing (rolling, supersaturation and artificial aging) created a structure consisting of a matrix (solid solution of alloying elements in aluminium) and coherent precipitates, which generated high tensile residual stresses. In the case of FSW joints, the structure after welding was different than for the sheets after rolling. Welding heats the material to high temperatures, which causes either partial dissolution of the precipitates in the matrix (those of smaller sizes) or loss of coherence of the precipitates

**Fig. 13** Schematic passive layer and substrate (colour figure online)

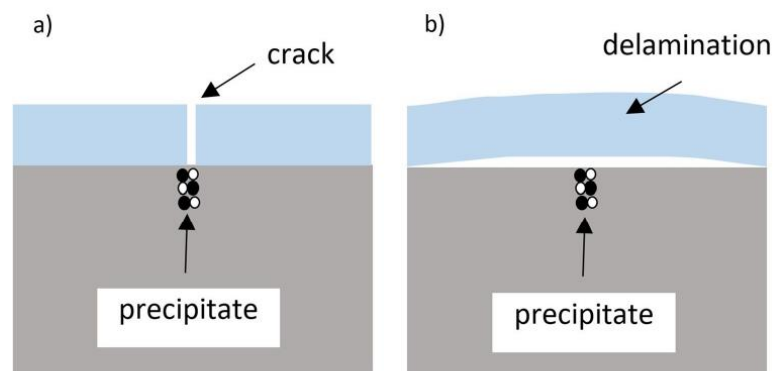
with the matrix (those of larger sizes), which contributes to increasing the heterogeneity of the chemical composition of the solid solution and reducing residual tensile stresses [29]. On the other hand, welding causes a large strain of the metal matrix, which in combination with high temperature causes dynamic recrystallization and, consequently, a reduction in the grain size with a simultaneous increase in the size of the crystallites. The density of  $\alpha\text{-Al}_2\text{O}_3$  ranges from 3.7 to 4.15  $\text{g/cm}^3$  [69, 70] and the density of aluminium alloys is 2.7  $\text{g/cm}^3$ . At the same time, the modulus of elasticity of Al alloys, measured in the indentation test, is in the range of 70.43–75.22 GPa and for  $\alpha\text{-Al}_2\text{O}_3$  the stiffness is 360 GPa [71]. These differences between the physical properties of the passive layer and the substrate, as well as the low fracture toughness of the passive layer in relation to the substrate (about 5–8  $\text{MPa}\cdot\text{m}^{1/2}$  for the passive layer and about 30  $\text{MPa}\cdot\text{m}^{1/2}$  for the substrate [72]), mean that in the presence of tensile residual stresses, the oxide layer tends to crack, which reduces corrosion resistance, because it is easier to transfer mass and charge through cracks (see Fig. 14a). Cracks can most easily be formed at the point contact of the oxide layer with precipitates—therefore the AA6082 alloy shows the lowest corrosion resistance, for which the volume fraction (and thus the area share, according to the Cavalieri-Hacquet principle) in the structure is about 1.99%. AA6060 alloy has slightly higher corrosion resistance due to the 6 times lower amount of precipitates compared to AA6082 alloy (despite 3 times higher tensile stresses). In turn, in the presence of compressive residual stresses, the oxide layer will tend to lose adhesion to the substrate and delamination will occur (see Fig. 14b), especially in the place of precipitation and grain boundaries, which also lowers corrosion resistance. For these reasons, the best corrosion resistance is shown by the W200 joint, for which the residual stresses are close to 0, and which has a similar number of precipitations as the W160 joint.

## 5 Conclusion

The above study was conducted to investigate the corrosion resistance of the welds produced by friction stir welding. Friction stir welding of dissimilar aluminium alloys AA6082 and AA6060 was performed using a tool rotational speed of 1250 rpm, a tool tilt angle of  $0^\circ$ , and two tool linear speeds: 160 and 200 mm/min. Williamson-Hall analysis and micro-indentation studies were performed to determine the effect of crystallite size and residual stress on corrosion resistance of the material. The obtained results allow to draw the following conclusions:

1. The crystallite size was larger in the case of the FSW welds compared to aluminum sheets.
2. Sheets manufacturing of AA6060 and AA6082 aluminium alloys generates tensile residual stresses, and welding of these sheets with the FSW method generates compressive residual stresses in the joints.
3. The linear speed 200 mm/min of welding results in lower compressive residual stresses compared to linear speed 160 mm/min.
4. The ranking of alloys and their joints in terms of their corrosion resistance, regardless of salinity, is: W200  $\rightarrow$  W160A  $\rightarrow$  A6060  $\rightarrow$  AA6082.
5. Higher dislocation densities were observed in FSW welds, in nugget zone, compared to native materials AA6082 and AA6060. Lower dislocation velocities in the W160 and W200 samples resulted in increased hardness in the welds.
6. A linear correlation between the crystallite size and corrosion resistance, in the form of the corrosion current density, was demonstrated. The same linear correlation exists for the relationship between residual stress and corrosion resistance.

**Fig. 14** Schematic passive layer and substrate for tensile (a) and compressive (b) residual stress



7. Degradation tests after placing the samples in 3.5(wt)% NaCl solution for 168 h confirmed the same corrosion resistance as obtained in the potentiodynamic tests and electrochemical impedance spectroscopy studies at 0.2(wt)%, 0.7(wt)% and 1.2(wt)% NaCl solution.
8. Scanning electron microscope observations indicated that the edges reflecting tool movement on the weld line can be considered as corrosion propagation centres for the welds.

**Acknowledgements** The authors would like to thank Maria Gazda from Faculty of Applied Physics and Mathematics of Gdańsk University of Technology for performing XRD tests.

### Declarations

**Conflict of interest** On behalf of all authors, the corresponding author states that there is no conflict of interest.

### References

1. Ancona, A., Daurelio, G., De Filippis, L. A. C., Ludovico, A. D., & Spera, A. M. (2002). CO<sub>2</sub> laser welding of aluminium shipbuilding industry alloys: AA 5083, AA 5383, AA 5059, and AA 6082. *XIV International Symposium on Gas Flow Chemical Lasers and High-Power Lasers*. <https://doi.org/10.1117/12.515825>
2. Dursun, T., & Soutis, C. (2014). Recent developments in advanced aircraft aluminium alloys. *Materials and Design*, *56*, 862–871. <https://doi.org/10.1016/j.matdes.2013.12.002>
3. Hirsch, J. (2011). Aluminium in innovative light-weight car design. *Materials Transactions*, *52*, 818–824. <https://doi.org/10.2320/matertrans.L-MZ201132>
4. Ertuğ, B., & Kumruoğlu, C. (2015). 5083 type Al-Mg and 6082 type Al-Mg-Si alloys for ship building. *American Journal of Engineering Research*, *4*, 146–50.
5. Laska, A., Szkodo, M., Koszelow, D., & Cavaliere, P. (2022). Effect of processing parameters on strength and corrosion resistance of friction stir-welded AA6082. *Metals (Basel)*, *12*, 1–16. <https://doi.org/10.3390/met12020192>
6. Öteyaka, M. Ö., & Ayrtüre, H. (2015). A study on the corrosion behavior in sea water of welds aluminum alloy by shielded metal arc welding, friction stir welding and gas tungsten arc welding. *International Journal of Electrochemical Science*, *10*, 8549–8557.
7. Zeng, Z., Lillard, R. S., & Cong, H. (2016). Effect of salt concentration on the corrosion behavior of carbon steel in CO<sub>2</sub> environment. *Corrosion*, *72*, 805–823. <https://doi.org/10.5006/1910>
8. Han, J., Carey, J. W., & Zhang, J. (2011). Effect of sodium chloride on corrosion of mild steel in CO<sub>2</sub>-saturated brines. *Journal of Applied Electrochemistry*, *41*, 741–749. <https://doi.org/10.1007/s10800-011-0290-3>
9. Reunamo, A. (2015). *Bacterial community structure and petroleum hydrocarbon degradation in the Baltic Sea*. University of Turku
10. Rendón, M. V., Calderón, J. A., & Fernández, P. (2011). Evaluation of the corrosion behavior of the Al-356 alloy in NaCl solutions. *Química Nova*, *34*, 1163–1166. <https://doi.org/10.1590/S0100-40422011000700011>
11. Fayomi, O. S. I., & Akande, I. G. (2019). Corrosion mitigation of aluminium in 3.65% NaCl medium using hexamine. *Journal of Bio- and Tribo-Corrosion*, *5*, 1–7. <https://doi.org/10.1007/s40735-018-0214-4>
12. Dudzik, K., & Jurczak, W. (2015). Influence of friction stir welding on corrosion properties of Al-7020M alloy in sea water. *Advances in Materials Science*, *15*, 7–13. <https://doi.org/10.1515/adms-2015-0002>
13. Meier, H. E. M., & Kauker, F. (2003). Sensitivity of the Baltic Sea salinity to the freshwater supply. *Climate Research*, *24*, 231–242. <https://doi.org/10.3354/cr024231>
14. Sinyavskii, V. S., & Kalinin, V. D. (2005). Marine corrosion and protection of aluminum alloys according to their composition and structure. *Protection of Metals*, *41*, 317–328. <https://doi.org/10.1007/s11124-005-0046-8>
15. Thomas WM, Nicholas ED, Needham JC, Murch MG, Temple-smith P, Dawes CJ. G. B. Patent Application No. 9125978.8, 1991
16. Sato, Y. S., Kokawa, H., Ikeda, K., Enomoto, M., Jogan, S., & Hashimoto, T. (2001). Microtexture in the friction-stir weld of an aluminum alloy. *Metallurgical and Materials Transactions A, Physical Metallurgy and Materials Science*, *32*, 941–948. <https://doi.org/10.1007/s11661-001-0351-z>
17. Kossakowski, P., Wcislik, W., & Bakalarz, M. (2018). Macrostructural analysis of friction stir welding (FSW) joints. *Journal of Chemical Information and Modeling*, *01*, 1689–1699. <https://doi.org/10.1017/CBO9781107415324.004>
18. Kah, P., Rajan, R., Martikainen, J., & Suoranta, R. (2015). Investigation of weld defects in friction-stir welding and fusion welding of aluminium alloys. *International Journal of Mechanical and Materials Engineering*. <https://doi.org/10.1186/s40712-015-0053-8>
19. Safeen, M. W., & Spena, P. R. (2019). Main issues in quality of friction stir welding joints of aluminum alloy and steel sheets. *Metals (Basel)*. <https://doi.org/10.3390/met9050610>
20. Zhang, J., Shen, Y., Yao, X., Xu, H., & Li, B. (2014). Investigation on dissimilar underwater friction stir lap welding of 6061-T6 aluminum alloy to pure copper. *Materials and Design*, *64*, 74–80. <https://doi.org/10.1016/j.matdes.2014.07.036>
21. Rajendran, C., Srinivasan, K., Balasubramanian, V., Balaji, H., & Selvaraj, P. (2019). Effect of tool tilt angle on strength and microstructural characteristics of friction stir welded lap joints of AA2014-T6 aluminum alloy. *Transactions of Nonferrous Metals Society of China*, *29*, 1824–35. [https://doi.org/10.1016/S1003-6326\(19\)65090-9](https://doi.org/10.1016/S1003-6326(19)65090-9)
22. Mishra, R., & Ma, Z. Y. (2005). Friction stir welding and processing. *Materials Science and Engineering Reports*, *50*, 1–78. <https://doi.org/10.1016/j.mser.2005.07.001>
23. Hamid, H. A. D., & Roslee, A. A. (2015). Study the role of friction stir welding tilt angle on microstructure and hardness. *Applied Mechanics and Materials*, *799–800*, 434–438. <https://doi.org/10.4028/www.scientific.net/amm.799-800.434>
24. Colligan, K. J. (2009). The friction stir welding process: An overview. *Woodhead Publishing Limited*. <https://doi.org/10.1533/9781845697716.1.15>
25. Machniewicz, T., Nosal, P., Korbel, A., & Hebda, M. (2020). Effect of FSW traverse speed on mechanical properties of copper plate joints. *Materials (Basel)*, *13*, 1–14. <https://doi.org/10.3390/ma13081937>
26. Palanivel, R., Koshy Mathews, P., Murugan, N., & Dinaharan, I. (2012). Effect of tool rotational speed and pin profile on microstructure and tensile strength of dissimilar friction stir welded AA5083-H111 and AA6351-T6 aluminum alloys. *Materials and Design*, *40*, 7–16. <https://doi.org/10.1016/j.matdes.2012.03.027>
27. Tasi P, Hajro I, Hodži D, Dobraš D. Energy Efficient Welding Technology : Fsw. 11th Int. Conf. Accompl. Electr. Mech. Engineering Inf. Technol., 2013, p. 429–42.
28. Sivaraj, P., Kanagarajan, D., & Balasubramanian, V. (2014). Effect of post weld heat treatment on tensile properties and

- microstructure characteristics of friction stir welded armour grade AA7075-T651 aluminium alloy. *Def Technol*, 10, 1–8. <https://doi.org/10.1016/j.dt.2014.01.004>
29. Laska, A., & Szkodo, M. (2020). Manufacturing parameters, materials, and welds properties of butt friction stir welded joints—overview. *Materials (Basel)*, 13, 1–46. <https://doi.org/10.3390/ma13214940>
  30. Long, Q. H., Zhang, H., Tong, S. D., & Zhuang, Q. (2015). Corrosion behavior of the friction-stir-welded joints of 2A14-T6 aluminum alloy. *International Journal of Minerals, Metallurgy, and Materials*, 22, 627–638. <https://doi.org/10.1007/s12613-015-1116-9>
  31. Gharavi, F., Matori, K. A., Yunus, R., Othman, N. K., & Fadaei-fard, F. (2016). Corrosion evaluation of friction stir welded lap joints of AA6061-T6 aluminum alloy. *Transactions of Nonferrous Metals Society of China*, 26, 684–96. [https://doi.org/10.1016/S1003-6326\(16\)64159-6](https://doi.org/10.1016/S1003-6326(16)64159-6)
  32. Ales, S. K., & Wang, L. (2017). Effects of friction stir welding on corrosion behaviors of AA2024-T4 aluminum alloy. *MATEC Web of Conferences*, 109, 5. <https://doi.org/10.1051/mateconf/201710902003>
  33. Frodal, B. H., Dæhli, L. E. B., Børvik, T., & Hopperstad, O. S. (2019). Modelling and simulation of ductile failure in textured aluminium alloys subjected to compression-tension loading. *International Journal of Plasticity*, 118, 36–69. <https://doi.org/10.1016/j.ijplas.2019.01.008>
  34. Shatkay, M. (1991). Dissolved oxygen in highly saline sodium chloride solutions and in the Dead Sea—measurements of its concentration and isotopic composition. *Marine Chemistry*, 32, 89–99. [https://doi.org/10.1016/0304-4203\(91\)90027-T](https://doi.org/10.1016/0304-4203(91)90027-T)
  35. Hakem, M., Khatir, M., Otmani, R. R., Fahssi, T., Debbache, N., & Allou, D. (2007). Heat treatment and welding effects on mechanical properties and microstructure evolution of 2024 and 7075 aluminium alloys. *Weld World*, 51, 163–170.
  36. Okamura, H., Aota, K., Sakamoto, M., Ezumi, M., & Ikeuchi, K. (2002). Behaviour of oxides during friction stir welding of aluminium alloy and their effect on its mechanical properties. *Welding International*, 16, 266–275. <https://doi.org/10.1080/09507110209549530>
  37. Zeng, X. H., Xue, P., Wang, D., Ni, D. R., Xiao, B. L., Wang, K. S., et al. (2018). Material flow and void defect formation in friction stir welding of aluminium alloys. *Science and Technology of Welding and Joining*, 23, 677–686. <https://doi.org/10.1080/13621718.2018.1471844>
  38. Khorsand, S., & Huang, Y. (2017). Integrated casting–extrusion (ICE) of an AA6082 aluminium alloy. *Journal of the Minerals Metals & Materials Society*. [https://doi.org/10.1007/978-3-319-51541-0\\_32](https://doi.org/10.1007/978-3-319-51541-0_32)
  39. Leszczyńska-Madej, B., Richert, M., Wąsik, A., & Szafron, A. (2018). Analysis of the microstructure and selected properties of the aluminium alloys used in automotive air-conditioning systems. *Metals (Basel)*. <https://doi.org/10.3390/met8010010>
  40. Debih, A., & Ouakdi, E. H. (2018). Anisotropic thermomechanical behavior of AA6082 aluminium alloy Al-Mg-Si-Mn. *International Journal of Materials Research*, 109, 34–41. <https://doi.org/10.3139/146.111580>
  41. Williamson, G. K., & Hall, W. H. (1953). X-ray line broadening from filed aluminium and wolfram. *Acta Metallurgica*, 1, 22–31. [https://doi.org/10.1016/0001-6160\(53\)90006-6](https://doi.org/10.1016/0001-6160(53)90006-6)
  42. Khoshkoo, M. S., Scudino, S., Thomas, J., Surreddi, K. B., & Eckert, J. (2011). Grain and crystallite size evaluation of cryomilled pure copper. *Journal of Alloys and Compounds*, 509, S343–S347. <https://doi.org/10.1016/j.jallcom.2011.02.066>
  43. Durst, K., Backes, B., Franke, O., & Göken, M. (2006). Indentation size effect in metallic materials: Modeling strength from pop-in to macroscopic hardness using geometrically necessary dislocations. *Acta Materialia*, 54, 2547–2555. <https://doi.org/10.1016/j.actamat.2006.01.036>
  44. Johnson, K. L. (1985). *Contact mechanics*. Cambridge University Press. <https://doi.org/10.1017/CBO9781139171731>
  45. Cho, J., Molinari, J. F., & Ancaix, G. (2017). Mobility law of dislocations with several character angles and temperatures in FCC aluminum. *International Journal of Plasticity*, 90, 66–75. <https://doi.org/10.1016/j.ijplas.2016.12.004>
  46. Zhuang Z., Liu Z., & Cui Y. (2019). Strain gradient plasticity theory at the microscale. In Z. Zhuang, Z. Liu, & Cui Y. (Eds.) *Dislocation mechanism-based crystal plasticity* (pp. 57–90). Elsevier Inc. <https://doi.org/10.1016/b978-0-12-814591-3.00003-0>
  47. Yamada, H., Ogasawara, N., Shimizu, Y., Horikawa, H., & Kobayashi, H. (2012). Effect of high strain rate on micro-indentation test in pure aluminum. *EPI Web of Conferences*, 26, 2–6. <https://doi.org/10.1051/epjconf/20122601028>
  48. Voyiadis, G. Z., & Abed, F. H. (2005). Effect of dislocation density evolution on the thermomechanical response of metals with different crystal structures at low and high strain rates and temperatures. *Archives of Mechanics*, 57, 299–343. <https://doi.org/10.24423/aom.190>
  49. Cassayre, L., Chamelot, P., Arurault, L., & Taxis, P. (2005). Anodic dissolution of metals in oxide-free cryolite melts. *Journal of Applied Electrochemistry*, 35, 999–1004. <https://doi.org/10.1007/s10800-005-6727-9>
  50. Yu, M., Zhao, X., Xiong, L., Xue, B., Kong, X., Liu, J., et al. (2018). Improvement of corrosion protection of coating system via inhibitor response order. *Coatings*, 8, 1–15. <https://doi.org/10.3390/coatings8100365>
  51. Kwolek, P. (2020). Corrosion behaviour of 7075 aluminium alloy in acidic solution. *RSC Advances*, 10, 26078–26089. <https://doi.org/10.1039/d0ra04215c>
  52. Popa, M. V., Vasilescu, E., Drob, P., Vasilescu, C., Drob, S. I., Mareci, D., et al. (2010). Corrosion resistance improvement of titanium base alloys. *Quimica Nova*, 33, 1892–1896. <https://doi.org/10.1590/S0100-40422010000900014>
  53. de Assis, S. L., & Costa, I. (2007). The effect of polarisation on the electrochemical behavior of Ti-13Nb-13Zr alloy. *Materials Research*, 10, 293–296. <https://doi.org/10.1590/s1516-14392007000300014>
  54. PN-H-04608:1978 Korozja metali -- Skala odpornosci metali na korozje. 1978.
  55. Zucchi, F., Trabanelli, G., & Grassi, V. (2001). Pitting and stress corrosion cracking resistance of friction stir welded AA 5083. *Werkstoffe Und Korrosion*, 52, 853–859. [https://doi.org/10.1002/1521-4176\(200111\)52:11%3c853::aid-maco853%3e3.0.co;2-1](https://doi.org/10.1002/1521-4176(200111)52:11%3c853::aid-maco853%3e3.0.co;2-1)
  56. Wang, H. F., Wang, J. L., Song, W. W., Zuo, D. W., & Shao, D. L. (2016). Analysis on the corrosion performance of friction stir welding joint of 7022 aluminum alloy. *International Journal of Electrochemical Science*, 11, 6933–6942. <https://doi.org/10.20964/2016.08.09>
  57. Losiewicz, B., Maszybrocka, J., Kubisztal, J., Skrabalak, G., & Stwora, A. (2021). Corrosion resistance of the cpTi g2 cellular lattice with tpms architecture for gas diffusion electrodes. *Materials (Basel)*, 14, 1–18. <https://doi.org/10.3390/ma14010081>
  58. Berradja, A. (2019). Electrochemical techniques for corrosion and tribocorrosion monitoring: methods for the assessment of corrosion rates. *Corrosion Inhibitors*. <https://doi.org/10.5772/intechopen.86743>
  59. Woo, W., Ungár, T., Feng, Z., Kenik, E., & Clausen, B. (2010). X-ray and neutron diffraction measurements of dislocation density and subgrain size in a friction-stir-welded aluminum alloy. *Metallurgical and Materials Transactions A Physical Metallurgy and Materials Science*, 41, 1210–1216. <https://doi.org/10.1007/s11661-009-9963-5>

60. Woo, W., Feng, Z., Hubbard, C. R., David, S. A., Wang, X. L., Clausen, B., et al. (2009). In-situ time-resolved neutron diffraction measurements of microstructure variations during friction stir welding in a 6061-T6 aluminum alloy. *ASM Proceedings of the International Conference*. <https://doi.org/10.1361/cp2008twr407>
61. Berezina, A. L., Budarina, N. N., Kotko, A. V., Molebny, O. A., Chayka, A. A., & Ischenko, A. Y. (2011). Structural changes in friction-stir welded Al-Li-Cu-Sc-Zr (1460) alloy. *Nanomaterials: Applications and Properties*, 2, 247–253.
62. Terasaki, T., & Akiyama, T. (2003). Mechanical behavior of joints in FSW: residual stress, inherent strain and heat input generated by friction stir welding. *Weld World*, 47, 24–31.
63. Lim, Y.-S., Kim, S.-H., & Lee, K.-J. (2018). Effect of residual stress on the mechanical properties of fsw joints with SUS409L. *Advances in Materials Science and Engineering*, 2018, 1–8.
64. Bai, L. Y., Gao, L., & Jiang, K. B. (2018). Influence of residual stress on the corrosion behaviors of welded structures in the nature seawater. *IOP Conference Series*. <https://doi.org/10.1088/1757-899X/392/4/042009>
65. Trdan, U., & Grum, J. (2015). Investigation of corrosion behaviour of aluminium alloy subjected to laser shock peening without a protective coating. *Advances in Materials Science and Engineering*. <https://doi.org/10.1155/2015/705306>
66. Saccenti, E., Hendriks, M. H. W. B., & Smilde, A. K. (2020). Corruption of the Pearson correlation coefficient by measurement error and its estimation, bias, and correction under different error models. *Science and Reports*, 10, 1–20. <https://doi.org/10.1038/s41598-019-57247-4>
67. Chen, D. Y., Shao, M. W., Cheng, L., Wang, X. H., & Ma, D. D. (2009). Strong and stable blue photoluminescence: The peapodlike SiO<sub>x</sub>@Al<sub>2</sub>O<sub>3</sub> heterostructure. *Applied Physics Letters*, 94, 2007–2010. <https://doi.org/10.1063/1.3070319>
68. Morinaga, M. (2019). A quantum approach to alloy design. In *An exploration of material design and development based upon alloy design theory and atomization energy method*, *Materials Today*. <https://doi.org/10.1016/b978-0-12-814706-1.00013-3>. <https://www.sciencedirect.com/book/9780128147061/a-quantum-approach-to-alloy-design>
69. Munro, R. G. (1997). Evaluated material properties for a sintered  $\alpha$ -alumina. *Journal of the American Ceramic Society*, 80, 1919–1928. <https://doi.org/10.1111/j.1151-2916.1997.tb03074.x>
70. Kimura, T., Matsuda, Y., Oda, M., & Yamaguchi, T. (1987). Effects of agglomerates on the sintering of alpha-Al<sub>2</sub>O<sub>3</sub>. *Ceramics International*, 13, 27–34. [https://doi.org/10.1016/0272-8842\(87\)90035-6](https://doi.org/10.1016/0272-8842(87)90035-6)
71. De Faoite, D., Browne, D. J., Chang-Díaz, F. R., & Stanton, K. T. (2012). A review of the processing, composition, and temperature-dependent mechanical and thermal properties of dielectric technical ceramics. *Journal of Materials Science*, 47, 4211–4235. <https://doi.org/10.1007/s10853-011-6140-1>
72. Szkodo, M., Stanisławska, A., Komarov, A., & Bolewski, Ł. (2021). Effect of MAO coatings on cavitation erosion and tribological properties of 5056 and 7075 aluminum alloys. *Wear*. <https://doi.org/10.1016/j.wear.2021.203709>

**Publisher's Note** Springer Nature remains neutral with regard to jurisdictional claims in published maps and institutional affiliations.



**Aleksandra Laska** She is a PhD student in the discipline of Mechanical Engineering at Gdańsk University of Technology, Faculty of Mechanical Engineering and Ship Technology, Institute of Machines and Materials Engineering. Her research topics focus on Friction Stir Welding method, with particular emphasis on the investigations of residual stresses in the joints. Her research area includes aluminium and its alloys in engineering applications.



**Marek Szkodo** He works in two scientific disciplines: materials Engineering and Mechanical Engineering. He is the author of many publications on the environmental degradation of engineering materials and the use of Friction Stir Welding Method in engineering applications. He is a graduate of the Faculty of Mechanical Engineering at the Gdańsk University of Technology.



**Łukasz Pawłowski** Research assistant and PhD student at the Institute of Machines and Materials Technology, Faculty of Mechanical Engineering and Ship Technology, Gdansk University of Technology. His research work concerns surface modification and characterization of titanium and titanium alloys. His research area includes electrochemical studies on metals and polymers.



**Grzegorz Gajowiec** He is a graduate of the faculty of Mechanical Engineering at the Gdańsk University of Technology. He is the author of many expert opinions for the industry. He deals with environmental degradation of engineering materials and scanning electron microscopy.



### **7.7. [P7] Influence of the Tool Rotational Speed on Physical and Chemical Properties of Dissimilar Friction-Stir-Welded AA5083/AA6060 Joints.**

**Laska A.**, Szkodo M., Cavaliere P.\*, Perrone A., Influence of the Tool Rotational Speed on Physical and Chemical Properties of Dissimilar Friction-Stir-Welded AA5083/AA6060 Joints. *Metals*. 12(10), 1658; 2022. doi: 10.3390/met12101658. (IF = 2.695, 70 points of the Polish Ministry of Science and Higher Education)

#### 7.7.1. Declaration of the contribution of the doctoral candidate

My contribution to the preparation of the manuscript consisted of preparing the literature review and obtaining the research material. I developed the methodology for the experiments. I fabricated AA5083/AA6060 aluminum alloy dissimilar welds by the FSW method using three different rotational speeds. I conducted macro- and microscopic observations. I performed indentation studies. I calculated dislocation density and dislocation mobility. I performed potentiodynamic studies and SEM observations. I analyzed the obtained experimental results. I conducted a discussion in the manuscript. I prepared figures and tables and drafted the manuscript. I prepared responses to the reviewers.

My percentage contribution to the preparation of the manuscript was equal to 80 %.

.....  
Aleksandra Laska

# Influence of the Tool Rotational Speed on Physical and Chemical Properties of Dissimilar Friction-Stir-Welded AA5083/AA6060 Joints

Aleksandra Laska <sup>1</sup>, Marek Szkodo <sup>1</sup>, Pasquale Cavaliere <sup>2\*</sup> and Angelo Perrone <sup>2</sup>

<sup>1</sup> Faculty of Mechanical Engineering and Ship Technology, Gdansk University of Technology, Narutowicza 11/12, 80-233 Gdansk, Poland

<sup>2</sup> Department of Innovation Engineering, University of Salento, Via per Arnesano, 73100 Lecce, Italy

\* Correspondence: pasquale.cavaliere@unisalento.it

**Abstract:** Aluminum alloys have been successfully used in the railroad and automotive industries because of their potential to significantly reduce component weights, and their good mechanical and anti-corrosion properties. Problems with joining aluminum alloys are characterized by low weldability, which influences the need for studies focused on unconventional methods. The environmentally friendly and low-cost friction-stir-welding method enables the material to be joined without melting. In the following study, dissimilar butt joints were produced from AA5083 and AA6060 alloys. A constant tool traverse speed of 100 mm/min and a tool tilt angle of 2° were used, combined with tool rotational speeds of 800, 1000 and 1200 RPM. It was revealed that as the tool speed increases, the hardness in the weld nugget zone increases, due to higher heat input and more effective recrystallization. The highest hardness of the weld nugget zone was observed for the weld that was produced with the highest tool rotational speed, and was equal to 1.07 GPa, compared to the hardness of both parent materials of 0.75 and 1.15 GPa for AA5083 and AA6060, respectively. Increasing the heat input also decreased the hardness of the heat-affected zone, where recrystallization was not observed. The lowest density of dislocations with the highest mobility was observed in the heat-affected zone on the AA6060 side, which also contributed to the reduction in strength in this zone. The produced welds exhibited corrosion resistance between both parent materials, with the lowest corrosion current density being  $6.935 \pm 0.199 \mu\text{A}\cdot\text{cm}^{-2}$  for the weld that was produced at a tool speed of 1200 RPM.

**Keywords:** friction-stir welding; solid state joining; corrosion; aluminum alloys; mechanical properties; dislocations

**Citation:** Laska, A.; Szkodo, M.; Cavaliere, P.; Perrone, A. Influence of the Tool Rotational Speed on Physical and Chemical Properties of Dissimilar Friction-Stir-Welded AA5083/AA6060 Joints. *Metals* **2022**, *12*, 1658. <https://doi.org/10.3390/met12101658>

Academic Editor: António Bastos Pereira

Received: 21 August 2022

Accepted: 28 September 2022

Published: 30 September 2022

**Publisher's Note:** MDPI stays neutral with regard to jurisdictional claims in published maps and institutional affiliations.



**Copyright:** © 2022 by the author. Licensee MDPI, Basel, Switzerland. This article is an open access article distributed under the terms and conditions of the Creative Commons Attribution (CC BY) license (<https://creativecommons.org/licenses/by/4.0/>).

## 1. Introduction

Aluminum alloys are increasingly being used in a wide range of industries, including the automotive and railroad industries. The biggest challenge in these sectors is to implement a material that is characterized by high strength, corrosion resistance and easy machinability [1]. In addition, rising transportation costs are necessitating further reductions in the weight of vehicular components, while maintaining their optimal properties. Aluminum alloys are an excellent alternative to steel. Their use enables the weight of the structure to be reduced by up to three times, resulting in a significant reduction in the cost of transportation [2]. The adoption of aluminum in train wagon bodies minimizes the weight and energy that are required to accelerate and decelerate them. This can increase vehicle payloads, leading to lower fuel consumption and lower machine operating costs [3].

Aluminum alloys are characterized by good corrosion resistance; however, even slight corrosion losses can contribute to a rapid reduction in the mechanical properties of the structure. Therefore, it is extremely important, in addition to ensuring high structural



strength, to determine the resistance of aluminum alloys to corrosion. Among the alloys with particularly high corrosion resistance are the ones that are in series 5XXX and 6XXX. AA5083 alloy is characterized by very good corrosion resistance and high strength [4,5]. AA6060 exhibits excellent machinability and high strength in plate form. AA6XXX alloy is commonly applied in high-speed train manufacturing, for example, in profiles and carriage components [6,7]. Welding dissimilar materials together is of great importance in the industry. It is necessary for a number of construction applications, in order to maximize the quality of structures and to improve strength, weight, and corrosion resistance.

In spite of the many advantages that are associated with the use of aluminum alloys in the transportation industry, a welding problem arises [8–10]. Aluminum alloys are characterized by poor weldability. Their joining by conventional methods carries a high risk of creating a structure with numerous defects and low strength [11].

Friction-stir welding (FSW) offers an alternative way of joining materials to avoid the risks of potential defects arising from conventional welding. During the FSW process, a specially designed tool, consisting of a pin and a shoulder, is used to join materials that are in contact with each other. The tool is put into rotary motion, and is placed between the components to be welded until contact between the surfaces of the components and the tool shoulder is achieved. The tool is then set into simultaneous linear motion along the joint line. The kinetic energy of the tool is converted into thermal energy, which is created by friction at the interface between the tool and work pieces. The heated material is plasticized, mixed by the pin and extruded in the backwards direction of the tool, which is moving along the edge of the contact line. As no melting point during welding is reached, solid-state FSW brings many advantages over conventional welding. The reduction in weld defects such as discontinuities and porosities, the lower solubility of hydrogen and the lower process costs associated with FSW are contributing to the growing interest in this method [12]. Due to lower energy consumption and the use of non-consumable tools, this method is also classified as a green technology [13].

The majority of studies and patents on FSW have been on aluminum and its alloys, according to an analysis by Magalhaes et al. [14], followed by iron alloys, magnesium, titanium and their alloys. Moreover, a number of previous studies on FSW involved dissimilar aluminum alloys. Ghaffarpour et al. [1] successfully joined AA5083-H12 and AA6061-T6 alloys with the FSW process. Tensile tests and hardness measurements were performed in order to investigate the strength of the produced samples. The lowest hardness was recorded in the heat-affected zone of the AA6061-T6 sheet. It was also noted that by increasing the tool rotational speed, the hardness of the mixing zone was reduced. Furthermore, Devaiah et al. [15] used a FSW process to produce AA5086/AA6061 joints that were characterized by a high tensile strength. Peel et al. [16] produced high-quality joints of AA5083/AA6082. In the study of Khodir et al. [17], the friction-stir-welded joints of AA2024/A7075 were found to exhibit high tensile strength and hardness. Palanivel et al. [18] investigated the effect of tool geometry on the tensile strength of AA5083-H111/AA6351-T6 joints. It was found that using straight square and hexagon pins yielded the best quality joints. Guo et al. [19] studied the mutual position of AA6061 and AA7075 alloys during welding. It was observed that the positioning of the AA6061 alloy on the advancing side promotes material mixing, and improves the mechanical properties of the weld. In a study by Mastanaiah et al. [20], it was found that by increasing the welding speed and decreasing the tool rotational speed, defect formation is more possible during the FSW of AA2219 and AA5083 alloys. Dong et al. [21] successfully used an FSW process on AA7003/AA6060, obtaining welds characterized by a high ultimate tensile strength that was equal to 78.2% of base material AA6060. Due to the different properties of the alloys used in this study, including the high corrosion resistance of the 5XXX series alloy and the high strength of the 6XXX alloy, welding them properly together is crucial in designing structures that provide such performance. Such examples include structures that are exposed to significant load transfer, and whose parts are simultaneously exposed to a corrosive environment, such as seawater or the atmosphere. To the best of the authors'

knowledge, there are no reports on dissimilar friction-stir welding of AA5083 and AA6060 aluminum alloys.

Therefore, the aim of the present study was to weld dissimilar AA5083-O and AA6060-T6 aluminum alloys together using FSW. The effect of tool rotational speed during the FSW process on the microstructure, hardness, dislocation density and mobility, as well as corrosion resistance, was investigated.

## 2. Materials and Methods

The friction-stir-welding method was applied to join commercial AA5083-O and AA6060-T6 aluminum alloys. The nominal chemical compositions of both alloys are presented in Table 1. The alloys were purchased in the form of rolled sheets that were 3 mm in thickness. The plates were butt-welded with AA5083 on the advancing side and AA6060 on the retreating side, parallel to the rolling direction. The welds were designed to be 200 mm in length from two plates with dimensions of 100 mm × 200 mm.

**Table 1.** Chemical compositions of the AA5083 and AA6060 alloys.

	Chemical Composition (wt%)								
	Si	Fe	Cu	Mn	Mg	Cr	Zn	Ti	Al
AA5083	0.40	0.40	0.10	0.60	4.50	0.15	0.25	0.15	balance
AA6060	0.40	0.20	0.10	0.10	0.40	0.05	0.15	0.10	balance

The process was performed on a conventional milling machine (FU251, Friedrich Engels Kazanluk, Sofia, Bulgaria). Figure 1 presents the schematic illustration of the process, as well as the geometry of the tool adopted for the studies. The tool shoulder was of a flat surface with a diameter equal to 18 mm. The length of the pin was 2.5 mm. The pin shape was hexagonal with a distance across the flats of 6 mm. The pin was designed with 0.5 mm long grooves for every 0.5 mm of the hexagonal pin's length. The pin was produced of 73MoV52 steel, while the shoulder was made of X210Cr12 steel. The measured hardness of the pin was 58 HRC and of the shoulder 61 HRC (Wilson Mechanical Instrument Co. Inc., New York, NY, USA). The welding of dissimilar joints was carried out at a constant tool traverse speed of 100 mm/min, and a constant tool tilt angle of 2°. The tool rotational speeds used were 800, 1000, and 1200 RPM. Table 2 presents the process parameters, as well as revolutionary pitch values, defined as the rotational speed of the tool divided by its traverse speed.

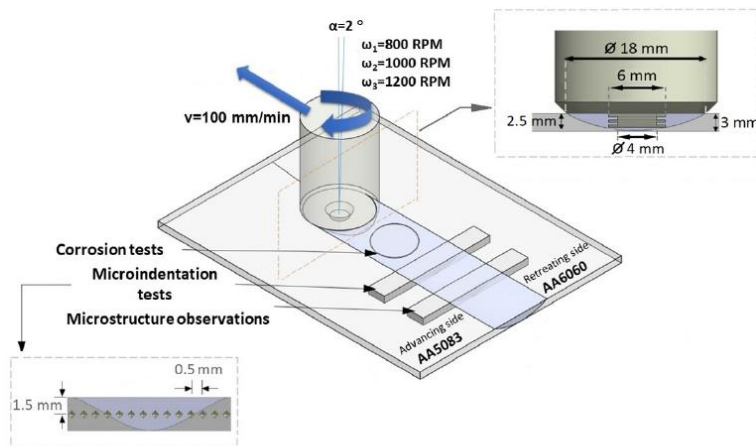


**Figure 1.** Schematic illustration of the process, geometry of the tool and location of the samples for the performed tests.

**Table 2.** FSW process parameters and corresponding revolutionary pitch values.

Material	Traverse Speed (mm/min)	Rotational Speed (RPM)	Tilt Angle (°)	Revolutionary Pitch (rot/mm)
AA5083/AA6060	100	800	2	8
AA5083/AA6060	100	1000	2	10
AA5083/AA6060	100	1200	2	12

Specimens of dimensions 300 mm × 10 mm were prepared for the microstructure observations. For this purpose, the samples were wet ground on the cross-sections of the welds to a final gradation of #4000, and polished with a 1-micrometer diamond suspension. A double-stage etching was performed using Weck's etchant. Firstly, the polished samples were immersed in a 2 wt% NaOH solution for 60 s. In the second stage, the samples were etched in a solution containing 4 g of  $\text{KMnO}_4$ , 1 g of NaOH and 100 mL of distilled water, for 10 s. The microstructure was observed using an optical microscope (BX51, OLYMPUS, Tokyo, Japan), according to the ASTM E3 standard guide for preparation of metallographic specimens.

Hardness measurements were conducted using indentation tests on the cross-sections of the samples, as presented in Figure 1 (NanoTest Vantage, Micro Materials, Wrexham, UK). The tests were conducted in the mid-thickness of the cross-sections, with the indents spaced at a distance of 0.5 mm, in accordance with the ASTM E384-17 standard test method for microindentation hardness of materials. A pyramidal diamond Berkovich indenter was used to carry out 60 independent measurements with a force of 1 N. The loading and unloading times were equal to 20 s. The dwell time was set to 5 s.

The electrochemical properties measurements were performed in accordance with the ASTM G5-94 standard reference test method for making potentiostatic and potentiodynamic anodic polarization measurements. Disc samples with an area of 1 cm<sup>2</sup> were cut from the weld nugget (Figure 1). The tests were conducted in 3.5 wt% NaCl (99.8% purity, Warchem, Warsaw, Poland) solution in distilled water, using a potentiostat/galvanostat (Atlas 0531, Atlas Sollich, Rębiechowo, Poland). The temperature of the solution during the tests was maintained at 20 °C. A three-electrode system was applied. A platinum electrode was used as a counter electrode, a saturated calomel electrode was used as a reference electrode, and a welded sample or a base material sample was used as a working electrode. The tests were initiated by measuring the open-circuit potential (OCP) for 60 min. The corrosion curves were obtained using the potentiodynamic method for a potential range from −2 V to +1 V. The potential scan rate was equal to 1 mV/s. The corrosive potential ( $E_{\text{corr}}$ ) and the corrosion current density ( $i_{\text{corr}}$ ) values were determined using the Tafel extrapolation method and AtlasLab software (ATLAS 0532 Electrochemical unit and Impedance Analyser, Atlas Sollich, Rębiechowo, Poland). The surfaces of the samples after the corrosion tests were investigated using a high-resolution scanning electron microscope (SEM) (Phenom XL, Thermo Fisher Scientific, Breda, Netherlands) with a back-scattered electron detector (BSE).

### 3. Results and Discussion

Visual inspections were conducted to determine the quality of the performed welds. The images of the weld seam surfaces are presented in Figure 2. No serious surface defects, such as lack of bonding or grooves, were found. A very little material outflow was observed in the case of the samples that were produced with tool rotational speeds of 800 and 1000 RPM. Moreover, the weld produced with the tool rotational speed of 800 RPM exhibited a slight cavitation defect on the retreating side. In the case of welds produced with lower tool rotational speeds (800 RPM and 1000 RPM), insufficient plasticization of

the material occurred as a result of the lower heat input, which led to the formation of defects. Small cavitation losses on the retreating side, as well as material outflows observed in both cases, were also caused by insufficient mixing of the material. For the weld produced with the highest tool rotational speed equal of 1200 RPM, no irregularities of the weld seam were found on the surface. The weld surface was smooth, and exhibited a periodic structure. It is believed that the key factors in determining the weld quality are sufficient heat input and proper mixing of the plasticized material. By increasing the tool rotational speed, higher heat is input; thus, sufficient plasticizing and mixing result in the formation of a non-defective weld seam.

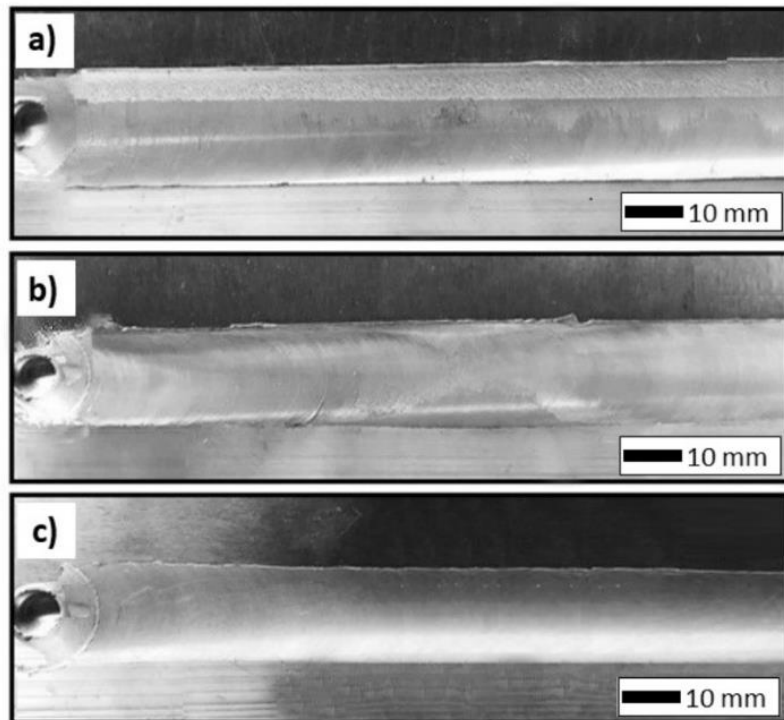


**Figure 2.** Friction-stir-welded samples produced with tool rotational speeds of 800 RPM (a), 1000 RPM (b) and 1200 RPM (c).

Figure 3 presents the macro- and microstructure of one selected weld that was produced with a tool rotational speed of 1200 RPM. Based on macroscopic observations, a characteristic basin shape of the weld nugget can be distinguished. The microscopic observations (Figure 3b–h) permit evaluation of the grain size and shape within all the specified zones. The heat input strongly influenced the microstructure of the heat-affected zone (HAZ), the thermo-mechanically affected zone (TMAZ) and the weld nugget zone (WN). During the process, frictional heating causes plasticization of the material. The amount of heat introduced to the material depends strongly on the process parameters. Husain et al. [22] noted that with increasing the tool rotational speed, the peak temperature during FSW becomes higher. The same conclusions were observed in the studies of Krishnan et al. [23], Liu et al. [24] and Salih et al. [25]. The nugget zone (Figure 3h) experienced the highest heat input, as well as plastic deformation, during mixing by the pin. It resulted in recrystallization within the zone, and led to the finest microstructure. Thermo-

mechanically affected zones (Figure 3f–g) on both sides of the welds also experienced high temperature peaks and plastic deformation due to the mixing by the tool. The recrystallization process was not observed in the TMAZ due to lower heat input. The heat-affected zones on both sides (Figure 3d,e) resulted only through thermal evolution. No recrystallization process occurred within the HAZ. By approaching both parent metals, the material already became characterized by the original microstructures of both alloys (Figure 3b,c).

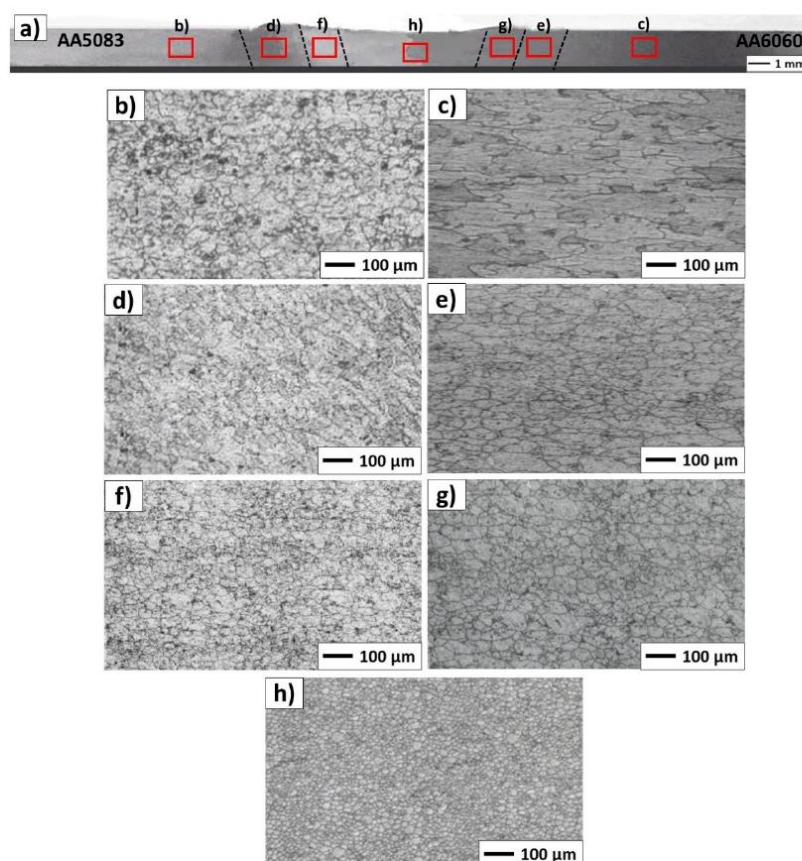


**Figure 3.** Macrostructure of the weld produced with a tool rotational speed of 1200 RPM (a), and microstructures of base metals AA5083 (b), AA6060 (c), HAZ on AA5083 side (d), HAZ on AA6060 side (e), TMAZ on AA5083 side (f), TMAZ on AA6060 side (g) and the weld nugget (h).

Figure 4 presents the hardness profiles on the mid-thickness of cross-sections of the produced welds. The hardnesses of the base metals were equal to approximately 0.75 GPa and 1.15 GPa for AA5083 and AA6060, respectively. The hardness profiles are asymmetrical due to the dissimilar welding of materials with different properties, classified in different groups of aluminum alloys, and delivered under different conditions. Aluminum alloys of the 5XXX series are classified as non-heat treatable. The strength of these alloys is initially formed by alloying pure aluminum by adding elements such as magnesium. Further increases in the strength of these alloys are achieved through various types of cold

working or hardening processes. On the contrary, aluminum alloys of the 6XXX series are classified as heat-treatable aluminum alloys. By adding alloying elements, such as magnesium and silicon, the strength of the alloy is initially formed. The alloying elements exhibit increasing solid solubility when the temperature increases. This provides significant additional strengthening to the heat-treatable alloys by subjecting them to solid solution treatment, quenching and, when applicable, precipitation heat-treatment known also as artificial aging, such as in the case of the AA6060-T6 used in this study. Due to the different behaviors of these alloys under deformation and temperature, differences in the hardness profile on the advancing and retreating sides can be observed. Analyzing the hardness profile from the side of the AA6060 alloy to the center of the joint, the typical shape of the hardness profile for FSW joints of 6xxx-T6 series aluminum alloys is maintained, characterized by a minimum of hardness in the heat-affected zone [26,27]. Softening observed in the heat-affected zone on the side of AA6060-T6 is an effect of precipitate coarsening and dissolution, due to sufficient heat input. The greatest recovery in strength can be observed in the nugget zone, as a result of the recrystallization process. The fine-grained structure resulting from the recrystallization process affects the increase in hardness. According to the Hall–Petch relationship, the increase in hardness can be observed as the average grain size decreases [28,29]. On the advancing side section of the hardness profile, the typical decrease in hardness in HAZ was not observed. At the sections of HAZ and TMAZ, an increase in hardness up to the weld nugget was observed. Welds produced from annealed metal, such as AA5083 in the O condition, do not exhibit a typical hardness drop in HAZ [16]. In the direction of the weld nugget, usually a higher hardness than the base metal in O condition can be noted due to modest hot work-hardening, and finally, grain refinement in the nugget zone [30]. The formation of the weld nugget eliminates the prior deformation microstructure in cold worked material and as a result, the hardness of the nugget zone is independent of the original base metal condition [31].

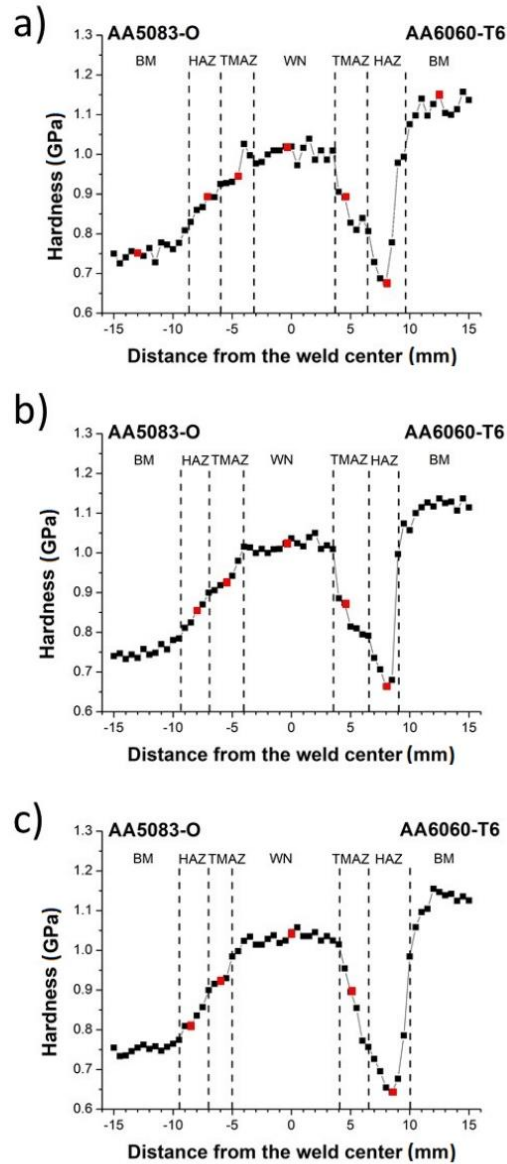


**Figure 4.** Hardness profiles of the joints produced with a tool rotational speed of 800 RPM (a), 1000 RPM (b) and 1200 RPM (c). Red dots indicate the exact locations of further dislocation density and mobility calculations.

Figure 5 presents the influence of the revolutionary pitch parameter on the maximum hardness of the nugget zone (a), minimum hardness of the heat-affected zone (b) and the size of the nugget zone (c). The size of the nugget zone was determined based on the hardness profiles in the center of the cross-sections, as indicated in Figure 4. It is clear that as tool rotational speed increases while maintaining a constant tool traverse speed, the

value of revolutionary pitch increases; thus, the amount of heat input during the process increases [32–34]. For the weld produced with a tool rotational speed of 1200 RPM and a tool traverse speed of 100 mm/min, the highest hardness of the weld nugget was observed. This is due to the highest heat input, which resulted in the most effective recrystallization and the finest microstructure. Meanwhile, decreasing the tool rotational speed resulted in a lower heat input; consequently, less effective dynamic recrystallization in the weld nugget was observed. It should be also noted that microstructural observations confirmed the above findings. By applying the highest revolutionary pitch, the highest heat input resulted, and thus the finest microstructure in the nugget zone and the highest hardness were noted. However, with a high amount of heat generated during the process, the temperature peak in the heat-affected zone also increased. There, the influence of heat served a negative effect, as grain refinement did not occur as a result of recrystallization; only the introduced heat caused the dissolution of strengthening precipitates. This relationship is shown in Figure 5b. As the revolutionary pitch increased, thereby increasing the amount of heat introduced, the hardness of HAZ decreased due to the intensified process of dissolution of strengthening precipitates. It is also noticeable that as the revolutionary pitch increased, the size of the nugget zone tended to increase as well (Figure 5c). This is also explained by an increase in the heat input observed during the process, since the revolutionary pitch was increased. The zone of interest in continuous dynamic recrystallization increased in size in this case, and subsequently the measured size increased, indicating a larger zone of improved hardness with regard to TMAZ and HAZ.

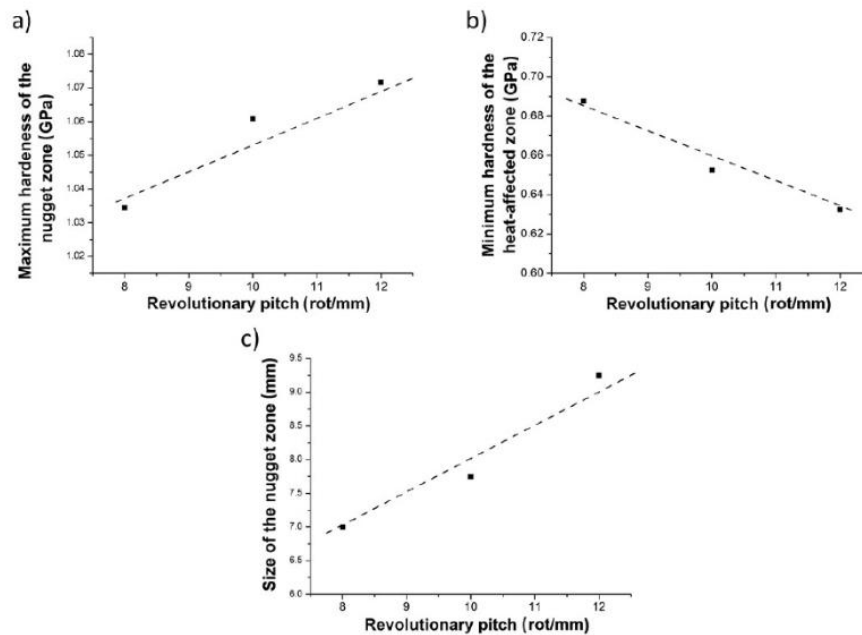


**Figure 5.** Relationship between the maximum hardness of the nugget zone and revolutionary pitch (a), minimum hardness of the heat-affected zone and revolutionary pitch (b) and size of the nugget zone and revolutionary pitch (c).

The hardness and strength of the material were also significantly affected by the dislocations in the material, particularly their density and mobility [35]. During indentation tests, especially when small forces were applied, a significant increase in the hardness of



the material was observed. This is because applied strains resulted in the formation of dislocations in the region under the indenter. Penetration of an indenter into material causes a local increase in dislocations. This phenomenon is referred to as the indentation size effect (ISE). During indentation, dislocations, called geometrically necessary dislocations (GNDs), appear in the material. Their existence increases the flow stress and the measured hardness value. Their density is inversely proportional to the indentation depth ( $h$ ), so this effect is particularly significant for small forces applied. With deeper penetration of an indenter, the steady state is reached, and the hardness depends only on statistically stored dislocations (SSDs). Geometrically necessary dislocations are necessary because they are introduced into the material to accommodate the shape of the indenter. The density of GNDs ( $\rho_{GND}$ ) is derived from the complete line length  $k$  of the dislocation loops, which are required to create the shape of the indenter. Hence, they enable the necessary lattice rotations. The total length of the line is then divided by the semispherical volume  $V$ , which is a storage volume of GNDs with a contact radius  $a_c$ . The geometry of the cross-section of a sample during indentation is presented in Figure 6. In the picture, an angle between the surface of a sample and the indenter is defined as  $\delta$ . For the Berkovich indenter, the value of this angle is equal to  $24.7^\circ$ . In the current considerations, the storage volume of GNDs is considered to be the plastically deformed volume under the indenter, instead of using the volume defined by the contact radius. As presented in Figure 6, the radius of the plastic zone is defined as  $a_{pz}$ , and  $f$  is a factor connecting  $a_c$  with  $a_{pz}$ . For metallic materials, the plastic zone radius is assumed to be larger than the contact radius, so  $f > 1$  [36]. In order to calculate the value of GNDs density ( $\rho_{GND}$ ), the following formula can be used:

$$\rho_{GND} = \frac{3}{2} \cdot \frac{1}{f^3} \cdot \frac{\tan^2 \delta}{b \cdot h} \quad (1)$$

where  $b$  is a magnitude of the Burgers vector (for aluminum  $b = 0.286$  nm). The maximum indenter displacement for plastic deformations  $h$  can be registered during indentation tests [37]. The calculated  $\rho_{GND}$  values are presented in Table 3.

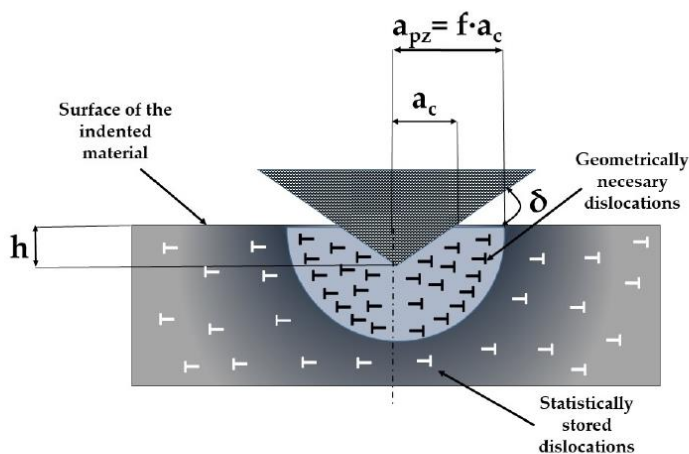


Figure 6. Cross-section of a sample during indentation tests.

It can be assumed that for a Berkovich indenter, a hemispherical shape of the plasticized zone can be observed. For soft metals, such as aluminum alloys, the volume of this zone significantly exceeds the volume defined by the contact radius. In the case of tests



on aluminum alloys using the Berkovich indenter, a factor  $f$  equal to 3 can be assumed [38].

In addition to geometrically necessary dislocations and statistically stored dislocations, the hardness of the material is also determined by the frictional stresses of the crystal lattice  $H_{fr}$ , and the hardening of the solid solution by dissolved alloy additives  $H_{ss}$ . These correlations can be represented by the following equation:

$$H_{ISE} = H_{ss} + H_{fr} + M C a G b \sqrt{\rho_{GND} + \rho_{SSD}} \quad (2)$$

Where  $M$  is a Taylor coefficient (here assumed to be equal to 3 [39]),  $C$  is a factor that transfers the complex stress state under the indenter into a uniaxial stress state (equal to 3 in this case [38]),  $a$  is a factor that depends on the dislocation substructure,  $G$  is a transverse elastic modulus of the test material and  $b$  is a magnitude of the Burgers vector. For both GNDs and SSDs, a value of factor  $a = 0.5$  can be assumed because of the complex stress field in the area under the Berkovich indenter. For aluminum, the value of the Burgers vector is equal to  $b = 0.286$  nm, and the transverse elastic modulus  $G$  is equal to 26 GPa [40]. In this analysis, only dislocation hardening will be considered. Thus, equation (2) can be expressed as follows:

$$H_{ISE} = M C a G b \sqrt{\rho_{GND} + \rho_{SSD}} \quad (3)$$

On the contrary, when the ISE is not considered, the relationship between macroscopic hardness  $H_0$  and SSD density ( $\rho_{SSD}$ ) is expressed by Taylor's relation [41]:

$$H_0 = M C a G b \sqrt{\rho_{SSD}} \quad (4)$$

Considering the  $H_{ISE}$  hardness values obtained in the indentation tests, the maximum depth of indenter displacement  $h$  and the constants introduced earlier, the density of SSDs can be calculated from the relationship, shown as follows:

$$\rho_{SSD} = \frac{H_{ISE}^2}{(M C a G b)^2} \cdot \rho_{GND} \quad (5)$$

In order to calculate the dislocation mobility, the following Orowan equation was used [42]:

$$\frac{d\varepsilon}{dt} = \dot{\varepsilon} = b \cdot \rho_{SSD} \cdot v \quad (6)$$

where  $\varepsilon$  is strain and  $v$  is dislocation mobility.

In order to calculate the strain derivative as a function of time, the stabilized fragment of creep during the indentation dwell time period at maximum force was approximated to a linear function. The calculations were performed for all the samples, in the exact areas of base materials AA5083 and AA6060, HAZ and TMAZ for both advancing and retreating sides and the weld nuggets. The exact measurement positions are presented in Figure 4 with red dots. The results of the analysis are presented in Figure 7. Finally, the calculations on dislocation mobilities were performed using a converted Equation (6):

$$v = \frac{\dot{\varepsilon}}{b \cdot \rho_{SSD}} \quad (7)$$

The results of the above calculations are presented in Table 3. Figure 7 presents hysteresis plots of load–depth for a single indentation in the distinguished zones of the samples produced with tool rotational speeds of 800, 1000 and 1200 RPM. Figure 8 shows the relationships between strain and time for the dwell period during the indentation tests in the base materials AA5083, AA6060, HAZ and TMAZ at both sides, and WN for the samples produced with 800 (a), 1000 (b) and 1200 RPM (c). The exact locations are indicated with red dots on the hardness profiles presented in Figure 4.

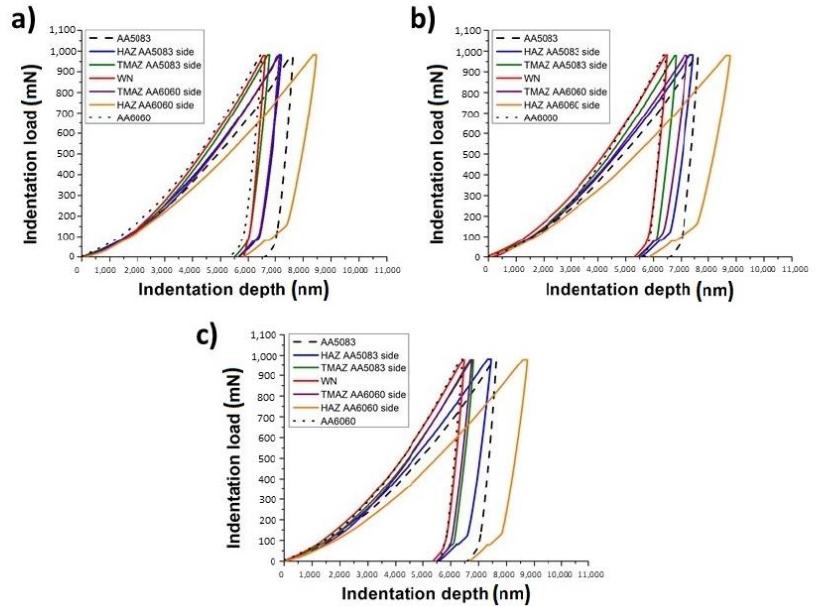


**Figure 7.** Hysteresis plots of load–depth for a single indentation in the base metals AA5083, AA6060, HAZ, TMAZ and WN, for the welds produced with tool rotational speeds of 800 RPM (a), 1000 RPM (b) and 1200 RPM (c).

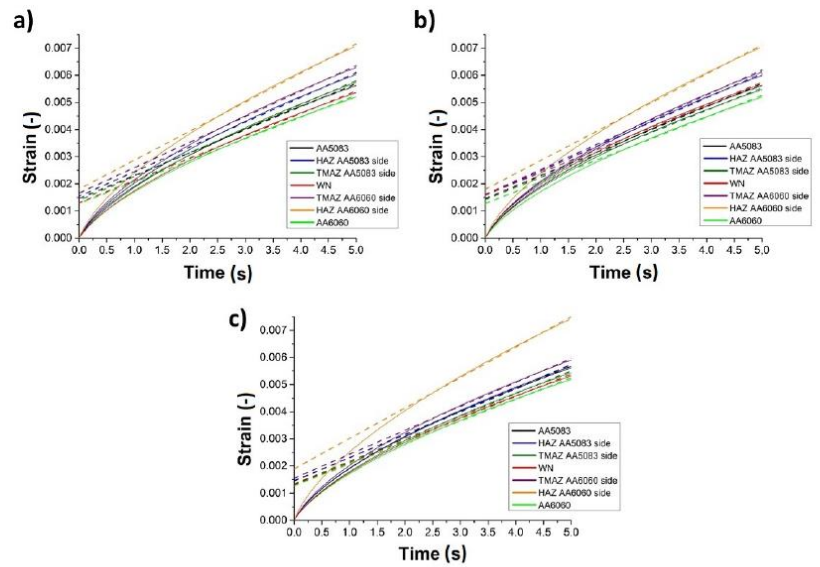


**Figure 8.** Strain versus time diagrams for the indentation dwell time period in the base metals AA5083, AA6060, HAZ, TMAZ and WN for the welds produced with tool rotational speeds of 800 RPM (a), 1000 RPM (b) and 1200 RPM (c).

**Table 3.** Hardness, maximum indenter displacement, density of GNDs, density of SSDs and dislocation mobilities for all of the tested samples in different zones.

Sample	$H_{ISE}$ (GPa)	$h_{max}$ ( $\mu\text{m}$ )	$\rho_{GND}$ ( $\frac{1}{m^2}$ )	$\rho_{SSD}$ ( $\frac{1}{m^2}$ )	$V$ ( $\frac{m}{s}$ )
- AA5083	0.754	7.629	$5.386 \times 10^{12}$	$6.679 \times 10^{14}$	$4.429 \times 10^{-9}$
- AA6060	1.103	6.283	$6.540 \times 10^{12}$	$9.785 \times 10^{14}$	$2.844 \times 10^{-9}$
$\omega = 800$ RPM HAZ side	0.881	7.226	$5.687 \times 10^{12}$	$7.811 \times 10^{14}$	$4.082 \times 10^{-9}$
$\omega = 800$ RPM TMAZ side	0.945	6.693	$6.140 \times 10^{12}$	$8.378 \times 10^{14}$	$3.681 \times 10^{-9}$
$\omega = 800$ RPM WN	1.034	6.518	$6.305 \cdot 10^{12}$	$9.171 \times 10^{14}$	$3.142 \times 10^{-9}$
$\omega = 800$ RPM TMAZ side	0.896	7.143	$5.753 \cdot 10^{12}$	$7.945 \times 10^{14}$	$4.137 \times 10^{-9}$
$\omega = 800$ RPM HAZ side	0.687	8.356	$4.918 \cdot 10^{12}$	$6.086 \times 10^{14}$	$6.142 \times 10^{-9}$
$\omega = 1000$ RPM HAZ side	0.843	7.338	$5.600 \cdot 10^{12}$	$7.124 \times 10^{14}$	$4.403 \times 10^{-9}$
$\omega = 1000$ RPM TMAZ side	0.932	6.922	$5.937 \cdot 10^{12}$	$8.264 \times 10^{14}$	$3.482 \times 10^{-9}$
$\omega = 1000$ RPM WN	1.060	6.503	$6.319 \cdot 10^{12}$	$9.404 \times 10^{14}$	$3.090 \times 10^{-9}$
$\omega = 1000$ RPM TMAZ side	0.883	7.219	$5.692 \cdot 10^{12}$	$7.829 \times 10^{14}$	$4.095 \times 10^{-9}$
$\omega = 1000$ RPM HAZ side	0.652	8.641	$4.755 \cdot 10^{12}$	$5.775 \times 10^{14}$	$6.442 \times 10^{-9}$
$\omega = 1200$ RPM HAZ side	0.845	7.333	$5.604 \cdot 10^{12}$	$7.490 \times 10^{14}$	$4.015 \times 10^{-9}$
$\omega = 1200$ RPM TMAZ side	0.943	6.910	$5.947 \cdot 10^{12}$	$8.362 \times 10^{14}$	$3.487 \times 10^{-9}$
$\omega = 1200$ RPM WN	1.071	6.435	$6.386 \cdot 10^{12}$	$9.501 \times 10^{14}$	$3.003 \times 10^{-9}$
$\omega = 1200$ RPM TMAZ side	0.925	7.049	$5.830 \cdot 10^{12}$	$8.203 \times 10^{14}$	$3.768 \times 10^{-9}$
$\omega = 1200$ RPM HAZ side	0.632	8.742	$4.700 \cdot 10^{12}$	$5.597 \times 10^{14}$	$7.009 \times 10^{-9}$

In the friction-stir-welded joints, the dislocation density results from strain and severe plastic deformations, as well as recrystallization in the WN [43,44]. The resulting

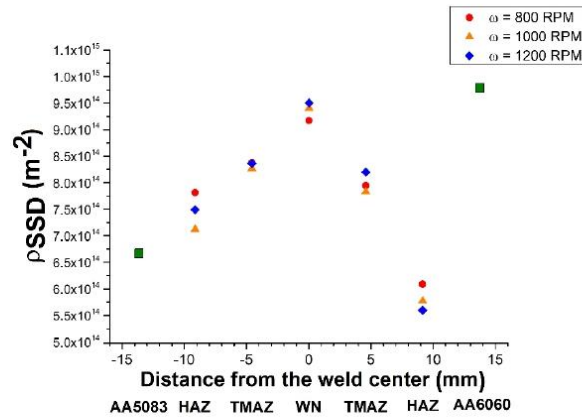


values of the dislocation density and mobility are influenced not only by process parameters, such as the rotational and traverse speed of the tool, the tilt angle and its geometry, but also by the properties of the parent materials. The amount of heat input, the process of plasticization of the material, its mixing, dissolution of strengthening precipitates and recrystallization, significantly affect the resulting joint properties.

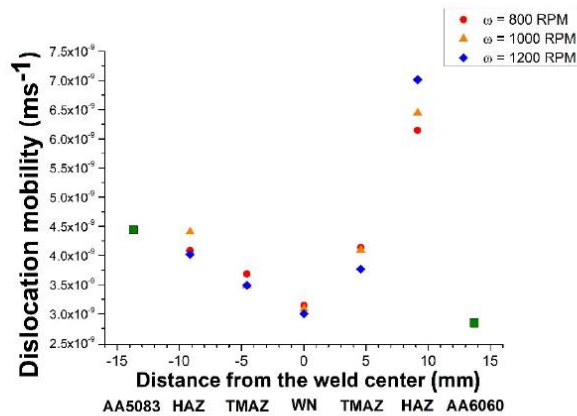
In all of the cases, the densities of geometrically necessary dislocations are significantly lower than the densities of statistically stored dislocations, due to the relatively high applied measurement forces. It should be noted that the highest density of statistically stored dislocations can be observed in AA6060 base metal. Furthermore, the weld nugget zones of all the produced welds exhibit high SSD dislocation densities of  $9.171 \times 10^{14}$ ,  $9.404 \times 10^{14}$  and  $9.501 \times 10^{14} \text{ m}^{-2}$  for the welds produced with tool rotational speeds of 800, 1000 and 1200 RPM, respectively. Higher heat input during the FSW process from increased tool rotational speed resulted in the increase in dislocation densities observed in the nugget zones of the produced welds. Studies conducted thus far do not indicate a clear trend that determines the effect of the FSW process on dislocation densities and mobility. In a studies by Woo et al. [45], it was observed that the dynamic recrystallization zone after the FSW process of AA6061-T6 was characterized by a lower dislocation density than that of the parent material. On the contrary, in another study of Woo et al. [46], a higher dislocation density was found in the weld nugget zone compared to AA6061-T6 parent material. Yuzbekova et al. [47] observed a higher dislocation density in friction-stir-welded AA5024 aluminum alloy. Moreover, Laska et al. [38] found higher dislocation densities in dissimilar friction-stir-welded joints of AA6060/AA6082, compared to both parent materials. Ni et al. [48] noted a lower dislocation density in the weld nugget zone of friction-stir-welded SiCp/AA2009-T351 compared to the base material. This was explained by the dynamic recrystallization processes occurring in the weld nugget, and a low cooling rate after the process. The lowest dislocation density was observed in heat-affected zones from the side of the AA6060 alloy, for all the produced welds. Similarly, in the study by Ni et al. [48], in the HAZ of the SiCp/AA2009-T351 FSWed joint, a significant decrease in dislocation density was noted through TEM observations. The reduction in dislocation density in the heat-affected zone is a result of the release of dislocations during the FSW thermal cycle [48].

By analyzing the dwell time of indentation studies, it is possible to determine the mobility of dislocations. In the above study, the lowest dislocation mobilities were observed in the AA6060 parent material and weld nugget zones. In contrast, the highest mobilities were registered in the HAZ zones of all welds on the retreating side of the AA6060 parent material. The calculated mobilities were equal to  $6.142 \times 10^{-9}$ ,  $6.442 \times 10^{-9}$  and  $7.009 \times 10^{-9} \frac{\text{m}}{\text{s}}$  for the welds produced with tool rotational speeds equal to 800, 100 and 1200 RPM, respectively. Compared to both parent materials, the calculated values were equal to  $4.429 \times 10^{-9}$  and  $2.844 \times 10^{-9} \frac{\text{m}}{\text{s}}$  for AA5083 and AA6060, respectively; the increase in the mobility was noticeable. It is also worth noting that by increasing the tool rotational speed, and consequently the heat input, the dislocations became characterized by higher mobility. According to Taylor and Orowan's theory, materials that are characterized by lower dislocation densities and high dislocation mobilities tend to exhibit lower strength [38]. Therefore, the reduction in hardness in the HAZ zones on the AA6060 side is also influenced by the high-mobility dislocations present in the material. The results of SSD density and dislocation mobility calculations are shown in the graphs of Figure 9.





(a)



(b)

**Figure 9.** Density of SSDs (a) and dislocation mobilities (b) for all of the tested samples in different zones.

Functional properties, in addition to the strength of welded components, are significantly affected by the corrosion resistance of the material. It is of particular importance in the case of structures that are used in corrosive environments. It should be also noted that in the case of even occasional contact with corrosive environments, small corrosion losses can significantly affect the strength of the structure. Figure 10 presents the open circuit potential (OCP) measurements (Figure 10a) and potentiodynamic polarization curves for the produced samples (Figure 10b) that were subjected to tests in 3.5 wt% NaCl solution. The OCP measurements preceded the potentiodynamic test, and were performed for 60 min, to reach stability. Potentiodynamic curves recorded in the study were subjected to the Tafel extrapolation. Based on the obtained data, the values of corrosive potential ( $E_{corr}$ ) and corrosion current density ( $i_{corr}$ ) were collected. Table 4 presents the results of the potentiodynamic studies.



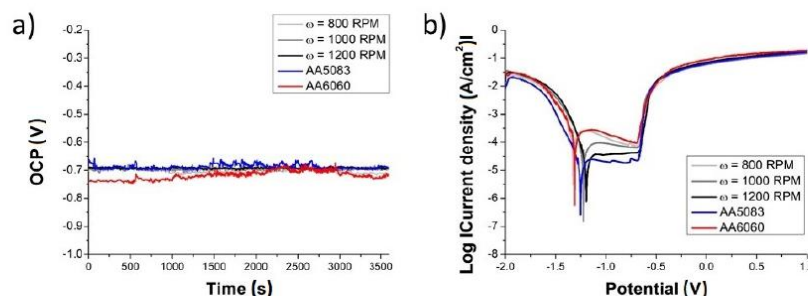


**Figure 10.** Open circuit potentials (OCP) (a) and potentiodynamic polarization curves (b) for all the tested samples in 3.5 wt% NaCl solution.

**Table 4.** Open circuit potentials (OCP), corrosion potentials ( $E_{corr}$ ) and corrosion current densities ( $i_{corr}$ ) for the tested samples.

Sample	$\omega = 800$ RPM	$\omega = 1000$ RPM	$\omega = 1200$ RPM	AA5083	AA6060
OCP (V)	$-0.697 \pm 0.039$	$-0.694 \pm 0.039$	$-0.679 \pm 0.007$	$-0.661 \pm 0.017$	$-0.738 \pm 0.013$
$E_{corr}$ (V)	$-1.328 \pm 0.015$	$-1.312 \pm 0.014$	$-1.299 \pm 0.015$	$-1.356 \pm 0.009$	$-1.196 \pm 0.001$
$i_{corr}$ ( $\mu\text{A}\cdot\text{cm}^{-2}$ )	$8.075 \pm 0.182$	$7.592 \pm 0.442$	$6.935 \pm 0.199$	$4.506 \pm 0.278$	$9.047 \pm 0.768$

The corrosion potential shifted from the minimum value of  $-0.738 \pm 0.013$  V for the base metal AA6060, to  $0.661 \pm 0.017$  V for the base metal AA5083. The corrosion potential for all the welded samples adopted values that were between both parent materials. The results of the conducted experiments indicate that the AA5083 parent material exhibited the highest corrosion resistance. In this case, the corrosion current density was equal to  $4.506 \pm 0.278 \mu\text{A}\cdot\text{cm}^{-2}$ . The lowest corrosion resistance and the highest corrosion current density of  $9.047 \pm 0.768 \mu\text{A}\cdot\text{cm}^{-2}$  were from the AA6060 alloy. In general, aluminum alloys in both 5XXX and 6XXX series exhibited good corrosion resistance. Alloys in series 5XXX are so-called seawater-resistant alloys, and are characterized by excellent electrochemical properties [49]. Sukiman et al. [50] also registered better corrosion resistance for AA5083 when compared to the AA6060 alloy. All of the welds displayed a corrosion resistance that was greater than that of alloy AA6060, but less than that of alloy AA6082. In a study by Kartsonakis et al. [51], it was demonstrated that the friction-stir welding process resulted in the production of dissimilar AA5083/AA6082 joints that were characterized by a corrosion resistance that was between both parent materials. Furthermore, the corrosion resistance of the AA5083 alloy was higher than that of the AA6XXX series alloy. Several scientific investigations indicated that the FSW process itself improves the corrosion resistance of welds. Qin et al. [52] revealed that the FSWed joints of 2A14 aluminum alloy were more resistant to corrosion processes in exfoliation corrosion solution. In the study of Zucchi et al. [53], it was observed that the FSWed joint of AA5083 was more resistant to exfoliation corrosion than its base metal. On the contrary, Maggiolino et al. [54] found no significant differences between the corrosion resistance of AA6060 alloy and its friction-stir-welded joint.

In the present study, the values of corrosion current density were equal to  $8.075 \pm 0.182$ ,  $7.592 \pm 0.442$  and  $6.935 \pm 0.199 \mu\text{A}\cdot\text{cm}^{-2}$  for the welds produced with tool rotational speeds of 800, 1000 and 1200 RPM, respectively. These observations are also presented in Figure 11. It is clearly visible that by increasing the revolutionary pitch, the corrosion current density decreases. This means that by increasing heat input, better corrosion properties of the weld may result. Important factors that affect the corrosion resistance of metals are grain size and distribution of precipitates. Microstructure serves an important role in the formation of a passive oxide layer on the metal surface that provides protection against

corrosion. A finer grain microstructure is characterized by a more reactive surface, thus formation of the oxide layer progresses more easily. Due to that fact, the corrosion rate of aluminum in NaCl solution has a tendency to decrease as the grain size decreases [55]. Song et al. [56] noted that when the finer grains are observed for pure aluminum, the resistance to pitting corrosion increases as a result of the denser oxide layer on the surface. The recrystallization processes that occur in the weld nugget provide refinement of the grains, as well as more uniform precipitate distributions, which also improves the corrosion resistance of the weld. Higher input heat results in more effective recrystallization; thus, the finer the microstructure, and better the corrosion resistance.

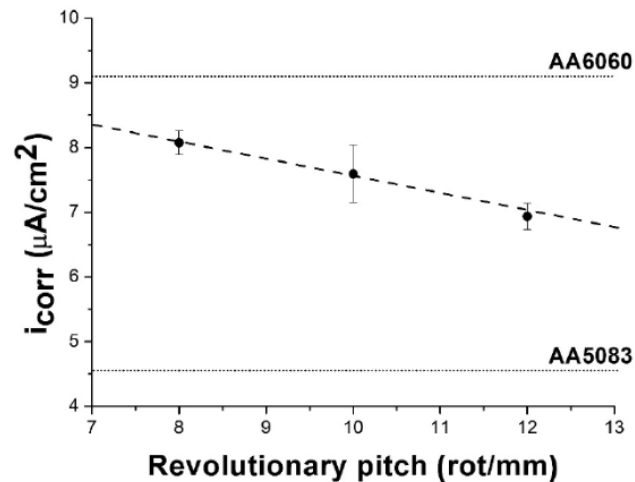


**Figure 11.** The relationship between corrosion current density ( $i_{corr}$ ) and revolutionary pitch for the produced welds.

Figure 12 depicts the scanning electron microscopy images of the surface of the welded samples, and both base materials, after corrosion tests. For welded samples, the characteristic geometry of the surface of the nugget, resulting from simultaneous tool traverse and rotational motions, is noticeable. For these samples, no significant differences were found based on SEM observations. Thus, it is not possible to determine the effect of process parameters on the corrosion resistance of welds, on the basis of microscopic observations alone. However, it should be noted that differences in corrosion resistance can be found in the samples of the native materials, which did not undergo thermomechanical processes. The corrosion losses on the AA6060 alloy (Figure 12b) are larger. In the case of the parent material AA5083 (Figure 12a), the area unaffected by corrosion processes was larger, so the corrosion resistance of this alloy in 3.5 wt% NaCl solution is greater. Although scanning electron microscope observations do not allow quantitative evaluations of the corrosion resistance of welds, the results obtained are consistent with Tafel's extrapolation results. A qualitative evaluation of the obtained images confirms that the AA5083 alloy has the highest corrosion resistance. Alloy AA6060 experienced high corrosion losses, while the produced welds showed moderate corrosion resistance. In their case, corrosion losses that were observed on the surface were higher than those of the AA5083 parent material, and lower than those of the AA6060 parent material. This is confirmed by the results of the potentiodynamic tests and Tafel extrapolations.





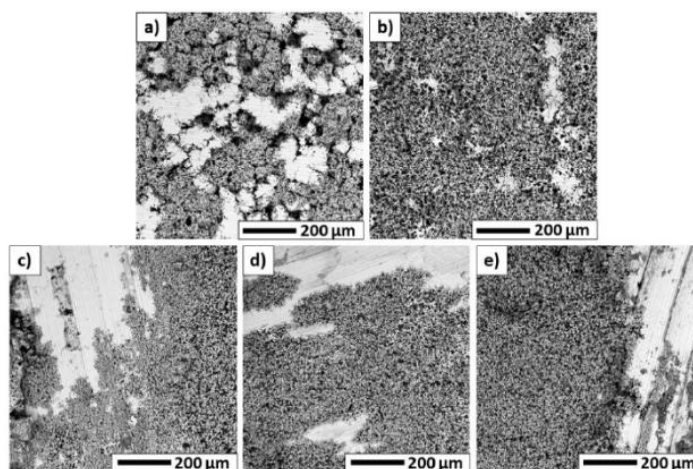


**Figure 12.** SEM images illustrating the surfaces of the samples after electrochemical tests on the base materials AA5083 (a), AA6060 (b), and the welds produced with tool rotational speeds of 800 RPM (c), 1000 RPM (d) and 1200 RPM (e).

#### 4. Conclusions

The friction-stir-welding process was applied to produce dissimilar butt welds with AA5083 and AA6060 aluminum alloys. Different tool rotational speed values were used (800, 1000, 1200 RPM), with a constant tool traverse speed (100 mm/min) and tool tilt angle ( $2^\circ$ ). The studies were conducted to evaluate the microstructure, hardness, dislocation density and mobility, as well as corrosion resistance, of the resulting welds. The following conclusions can be drawn from this study:

1. The use of a hexagonal tool with grooves, along with the selection of the above process parameters, yielded sound welds that were characterized by an absence of surface defects. The typical microstructure characterized by zones of HAZ, TMAZ and fine-grained WN was revealed.
2. Hardness measurements were taken on cross sections of the joints using indentation tests. A reduction in hardness values was observed in the heat-affected zones on the AA6060 alloy side of the produced welds. The lowest hardness was noted for the HAZ of the weld that was produced with a tool rotational speed of 1200 RPM, and was equal to 0.64 GPa. In addition, it was observed that the maximum hardness of the nugget zone increased with increasing tool rotational speed. This is explained by a more efficient recrystallization process occurring as a result of higher heat input. The highest hardness of the WN zone was observed for the weld that was produced with the highest tool rotational speed of 1200 RPM, and was equal to 1.07 GPa.
3. Based on the results of the indentation tests, in particular, the dwell time period, the densities and mobilities of dislocations in the individual zones of weld cross sections were calculated. The lowest dislocation density of  $5.597 \times 10^{14} \text{ m}^{-2}$ , with the highest mobility of  $7.009 \times 10^{-9} \frac{\text{m}}{\text{s}}$ , was observed in the heat-affected zones on the AA6060 side of the resulting welds, which may explain the significant strength reduction in this zone.
4. The conducted potentiodynamic tests in 3.5 wt% NaCl revealed that the AA5083 base material was characterized by the highest corrosion resistance, and the corrosion current density was equal to  $4.506 \pm 0.278 \mu\text{A}\cdot\text{cm}^{-2}$ . The highest corrosion current density  $9.047 \pm 0.768 \mu\text{A}\cdot\text{cm}^{-2}$  was noted for the base metal AA6060. The corrosion current



densities for all welded samples yielded average values that fell between both parent materials. By increasing the tool rotational speed, there was higher heat input. This resulted in more effective recrystallization, and better corrosion resistance of the welds.

**Author Contributions:** Conceptualization, A.L.; methodology, A.L.; validation, A.L., M.S., A.P. and P.C.; formal analysis, P.C. and M.S.; investigation, A.L.; writing—original draft preparation, A.L.; writing—review and editing, P.C. and M.S.; visualization, A.L. and A.P.; supervision, P.C. and M.S. All authors have read and agreed to the published version of the manuscript.

**Funding:** This research received no external funding.

**Data Availability Statement:** Not applicable.

**Conflicts of Interest:** The authors declare no conflicts of interest.

## References

- Ghaffarpour, M.; Kolahgar, S.; Dariani, B.M.; Dehghani, K. Evaluation of dissimilar welds of 5083-H12 and 6061-T6 produced by friction stir welding. *Metall. Mater. Trans. A Phys. Metall. Mater. Sci.* **2013**, *44*, 3697–3707. <https://doi.org/10.1007/s11661-013-1739-2>.
- Ancona, A.; Daurelio, G.; De Filippis, L.A.C.; Ludovico, A.D.; Spera, A.M. CO<sub>2</sub> Laser Welding of Aluminium Shipbuilding Industry Alloys: AA 5083, AA 5383, AA 5059, and AA 6082. In Proceedings of the XIV International Symposium on Gas Flow, Chemical Lasers, and High-Power Lasers, Wroclaw, Poland, 25–30 August 2002; pp. 577–587.
- Kawasaki, T.; Makino, T.; Masai, K.; Ohba, H.; Ina, Y.; Ezumi, M. Application of friction stir welding to construction of railway vehicles. *JSME Int. J. Ser. A Solid Mech. Mater. Eng.* **2004**, *47*, 502–511. <https://doi.org/10.1299/jsmea.47.502>.
- Vasudevan, N.; Bhaskar, G.B.; Rajendra Prasad, A.; Suresh, S.M. Corrosion study on AA5083 aluminum alloy—Boron carbide composite. *Mater. Today Proc.* **2019**, *16*, 1124–1129. <https://doi.org/10.1016/j.matpr.2019.05.204>.
- Samuel Ratna Kumar, P.S.; Robinson Smart, D.S.; John Alexis, S. Corrosion behaviour of Aluminium Metal Matrix reinforced with Multi-wall Carbon Nanotube. *J. Asian Ceram. Soc.* **2017**, *5*, 71–75. <https://doi.org/10.1016/j.jascer.2017.01.004>.
- Liu, Q.; Han, R.; Gao, Y.; Ke, L. Numerical investigation on thermo-mechanical and material flow characteristics in friction stir welding for aluminum profile joint. *Int. J. Adv. Manuf. Technol.* **2021**, *114*, 2457–2469. <https://doi.org/10.1007/s00170-021-06978-8>.
- Chen, X.; Peng, Y.; Peng, S.; Yao, S.; Chen, C.; Xu, P. Flow and fracture behavior of aluminum alloy 6082-T6 at different tensile strain rates and triaxialities. *PLoS ONE* **2017**, *12*, e0181983. <https://doi.org/10.1371/journal.pone.0181983>.
- Baratzadeh, F.; Boldsaikhan, E.; Nair, R.; Burford, D.; Lankarani, H. Investigation of mechanical properties of AA6082-T6/AA6063-T6 friction stir lap welds. *J. Adv. Join. Processes* **2020**, *1*, 100011. <https://doi.org/10.1016/j.jajp.2020.100011>.
- Varma, K.V.K.; Baig, I.; Kumar, B.V.R.R.; Ramana, M.V. Effect of friction stir welding parameters on tool geometry and metallurgical properties of AA 6082-T6 weldments at different weld zones. *Mater. Today Proc.* **2021**, *45*, 3195–3200. <https://doi.org/10.1016/j.matpr.2020.12.370>.
- Maciel, R.; Bento, T.; Braga, D.F.O.; da Silva, L.F.M.; Moreira, P.M.G.P.; Infante, V. Fatigue properties of combined friction stir and adhesively bonded AA6082-T6 overlap joints. *Fatigue Fract. Eng. Mater. Struct.* **2020**, *43*, 2169–2180. <https://doi.org/10.1111/ffe.13287>.
- Li, Y.; Zou, W.; Lee, B.; Babkin, A.; Chang, Y. Research progress of aluminum alloy welding technology. *Int. J. Adv. Manuf. Technol.* **2020**, *109*, 1207–1218. <https://doi.org/10.1007/s00170-020-05606-1>.
- Safeen, M.W.; Spena, P.R. Main issues in quality of friction stir welding joints of aluminum alloy and steel sheets. *Metals* **2019**, *9*, 610. <https://doi.org/10.3390/met9050610>.
- Laska, A.; Szkodo, M. Manufacturing Parameters, Materials, and Welds Properties of Butt Friction Stir Welded Joints—Overview. *Materials* **2020**, *13*, 4940. <https://doi.org/10.3390/ma13214940>.
- Magalhães, V.M.; Leitão, C.; Rodrigues, D.M. Friction stir welding industrialisation and research status. *Sci. Technol. Weld. Join.* **2018**, *23*, 400–409. <https://doi.org/10.1080/13621718.2017.1403110>.
- Devaiah, D.; Kishore, K.; Laxminarayana, P. Optimal FSW process parameters for dissimilar aluminium alloys (AA5083 and AA6061) Using Taguchi Technique. *Mater. Today Proc.* **2018**, *5*, 4607–4614. <https://doi.org/10.1016/j.matpr.2017.12.031>.
- Peel, M.J.; Steuwer, A.; Withers, P.J.; Dickerson, T.; Shi, Q.; Shercliff, H. Dissimilar friction stir welds in AA5083-AA6082. Part I: Process parameter effects on thermal history and weld properties. *Metall. Mater. Trans. A Phys. Metall. Mater. Sci.* **2006**, *37*, 2183–2193. <https://doi.org/10.1007/BF02586138>.
- Khodir, S.A.; Shibayanagi, T. Friction stir welding of dissimilar AA2024 and AA7075 aluminum alloys. *Mater. Sci. Eng. B Solid-State Mater. Adv. Technol.* **2008**, *148*, 82–87. <https://doi.org/10.1016/j.mseb.2007.09.024>.
- Palanivel, R.; Koshy Mathews, P.; Murugan, N.; Dinaharan, I. Effect of tool rotational speed and pin profile on microstructure and tensile strength of dissimilar friction stir welded AA5083-H111 and AA6351-T6 aluminum alloys. *Mater. Des.* **2012**, *40*, 7–16. <https://doi.org/10.1016/j.matdes.2012.03.027>.

19. Guo, J.F.; Chen, H.C.; Sun, C.N.; Bi, G.; Sun, Z.; Wei, J. Friction stir welding of dissimilar materials between AA6061 and AA7075 Al alloys effects of process parameters. *Mater. Des.* **2014**, *56*, 185–192. <https://doi.org/10.1016/j.matdes.2013.10.082>.
20. Mastanaiah, P.; Sharma, A.; Reddy, G.M. Dissimilar Friction Stir Welds in AA2219-AA5083 Aluminium Alloys: Effect of Process Parameters on Material Inter-Mixing, Defect Formation, and Mechanical Properties. *Trans. Indian Inst. Met.* **2016**, *69*, 1397–1415. <https://doi.org/10.1007/s12666-015-0694-6>.
21. Dong, J.; Zhang, D.; Zhang, W.; Zhang, W.; Qiu, C. Microstructure evolution during dissimilar friction stir welding of AA7003-T4 and AA6060-T4. *Materials* **2018**, *11*, 342. <https://doi.org/10.3390/ma11030342>.
22. Husain, M.M.; Sarkar, R.; Pal, T.K.; Prabhu, N.; Ghosh, M. Friction Stir Welding of Steel: Heat Input, Microstructure, and Mechanical Property Co-relation. *J. Mater. Eng. Perform.* **2015**, *24*, 3673–3683. <https://doi.org/10.1007/s11665-015-1652-5>.
23. Krishnan, M.; Subramaniam, S.K. Investigation of Mechanical and Metallurgical Properties of Friction Stir Corner Welded Dissimilar Thickness AA5086-AA6061 Aluminium Alloys. *Mater. Res.* **2018**, *21*, e20171045. <https://doi.org/10.1590/1980-5373-MR-2017-1045>.
24. Liu, F.J.; Fu, L.; Chen, H.Y. Effect of high rotational speed on temperature distribution, microstructure evolution, and mechanical properties of friction stir welded 6061-T6 thin plate joints. *Int. J. Adv. Manuf. Technol.* **2018**, *96*, 1823–1833. <https://doi.org/10.1007/s00170-018-1736-0>.
25. Salih, O.S.; Ou, H.; Wei, X.; Sun, W. Microstructure and mechanical properties of friction stir welded AA6092/SiC metal matrix composite. *Mater. Sci. Eng. A* **2019**, *742*, 78–88. <https://doi.org/10.1016/j.msea.2018.10.116>.
26. Morozova, I.; Obrosov, A.; Naumov, A.; Króllicka, A.; Golubev, I.; Bokov, D.O.; Doynov, N.; Weiß, S.; Michailov, V. Impact of impulses on microstructural evolution and mechanical performance of al-mg-si alloy joined by impulse friction stir welding. *Materials* **2021**, *14*, 347. <https://doi.org/10.3390/ma14020347>.
27. Laska, A.; Szkodo, M.; Koszelow, D.; Cavaliere, P. Effect of Processing Parameters on Strength and Corrosion Resistance of Friction Stir-Welded AA6082. *Metals* **2022**, *12*, 192. <https://doi.org/10.3390/met12020192>.
28. Naik, S.N.; Walley, S.M. The Hall–Petch and inverse Hall–Petch relations and the hardness of nanocrystalline metals. *J. Mater. Sci.* **2020**, *55*, 2661–2681. <https://doi.org/10.1007/s10853-019-04160-w>.
29. Bahrami, M.; Dehghani, K.; Besharati Givi, M.K. A novel approach to develop aluminum matrix nano-composite employing friction stir welding technique. *Mater. Des.* **2014**, *53*, 217–225. <https://doi.org/10.1016/j.matdes.2013.07.006>.
30. Sangalli, G.; Lemos, G.V.B.; Martinazzi, D.; De Lima Lessa, C.R.; Beskow, A.B.; Reguly, A. Towards qualification of friction stir welding to AA5083-O and AA5052-O aluminum alloys. *Mater. Res.* **2019**, *22*, e20190349. <https://doi.org/10.1590/1980-5373-MR-2019-0349>.
31. Threadgill, P.L.; Leonard, A.J.; Shercliff, H. Friction Stir Welding of Aluminium Alloys. *Int. Mater. Rev.* **2009**, *54*, 49–93. <https://doi.org/10.1179/174328009X411136>.
32. Sato, Y.S.; Onuma, T.; Ikeda, K.; Kokawa, H. Experimental verification of heat input during friction stir welding of Al alloy 5083. *Sci. Technol. Weld. Join.* **2016**, *21*, 325–330. <https://doi.org/10.1080/13621718.2015.1112469>.
33. Zhang, Z.; Zhang, Z.; Zhang, H. Numerical investigations of size effects on residual states of friction stir weld. *Proc. Inst. Mech. Eng. Part B J. Eng. Manuf.* **2014**, *228*, 572–581. <https://doi.org/10.1177/0954405413506191>.
34. Sedmak, A.S.; Kumar, R.; Chattopadhyaya, S.; Hloch, S.; Tadić, S.S.; Djurdjević, A.A.; Čeković, I.R.; Dončeva, E. Heat input effect of friction stir welding on aluminum alloy AA 6061-T6 welded joint. *Therm. Sci.* **2016**, *20*, 637–641. <https://doi.org/10.2298/TSCI150814147D>.
35. Thirathipviwat, P.; Song, G.; Bednarcik, J.; Kühn, U.; Gemming, T.; Nielsch, K.; Han, J. Compositional complexity dependence of dislocation density and mechanical properties in high entropy alloy systems. *Prog. Nat. Sci. Mater. Int.* **2020**, *30*, 545–551. <https://doi.org/10.1016/j.pnsc.2020.07.002>.
36. Durst, K.; Backes, B.; Franke, O.; Göken, M. Indentation size effect in metallic materials: Modeling strength from pop-in to macroscopic hardness using geometrically necessary dislocations. *Acta Mater.* **2006**, *54*, 2547–2555. <https://doi.org/10.1016/j.actamat.2006.01.036>.
37. Yamada, H.; Ogasawara, N.; Shimizu, Y.; Horikawa, H.; Kobayashi, H. Effect of high strain rate on micro-indentation test in pure aluminum. *EPJ Web Conf.* **2012**, *26*, 2–6. <https://doi.org/10.1051/epjconf/20122601028>.
38. Laska, A.; Szkodo, M.; Pawłowski, Ł.; Gajowiec, G. Corrosion properties of dissimilar AA6082/AA6060 friction stir welded butt joints in different NaCl concentrations. *Int. J. Precis. Eng. Manuf. Green Technol.* **2022**. <https://doi.org/10.1007/s40684-022-00441-z>.
39. Johnson, K.L. *Contact Mechanics*; Cambridge University Press: Cambridge, UK, 1985; ISBN 9780521255769.
40. Cho, J.; Molinari, J.F.; Ancaux, G. Mobility law of dislocations with several character angles and temperatures in FCC aluminum. *Int. J. Plast.* **2017**, *90*, 66–75. <https://doi.org/10.1016/j.ijplas.2016.12.004>.
41. Zhuang, Z.; Liu, Z.; Cui, Y. Strain Gradient Plasticity Theory at the Microscale. In *Dislocation Mechanism-Based Crystal Plasticity*; Academic Press, Cambridge, UK, 2019; pp. 57–90, ISBN 9780128145913.
42. Voyiadjis, G.Z.; Abed, F.H. Effect of dislocation density evolution on the thermomechanical response of metals with different crystal structures at low and high strain rates and temperatures. *Arch. Mech.* **2005**, *57*, 299–343. <https://doi.org/10.24423/aom.190>.
43. Jata, K.V.; Sankaran, K.K.; Ruschau, J.J. Friction-stir welding effects on microstructure and fatigue of aluminum alloy 7050-T7451. *Metall. Mater. Trans. A Phys. Metall. Mater. Sci.* **2000**, *31*, 2181–2192. <https://doi.org/10.1007/s11661-000-0136-9>.
44. Prangnell, P.B.; Heason, C.P. Grain structure formation during friction stir welding observed by the “stop action technique”. *Acta Mater.* **2005**, *53*, 3179–3192. <https://doi.org/10.1016/j.actamat.2005.03.044>.

45. Woo, W.; Balogh, L.; Ungár, T.; Choo, H.; Feng, Z. Grain structure and dislocation density measurements in a friction-stir welded aluminum alloy using X-ray peak profile analysis. *Mater. Sci. Eng. A* **2008**, *498*, 308–313. <https://doi.org/10.1016/j.msea.2008.08.007>.
46. Woo, W.; Ungár, T.; Feng, Z.; Kenik, E.; Clausen, B. X-ray and neutron diffraction measurements of dislocation density and subgrain size in a friction-stir-welded aluminum alloy. *Metall. Mater. Trans. A Phys. Metall. Mater. Sci.* **2010**, *41*, 1210–1216. <https://doi.org/10.1007/s11661-009-9963-5>.
47. Yuzbekova, D.; Kulitskiy, V.; Mogucheva, A.; Kaibyshev, R. Effect of friction stir welding on microstructure of a 5024 alloy. *Mater. Sci. Forum* **2017**, *879*, 2249–2254. <https://doi.org/10.4028/www.scientific.net/MSF.879.2249>.
48. Ni, D.R.; Chen, D.L.; Wang, D.; Xiao, B.L.; Ma, Z.Y. Tensile properties and strain-hardening behaviour of friction stir welded SiCp/AA2009 composite joints. *Mater. Sci. Eng. A* **2014**, *608*, 1–10. <https://doi.org/10.1016/j.msea.2014.04.060>.
49. Nişancioğlu, K. Corrosion and protection of aluminum alloys in seawater. In *Corrosion Behaviour and Protection of Copper and Aluminium Alloys in Seawater*; European Federation of Corrosion (EFC) Series; Woodhead Publishing, Sawston, UK, 2007; pp. 145–155, ISBN 9781845692414.
50. Sukiman, N.L.; Zhou, X.; Birbilis, N.; Hughes, A.E.; Mol, J.M.C.; Garcia, S.J.; Thompson, G.E. Durability and Corrosion of Aluminium and Its Alloys: Overview, Property Space, Techniques and Developments. In *Aluminium Alloys—New Trends in Fabrication and Applications*; IntechOpen, London, UK, 2012; pp. 47–97, ISBN 978-953-51-0861-0.
51. Kartsonakis, I.A.; Dragatogiannis, D.A.; Koumoulos, E.P.; Karantonis, A.; Charitidis, C.A. Corrosion behaviour of dissimilar friction stir welded aluminium alloys reinforced with nanoadditives. *Mater. Des.* **2016**, *102*, 56–67. <https://doi.org/10.1016/j.matdes.2016.04.027>.
52. Qin, H.; Zhang, H.; Sun, D.; Zhuang, Q. Corrosion behavior of the friction-stir-welded joints of 2A14-T6 aluminum alloy. *Int. J. Miner. Metall. Mater.* **2015**, *22*, 627–638. <https://doi.org/10.1007/s12613-015-1116-9>.
53. Zucchi, F.; TrabANELLI, G.; Grassi, V. Pitting and stress corrosion cracking resistance of friction stir welded AA 5083. *Werkst. Und Korros.* **2001**, *52*, 853–859. [https://doi.org/10.1002/1521-4176\(200111\)52:11<853::aid-maco853>3.0.co;2-1](https://doi.org/10.1002/1521-4176(200111)52:11<853::aid-maco853>3.0.co;2-1).
54. Maggiolino, S.; Schmid, C. Corrosion resistance in FSW and in MIG welding techniques of AA6XXX. *J. Mater. Process. Technol.* **2008**, *197*, 237–240. <https://doi.org/10.1016/j.jmatprotec.2007.06.034>.
55. Ralston, K.D.; Fabijanic, D.; Birbilis, N. Effect of grain size on corrosion of high purity aluminium. *Electrochim. Acta* **2011**, *56*, 1729–1736. <https://doi.org/10.1016/j.electacta.2010.09.023>.
56. Song, D.; Ma, A.; Jiang, J.; Lin, P.; Yang, D. Corrosion behavior of ultra-fine grained industrial pure Al fabricated by ECAP. *Trans. Nonferrous Met. Soc. China* **2009**, *19*, 1065–1070. [https://doi.org/10.1016/S1003-6326\(08\)60407-0](https://doi.org/10.1016/S1003-6326(08)60407-0).

## 8. DECLARATIONS OF THE CONTRIBUTION OF CO-AUTHORS

### 8.1. [P1] Friction Stir Welding – an overview of tool geometry and process parameters.



Gdańsk, 30.05.2023

Dr hab. inż. Marek Szkodo, prof. GUT  
Faculty of Mechanical Engineering  
and Ship Technology  
Gdańsk University of Technology  
Narutowicza 11/12  
80-233 Gdańsk, Poland  
marek.szkodo@pg.edu.pl

#### DECLARATION

I hereby declare that my contribution to the preparation of the manuscript entitled:

Laska, A, Szkodo, M. Friction Stir Welding – an overview of tool geometry and process parameters.

involved the analysis of the collected data and the supervision of the preparation of the manuscript.

In addition, I declare that Aleksandra Laska had a dominant contribution to the preparation of this research publication. I agree to submit this publication as a part of the doctoral dissertation of Aleksandra Laska in the form of a coherent thematic collection of publications.

Sincerely,



Marek Szkodo

## 8.2. [P2] Manufacturing Parameters, Materials, and Welds Properties of Butt Friction Stir Welded Joints – Overview.



FACULTY OF  
MECHANICAL ENGINEERING  
AND SHIP TECHNOLOGY

Gdańsk, 30.05.2023

Dr hab. inż. Marek Szkodo, prof. GUT  
Faculty of Mechanical Engineering  
and Ship Technology  
Gdańsk University of Technology  
Narutowicza 11/12  
80-233 Gdańsk, Poland  
marek.szkodo@pg.edu.pl

### DECLARATION

I hereby declare that my contribution to the preparation of the manuscript entitled:

Laska, A, Szkodo, M. Manufacturing Parameters, Materials, and Welds Properties of Butt Friction Stir Welded Joints—Overview. *Materials*. 2020, 13(21), 4940. <https://doi.org/10.3390/ma13214940>

was equal to 5 %. My contribution involved the analysis of the collected data and the supervision of the preparation of the manuscript.

In addition, I declare that Aleksandra Laska had a dominant contribution to the preparation of this research publication. I agree to submit this publication as a part of the doctoral dissertation of Aleksandra Laska in the form of a coherent thematic collection of publications.

Sincerely,

Marek Szkodo

### 8.3. [P3] Temperature evolution, material flow and resulting mechanical properties as a function of tool geometry during Friction Stir Welding of AA6082.



**UNIVERSITÀ  
DEL SALENTO**

Lecce, 31.05.2023

PhD Behzad Sadeghi  
Department of Innovation Engineering  
University of Salento  
Via per Arnesano  
73100 Lecce, Italy  
b.sadeghi2020@gmail.com

#### DECLARATION

I hereby declare that my contribution to the preparation of the manuscript entitled:

Laska A, Sadeghi B, Sadeghian B, Taherizadeh A, Szkodo M, Cavaliere P. Temperature evolution, material flow and resulting mechanical properties as a function of tool geometry during Friction Stir Welding of AA6082.

involved the development of the research plan, conducting computer simulations and the analysis of the results obtained.

In addition, I declare that Aleksandra Laska had a dominant contribution to the preparation of this research publication. I agree to submit this publication as a part of the doctoral dissertation of Aleksandra Laska in the form of a coherent thematic collection of publications.

Sincerely,

Behzad Sadeghi



Isfahan, 31.05.2023

PhD Behzad Sadeghian  
Department of Materials Engineering  
Isfahan University of Technology  
Isfahan 8415683111 Iran  
behzadsadeghian91@gmail.com

#### DECLARATION

I hereby declare that my contribution to the preparation of the manuscript entitled:

Laska A, Sadeghi B, Sadeghian B, Taherizadeh A, Szkodo M, Cavaliere P. Temperature evolution, material flow and resulting mechanical properties as a function of tool geometry during Friction Stir Welding of AA6082.

involved the development of the research plan, conducting computer simulations and the analysis of the results obtained.

In addition, I declare that Aleksandra Laska had a dominant contribution to the preparation of this research publication. I agree to submit this publication as a part of the doctoral dissertation of Aleksandra Laska in the form of a coherent thematic collection of publications.

Sincerely,

Behzad Sadeghian







Isfahan, 31.05.2023

PhD Aboozar Taherizadeh  
Department of Materials Engineering  
Isfahan University of Technology  
Isfahan 8415683111 Iran  
a.taheri@iut.ac.ir

#### DECLARATION

I hereby declare that my contribution to the preparation of the manuscript entitled:

Laska A, Sadeghi B, Sadeghian B, Taherizadeh A, Szkodo M, Cavaliere P. Temperature evolution, material flow and resulting mechanical properties as a function of tool geometry during Friction Stir Welding of AA6082.

involved the development of the research plan, conducting computer simulations and the analysis of the results obtained.

In addition, I declare that Aleksandra Laska had a dominant contribution to the preparation of this research publication. I agree to submit this publication as a part of the doctoral dissertation of Aleksandra Laska in the form of a coherent thematic collection of publications.

Sincerely,

Aboozar Taherizadeh



Gdańsk, 30.05.2023

Dr hab. inż. Marek Szkodo, prof. GUT  
Faculty of Mechanical Engineering  
and Ship Technology  
Gdańsk University of Technology  
Narutowicza 11/12  
80-233 Gdańsk, Poland  
marek.szkodo@pg.edu.pl

#### DECLARATION

I hereby declare that my contribution to the preparation of the manuscript entitled:

Laska A, Sadeghi B, Sadeghian B, Taherizadeh A, Szkodo M, Cavaliere P. Temperature evolution, material flow and resulting mechanical properties as a function of tool geometry during Friction Stir Welding of AA6082.

involved the development of the methodology, the analysis of the collected data, supervision, reviewing and editing of the manuscript.

In addition, I declare that Aleksandra Laska had a dominant contribution to the preparation of this research publication. I agree to submit this publication as a part of the doctoral dissertation of Aleksandra Laska in the form of a coherent thematic collection of publications.

Sincerely,



Marek Szkodo



**UNIVERSITÀ  
DEL SALENTO**

Lecce, 21.02.2023

Prof. Pasquale Cavaliere  
Department of Innovation Engineering  
University of Salento  
Via per Arnesano  
73100 Lecce, Italy  
pasquale.cavaliere@unisalento.it

#### DECLARATION

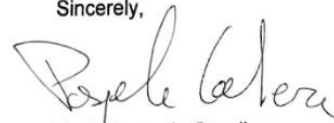
I hereby declare that my contribution to the preparation of the manuscript entitled:

Laska A, Sadeghi B, Sadeghian B, Taherizadeh A, Szkodo M, Cavaliere P. Temperature evolution, material flow and resulting mechanical properties as a function of tool geometry during Friction Stir Welding of AA6082.

involved the development of the research plan, the analysis of the results obtained, and the supervision of the preparation of the manuscript.

In addition, I declare that Aleksandra Laska had a dominant contribution to the preparation of this research publication. I agree to submit this publication as a part of the doctoral dissertation of Aleksandra Laska in the form of a coherent thematic collection of publications.

Sincerely,



Prof. Pasquale Cavaliere

#### 8.4. [P4] Effect of Processing Parameters on Strength and Corrosion Resistance of Friction Stir-Welded AA6082.



FACULTY OF  
MECHANICAL ENGINEERING  
AND SHIP TECHNOLOGY

Gdańsk, 30.05.2023

Dr hab. inż. Marek Szkodo, prof. GUT  
Faculty of Mechanical Engineering  
and Ship Technology  
Gdańsk University of Technology  
Narutowicza 11/12  
80-233 Gdańsk, Poland  
marek.szkodo@pg.edu.pl

#### DECLARATION

I hereby declare that my contribution to the preparation of the manuscript entitled:

Laska A, Szkodo M, Koszelow D, Cavaliere P. Effect of Processing Parameters on Strength and Corrosion Resistance of Friction Stir-Welded AA6082. *Metals*. 2022; 12(2):192. <https://doi.org/10.3390/met12020192>.

was equal to 25 %. My contribution involved the analysis of the collected data, supervision, reviewing and editing of the manuscript.

In addition, I declare that Aleksandra Laska had a dominant contribution to the preparation of this research publication. I agree to submit this publication as a part of the doctoral dissertation of Aleksandra Laska in the form of a coherent thematic collection of publications.

Sincerely,

Marek Szkodo



FACULTY OF ELECTRONICS,  
TELECOMMUNICATIONS  
AND INFORMATICS

Gdańsk, 30.05.2023

MSc Eng. Damian Koszelow  
Faculty of Electronics, Telecommunications  
and Informatics  
Gdańsk University of Technology  
Narutowicza 11/12  
80-233 Gdańsk, Poland  
damian.koszelow@pg.edu.pl

#### DECLARATION

I hereby declare that my contribution to the preparation of the manuscript entitled:

Laska A, Szkodo M, Koszelow D, Cavaliere P. Effect of Processing Parameters on Strength and Corrosion Resistance of Friction Stir-Welded AA6082. *Metals*. 2022; 12(2):192. <https://doi.org/10.3390/met12020192>.

was equal to 5 %. My contribution involved the scanning electron microscopy observations and the analysis of the results obtained.

In addition, I declare that Aleksandra Laska had a dominant contribution to the preparation of this research publication. I agree to submit this publication as a part of the doctoral dissertation of Aleksandra Laska in the form of a coherent thematic collection of publications.

Sincerely,

Damian Koszelow



**UNIVERSITÀ  
DEL SALENTO**

Lecce, 21.02.2023

Prof. Pasquale Cavaliere  
Department of Innovation Engineering  
University of Salento  
Via per Arnesano  
73100 Lecce, Italy  
pasquale.cavaliere@unisalento.it

#### DECLARATION

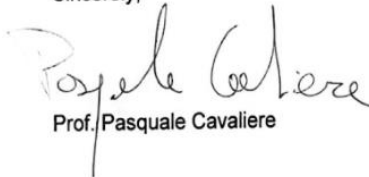
I hereby declare that my contribution to the preparation of the manuscript entitled:

Laska A, Szkodo M, Koszelow D, Cavaliere P. Effect of Processing Parameters on Strength and Corrosion Resistance of Friction Stir-Welded AA6082. *Metals*. 2022; 12(2):192. <https://doi.org/10.3390/met12020192>.

was equal to 10 %. My contribution involved the development of the research plan, the analysis of the results obtained, and the supervision of the preparation of the manuscript.

In addition, I declare that Aleksandra Laska had a dominant contribution to the preparation of this research publication. I agree to submit this publication as a part of the doctoral dissertation of Aleksandra Laska in the form of a coherent thematic collection of publications.

Sincerely,



Prof. Pasquale Cavaliere



## 8.5. [P5] Analysis of Residual Stresses and Dislocation Density of AA6082 Butt Welds Produced by Friction Stir Welding.



Gdańsk, 30.05.2023

Dr hab. inż. Marek Szkodo, prof. GUT  
Faculty of Mechanical Engineering  
and Ship Technology  
Gdańsk University of Technology  
Narutowicza 11/12  
80-233 Gdańsk, Poland  
marek.szkodo@pg.edu.pl

### DECLARATION

I hereby declare that my contribution to the preparation of the manuscript entitled:

Laska A, Szkodo M, Cavaliere P, Moszczyńska D, Mizera J. Analysis of Residual Stresses and Dislocation Density of AA6082 Butt Welds Produced by Friction Stir Welding. Metallurgical and Materials Transactions A – Physical Metallurgy and Materials Science. 2023; 54, 211-225. <https://doi.org/10.1007/s11661-022-06862-4>.

was equal to 25 %. My contribution involved the analysis of the collected data, supervision, reviewing and editing of the manuscript.

In addition, I declare that Aleksandra Laska had a dominant contribution to the preparation of this research publication. I agree to submit this publication as a part of the doctoral dissertation of Aleksandra Laska in the form of a coherent thematic collection of publications.

Sincerely,



Marek Szkodo



**UNIVERSITÀ  
DEL SALENTO**

Lecce, 21.02.2023

Prof. Pasquale Cavaliere  
Department of Innovation Engineering  
University of Salento  
Via per Arnesano  
73100 Lecce, Italy  
pasquale.cavaliere@unisalento.it

#### DECLARATION

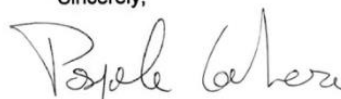
I hereby declare that my contribution to the preparation of the manuscript entitled:

Laska A, Szkodo M, Cavaliere P, Moszczyńska D, Mizera J. Analysis of Residual Stresses and Dislocation Density of AA6082 Butt Welds Produced by Friction Stir Welding. *Metallurgical and Materials Transactions A – Physical Metallurgy and Materials Science*. 2023; 54, 211-225. <https://doi.org/10.1007/s11661-022-06862-4>.

was equal to 5 %. My contribution involved the development of the research plan, the analysis of the results obtained, and the supervision of the preparation of the manuscript.

In addition, I declare that Aleksandra Laska had a dominant contribution to the preparation of this research publication. I agree to submit this publication as a part of the doctoral dissertation of Aleksandra Laska in the form of a coherent thematic collection of publications.

Sincerely,



Prof. Pasquale Cavaliere





Warszawa, 30.05.2023

Dr inż. Dorota Moszczyńska  
Faculty of Materials Science  
and Engineering  
Warsaw University of Technology  
Wolowska 141  
02-507 Warsaw, Poland  
dorota.moszczyńska@pw.edu.pl

#### DECLARATION

I hereby declare that my contribution to the preparation of the manuscript entitled:

Laska A, Szkodo M, Cavaliere P, Moszczyńska D, Mizera J. Analysis of Residual Stresses and Dislocation Density of AA6082 Butt Welds Produced by Friction Stir Welding. Metallurgical and Materials Transactions A – Physical Metallurgy and Materials Science. 2023; 54, 211-225. <https://doi.org/10.1007/s11661-022-06862-4>.

was equal to 5 %. My contribution involved the development of the research plan, the electron backscatter diffraction (EBSD) observations and the analysis of the obtained results.

In addition, I declare that Aleksandra Laska had a dominant contribution to the preparation of this research publication. I agree to submit this publication as a part of the doctoral dissertation of Aleksandra Laska in the form of a coherent thematic collection of publications.

Sincerely,

Dorota Moszczyńska



Warszawa, 30.05.2023

Prof. dr hab. inż. Jarosław Mizera  
Faculty of Materials Science  
and Engineering  
Warsaw University of Technology  
Wolaska 141  
02-507 Warsaw, Poland  
jaroslaw.mizera@pw.edu.pl

#### DECLARATION

I hereby declare that my contribution to the preparation of the manuscript entitled:

Laska A, Szkodo M, Cavaliere P, Moszczyńska D, Mizera J. Analysis of Residual Stresses and Dislocation Density of AA6082 Butt Welds Produced by Friction Stir Welding. Metallurgical and Materials Transactions A – Physical Metallurgy and Materials Science. 2023; 54, 211-225. <https://doi.org/10.1007/s11661-022-06862-4>.

was equal to 5 %. My contribution involved the development of the methodology, formal analysis, supervision and reviewing the manuscript.

In addition, I declare that Aleksandra Laska had a dominant contribution to the preparation of this research publication. I agree to submit this publication as a part of the doctoral dissertation of Aleksandra Laska in the form of a coherent thematic collection of publications.

Sincerely,

A handwritten signature in black ink that reads 'Jarosław Mizera'. The signature is fluid and cursive, with a long horizontal stroke at the end.

Jarosław Mizera

## 8.6. [P6] Corrosion Properties of Dissimilar AA6082/AA6060 Friction Stir Welded Butt Joints in Different NaCl concentrations.



FACULTY OF  
MECHANICAL ENGINEERING  
AND SHIP TECHNOLOGY

Dr hab. inż. Marek Szkodo, prof. GUT  
Faculty of Mechanical Engineering  
and Ship Technology  
Gdańsk University of Technology  
Narutowicza 11/12  
80-233 Gdańsk, Poland  
marek.szmodo@pg.edu.pl

Gdańsk, 30.05.2023

### DECLARATION

I hereby declare that my contribution to the preparation of the manuscript entitled:

Laska A, Szkodo M, Pawłowski Ł, Gajowiec G. Corrosion Properties of Dissimilar AA6082/AA6060 Friction Stir Welded Butt Joints in Different NaCl Concentrations. International Journal of Precision Engineering and Manufacturing-Green Technology. 2023; 10, 457-477. <https://doi.org/10.1007/s40684-022-00441-z>

was equal to 40 %. My contribution involved the development of the research plan, the analysis of the obtained results, the discussion on the results, preparing some figures and the supervision of the preparation of the manuscript.

In addition, I declare that Aleksandra Laska had a dominant contribution to the preparation of this research publication. I agree to submit this publication as a part of the doctoral dissertation of Aleksandra Laska in the form of a coherent thematic collection of publications.

Sincerely,



Marek Szkodo





Gdańsk, 30.05.2023

MSc Eng. Łukasz Pawłowski  
Faculty of Mechanical Engineering  
and Ship Technology  
Gdańsk University of Technology  
Narutowicza 11/12  
80-233 Gdańsk, Poland  
lukasz.pawlowski@pg.edu.pl

#### DECLARATION

I hereby declare that my contribution to the preparation of the manuscript entitled:

Laska A, Szkodo M, Pawłowski Ł, Gajowiec G. Corrosion Properties of Dissimilar AA6082/AA6060 Friction Stir Welded Butt Joints in Different NaCl Concentrations. International Journal of Precision Engineering and Manufacturing-Green Technology. 2023; 10, 457-477. <https://doi.org/10.1007/s40684-022-00441-z>

was equal to 3 %. My contribution involved the impedance spectroscopy measurements and the analysis of the results obtained.

In addition, I declare that Aleksandra Laska had a dominant contribution to the preparation of this research publication. I agree to submit this publication as a part of the doctoral dissertation of Aleksandra Laska in the form of a coherent thematic collection of publications.

Sincerely,



Łukasz Pawłowski



FACULTY OF  
MECHANICAL ENGINEERING  
AND SHIP TECHNOLOGY

Gdańsk, 30.05.2023

PhD Eng. Grzegorz Gajowiec  
Faculty of Mechanical Engineering  
and Ship Technology  
Gdańsk University of Technology  
Narutowicza 11/12  
80-233 Gdańsk, Poland  
grzegorz.gajowiec@pg.edu.pl

#### DECLARATION

I hereby declare that my contribution to the preparation of the manuscript entitled:

Laska A, Szkodo M, Pawłowski Ł, Gajowiec G. Corrosion Properties of Dissimilar AA6082/AA6060 Friction Stir Welded Butt Joints in Different NaCl Concentrations. International Journal of Precision Engineering and Manufacturing-Green Technology. 2023; 10, 457-477. <https://doi.org/10.1007/s40684-022-00441-z>

was equal to 2 %. My contribution involved the scanning electron microscopy observations and the analysis of the results obtained.

In addition, I declare that Aleksandra Laska had a dominant contribution to the preparation of this research publication. I agree to submit this publication as a part of the doctoral dissertation of Aleksandra Laska in the form of a coherent thematic collection of publications.

Sincerely,

Grzegorz Gajowiec

## 8.7. [P7] Influence of the Tool Rotational Speed on Physical and Chemical Properties of Dissimilar Friction-Stir-Welded AA5083/AA6060 Joints.



FACULTY OF  
MECHANICAL ENGINEERING  
AND SHIP TECHNOLOGY

Gdańsk, 30.05.2023

Dr hab. inż. Marek Szkodo, prof. GUT  
Faculty of Mechanical Engineering  
and Ship Technology  
Gdańsk University of Technology  
Narutowicza 11/12  
80-233 Gdańsk, Poland  
marek.szkodo@pg.edu.pl

### DECLARATION

I hereby declare that my contribution to the preparation of the manuscript entitled:

Laska A, Szkodo M, Cavaliere P, Perrone A. Influence of the Tool Rotational Speed on Physical and Chemical Properties of Dissimilar Friction-Stir-Welded AA5083/AA6060 Joints. *Metals*. 2022; 12(10):1658. <https://doi.org/10.3390/met12101658>.

was equal to 14 %. My contribution involved the development of the methodology, the analysis of the collected data, supervision, reviewing and editing of the manuscript.

In addition, I declare that Aleksandra Laska had a dominant contribution to the preparation of this research publication. I agree to submit this publication as a part of the doctoral dissertation of Aleksandra Laska in the form of a coherent thematic collection of publications.

Sincerely,

Marek Szkodo



**UNIVERSITÀ  
DEL SALENTO**

Lecce, 21.02.2023

Prof. Pasquale Cavaliere  
Department of Innovation Engineering  
University of Salento  
Via per Arnesano  
73100 Lecce, Italy  
pasquale.cavaliere@unisalento.it

#### DECLARATION

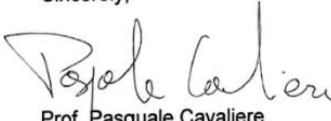
I hereby declare that my contribution to the preparation of the manuscript entitled:

Laska A, Szkodo M, Cavaliere P, Perrone A. Influence of the Tool Rotational Speed on Physical and Chemical Properties of Dissimilar Friction-Stir-Welded AA5083/AA6060 Joints. *Metals*. 2022; 12(10):1658. <https://doi.org/10.3390/met12101658>.

was equal to 3 %. My contribution involved the development of the research plan, the analysis of the results obtained, and the supervision of the preparation of the manuscript.

In addition, I declare that Aleksandra Laska had a dominant contribution to the preparation of this research publication. I agree to submit this publication as a part of the doctoral dissertation of Aleksandra Laska in the form of a coherent thematic collection of publications.

Sincerely,



Prof. Pasquale Cavaliere



**UNIVERSITÀ  
DEL SALENTO**

Lecce, 21.02.2023

PhD Eng. Angelo Perrone  
Department of Innovation Engineering  
University of Salento  
Via per Arnesano  
73100 Lecce, Italy  
angelo.perrone@unisalento.it

#### DECLARATION

I hereby declare that my contribution to the preparation of the manuscript entitled:

Laska A, Szkodo M, Cavaliere P, Perrone A. Influence of the Tool Rotational Speed on Physical and Chemical Properties of Dissimilar Friction-Stir-Welded AA5083/AA6060 Joints. *Metals*. 2022; 12(10):1658. <https://doi.org/10.3390/met12101658>.

was equal to 3 %. My contribution involved the development of the methodology, the analysis of the obtained results and the review and editing of the manuscript.

In addition, I declare that Aleksandra Laska had a dominant contribution to the preparation of this research publication. I agree to submit this publication as a part of the doctoral dissertation of Aleksandra Laska in the form of a coherent thematic collection of publications.

Sincerely,

PhD Eng. Angelo Perrone



## 9. SCIENTIFIC AND ORGANIZATIONAL ACHIEVEMENTS OF THE DOCTORAL CANDIDATE

### 9.1. Bibliometric indicators

Source	Web of Science	Scopus	Google Scholar
<b>h-index</b>	3	3	5
<b>Number of publications</b>	13	12	13
<b>Number of citations</b>	37	41	57
<b>Number of citations excluding auto-citations</b>	28	31	-

\*

**Total IF: 41.252**

**Total points of the Polish Ministry of Science and Higher Education: 1320**

**Review activity:**

- Journal of Materials Engineering and Performance (6 reviews)
- Steel Research International (2 reviews)
- Thermochemica Acta (2 reviews)
- International Journal of Pressure Vessels and Piping (1 review)
- Materialia (1 review)
- Surface and Coatings Technology (1 review)
- Physica status solidi (RRL) - Rapid Research Letters (1 review)

Data for the date 05.06.2023

### 9.2. List of publications

1. Laska, A., Szkodo, M., Cavaliere, P., Moszczyńska, D., Mizera, J., Analysis of Residual Stresses and Dislocation Density of AA6082 Butt Welds Produced by Friction Stir Welding (2023), Metallurgical and Materials Transactions A: Physical Metallurgy and Materials Science, 54, 211-225. <https://doi.org/10.1007/s11661-022-06862-4>

2. Laska, A., Szkodo, M., Pawłowski, Ł., Gajowiec, G., Corrosion Properties of Dissimilar AA6082/AA6060 Friction Stir Welded Butt Joints in Different NaCl Concentrations (2023), *International Journal of Precision Engineering and Manufacturing - Green Technology*, 10, 457-477. <https://doi.org/10.1007/s40684-022-00441-z>
3. Laska, A., Szkodo, M., Cavaliere, P., Perrone, A., Influence of the Tool Rotational Speed on Physical and Chemical Properties of Dissimilar Friction-Stir-Welded AA5083/AA6060 Joints (2022), *Metals*, 12, 1658. <https://doi.org/10.3390/met12101658>
4. Laska, A., Szkodo, M., Koszelow, D., Cavaliere, P., Effect of Processing Parameters on Strength and Corrosion Resistance of Friction Stir-Welded AA6082 (2022), *Metals*, 12, 192. <https://doi.org/10.3390/met12020192>
5. Laska, A., Szkodo, M., Manufacturing Parameters, Materials, and Welds Properties of Butt Friction Stir Welded Joints—Overview (2020), *Materials*, 13, 4940. <https://doi.org/10.3390/ma13214940>
6. Laska, A., Bartmański, M., Parameters of the electrophoretic deposition process and its influence on the morphology of hydroxyapatite coatings. Review (2020), *Inżynieria Materiałowa*, 1, 20-25. <https://doi.org/10.15199/28.2020.1.3>
7. Sadeghi, B., Sadeghian, B., Taherizadeh, A., Laska, A., Cavaliere, P., Gopinathan, A., Effect of Porosity on the Thermo-Mechanical Behavior of Friction-Stir-Welded Spark-Plasma-Sintered Aluminum Matrix Composites with Bimodal Micro- and Nano-Sized Reinforcing Al<sub>2</sub>O<sub>3</sub> Particles (2022), *Metals*, 12, 1660. <https://doi.org/10.3390/met12101660>
8. Sadeghi, B., Cavaliere, P., Laska, A., Perrone, A., Blasi, G., Gopinathan, A., Shamanian, M., Ashrafizadeh, F., Effect of processing parameters on the cyclic behaviour of aluminium friction stir welded to spark plasma sintered aluminium matrix composites with bimodal micro-and nano-sized reinforcing alumina particles (2023), *Materials Characterizations*, 195, 112535. <https://doi.org/10.1016/j.matchar.2022.112535>
9. Cavaliere, P., Perrone, A., Silvello, A., Laska, A., Blasi, G., Cano, I. G., Sadeghi, B., Nagy, S., Cyclic behavior of FeCoCrNiMn high entropy alloy coatings produced through cold spray (2023), *Journal of Alloys and Compounds*, 931, 167550. <https://doi.org/10.1016/j.jallcom.2022.167550>
10. Sadeghi, B., Shabani, A., Heidarinejad, A., Laska, A., Szkodo, M., Cavaliere, P., A Quantitative Investigation of Dislocation Density in an Al Matrix Composite Produced

by a Combination of Micro-/Macro-Rolling (2022), *Journal of Composites Science*, 6, 199. <https://doi.org/10.3390/jcs6070199>

11. Najafizadeh, M., Ghasempour-Mouziraji, M., Hosseinzadeh, M., Yazdi, S., Sarrafan, A., Bozorg, M., Cavaliere, P., Laska, A., Szkodo, M., Optimization of biocorrosion resistance and mechanical properties of PM Ti–XAl–2Fe–3Cu alloys by response surface methodology (2022), *Journal of materials science*, 57, 18669-18689. <https://doi.org/10.1007/s10853-022-07768-7>
12. Cavaliere, P., Perrone, A., Silvello, A., Laska, A., Blasi, G., Cano, I. G., Fatigue Bending of V-Notched Cold-Sprayed FeCoCrNiMn Coatings (2022), *Metals*, 12, 780. <https://doi.org/10.3390/met12050780>
13. Kowalczyk, Łukasz, Korol, J., Chmielnicki, B., Laska, A., Chuchała, D., Hejna, A., One More Step Towards a Circular Economy for Thermal Insulation Materials— Development of Composites Highly Filled with Waste Polyurethane (PU) Foam for Potential Use in the Building Industry (2023), *Materials*, 16, 782. <https://doi.org/10.3390/ma16020782>

### 9.3. Conference presentations

1. Oral presentation:

Laska A., *FSW method as an innovative welding technique on the example of aluminum alloys*, Belzona – Innovation in Technology VI edition, 16 May 2023, Gdansk, Poland

2. Oral presentation:

Laska A., *Influence of the process parameters on the properties of AA6082 joints welded by the FSW method*, 3rd International Conference on Materials Science & Engineering, 28 March 2023, On-line

3. Oral presentation:

Laska A., *Modern method of joining materials - Friction Stir Welding and its influence on the properties of aluminum alloy joints*, 3rd International Virtual Conference on Advanced Functional Materials (ICAFM-2022), 1-3 December 2022, On-line

4. Oral presentation:

Laska A., *The influence of friction stir welding process parameters on residual stresses and dislocation density in AA6082 welds*, 24th International Conference Materials, Methods and Technologies, 19-22 August 2022, Burgas, Bulgaria

5. Oral presentation:

Laska A., *The effect of residual stresses and dislocation density on the electrochemical properties of AA6082/AA6060 dissimilar joints produced by Friction Stir Welding method*, Belzona – Innovation in Technology V edition 18 May 2022, Gdansk, Poland

6. Oral presentation:

Laska A., Szkodo M., *The influence of residual stresses and dislocation density on the electrochemical properties of dissimilar AA6082/AA6060 joints fabricated by the FSW method*, 2nd International Conference on advanced joining processes, 21-22 October 2021, Sintra, Portugal

7. Oral presentation:

Laska A., Szkodo M., *Analysis of residual stresses and crystallite size of AA6082/AA6060 friction stir welded butt joints produced with different tool traverse speed*, 23rd International Conference Materials, Methods and Technologies, 19-22 August 2021, Burgas, Bulgaria

8. Poster presentation:

Laska A., *Corrosion properties of dissimilar AA6082/AA6060 friction stir welded butt joints in different NaCl concentrations*, 5th International Conference on Materials Research and Nanotechnology ICMRN-2023, 20-21 April 2023, On-line

#### 9.4. Projects

Implementation of activities in the project NEW APPROACH TO INNOVATIVE TECHNOLOGIES IN MANUFACTURING "NEPTUN" **101079398-NEPTUN-HORIZON-WIDERA-2021\_ACCESS-03** (European Research Executive Agency REA)

#### 9.5. Professional training

- Certified training in the use of MEASURLINK v.9 software - 2023
- Certified training in the use of nanoindenter Alemnis In-situ SEM - 2022
- Certified training in the use and analysis of microtomography instrument - V/TOME/X S Waygate Technology – 2021

## 9.6. Research internships

- **June 2023 (one week)**

Department of Innovation Engineering, University of Salento, Lecce, Italy, Research Intern - a research team led by Prof. Pasquale Cavaliere – project on direct hydrogen reduction of iron oxide pellet

- **January 2023 (one week)**

The Brandenburg University of Technology Cottbus-Senftenberg (BTU), Department of Welding and Joining, Cottbus, Germany, Research Visitor – project on Impulse Friction Stir Welding of aluminum alloys

- **June 2022 (one week)**

Research Welding Institute, Research and Development Division of Welding Technologies and Equipment, Bratislava, Slovakia, Research Visitor – project on Friction Stir Welding of aluminum alloys

- **November 2021 (one month)**

Department of Innovation Engineering, University of Salento, Lecce, Italy, Research Intern - a research team led by Prof. Pasquale Cavaliere – project on Friction Stir Welding of aluminum alloys

- **September 2019 (one month)**

Belarusian State University of Informatics and Radioelectronics, Minsk, Belarus Project Intern- a research team led by Prof. Vadim Bogush – project on computer simulations of physical properties of nanoparticles

- **July 2018 - September 2018 (3 months)**

Faculty of Engineering, Tarbiat Modares University, Tehran, Iran, Project Intern - a research team led by Prof. Hamid Delavari – project on the production of carbon quantum dots

## 9.7. Awards

- In 2015/2016, 2016/2017, 2017/2018, and 2018/2019 GUT rector's academic scholarship for the best students.
- In 2021/2022 and 2022/2023, scholarship FRANCIUM for outstanding doctoral students IDUB GUT.
- In 2022/2022 scholarship for scientific achievements under the POWER project POWR.03.02.00-IP.08-00-DOK/16.

- In 2021 - travel scholarship within the PROM NAWA project - International scholarship exchange of doctoral students and academic staff in the field of modern technologies
- Completion of bachelor's and master's degrees with the rector's distinction

#### **9.8. Organizational activities**

- Member of the Faculty Committee for Ensuring the Quality of Education, for the 2021-2024 term, Faculty of Mechanical Engineering and Ship Technology, Gdańsk University of Technology
- Volunteering at the Foundation for Nanotechnology and Nanoscience Support NANONET (October 2017 – present)
- Member of the Organizing Committee, 4th National Scientific Conference IMPLANTS 2022, 27-28 May 2022, Gdańsk, Poland
- Member of the Organizing Committee, 3rd National Scientific Conference IMPLANTS 2021, 18 May 2021, on-line
- Member of the Organizing Committee, 2nd National Scientific Conference IMPLANTS 2019, 28-29 May 2019, Gdańsk, Poland